



**HAL**  
open science

# Methodology for Modeling and Detection of inter-turn short-circuit faults of a Permanent Magnet Assisted Synchronous Reluctance Motor in Electric vehicles

Pakédam Lare

► **To cite this version:**

Pakédam Lare. Methodology for Modeling and Detection of inter-turn short-circuit faults of a Permanent Magnet Assisted Synchronous Reluctance Motor in Electric vehicles. Electric power. Université Paris-Saclay, 2023. English. NNT : 2023UPAST198 . tel-04509413

**HAL Id: tel-04509413**

**<https://theses.hal.science/tel-04509413>**

Submitted on 18 Mar 2024

**HAL** is a multi-disciplinary open access archive for the deposit and dissemination of scientific research documents, whether they are published or not. The documents may come from teaching and research institutions in France or abroad, or from public or private research centers.

L'archive ouverte pluridisciplinaire **HAL**, est destinée au dépôt et à la diffusion de documents scientifiques de niveau recherche, publiés ou non, émanant des établissements d'enseignement et de recherche français ou étrangers, des laboratoires publics ou privés.

Méthodologie de modélisation et de  
détection des défauts de court-circuit  
inter-spores d'un Moteur Synchrone  
Réductant Assisté par Aimant  
Permanent dans les véhicules électriques  
*Methodology for Modeling and Detection of inter-turn  
short-circuit faults of a Permanent Magnet Assisted  
Synchronous Reluctance Motor in Electric vehicles*

Thèse de doctorat de l'université Paris-Saclay

École doctorale n° 575 : Electrical, Optical, Bio : Physics And Engineering (EOBE)  
Spécialité de doctorat : Génie électrique  
Graduate School : Sciences de l'ingénierie et des systèmes. Référent :  
CentraleSupélec

Thèse préparée au **Laboratoire Génie Electrique et Electronique de Paris**,  
(Université Paris-Saclay, CentraleSupélec, CNRS), **Laboratoire des Signaux et  
Systèmes** (Université Paris-Saclay, CNRS, CentraleSupélec) et à l'**IFP Energies  
Nouvelles/ Mobilité & Systèmes**, sous la direction de **Demba DIALLO**, Professeur à  
l'Université Paris-Saclay et le co-encadrement de **Claude DELPHA**, Professeur à  
l'Université Paris-Saclay, **Siyamak SARABI**, Chercheur-PhD à l'IFP Energies Nouvelles,  
**Laid KEFSI**, Chercheur-PhD à l'IFP Energies Nouvelles

Thèse soutenue à l'IFP Energies Nouvelles, le 29 novembre 2023, par

**Pakédam LARE**

**Composition du jury**

Membres du jury avec voix délibérative

<b>Mohamed GABSI</b> Professeur des Universités, ENS Paris Saclay, SATIE	Président du jury
<b>Raphaël ROMARY</b> Professeur des Universités, Université d'Artois, LSEE	Rapporteur & Examineur
<b>Didier THEILLIOL</b> Professeur des Universités, Université de Lorraine, CRAN	Rapporteur & Examineur
<b>Xuefang SHI-LIN</b> Professeure des Universités, INSA de Lyon, Ampere	Examinatrice

**Titre:** Méthodologie de modélisation et de détection des défauts de court-circuit inter-spires d'un Moteur Synchrone Réductant Assisté par Aimant Permanent dans les véhicules électriques

**Mots clés:** Détection de défaut, Machine Synchro-Réductant Assistée d'Aimants Permanents (MSRAP), Suivi d'état de santé, Maintenance prédictive, Traitement de l'information.

**Résumé:** L'essor des véhicules électrifiés (VE) dans le transport routier a accru les préoccupations concernant la fiabilité et la sécurité. Par conséquent, il existe une demande impérieuse de stratégies de détection précoce des défauts dans le groupe motopropulseur électrique (GMPE), crucial pour l'exploitation des véhicules électriques. Cette thèse propose une méthodologie de modélisation des groupes motopropulseurs électriques (GMPE) et de détection de défaut dans leurs machines électriques. Notre étude de cas s'est portée sur la détection des défauts de court-circuit inter-spires dans un Moteur Synchro-Réductant Assistée d'Aimants Permanent (MSRAP). Les analyses proposées pour la détection de défaut sont exclusivement basées sur les signaux des courants statoriques du moteur électrique, une approche considérée économiquement et techniquement viable pour un dispositif de diagnostic embarqué. Pour obtenir la précision nécessaire à la modélisation des défauts du moteur et la vitesse de calcul requise par les contrôleurs en boucle fermée, un modèle hybride du MSRAP combinant son modèle analytique et son modèle éléments finis a été proposé pour représenter le comportement du moteur. Un GMPE a été simulé avec ce modèle du MSRAP dans diverses conditions de fonctionnement et entraînements en boucle fermée pour générer un ensemble de données synthétiques destinées au diagnostic de défaut.

Dans la phase préliminaire de détection de défaut, l'écart absolu médian, le skewness et le kurtosis calculés sur des fenêtres glissantes ont été sélectionnés pour extraire les caractéristiques de notre ensemble de données. Pour détecter les défauts dans les différentes conditions de fonctionnement, nous avons proposé une extension de l'Analyse de Composantes Principales (ACP) basée sur la projection d'attributs de nuisance. Cette approche nous a permis d'atténuer la non-stationnarité des données liée à la variation de charge, permettant ainsi la mise en œuvre d'une détection de défauts insensible aux variations de charge. À la suite d'une évaluation des performances de détection des défauts, nous avons sélectionné le  $T^2$  de Hotelling comme mesure de surveillance fiable pour la détection des défauts de court-circuit inter-spires par l'ACP. Pour estimer la sévérité du défaut, nous avons développé un modèle analytique de la pente de la fonction de décision CUSUM de  $T^2$ . À partir de ce modèle analytique, nous avons pu estimer la sévérité du défaut, des données sans bruit avec une précision supérieure à 99%. La robustesse de notre méthode d'estimation de sévérité de défaut a pu être démontrée à des niveaux de bruit allant jusqu'au rapport signal/bruit ( $SNR = 30dB$ ). En conclusion, nous discutons des limites inhérentes à notre approche et formulons des pistes pour des recherches futures.

**Title:** Methodology for Modeling and Detection of inter-turn short-circuit faults of a Permanent Magnet Assisted Synchronous Reluctance Motor in Electric vehicles

**Keywords:** Fault detection, Permanent Magnet-Assisted Synchronous Reluctance Machine (PMASynRM), Condition monitoring, Predictive maintenance, Information processing.

**Abstract:**

The proliferation of Electrified Vehicles (EVs) in road transportation has heightened concerns regarding reliability and safety. Consequently, there is a pressing demand for early fault detection strategies in the electric powertrain (EPT), pivotal for the operation of electric vehicles. This thesis proposes a methodology for modeling electric powertrains (EPTs) and detecting faults in their electric machines. Our case study focused on detecting inter-turn short-circuit faults in a Permanent Magnet Assisted Synchronous Reluctance Motor (PMASynRM). The proposed fault detection analyses exclusively rely on the stator current signals of the electric motor, an approach considered economically and technically viable for onboard diagnostic devices. To achieve the precision required for motor fault modeling and the computational speed demanded by closed-loop controllers, a hybrid model of the PMASynRM, combining its analytical and finite element models, was proposed to represent the motor's behavior. An EPT was simulated with this PMASynRM modelled under various operating conditions and closed-loop drives to generate a synthetic dataset for fault diagnosis. In the preliminary

fault detection phase, the median absolute deviation, skewness, and kurtosis computed over sliding windows were selected to extract features from our dataset. To detect faults under different operating conditions, we proposed an extension of Principal Component Analysis (PCA) based on the Nuisance Attribute Projection. This approach allowed us to mitigate the non-stationarity of data associated with load variation, enabling the implementation of a fault detection mechanism insensitive to load fluctuations. Following an assessment of fault detection performance, Hotelling's  $T^2$  was chosen as a reliable surveillance measure for detecting inter-turn short-circuit faults through PCA. To estimate the severity of the fault, we developed an analytical model of the slope of the CUSUM decision function of  $T^2$ . Using this analytical model, we could estimate fault severity from noise-free data with an accuracy exceeding 99%. The robustness of our fault severity estimation method was demonstrated under noise levels up to a signal-to-noise ratio ( $SNR = 30dB$ ). In conclusion, we discuss the inherent limitations of our approach and propose avenues for future research.

# Acknowledgements (Remerciements)

Mes sincères remerciements s'adressent à mes encadrants, mon directeur de thèse Demba Diallo, ainsi qu'aux co-encadrants Claude Delpha, Siyamak Sarabi et Laid Kefsi, pour leur soutien inébranlable, leur disponibilité et leur patience. Leurs conseils judicieux ont grandement enrichi ma réflexion tout au long de ce projet et leurs contributions ont été d'une valeur inestimable.

Je suis profondément reconnaissant envers l'ensemble des membres de mon jury. Mes remerciements vont à Raphaël Romary et Didier Thelliol pour avoir accepté de juger mon travail, ainsi que pour leurs rapports de grande qualité et leur réflexion approfondie. Je tiens également à exprimer ma gratitude envers Mohamed Gabsi et Xuefang Shi-Lin pour leur évaluation de mon travail, leurs questions pertinentes et nos discussions enrichissantes.

L'expérience de travailler au sein de la Division Mobilité et Systèmes de l'IFPEN, en collaboration avec les laboratoires GeePs et L2S, a été extraordinaire. J'exprime ma gratitude envers tous les membres du département R107 à l'IFPEN, du Pôle Énergie au GeePs et de l'équipe GME au L2S, qui m'ont permis d'acquérir des connaissances significatives. Je tiens à adresser des remerciements particuliers à Andre Nasr pour son initiation à l'outil FEM Tools et sa contribution essentielle à la phase initiale de ma thèse portant sur la modélisation de la machine Synchro-Réductante Assistée par Aimant. Ma reconnaissance s'étend également à Najla pour nos échanges sur le choix des défauts et les méthodes de leurs modélisations, à Fabien pour ses conseils éclairés sur le contrôle des machines électriques, ainsi qu'à Alexandre et Malik pour leur soutien constant.

Ma profonde gratitude va à Christian Angelberger et à Fabrice Le Berr pour leur soutien constant et leur suivi attentif de mon projet au cours de ces trois années à l'IFPEN. Je les remercie pour le temps qu'ils ont investi dans la facilitation des formalités administratives, ainsi que pour mon inscription aux différentes formations qui ont contribué au développement des compétences nécessaires à ma thèse.

Mes remerciements s'adressent également à Daniel et Antoine pour les moments agréables partagés au cours de ces trois années, ainsi qu'à mes autres collègues doctorants, tant ceux qui m'ont précédé dans cette aventure, tels que Flavia, Erwan, Mouad, Ivano, que ceux actuellement engagés dans l'aventure, à savoir Jérémy, Sandra, Ahmed, Ryadh, Loic, Carole, Lucas et Ignes, pour leur contribution à la bonne ambiance à l'IFPEN. Nos discussions et échanges d'idées ont été inestimables.

Je souhaite exprimer ma gratitude envers tous ceux avec qui j'ai collaboré, y compris Guillaume Krebs et Maya Hage-Hassan du GeePs. Une mention spéciale revient à Ezzo Arfa pour son soutien et ses encouragements lorsque je considérais la possibilité de postuler pour des sujets de thèse.

Bien entendu, ma gratitude la plus profonde va à ma famille pour son soutien indéfectible. En conclusion, je tiens à remercier les membres de EIC, avec des remerciements particuliers à Paul, Hervé, Akko, Heeran, Cassandra et Esther, pour leur soutien constant.

# Contents

<b>Acknowledgements (Remerciements)</b>	<b>i</b>
<b>Contents</b>	<b>iv</b>
<b>List of Figures</b>	<b>vii</b>
<b>List of Tables</b>	<b>viii</b>
<b>Nomenclature</b>	<b>viii</b>
<b>1 General Introduction</b>	<b>1</b>
1.1 The Societal context . . . . .	1
1.2 Electrified vehicles Health monitoring . . . . .	2
1.3 Trends of Electric Motors for Electrified Vehicles . . . . .	4
1.4 Electric powertrain component faults . . . . .	5
1.5 PhD thesis scope . . . . .	5
1.6 Outline of the manuscript . . . . .	6
<b>2 Reliability of the electric vehicles' powertrain</b>	<b>8</b>
2.1 Introduction . . . . .	8
2.2 Electric powertrain main components . . . . .	8
2.2.1 Classification of electric motors for electric vehicles . . . . .	9
2.2.2 EV power converters . . . . .	15
2.2.3 Electronic controllers . . . . .	20
2.3 Statistical study of electric motor faults . . . . .	20
2.4 Electric motor faults in Electric vehicles . . . . .	22
2.4.1 Stator winding faults . . . . .	22
2.4.2 Demagnetization faults . . . . .	23
2.4.3 Airgap eccentricity faults . . . . .	24
2.4.4 Bearing faults . . . . .	25
2.5 Power converter faults . . . . .	26
2.5.1 Power switches Fault . . . . .	26
2.5.2 DC-link capacitor faults . . . . .	28
2.6 Electric motor faults detection and diagnosis: State of the art . . . . .	29
2.6.1 Modelling . . . . .	29
2.6.2 Data collection . . . . .	30
2.6.3 Data preprocessing and feature extraction . . . . .	31
2.6.4 Fault detection and identification methods . . . . .	33

2.7	Conclusion . . . . .	34
<b>3</b>	<b>PMaSynRM modelling for fault diagnosis</b>	<b>36</b>
3.1	Introduction . . . . .	36
3.2	PMaSynRM modelling . . . . .	36
3.2.1	Models Based on Coupled Circuits . . . . .	38
3.2.2	Finite Element models . . . . .	44
3.2.3	Hybrid models . . . . .	48
3.3	Controller design for the PMaSynRM drive . . . . .	49
3.3.1	Field Oriented Control techniques . . . . .	49
3.3.2	Direct Torque Control techniques . . . . .	50
3.4	Hybrid model of the PMaSynRM motor drive . . . . .	51
3.4.1	Analytical-finite element model of the PMaSynRM . . . . .	53
3.4.2	FOC for the hybrid model of the PMaSynRM . . . . .	55
3.4.3	Simulation results of the Hybrid model of the PMaSynRM . . . . .	60
3.5	Simulation of the Hybrid model of the PmaSynRM with Inter-turn Short-circuit fault . . . . .	68
3.5.1	Stator winding inter-turn short-circuit fault modelling . . . . .	68
3.5.2	Simulation results of the drive with inter-turn short-circuit fault . . . . .	69
3.6	Simulation of the Hybrid model of the PMaSynRM with Dynamic eccentricity fault . . . . .	70
3.7	Conclusion . . . . .	74
<b>4</b>	<b>EV powertrain fault detection methodology based on statistical approaches</b>	<b>75</b>
4.1	Introduction . . . . .	75
4.2	Univariate statistical methods for fault detection . . . . .	75
4.2.1	Shewhart chart . . . . .	76
4.2.2	EWMA chart . . . . .	77
4.2.3	CUSUM chart . . . . .	77
4.3	Multivariate statistical methods for fault detection . . . . .	79
4.3.1	Principal Component Analysis . . . . .	80
4.3.2	PCA for fault detection . . . . .	82
4.4	Performance analysis of the statistical control charts . . . . .	85
4.4.1	Concepts and definitions . . . . .	85
4.4.2	Average run length ( <i>ARL</i> ) . . . . .	87
4.4.3	Receiver operating characteristic (ROC) curve . . . . .	87
4.5	Stator inter-turn short-circuit detection . . . . .	88
4.5.1	Modelling and data collection . . . . .	88
4.5.2	Data preprocessing . . . . .	88
4.6	PCA for inter-turn fault detection . . . . .	98
4.6.1	Fault detection under stationary conditions . . . . .	99
4.6.2	Fault detection under non-stationary condition . . . . .	103
4.6.3	Fault diagnosis for noisy data . . . . .	107
4.7	Inter-turn fault severity estimation . . . . .	113
4.8	Conclusion . . . . .	116
<b>5</b>	<b>General Conclusion</b>	<b>117</b>

5.1	Conclusion . . . . .	117
5.2	Contribution . . . . .	119
5.3	Perspectives . . . . .	120
5.3.1	Improvement of the electric powertrain modelling for fault diagnosis .	120
5.3.2	Methodology improvement toward fault prognosis . . . . .	121
	<b>Résumé en Français</b>	<b>130</b>
	<b>Bibliography</b>	<b>150</b>
	<b>Appendix</b>	<b>151</b>
A.1	Permeance factors of the end windings . . . . .	151
A.2	Solutions of the speed PI parameters . . . . .	151
A.3	NAP Projection Effect minimization problem . . . . .	152



# List of Figures

1.1	Onboard diagnostic of an electric vehicle . . . . .	3
1.2	Characteristics comparison of IM, PMSM and PMSynRM for electrified vehicles' applications . . . . .	4
2.1	Functional block diagram of EV powertrain . . . . .	9
2.2	Schematic representation of a dc motor . . . . .	11
2.3	Schematic representation of an Induction motor . . . . .	12
2.4	Radial-flux rotors with surface- and internal-mounted magnets . . . . .	12
2.5	PMSM of Toyota Prius-2004 . . . . .	13
2.6	Schematic representation of an SBM . . . . .	14
2.7	Power control unit in the Toyota Prius . . . . .	16
2.8	Two-level VSI . . . . .	17
2.9	Classification of DC-DC converters . . . . .	18
2.10	IGBT-based inverter in Nissan Leaf . . . . .	19
2.11	Failure rates of electric machine main components: a- Low voltage machines, b- Medium voltage machine and c- High voltage machine . . . . .	21
2.12	Failure rates in power converter components . . . . .	21
2.13	Failure rates of components in the energy conversion chain . . . . .	22
2.14	Stator winding faults . . . . .	23
2.15	PM operating point (demagnetization curve and load line). Irreversible demagnetization due to (a) external demagnetizing MMF. (b) Operation at high temperature (SmCo- or NdFeB-based magnets) . . . . .	24
2.16	Eccentricity fault types: a-Static, b-Dynamic, c-Mixed . . . . .	25
2.17	Rolling element bearing . . . . .	25
2.18	Bearing faults: a- outer race fault, b- inner race fault, c- ball fault . . . . .	26
2.19	Potential inverter faults . . . . .	27
2.20	General fault detection and diagnosis approach . . . . .	29
3.1	Electrical Motor modelling techniques . . . . .	37
3.2	Rotor structure of a PMSynRM . . . . .	37
3.3	Equivalent circuit of a PMSynRM . . . . .	38
3.4	Coordinate transformations $abc$ to $\alpha - \beta$ and $\alpha - \beta$ to $d - q$ . . . . .	41
3.5	Phasor diagram of a PMSynRM . . . . .	42
3.6	FOC for PMSynRM . . . . .	50
3.7	DTC for PMSynRM . . . . .	51
3.8	Schematic representation of the drive modelling . . . . .	52
3.9	Selection of the connected domain $\Omega'_W$ . . . . .	53

3.10	FOC for the hybrid model of the PMSynRM . . . . .	56
3.11	Bode plot of the current $i_q$ closed-loop for $I_{peak} = 50A$ . . . . .	58
3.12	Step response of $i_q$ closed-loop at $I_{peak} = 50A$ . . . . .	58
3.13	The speed control loop . . . . .	59
3.14	Bode plot of the speed closed-loop for $I_{peak} = 50A$ . . . . .	60
3.15	Step response of the current $i_q$ closed loop at $I_{peak} = 50A$ . . . . .	60
3.16	Design of the PMSynRM . . . . .	62
3.17	Torque-Speed curves of the PMSynRM drive . . . . .	62
3.18	Power-Speed curves of the PMSynRM drive . . . . .	63
3.19	FEA Self and Mutual inductances of PMSynRM for $I_{peak} = 50A$ . . . . .	64
3.20	FEA Self and Mutual inductances of PMSynRM for $I_{peak} = 300A$ . . . . .	64
3.21	FEA Self and Mutual inductances of PMSynRM for $I_{peak} = 700A$ . . . . .	64
3.22	Speed and Torque response of the SVM using FOC . . . . .	65
3.23	Stator phase $a$ current for the three load cases . . . . .	65
3.24	Snapshot of the experimental PMSynRM drive . . . . .	66
3.25	Simulated and measured currents for load 1 . . . . .	67
3.26	Simulated and measured currents for load 2 . . . . .	67
3.27	Simulated and measured currents for load 3 . . . . .	67
3.28	Elementary coils circuit in the 3-phase motor . . . . .	68
3.29	Interturn short-circuit fault in an elementary coil of one phase . . . . .	68
3.30	Motor windings with an inter-turn short-circuit fault in phase $a$ . . . . .	70
3.31	Speed and Torque response of the PMSynRM with inter-turn short-circuit Fault (level 2) for the three loads . . . . .	71
3.32	Time series of stator current in phase $a$ of the PMSynRM with inter-turn short-circuit Fault (level 2) for the three loads . . . . .	71
3.33	Schematic representation of dynamic eccentricity . . . . .	72
3.34	FEM inductances under healthy and faulty conditions . . . . .	73
3.35	Stator phase $a$ current under healthy and faulty conditions . . . . .	73
4.1	Shewhart control chart . . . . .	76
4.2	Example of CUSUM chart . . . . .	79
4.3	Receiver Operation Characteristic curve illustration . . . . .	87
4.4	Layout of the dataset . . . . .	89
4.5	Fitting normal distribution to Median Absolute deviation . . . . .	91
4.6	Fitting normal distribution to Variance . . . . .	92
4.7	Fitting normal distribution to Skewness . . . . .	93
4.8	Fitting normal distribution to Kurtosis . . . . .	94
4.9	Features' variables in healthy condition . . . . .	96
4.10	Features' variables for data with $CC2$ fault . . . . .	97
4.11	Typical EV motor speed-torque characteristics . . . . .	98
4.12	Flowchart of PCA for fault detection . . . . .	99
4.13	Variance captured by each principal component . . . . .	100
4.14	Fault level 2 detection with PCA at $Load_1$ condition . . . . .	101
4.15	Fault level 2 detection with PCA at $Load_2$ condition . . . . .	101
4.16	Fault level 2 detection with PCA at $Load_3$ condition . . . . .	101
4.17	Flowchart of the NAP-based PCA for fault detection . . . . .	103

4.18	Schematic diagram of the NAP principle . . . . .	105
4.19	Comparison of MAD features before and after NAP . . . . .	106
4.20	Comparison of variance features before and after NAP . . . . .	107
4.21	Comparison of kurtosis features before and after NAP . . . . .	108
4.22	Variance captured by each principal component for the the NAP score data	109
4.23	Fault level 2 detection with NAP-based PCA . . . . .	109
4.24	Comparison of the noise-free and the noisy data and selected features . . . .	110
4.25	Variance captured by each principal component for the noise-free and noisy data . . . . .	111
4.26	CUSUM for fault monitoring . . . . .	113
4.27	Slope of CUSUM decision function . . . . .	114
4.28	Analytical approximation of $dS_N$ . . . . .	115
4.29	Fault severity estimation . . . . .	115
4.30	Fault estimation and noise interference . . . . .	116
5.1	Statistiques des défauts des composants des machines électriques : a- Ma- chines basse tension, b- Machine moyenne tension et c- Machine haute tension	124
5.2	Représentation schématique de la modélisation du systèmé de traction élec- trique . . . . .	125
5.3	Modèle d'ensemble de données . . . . .	127
5.4	Flowchart of the NAP-based PCA for fault detection . . . . .	129
A.1	Permeance factors of the end windings in a synchronous machine . . . . .	151

# List of Tables

2.1	Evaluation of EV motors . . . . .	15
2.2	Fault indicators for different motor faults . . . . .	30
2.3	Statistical features . . . . .	32
3.1	Coupled Circuits models of electric motor including faults . . . . .	43
3.2	Finite element models of electric motor faults . . . . .	48
3.3	PMaSynRM characteristics . . . . .	61
3.4	Simulation parameters . . . . .	63
4.1	Summary of PCA-based CUSUM and EWMA fault detection framework . . . . .	85
4.2	Performance evaluation of the fault detection with PCA . . . . .	102
4.3	Performance evaluation of the fault detection with NAP-based PCA . . . . .	110
4.4	Comparison of fault detection performance with noise-free and noisy data . . . . .	112
5.1	Performance evaluation of the fault detection with PCA . . . . .	128
5.2	Performance evaluation of the fault detection with NAP-based PCA . . . . .	130

# Chapter 1

## General Introduction

### 1.1 The Societal context

Electrification currently occupies a position of preeminence within contemporary society. While the beginning of the 20th century witnessed a major electrical revolution, mainly in stationary applications, the beginning of the 21st century also saw electricity significantly transforming all onboard applications. Electric power has proven to be an extremely convenient way to transport and convert energy. The considerable progress in power electronics has opened new perspectives for most energy conversion systems. For example, notable advances have been made through the growing adoption of electrified vehicles. Electrified vehicles include today Hybrid Electric Vehicles, Plug-In Hybrid Electric Vehicles, and Electric Vehicles. They come as a solution to reduce environmental pollution due to road transport and bypass the concern of the rising cost of crude oil. Hence, the Member States of the European Union have significantly progressed in developing European climate policy. They have approved the new regulation under which, from 2035, all new au vehicles registered in the European Union must display zero emissions. Similar regulations have also been proposed in California to move closer to banning the sale of new vehicles running exclusively on gasoline by the year 2035 [1]. However, these innovations remain limited by energy storage and recharging capacities that are still significantly lower than those offered by oil. The advantages of electrification are evident in ease of installation and modularity. Indeed, the wide use of electrified vehicles has resulted in material cost issues, which require the adoption of optimization in design to reduce cost, mass, and volume. In addition to weight reduction, compactness, efficiency, and reduction of manufacturing costs, availability and reliability are other challenges of the electric automobile industry. To face these critical safety issues, the automotive industries have defined the safety standard - ISO 26262 to help prevent potential hazards [2].

Electric actuators are multiplying in the electrification of vehicles; while some make the powertrain, others aim to improve comforts like adjusting electric seats, operating car windows, or operating mirrors. In all these systems tending progressively towards electricity, the electro-mechanical components at the end of the chain are primarily electrical machines. The latter can be actuators producing electricity while being powered by an internal combustion engine or generating mechanical energy to accomplish a specific function. In vehicle electrification, the operational reliability of the motor drive system, which is at the heart of the operation, is becoming a major industrial issue. The motor drive system consisting of the electric motor, the power electronics, and the control systems is mainly subjected to frequent and repeated transient cycles that induce mechanical and

thermal stresses. Any malfunction could spread further, resulting in reduced efficiency and additional costs for diagnosis and repairs. This can also affect the operation of the vehicle and endanger the passengers. To ensure the safety and reliability of electric vehicles, anticipation of system failures is a significant concern [3].

## 1.2 Electrified vehicles Health monitoring

As electrified vehicles gain increased notoriety within the transport industry, fleet operators and car manufacturers face a crucial maintenance problem to ensure the continuity of operations. The control unit of modern combustion vehicles monitoring and evaluating the entire system is generally referred to as OBD (Onboard Diagnostics). On the other hand, in electric vehicles, the absence of a standardized onboard diagnostic system poses significant challenges, making the precise identification of malfunctions complex. This situation is expected to change by the 2026 model year. California law will require automakers to phase in a standard EV diagnostic system under the state's Advanced Clean Cars II program. Although this regulation is initially limited to California, it is likely to become the industry standard. These systems will also be applicable to plug-in hybrid vehicles and hydrogen fuel cell vehicles. The EVs on-board diagnostics must encompass every component of an electric vehicle's powertrain, including its battery, electric motors, power electronics and charging system [4]. Nevertheless, the OBD system, initially designed for diagnosis and emissions management of combustion vehicles, has been integrated into electric vehicles. This integration aims to leverage standard error code standards and evolving technical principles to improve the ease of malfunction diagnosis and maintenance of electric vehicles. Through the fault diagnosis systems of the various components of the electric powertrain, a fault warning system can be triggered for the attention of the driver. Additionally, the Controller Area Network (CAN) bus can be used to transmit standard error codes and status parameters from the electric powertrain to the vehicle controller, making Diagnosis Trouble Codes (DTC) easier to read. Figure 1.1 shows an example of an Onboard diagnostic system of an electric vehicle with the Electric Drive System (EDS), the DC/DC converter and the Battery Management System (BMS) Electronic Control Units (ECUs). The ECUs have the role to detect faults conditions internally and if any of these condition is reached, store the DTC [5].

Traditional maintenance methodologies, due to their potential for inefficiency and high costs, can lead to unexpected incidents and extended periods of vehicle downtime. Fortunately, predictive maintenance systems are emerging as a game-changer in the maintenance of electric vehicles [6]. They have been proposed in various industrial fields to improve reliability and reduce the costs associated with unplanned downtime. By leveraging advanced analytical techniques, machine learning, and real-time data mining, these systems are proving to identify maintenance needs with exceptional accuracy. They are primarily based on monitoring the evolution of faults, which makes it possible to give the state of degradation of the components before their complete deterioration. In electrified vehicles, it consists of continuous monitoring and analysis of condition parameters (electrical, vibration, temperature, etc). The Electric Signature Analysis (ESA) has been increasingly applied in electric motor drive applications, thanks to its non-intrusiveness, dependency solely on electrical quantities, and technical and economic viability. The fundamental transformations induced by the predictive maintenance technology in the maintenance of the electric

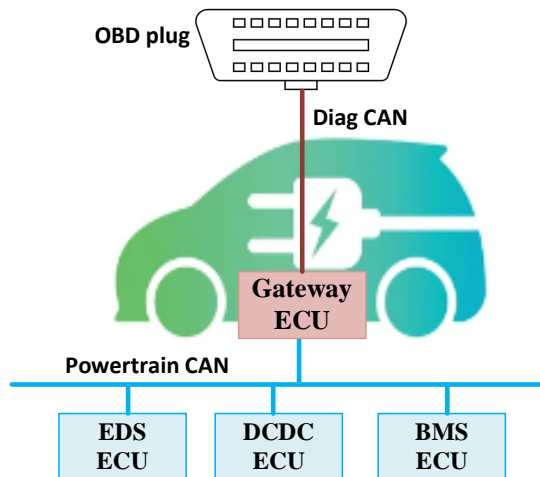


Figure 1.1: Onboard diagnostic of an electric vehicle

vehicle are as follows [7]:

- **Reduce Downtime**

Downtime is a significant concern for vehicle owners due to its impact on vehicle availability and revenue generation. Unplanned failures that require emergency maintenance can cause significant disruptions to fleet operations. However, thanks to a predictive maintenance system, potential vehicle faults are detected before they reach a critical threshold. This capability helps to meet planned maintenance schedules and ensure vehicles to remain in their best operating condition.

- **Minimise Maintenance Costs**

Traditional maintenance typically involves inspection and component replacement procedures on pre-established schedules, regardless of the vehicle's actual condition, which can result in unnecessary maintenance expenses. However, through a predictive maintenance system, the condition of electric vehicles can be accurately assessed based on real-time data from various vehicle sensors, driving patterns, and other parameters. This approach allows only to undertake maintenance when necessary, removing unnecessary servicing costs.

- **Improve vehicle performance**

The maintenance of electric vehicles is of crucial importance to ensure optimal performance and extend the vehicle's lifetime. Predictive maintenance allows real-time monitoring of electric vehicles, detecting any latent anomaly that could affect vehicle operating conditions. By taking a proactive approach to these issues, the vehicle's optimal performance can be maintained, resulting in improved efficiency and overall performance.

- **Enhance safety**

Predictive maintenance can help to early identify potential electric vehicle safety risks, such as brake problems or powertrain failures, before they turn into potential threats of accidents.

### 1.3 Trends of Electric Motors for Electrified Vehicles

Following the success of electric vehicles, optimizing the appropriate powertrain is becoming a growing concern. Basically, the electric powertrain consists of a unit comprising an energy storage device, electric machine, inverter with a software suite, and mechanical transmission. The electric motor is a central element of the powertrain, for which various technologies and configurations have been examined. Currently, solutions based on rare earth (RE) permanent magnets, such as permanent magnet synchronous motors (PMSM) or permanent magnet assisted synchronous reluctance motors (PMSynRM), are widely adopted, followed by induction motors (IM) [8].

Permanent magnet-based motors provide optimum performance for traction applications due to their high power density, specific torque, power factor, efficiency, and notable ability to regulate the magnetic flux. All of these features are critical for automotive applications, as they help minimize component mass, reduce the size of the power electronic control unit, and minimize energy losses. However, solutions based on RE magnets face an unstable and risky supply chain, leading to significant price volatility. A recent study by the JRC highlights that the European Union could become vulnerable regarding the supply of various essential materials, including rare earths [9]. Magnet-free solutions are being explored to reduce or eliminate the reliance on rare earth permanent magnets in the manufacturing of electric motors. This is driving increased interest in induction motors and synchronous reluctance as next-generation technologies for electric motors for traction applications. Figure 1.2 summarizes the advantages and disadvantages of the three main motor types (PMSM, PMSynRM, IM) in terms of essential characteristics for electric vehicles.

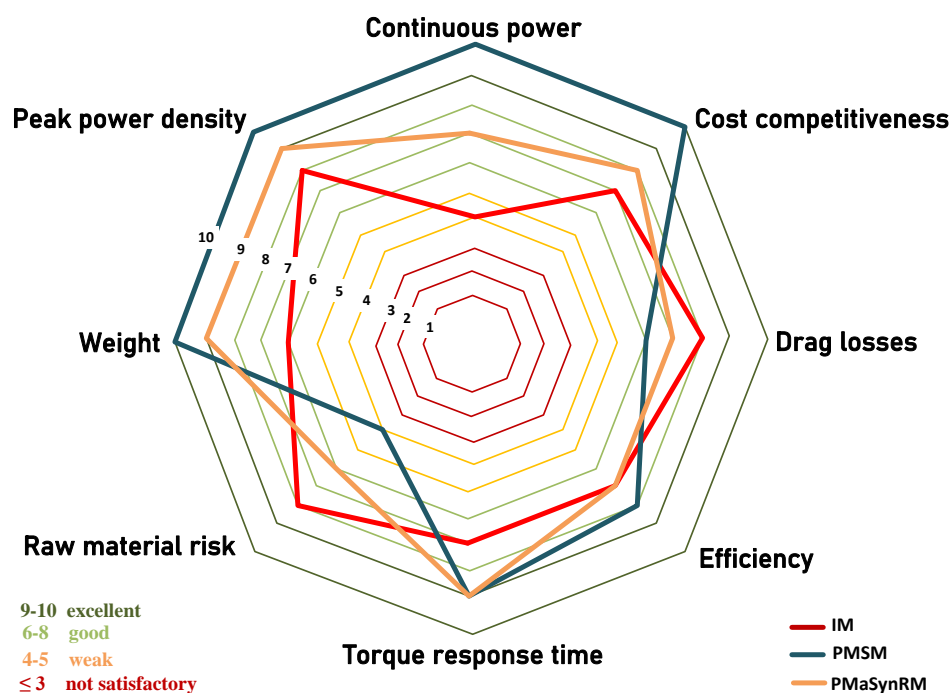


Figure 1.2: Characteristics comparison of IM, PMSM and PMSynRM for electrified vehicles' applications [10, 11]



Given differences in the performance of each technology in terms of the characteristics mentioned in Figure 1.2, some requirements can significantly impact overall costs, performance, and other benefits. An individual assessment is always necessary based on the specific application while considering the desired operational strategy. In this work, our interest focuses on PMSynRM, which is currently one of the promising motor technologies for electric vehicle applications.

## 1.4 Electric powertrain component faults

The complex and compact architecture and the different operating modes of modern electric vehicles, such as start-stop and energy recovery during braking, place significant constraints on the electric motors and their drive systems. In addition, the vibration and thermal stresses to which these components are exposed increase the probability of failure occurrence. These main failures can be classified into three categories: electrical (linked to problems with the insulation of the windings), magnetic (linked to the loss of magnetization), or mechanical (such as the eccentricity of the air gap or bearings). These failures can damage either the stator or the rotor. Winding faults, bearing faults, eccentricity and demagnetization are the most representative faults in electric motors [12, 13].

The short-circuit fault between winding turns also known as inter-turn fault is the most important of the stator winding faults as it often leads to other faults if not dealt with in time. It is a significant concern for electric motor monitoring, as a high amplitude current can flow in short-circuited windings. The study in [14] has shown that the current flowing in a short circuit fault between windings creates a reverse magnetic field that can lead to demagnetization [15]. Bearing faults are manifested by damage to the rolling element, the cage, or the inner and outer rings. These alterations can cause vibration and acoustic phenomena, as well as increased wear. The predominant causes of bearing failure in electrical machines are attributable to improper operating conditions, including adverse road conditions. Like the bearing faults, eccentricity faults have undesirable consequences on the machine, including accelerated bearing wear, generation of undesirable and potentially damaging vibrations, increased energy losses, reduced overall efficiency, and increased temperature. If these faults are not treated early, they can lead to improper contact between the rotor and the stator, subsequently leading to damage to the stator core and associated windings [16]. To prevent or limit the effect of the aforementioned faults, solution based on new materials, new architectures and fault-tolerant drive are being explored.

## 1.5 PhD thesis scope

The main objective of this PhD thesis work is to develop a structured methodology for the deployment of predictive maintenance techniques for electrical synchronous machines used in electric powertrain. The objectives are:

1. To investigate on the mechanical and electrical faults in the electrified vehicle powertrain to find their relevance and the link between them to select the most relevant ones.
2. To build an electric powertrain model for fault diagnosis purposes with a focus on the selected fault under study.

3. For each fault under study, find the indicators that are the most sensitive to the fault occurrence and evolutive, robust to the load variations and the disturbances.
4. With regard to these fault indicators find the best methodologies to detect the faults, especially at their early stages.
5. And finally develop a diagnosis methodology for predictive maintenance.

Though the aforementioned solutions to mitigate motor faults, winding faults are still common and their detection remains an issue. The focus of this work will be on the inter-turn faults for their relevance to avoid most of the electric motor drives' faults. The modelling of motor drive system fault analysis makes it possible to perform numerical simulations, which are used to evaluate diagnostic methods without resorting to costly and potentially destructive tests. It is essential that these models are accurate under both normal and faulty operating conditions, while accounting for transients and steady states, to develop fault-sensitive detection and diagnostic algorithms. Models of electrical machines can be broadly classified into two categories: analytical models, which are relatively simple and fast but less accurate, and numerical models through finite element method (FEM), which are accurate but more expensive in terms of computation. The combination of these two modeling techniques leads to hybrid models, which can benefit from both the precision of numerical models and the calculation speed of analytical models.

As part of our study, we develop a hybrid model by combining an analytical model in the three-phase reference frame with a model based on the finite element method. The analytical model is based on the concept of inductances. Therefore, to build our fault analysis model, we will carry out the computation of inductances under normal and faulty operating conditions using finite element analysis. The results of these computations are then saved in multidimensional lookup tables (LUTs), which will subsequently be integrated into the analytical model. A validation has been conducted by comparing the characteristics of the model with the measured ones on the experimental bench. An in-depth analysis of existing perspectives in the field of electric motor condition monitoring has led to the identification of gaps in the research field related to electrified vehicle applications. These gaps include:

- the lack of fault diagnosis considering the varying operating conditions of electric motors in electrified vehicles,
- the lack of motor fault diagnosis in closed-loop drives.

To fill this gap, we are proposing a methodology to detect stator inter-turn short-circuits despite the closed-loop operation in which the action of the controllers could mask fault signatures. The exploitation of signals already available in the control unit is chosen as a relevant approach to build an onboard diagnosis tool for fault detection. The challenging task is to detect, classify, and estimate the severity of the faults by processing the measured phase current time-series. For the fault diagnosis, we adopt statistical analysis techniques for their ability to extract information from raw data and derive succinct set of rules or metrics.

## 1.6 Outline of the manuscript

The continuity of this research work is structured as follows:

**Chapter 2** provides a comprehensive review of the overall powertrain architecture of electrified vehicles, in accordance with the established definition. It is also dedicated to in-depth investigation, focused on identifying critical safety and reliability issues within the electric powertrain. Additionally, this chapter sheds light on the various electrical machines employed in electric vehicles. It also focuses on the analysis of the different types of faults that can affect the electric motor of the powertrain. It presents at the end a state-of-the-art methodologies for fault detection and diagnosis, which are reviewed for their relevance to our analysis.

**Chapter 3** examines the three different modeling methodologies used to represent electric motor faults, namely models based on coupled circuits, models based on numerical methods, and hybrid models. We also outlined the adoption of the latter approach in modeling PMSynRM in the context of short-circuit fault analysis. To evaluate the quality of our developed machine model, a precision measurement was carried out. As part of this study, we also presented an analysis of PMSynRM parameters under fault conditions, highlighting that stator currents are potentially exceptional fault characteristics for this type of failure.

**Chapter 4** provides a comprehensive review of statistical methods, both univariate and multivariate, used in fault detection and diagnosis. Additionally, it includes a presentation of various performance evaluations of these methods. A specific case study on stator interturn fault detection is also proposed. As part of this study, we created a dataset comprising stator current measurements in healthy and faulty operating states, covering fault cases ranging from incipient stage to the most severe. An analysis was carried out to identify relevant tools allowing the extraction of essential characteristics of the data. Additionally, we described the statistical methodology that we developed to meet the initial objectives of the thesis. At the end of the chapter, we highlighted the limitations of this proposed methodology, thus demonstrating its constraints and areas of applicability.

Final conclusions and considerations for future work are presented in **Chapter 5**.

## Chapter 2

# Reliability of the electric vehicles' powertrain

### 2.1 Introduction

As stated in the introduction chapter, the main goal of this thesis project is to develop fault detection methodologies that will help to build a Predictive Maintenance System (PMS) for the electric powertrain to enhance the safety and maintainability of electric vehicles. In order to achieve this, a general electric vehicle (EV) powertrain architecture has been defined. The components must be analyzed to investigate relevant safety and reliability issues and hence some existing PMS methodologies will be analyzed as well.

At first, the different electric machines used in electric vehicles will be presented. Then, the different types of faults of the electric vehicle powertrain will be reviewed. Finally, the state-of-the-art faults detection and diagnosis methodologies will be presented.

### 2.2 Electric powertrain main components

Electrified vehicles can be classified into two categories according to the nature of motorization: hybrid electric vehicles (HEV), which powertrain consists of electric motors combined with internal combustion engines, and electric vehicles, in which we will find only electric motors. For this last category, we speak about battery electric vehicles (BEV) when batteries bring energy. It is this category that will be studied in this work. We will be interested more precisely in the elements of the electric propulsion system [17].

The electric powertrain system is a set of components that generate power to move the vehicle. It mainly consists of battery packs, power converters, electric motors, and electronic controllers. In motor mode, the electric machine converts electrical energy into mechanical energy. It operates in generator mode during the braking phase to charge the energy storage unit. This process is known as regenerative braking. It is a key process for Electric vehicle appeal because it enhances vehicle efficiency between 20-25% [18]. The power converters are the interfaces between the power sources and the electrical machines. Electronic controllers provide control signals to the power converter and so they control the electric motor behavior to achieve the requested torque and speed, according to the driving conditions [19, 20]. Figure 2.1 shows the functional block diagram of the electric vehicle powertrain. The choice of components mainly depends on three factors: the user driver expectation, the vehicle constraints, and the energy source. The driver's expectation depends on the vehicle's performance and driving cycle. Car manufacturers must consider that customers will compare the performance of ICE vehicles to Electric Vehicles

one. The vehicles' constraints are linked to vehicle type, weight, and payload. The electric powertrain structure may depend on the types of energy sources, such as batteries, ultra-capacitors, flywheels, fuel cells, and various hybrid sources. The main requirements of the electric powertrain for the successful adoption of electric vehicles are as follows:

- Long range to meet driving,
- Quick charging time for the battery packs,
- High power density of the powertrain components which increases the vehicle's range,
- High torque at low speed for starting as well as low torque at high speed for cruising,
- Ruggedness and reliability for various operating conditions in any environmental condition,
- Maintenance needs and safety requirements,
- Affordable cost.

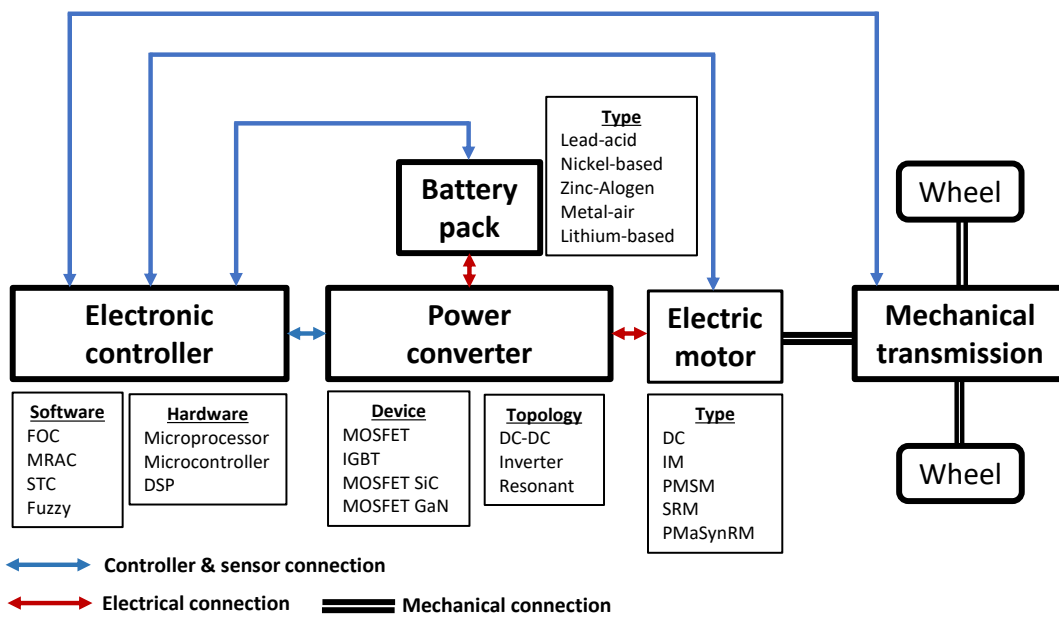


Figure 2.1: Functional block diagram of EV powertrain [21]

### 2.2.1 Classification of electric motors for electric vehicles

The great variety of motor topologies and the different specifications of EVs result in a segmented market with the DC motor, Induction Motor (IM), PM Synchronous Motor (PMSM), Synchronous Reluctance Motor (SRM), and some hybrid topologies. For EV

applications, the efficiency of electric motors depends on the operating points requirements related to driving cycles. The motor efficiency is characterized by power–speed or torque–speed efficiency maps. The performance of the motor for a wide range of speeds and powers is defined by the design, although each type of motor has a specific torque–speed curve. The efficiency is also dependent on the voltage level. High-voltage rated powertrains are more efficient. On the other hand, the efficiency drops when the powertrain is operated below the rated voltage.

The selection of motors for an electric vehicle powertrain must fulfill the requirements on rated power, voltage and current capacities, torque, and speed characteristics, controllability, and reliability as well. In addition, some important factors like cost and dependence on rare earth materials have also to be considered. In the following, the major motor topologies will be discussed in terms of rotor and stator topologies, merits, and demerits.

### 2.2.1.1 Rotor topologies

#### 1. DC motors:

DC motors consist of a stator with a stationary field and a wound rotor with a brush commutation system as shown in Figure 2.2. The field in the stator is usually induced by coils, although small machines could use permanent magnet for the excitation. The field winding can be connected in series or in shunt with the rotor coils depending on the characteristics required. The commutator is made up of a set of copper segments, inducing more friction than slip rings and therefore producing dust.

The powertrains based on DC motors have great advantages such as high overload capacity, a broad range of speed regulation, linear regulating characteristics, structure simplicity, and ease of control. Despite all these advantages, its usage in electric vehicle applications is obstructed by the presence of mechanical brush-collector units, which decreases the reliability and durability [22].

The development of rugged power semiconductors has made it increasingly practical to introduce AC motors which are mature to replace the DC motor in traction applications. These brushless motors are attractive because of their reliability and maintenance-free operation. Nevertheless, when it comes to the cost of the inverter, variable frequency drives are usually only used for higher power. For low powers, the DC motor remains more than an alternative. This is the case of the French car manufacturer PSA Peugeot Citroën, which presented the HEV version of their Berlingo model called Dynavolt, with a DC motor as electric propulsion [23].

#### 2. Induction motors:

Induction Motors (IM) consist of a stack of laminated steel with short-circuited aluminum bars in the shape of a squirrel cage as shown in Figure 2.3. The magnetic field of the stator rotates at a slightly higher speed than the rotor. The slip between rotor and stator frequencies induces rotor currents that produce the motor torque [23]. They are widely accepted for EVs propulsion thanks to their low cost, high reliability, and maintenance free. At present, it is one of the most mature technologies among various brushless motor drives. The main advantages are their light weight, small volume, low initial cost, high efficiency, and low maintenance [19].

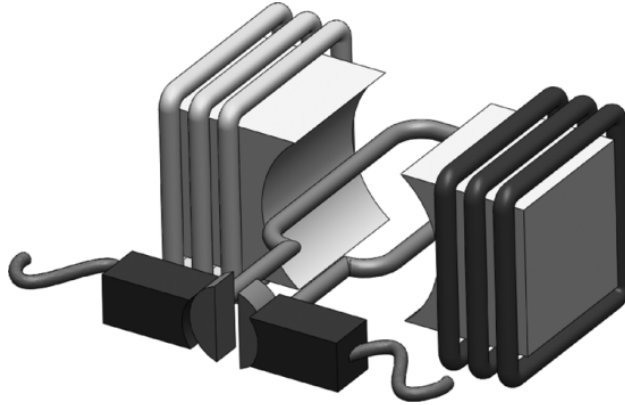


Figure 2.2: Schematic representation of a dc motor [17]

In general, induction motors faced several drawbacks that kept them out of the electric vehicle powertrain. These disadvantages are mainly high loss, low efficiency, low power factor, and low inverter-usage factor, which is more serious for high-speed and high-power motors. Some research proposes to take these problems into account in the design stage. To improve the efficiency of induction motors, a new generation of control techniques has been proposed. For example, to extend the constant power region without oversizing the motor, the use of a polyphase pole-changing IM drive has been proposed. Another approach to enlarge the constant power region has been to use dual inverters. It should be noted that some research work tends to introduce doubly fed IM as electric propulsion, because of their excellent performance at low speeds. Induction motors have been used by car makers like Renault in their Kangoo model and Chevrolet in their Silverado model [24]. Tesla Motor has adopted them too, in their first flagship vehicle Model S [25].

### 3. Permanent Magnet synchronous motors:

PM Synchronous Motors (PMSM) are characterized by their constant rotor magnetization. PMs in the rotor induce high magnetic fields in the air gap, without excitation currents, leading to high power density. They are very efficient and require less cooling due to the lack of exciting currents. This comes at the cost of more complex control as the excitation field may not be regulated. They also present several drawbacks like their high initial cost, limited constant power range, magnet demagnetization, and small speed range [19, 27].

The development of high-coercivity neodymium-iron-boron magnets in the 1980s opened up new possibilities for PMSMs, and they are now used in automotive applications. There is a wide variety of possible PM arrangements and geometries. Regarding the flow path, the most common types of machines are radial or axial flow. There are many different strategies for mounting the magnets to the rotor. Axial flux machines usually have magnets mounted on the surface of the rotor, while radial flux machines can have the magnets either surface or internally mounted [28] as shown in Figure 2.4.

They have been adopted by car makers like Nissan, Honda, and Toyota in their models Tino, Insight, and Prius respectively [24]. They have been adopted by Tesla Model 3. An example of the PMSM used in Toyota Prius 2014 is shown in Figure 2.5.

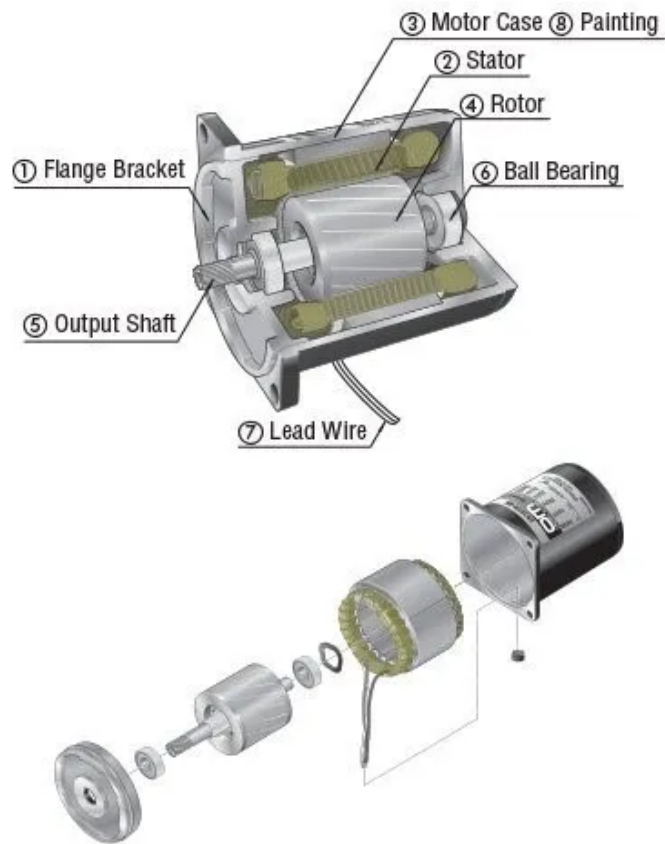


Figure 2.3: Schematic representation of an Induction motor [26]

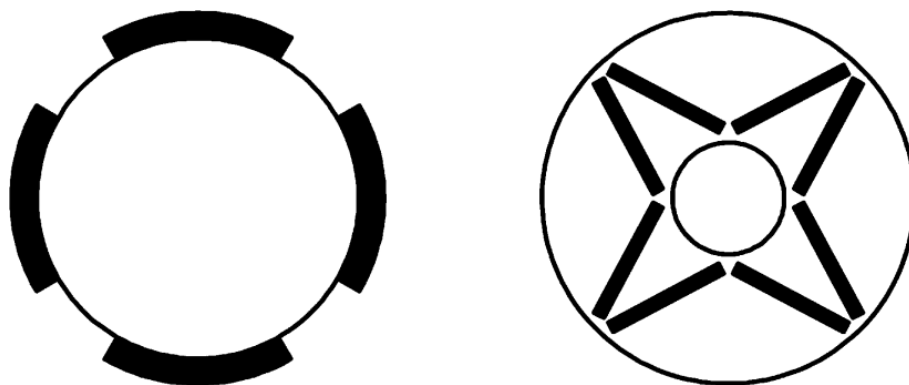


Figure 2.4: Radial-flux rotors with surface- and internal-mounted magnets [17]





Figure 2.5: PMSM of Toyota Prius-2004 [26]

#### 4. **Reluctance motors:**

Reluctance Motors (RM) have gained attention due to the concern of price increases or shortage of magnetic material when electric vehicles enter mass production [29]. Their main characteristic is the use of rotor salient poles. The torque is solely produced by the difference between the direct axis and quadrature axis synchronous reactance as the rotor lacks excitation.

They have the merits of simple structure, low initial cost, and adequate torque-speed characteristics. The peak efficiency is equivalent to the IM, whereas the efficiency remains high over a wide speed range. Efficiency values over 95% have been reported [30]. The high rotor inductance ratio makes sensorless control easier to implement.

Despite these advantages, they have several weaknesses like their design and control complexity and high ripple torque resulting in higher noise. These motors have been used in EV applications by the Australian car maker Holden in their Ecommodore Models [24].

#### 5. **Synchronous Brusheed Motors:**

The Synchronous Brusheed Motor (SBM) has been chosen by Renault for its mid-size models. This motor consists of a coil in the rotor connected to a fixed voltage source through a slip ring. Electric current flows from a stationary carbon brush through a rotating steel slip ring. The magnetic field in the rotor is induced by the field current through the rotor coil. The rotor is robust and the temperature is limited only by the insulation of the conductors [31]. A schematic representation of an SBM is shown in Figure 2.6. The ability to regulate magnetic flux binding is the main advantage of this technology. At part-load operation, iron and excitation losses can be reduced, extending the high-efficiency operating range. The technology also offers high starting torque. The control is simpler and robust compared to the PMSM. The magnetizing current undergoes Joule losses. Thus, the operating efficiency at full load is lower than that of comparable machines with no current in the stator. The coal brushes of slip

rings wear less than those of DC commutators and are virtually maintenance free [17].

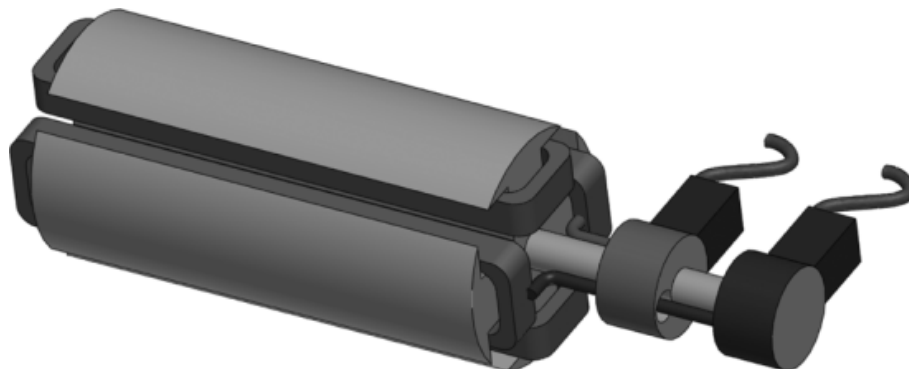


Figure 2.6: Schematic representation of an SBM [17]

## 6. Permanent Magnet Hybrid motors:

There are different kinds of hybridization, namely the PM and reluctance hybrid, the PM and hysteresis hybrid, and the PM and field-winding hybrid. Each type has the merits of high efficiency, high power density, wide speed range, and quiet operation. Their most important demerits are their low technological maturity and higher cost.

The recent improvement in motors designs and performance have made the Permanent Magnet Synchronous Reluctance Motors (PMSynRM) one of the most efficient motors for EV applications. This high efficiency increases the range of the vehicle on a single charge, which is an important feature for BEVs. This is why it has been adopted in the latest Tesla Model 3 [32].

Similarly to the PMSM, the magnets used in PMSynRM are usually made from alloys that include rare earth materials such as Neodymium, terbium, dysprosium. They are mainly extracted in China, the main supplier of rare earth materials in the world [33]. With this low resource variability, the rare earth prices and supply can be highly volatile in the future which could disturb the efforts of making electric vehicles a sustainable means of transportation. Hence, to bring more certainty to the future of electric vehicles, many efforts are being made to reduce or eliminate the dependency on rare earth permanent magnets in electric motors production. One of the alternatives is to replace rare earth magnets with other types of magnets like ferrite magnets [34]. Among the current mature motor technologies for electric vehicle applications, the PMSynRM is still gaining more interest because of its good performance and low dependence on rare earth materials.

In Table 2.1, the results of comparative analysis of electric motors by a grading system are depicted: each type of motor is evaluated through six major characteristics with rate raking from 1 to 5 points. At the end of each column, there is the final rating. The induction motor and PMSM motors have the highest ratings.

### 2.2.1.2 Stator topologies

#### 1. Coreless Motors:

**Table 2.1:** Evaluation of EV motors [35, 36]

	DC motor	Induction motor	PMSM motor	SR motor	PM hybrid motor
Power density	2.5	3.5	5	3.5	4
Efficiency	2.5	3.5	5	3.5	5
controllability	5	3	4	3	4
Reliability	3	5	4	5	4
Maturity	5	5	4	4	3
Cost	4	5	3	4	3
Total	22	25	25	23	23

Coreless machines (CM), consist of windings that are placed in a nonmagnetic material stator. Thus, they have no iron losses. The absence of iron in the stator teeth increases the reluctance of the magnetic circuit. The absence of iron weight and iron losses in the stator compensates for the increased use of expensive active material in these motor topologies. Coreless motors are present in high-performance applications, where weight and efficiency prevail over economic considerations [37, 38].

## 2. Multiple-Phase Motors:

The standard three-phase power systems have many advantages: three is the minimum number of phases that deliver constant power over each cycle. An increase in the number of phases increases the complexity of the system. It is only recommended when special performance is required. Intrinsic advantages of the three phases are a reduction in the harmonic content, low acoustic noise, and an increase in efficiency and torque density. However, fault tolerance and lower power rating per phase have been identified as the main factors of multiple-phase motors' adoption [39, 40]. Fault tolerance plays a key role in fulfilling the safety requirements. Lower power ratings per phase allow the use of robust and less-expensive power electronic devices. Sometimes, multiple-phase systems consist of duplicate three-phase systems with an angle shift. In principle, any number of phases above four is possible. Systems with more than three phases are uncommon in road vehicles but are used in propulsion motors for ships and planes. The high torque capability makes them suitable candidates for in-Wheel motors [41].

## 3. In-Wheel Motors:

In in-Wheel Motors (IWM), the outer diameter is limited to the space available inside the wheel. They may be directly driven, although some designs include a planetary gear and a brake disk [42]. In principle, all topologies are suitable, but PM motors with outer rotors or axial-flux configurations have a better power density and volume utilization. Additionally, there are in-wheel induction and RM configurations [43].

### 2.2.2 EV power converters

#### 1. Converter topologies:

A power converter is an electrical device that connects the energy source to the motor. It modulates the electrical energy voltage amplitude and frequency. The evolution of power

converter topologies follows that of power devices. The evolution is basically toward achieving higher power density, efficiency, controllability, and reliability. There are several types of power converters, namely AC-DC, AC-AC at the same frequency, AC-AC at different frequencies, DC-DC, and DC-AC. Electrical machines convert electrical energy into mechanical energy using a rotating electromagnetic field that generates torque. This rotating electromagnetic field is generated by a DC-AC Voltage Source Inverter (VSI) powered by a DC link. Using vector control, the torque and speed characteristics of the machine can be controlled from a user interface determined by the drive cycle. Modern electric vehicle architectures are comprised of a DC battery, a DC-DC boost converter required to step-up the battery voltage, a VSI, and an electric machine for traction. Modern electric powertrains are also capable of regenerative braking where the slowing down of the vehicle is initiated not by running the motor as a generator. The AC power generated by the traction motor is then rectified by the converter and used to recharge the battery thereby improving the energy efficiency of the overall system. Figure 2.7 shows a typical example of such a powertrain from Toyota.

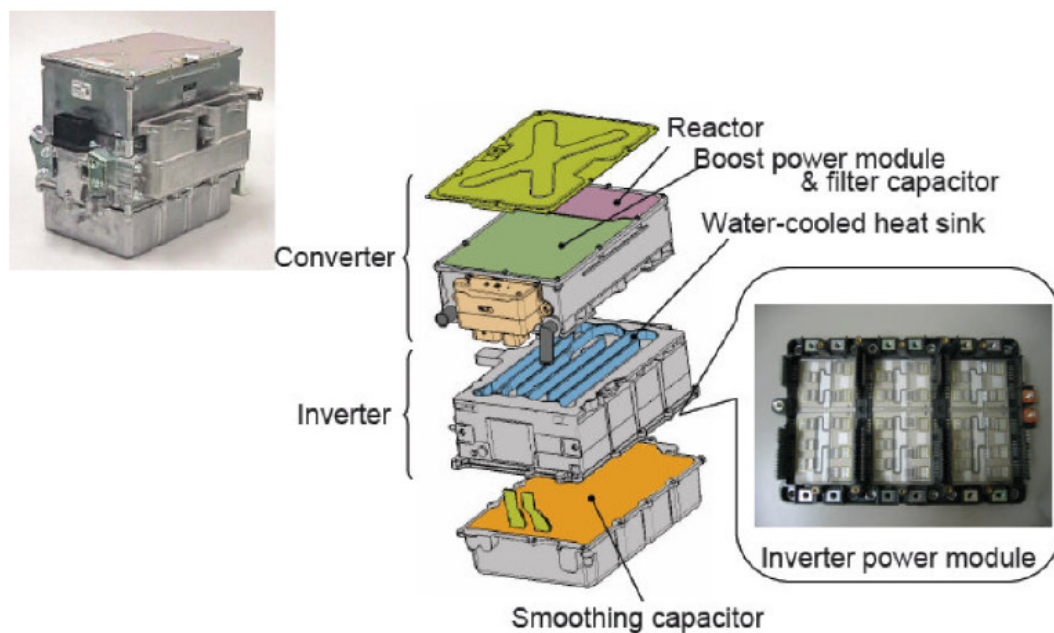


Figure 2.7: Power control unit in the Toyota Prius [44]

The power electronic converter is critical to the efficiency and power density of the electric powertrain system. The converter is voltage sourced since the DC side voltage is constant and the DC side current determines the direction of power flow. It is also a self-commutated converter since the phase-to-phase commutation of the current within the converter is determined by the switching of the power electronic devices. The VSI is a 2-level converter shown in Figure 2.8. It is composed of 6 power devices each with an anti-parallel diode ( $S_1$  and  $S_4$ ,  $S_3$  and  $S_6$ , and  $S_5$  and  $S_2$ ). The anti-parallel diodes have the role to provide a path for the reverse current in each phase [27]. This converter

has eight possible switching states two of them being redundant.

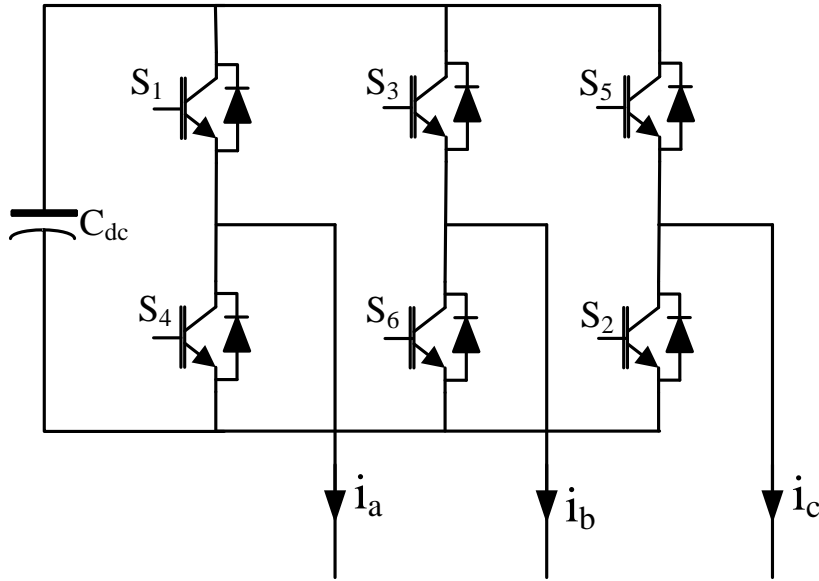


Figure 2.8: Two-level VSI [45, 46]

Generally, the Energy Storage System (ESS) delivers the required energy to the motor through the DC-AC inverter. However, the power delivered by ESS has unstable characteristics and considerable voltage drops [47]. The connection from the DC-DC converter to the electric motor is established through a high-voltage DC bus followed by a DC-AC inverter. Thus, DC-DC converters play a key role in converting the unregulated power flow to a regulated one [48]. Some latest topologies of these converters for battery-fed applications include resonant converters. They have either a parallel or series resonant circuit, thus providing either zero-voltage-switching (ZVS) or zero-current switching (ZCS) conditions. Outweighing the additional cost due to the resonant tank and increased control complexity, they have the advantages of zero switching loss, low heat sinking requirement, high power density, less severe EMI problem, very small acoustic noise, and improved reliability. Because of these merits, resonant dc-link inverters have promising applications for EV propulsion. A classification of the DC-DC converter has been presented in [49] (Figure 2.9).

## 2. **Power devices:**

In the past few years, power device technology has made tremendous progress. These power devices have grown in power rating and performance through an evolutionary process. The recently introduced power devices are the gate-turnoff thyristor (GTO), power bipolar-junction transistor (BJT), power metal-oxide field-effect transistor (MOSFET), insulated-gate bipolar transistor (IGBT), static-induction transistor (SIT), static-induction thyristor (SITH), and MOS-controlled thyristor (MCT) [50].

Active research is still being pursued on the development of high-performance power devices. The selection of power devices for electric vehicle propulsion is generally based

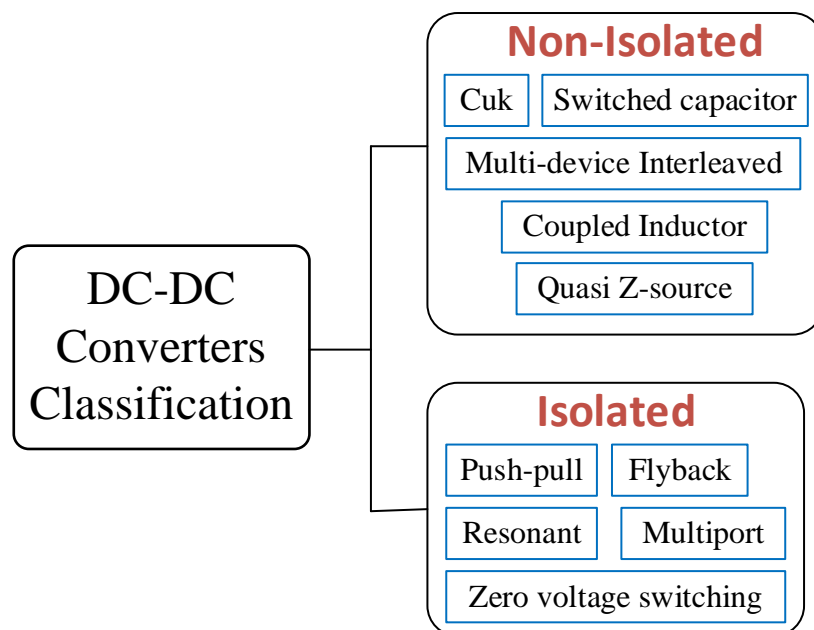


Figure 2.9: Classification of DC-DC converters [49]

on the requirements of the voltage rating, current rating, switching frequency, power loss, and dynamic characteristics. The voltage rating depends on the battery's nominal voltage, maximum voltage during charging, and maximum voltage during regenerative braking. The current rating depends on the motor's peak power rating and the number of devices connected in parallel. The switching frequency should be high enough to reduce the acoustic noise, size of filters, and EMI problems. On the other hand, higher switching frequencies increase the switching loss. Since an extra 1% efficiency in EV propulsion can enable an additional distance in the EV driving range, the power loss including both switching and conduction losses should be minimum. The dynamic characteristic should be good enough to allow for high capability, high capability, simple driving, and easy paralleling. The device protection, packaging, reliability, and cost should also be considered [28]. Among the available power devices, the GTO, BJT, MOSFET, IGBT, and MCT are particularly suitable for EV propulsion [51]. At present, the IGBT is the most attractive because it possesses high input impedance and the high-speed characteristics of a MOSFET with the conductivity characteristic of a BJT. A typical IJBT-based inverter in Nissan Leaf drivetrain is shown in Figure 2.10.

Wide bandgap semiconductors such as SiC and GaN are two candidates being investigated for future drive systems in electric vehicle applications. Toyota is involved in the development of GaN devices [53]. The high-temperature operation, high switching frequency, and high breakdown voltage properties of these wide bandgap semiconductors make the SiC-based components for electric vehicle applications.

### 2.2.3 Electronic controllers

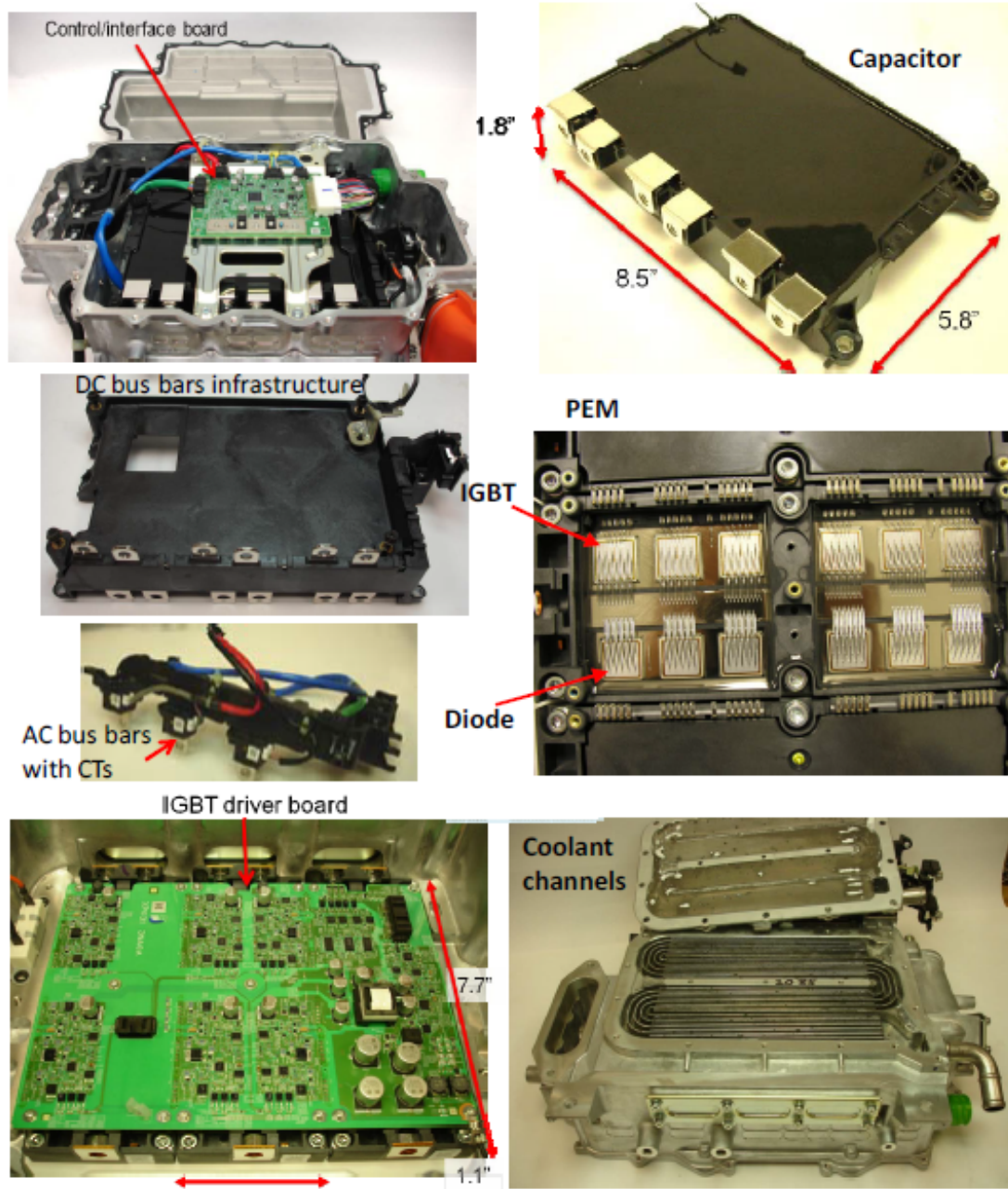


Figure 2.10: IGBT-based inverter in Nissan Leaf [52]

Conventional linear control such as PID can no longer satisfy the stringent requirements placed on high-performance EV's. In recent years, many modern control strategies such as model-referencing adaptive control (MRAC), self-tuning control (STC), variable structure control (VSC), fuzzy control, and neural network control (NNC) have been proposed. Both MRAC and STC have been successfully applied to EV propulsion [54]. Using sliding mode, VSC has also been applied to motor drives [55]. By employing emerging technologies of fuzzy logic and neural networks to realize the concept of intelligent controllers, fuzzy control and NNC have promising applications for EV propulsion. In order to implement the aforementioned modern control strategies, powerful microelectronic devices are necessary. Modern microelectronic devices include microprocessors, microcontrollers, digital signal processors (DSP), and transputers. Microprocessors are usually used to recognize the milestone of the development of microelectronics such as the 8086, 80186, 80286, 80386, 80486, and Pentium. Unlike microprocessors, which are the CPU of microcomputer systems, microcontrollers include all resources to serve as standalone single-chip controllers. Thus, microcontroller-based EV propulsion systems possess definite advantages of minimum hardware [56]. The state-of-the-art microcontrollers are the 8096, 80196, and 80960. DSPs such as the TMS32030, TMS32040, and i860 possess the capability of high-speed floating-point computation which is very useful to implement sophisticated control algorithms for high-performance EV propulsion systems. Transputers such as the T400, T800, and T9000 are particularly designed for parallel processing applications. By employing multiple chips of transputers, sophisticated control algorithms can be implemented.

### 2.3 Statistical study of electric motor faults

From the survey conducted by IEEE-IAS and EPRI cited in [57] on medium-sized induction machines, and the one in [58] on medium to high-voltage large induction machines, it is shown that the faults distribution in electrical machines is related to their sizes (Figure 2.11). For low-voltage electrical machines, bearing faults are the predominant faults. For medium-voltage machines, the stator faults are of equivalent importance to the bearing faults. However, for high-voltage machines, the stator faults are the predominant faults and account for two-thirds of the total faults rate. The low bearing faults rate is mainly due to the use of sleeve bearings, which are more fault-tolerant than rolling element bearings used in low-voltage machines. Even though the stator winding of the medium voltage motors is normally form-wound windings with advanced insulation, winding faults are still common. This is due to the higher electrical and thermal stresses on medium-voltage electrical machines. Similarly, as their rotors are also under high thermal, mechanical, and electrical stresses, they are typically more vulnerable compared to those of small motors [59, 16].

The investigation conducted in [62] on failure modes of an inverter feeding induction machines has identified the most important faults as input supply single phase to ground fault, the dc link capacitor short-circuit, rectifier diode short-circuit, transistor base drive open fault and transistor short-circuit. According to the survey in [63], power semiconductor devices are ranked as the most fragile components, followed by capacitors and gate drives. Figures 2.12 and 2.13 show the rates of most frequent faults encountered in an electric powertrain's power converter and energy conversion chain respectively.

A statistical study on the faults in electrified vehicles is not publicly available because



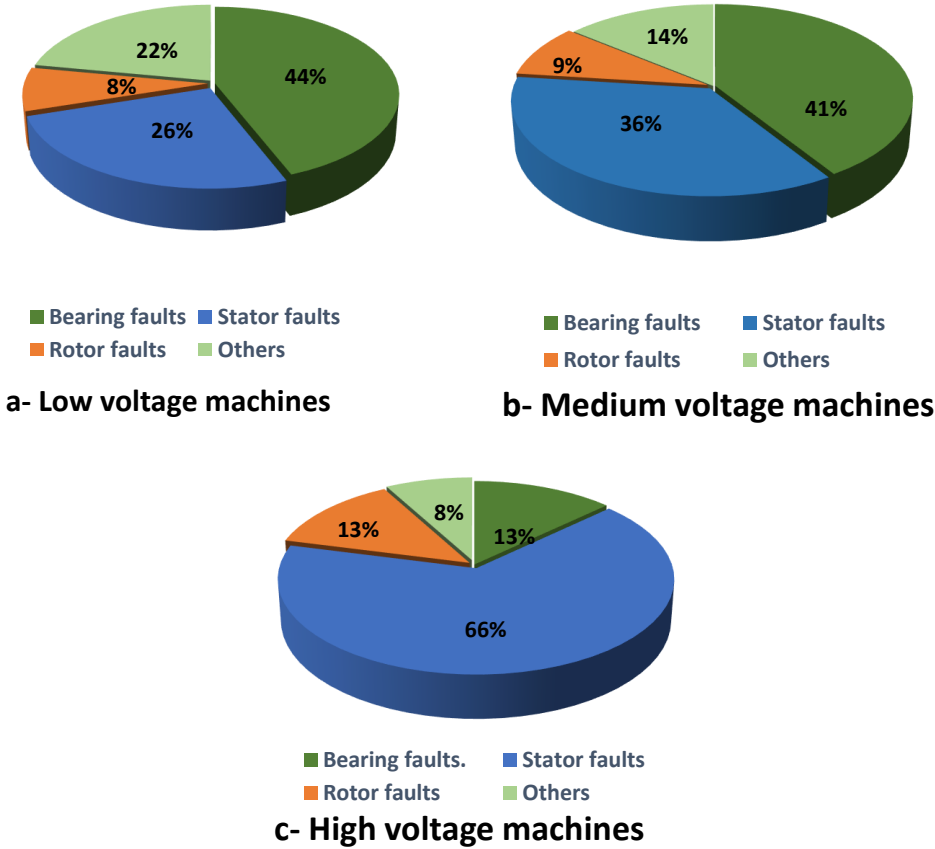


Figure 2.11: Failure rates of electric machine main components: a- Low voltage machines, b- Medium voltage machine and c- High voltage machine [60, 61, 59]

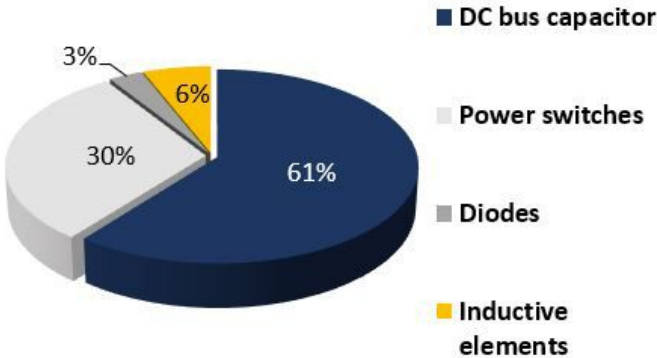


Figure 2.12: Failure rates in power converter components

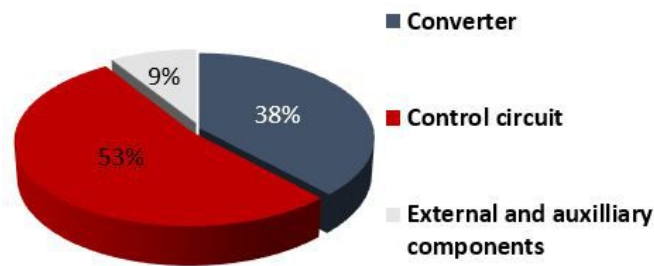


Figure 2.13: Failure rates of components in the energy conversion chain [64]

of the low operating times of electrified vehicles and the manufacturers' scarcity of data. However, some statistics are available for similar devices used in other applications. In EV applications electrical machines are reported to have at least 1 kV RMS voltage rating [65]. Traction battery pack voltages for hybrid and electric vehicles range from 120 V to 650 V [66]. This analysis places the electric machines used in electric vehicle applications into the family of high-voltage machines. Thus, the most common failure of electric machines in EVs powertrain are related to stator winding followed by the bearing and the rotor faults at equal rates (Figure 2.11). In the following, the different electric motor faults will be analyzed with a focus on stator winding and rotor (airgap eccentricity) faults.

## 2.4 Electric motor faults in Electric vehicles

The complex and compact architecture and various operating modes of modern electric vehicles (such as the traditional start–stop operation and regenerative braking) put much stress on the electrical machines and drive systems used in the electric vehicle powertrain. In addition, the vibratory and thermal constraints they are subjected to, increase the probability of fault occur. The main faults in electrical machines can be electrical (winding faults), magnetic (demagnetization faults), or mechanical (airgap eccentricity and bearing faults) and they affect either the stator or the rotor.

### 2.4.1 Stator winding faults

As shown in the failure statistics graph in Figure 2.11 the stator winding fault is one of the most in PMSynRMs. Stator faults include various types of short-circuits as shown in Figure 2.14: inter-turn short-circuits, short-circuits between the coils in one phase, phase-to-phase short-circuits, phase-to-ground short-circuits and open-circuits [14]. However, the most common situation is the inter-turn short-circuit. It is mainly caused by stator winding insulation damage due to electrical stresses, mechanical stresses, and overload. An imperceptible short circuit between adjacent turns can spread very quickly over the whole winding, causing the main short-circuit. This results in a large circulating fault current causing a significant temperature rise that degrades the windings' insulation. Moreover, stator winding faults can have a negative impact on rotor permanent magnets. Due to the high temperature in the shorted part of the stator winding, a magnetic field higher than magnet coercivity may occur leading to partial or complete irreversible demagnetization.

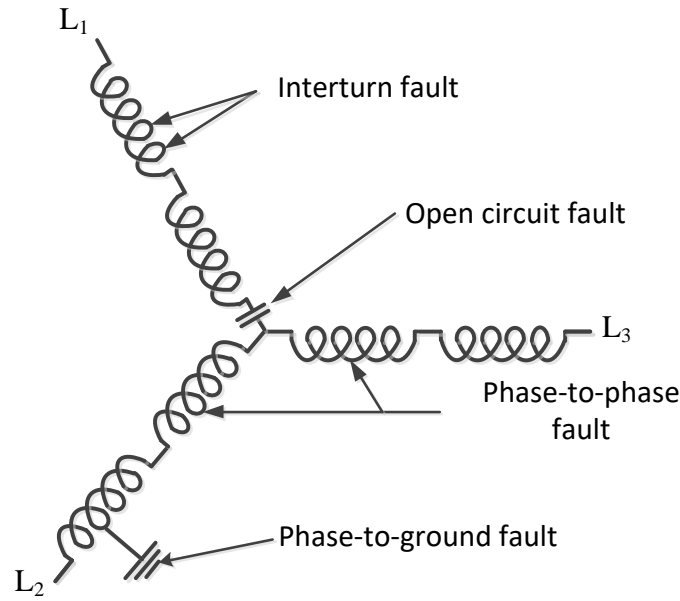


Figure 2.14: Stator winding faults

### 2.4.2 Demagnetization faults

Any Permanent magnet (PM) material can be described by its magnetic hysteresis loop. The most important part of this characteristic is its demagnetization part in the second quadrant of the B-H plane. This section is used to analyse how the magnetic flux density varies with the demagnetization field. The demagnetization curve of modern PM materials, such as NdFeB and SmCo, is linear and it sharply drops when approaching the knee. The operating point of a PM machine is at intersection of the load and magnetization curves and this depends on the magnetic circuit configuration and current of the machine. The operating point in the linear part of the demagnetization curve can move up and down without leaving the curve and this behavior is called “reversible.” However, if due to any reason, the operating point leaves the linear part and moves to under knee by demagnetization field, the PM will follow the other recoil line and residual flux density becomes less than the main value. This is called “irreversible demagnetization” phenomenon. High starting torque, symmetrical and asymmetrical short-circuit faults, and open-circuit faults are the factors that increase the current of the machine and move the operating point under the knee of the magnetization curve. As shown in Figure 2.15 (a), the operating point of the PM machine is at point  $a'$  under healthy condition, and it moves to point  $a''$  under the previous faulty conditions. After removing the magnetic field, PM follows the dashed line path and the residual flux density approaches  $B_r$  with a value lower than  $B_r$  [67]. The impact of heat on the demagnetization curve can facilitate the demagnetization occurrence due to demagnetization fields even in healthy operating conditions. Generally, by temperature rise, the PM residual magnetic flux density  $B_r$  decreases but the behavior of the magnetic coercivity  $H_c$  changes depending on the different PMs. In ceramic PM,  $H_c$  increases with the temperature rise while it is the opposite for SmCo and NdFeB PMs. High-energy magnets such as NdFeB and SmCo lose coercivity as temperature rises [68].

Figure 2.15 (b) shows an NdFeB PM performance under normal conditions when temperature rises from  $T_1$  to  $T_2$ . As seen, even under normal conditions, temperature rise displaces the operating point under the knee of magnetization curve. In this case, by changing the PM operating point, it follows the recoil line  $c'' - B_r''$ . If the temperature again decreases to  $T_1$ , the operating point does not follow the previous demagnetization curve, and its operating point is placed on the recoil line  $a'' - B_r''$ . In this case, PM has a lower residual flux density and irreversible [69].

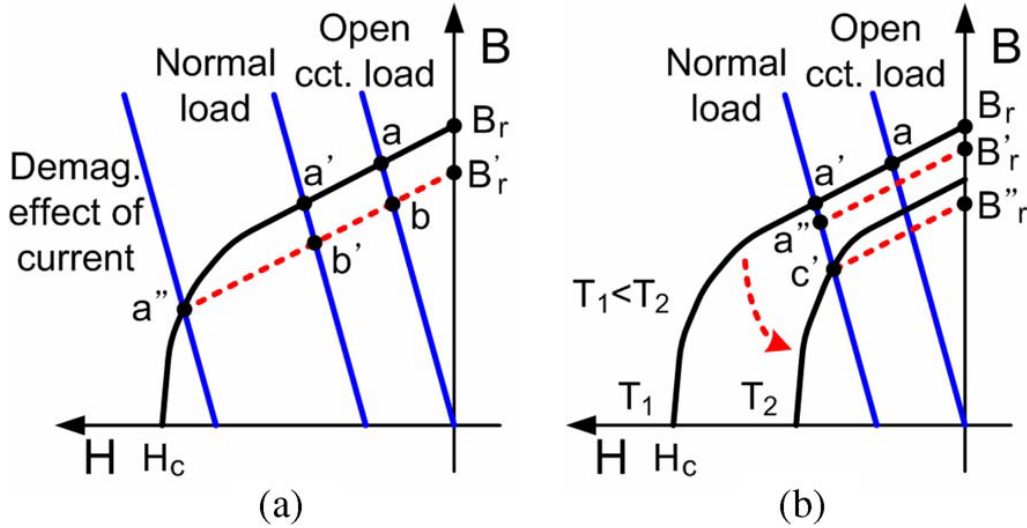


Figure 2.15: PM operating point (demagnetization curve and load line). Irreversible demagnetization due to (a) external demagnetizing MMF. (b) Operation at high temperature (SmCo- or NdFeB-based magnets) [67]

Oxidation and corrosion change the metallurgical structure of modern PMs and lead to irreversible demagnetization. Heat, humidity, and environments containing chlorides can accelerate this process. In addition, graduate reduction of the PM strength, PM aging, and PM damage (crack, chips, etc.) can also reduce the PM magnetic flux. Since the permeability of the PM is very similar to that in air, PM breakage does not cause unbalanced inductances of the machine; so, its behavior is very similar to demagnetization [70].

### 2.4.3 Airgap eccentricity faults

Eccentricity faults are categorized into three groups: static, dynamic, and mixed. In the case of static eccentricity fault, the axis of rotation  $O_B$  coincides with the axis of rotor  $O_R$  but it is displaced from the stator axis  $O_A$ . In the case of dynamic fault, the axis of rotation  $O_B$  coincides with the stator axis  $O_A$  but not with the motor axis  $O_R$ . In mixed fault, the axis of rotation  $O_B$  is different from both axis of the stator and rotor (Figure 2.16). The main reasons for static eccentricity fault may be the oval shape of the stator core, inaccurate positioning of the rotor or stator at the manufacturing stage, wrong positioning of bearings, and bearings' deterioration.

Dynamic eccentricity fault could result from an inclination of the rotor shaft, wearing of bearings, mechanical resonance at critical speed, unbalanced magnetic pull due to static

eccentricity fault, shaft misalignment, and unbalanced torque. In mixed eccentricity faults, both static and dynamic eccentricity faults are present.

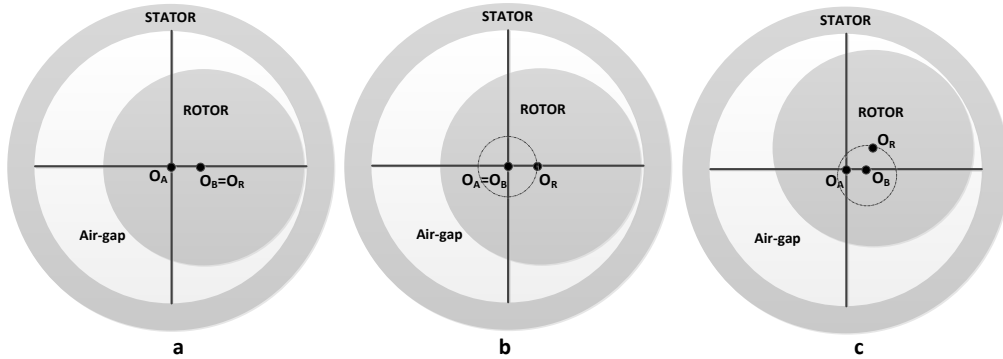


Figure 2.16: Eccentricity fault types: a-Static, b-Dynamic, c-Mixed [71]

Eccentricity faults have undesirable impacts on the machine, including accelerated wearing of bearings, unwanted and potentially harmful vibrations, increased losses, decreased efficiency, and heating. If these faults are not handled in time, they would lead to rotor-stator rub and subsequently destroy the stator core and windings [16].

#### 2.4.4 Bearing faults

Rolling element bearings are key components in electric vehicle motors. They support radial and axial loads by reducing rotational friction and hence carry heavy loads on the machinery. They ensure critical optimal performance of the electrical machine [72]. The most used bearings in electrical machines are ball ones. They consist of two rings, an inner ring and an outer ring as shown in Figure 2.17. The inner race is normally mounted on the motor shaft. The balls are located between the two rings.

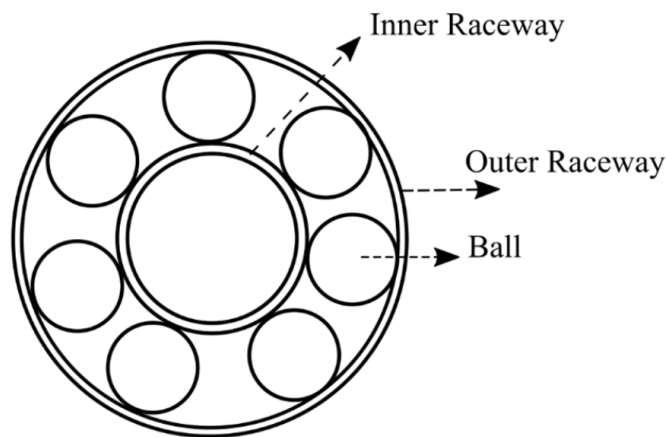


Figure 2.17: Rolling element bearing [73]

The bearing faults consist of damage of rolling element, cage, inner, and outer race. These faults may produce vibration and noise, flaking or spalling, and an increase in wearing. The most common causes of bearing failure in electrical machines are poor road conditions,

unbalanced tyres, overweight loads, and improper mounting. Other causes could be internal stresses and inherent eccentricity; electrical stresses due to shaft current; environmental stresses due to contamination and corrosion [74]. The most common bearing faults are depicted in Figure 2.18 where the fault can be on the outer race (a), on the inner race (b), and on the balls (c).

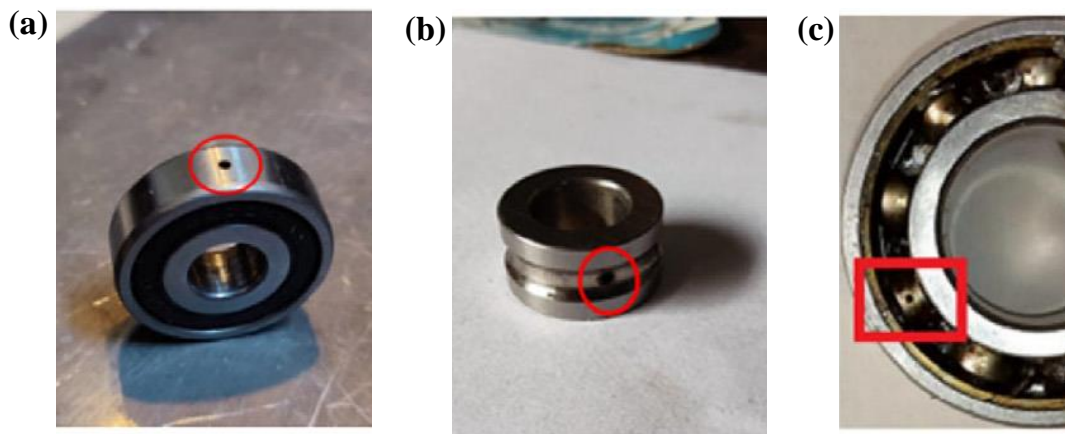


Figure 2.18: Bearing faults: a- outer race fault, b- inner race fault, c- ball fault [75]

## 2.5 Power converter faults

Since the connection between different power components in an EV powertrain is established by power electronic converters, the reliability of power electronic converters influences that of the whole powertrain. It is estimated that about 38% of the faults in variable speed ac drives are due to failures of power devices [76]

Faults in power electronic converters can be divided into four levels: 1) switch-level; 2) leg-level; 3) module-level; 4) system level [77]. As power electronic devices such as semiconductor switches are prone to fail, switch-level faults are commonly observed. Even such a level of fault may result in strike of large-scale equipment, which significantly deteriorates the quality of power generation [78]. For instance, serious traffic accidents may occur if the three-phase inverter fails owing to switch-level faults in an EV [79]. As shown in Figure 2.12, the DC-link capacitor ( $F_3$  in Figure2.19) and semiconductor devices faults are the most frequent faults in the power converters. They count for 61% and 30% of the total converter faults respectively. The most usual switch faults are: open-circuit ( $F_1$  in Figure2.19) and short-circuit ( $F_2$  in Figure2.19) [80].

### 2.5.1 Power switches Fault

#### 2.5.1.1 Open-circuit faults

Converter open-circuit faults can occur because of external disconnection, and also bond wires lift-off caused by excessive short-circuit current. After some time, it may cause ripples

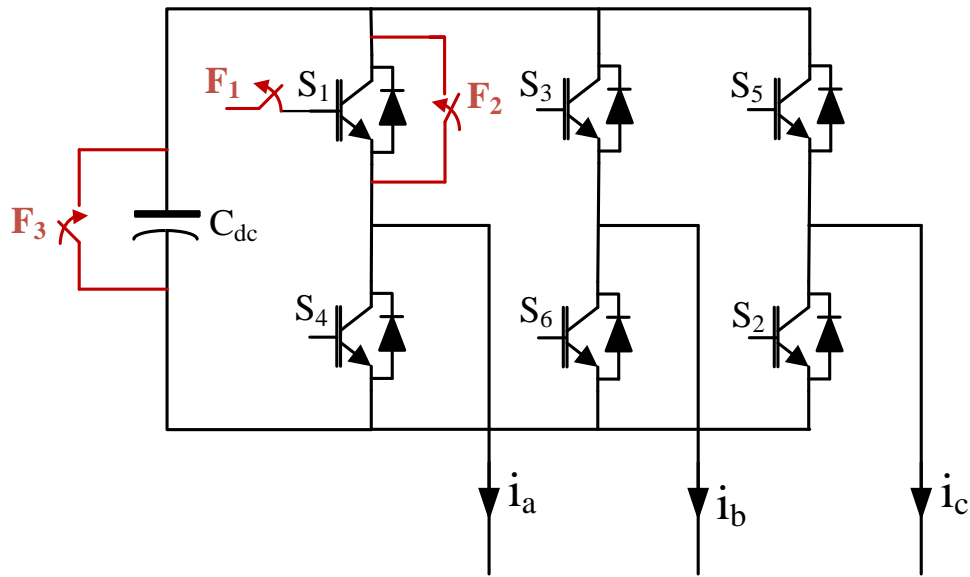


Figure 2.19: Potential inverter faults [81]

in the current and output voltage, output current distortion, and subsequent faults in other components [82]. An open circuit fault can also be caused by a faulty gate drive signal. The most prevalent causes are driver element breakage and a disconnection between the driver circuit and the converters.

### 1. Bond wire lift-off

The bond wire lift-off faults can occur as a result of a short-circuit due to mechanical issues in the converter circuit. The major causes are associated with a mismatch in thermal expansion between Aluminium and Silicon, as well as significant temperature gradients. The break begins at the bonding interface's edge, and the bond wire eventually pulls off as the crack propagates to the weaker central bond region [83]. Normally, the central emitter bond wires fail first, followed by the survivor bond wires. Bond wire rupture is another failure mechanism that occurs after extended power cycle testing and is slower than lift-off [84].

### 2. Gate driver faults

There are other reasons for faults in the gate driver circuit, including faulty power stage transistors and unconnected cables between the gate drive circuit and the converters [85]. The breakdown of the driver circuit may result in sporadic misfiring of converters, reduced voltage, and overstressing of other transistors and capacitors. Abnormal working states in IGBT terminals can also cause driver failure. Continuous narrow voltage spikes between emitter and collector may open the gate emitter resistance, whereas IGBT collector fault current may cause gate-emitter resistance degradation [86]. Thermal runaway or excessive power dissipation can occur as a result of gate open-circuit failure [87], although an extensive study on the failure mechanism is still missing.

Furthermore, current IGBTs might have junction temperature as high as 150°C, imply-

ing that the case temperature can reach 100°C, while most of the components in the driver cannot function correctly at such high temperatures.

### 2.5.1.2 Short-circuit faults

A single short-circuit fault has the potential to destroy power converter as it causes an uncontrolled high current. One of the major sources of short-circuit fault is thermal runaway of the devices due to overload or unnatural operation. Moreover, short-circuit faults can occur due to the following reasons.

#### 1. High voltage breakdown faults

The high voltage spikes caused by a fast-dropping rate of stray inductance and collector current can damage the converter circuit during the turn-off process [87]. This is because the strong turn-off voltage spike and the electric field can exceed the critical field and initiate faults in one or a few transistors, resulting in a significant increase of current and temperature. After the voltage surge, the collector-emitter voltage decreases, collector current of the transistor increases. Moreover, the gate driver circuit can fail because of the significant rise in the gate driver circuit voltage [88].

#### 2. Static or dynamic latch-up

Latch-up is a state in which the gate driver voltage no longer controls the collector current, and it occurs whenever the transistor (NPN) is switched on and acts as a transistor (PNP) [89]. There are two forms of IGBT latch-up: static latch-up and dynamic latch-up. In general, for high collector currents, static latch-up occurs, which turns on the NPN transistor by raising the voltage across the load resistance. Dynamic latch-up occurs during transients by switching process, most commonly during switched off, while the NPN transistor is driven by the displaced current via capacitance on junction between the N-base and deep regions [90]. Dynamic latch-up can occur because of two unique circumstances. One example is when the gate voltage decreases extremely fast, causing an excess of displaced current to flow through gate and the resistance.

### 2.5.2 DC-link capacitor faults

Electrolyte capacitors may be the most vulnerable components in electric drives due to their high degradation rate [91]. The failure of a DC capacitor results in DC supply voltage ripples, and thus accelerates the failure of the rest of the components in the electric drive system. The failure mechanisms of an aluminum electrolytic capacitor can be classified into catastrophic faults (open circuit and short circuit) and degradation faults. The former type of fault can be avoided through some aging tests, while the latter type of fault is inevitable due to the physical limitations of the materials [92]. The degradation of DC capacitors is often reflected in capacity decrease and ESR increase. High temperature, over-voltage, and frequent charge and discharge are the root causes of capacitor degradation.



## 2.6 Electric motor faults detection and diagnosis: State of the art

A general fault detection and diagnosis flowchart is shown in Figure 2.20. It consists of five steps. The first one is the modelling which is knowledge building. The model can be based on analytical relations, language description, or historical data. The second step consists of preprocessing the raw data in the most appropriate information domain to extract the fault sensitivity features or signatures in the third step. The fourth and fifth steps are dedicated to the analysis of features to make the final decision on the health states. In the following, the different techniques applied in each step are reviewed.

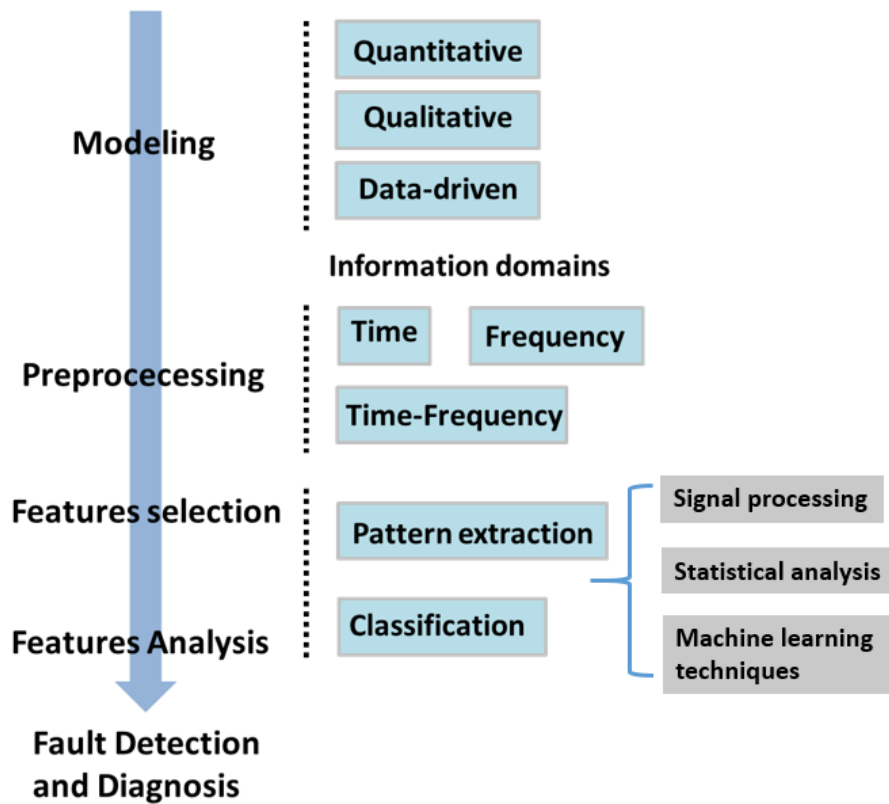


Figure 2.20: General fault detection and diagnosis approach [93]

### 2.6.1 Modelling

The first step in the development of fault detection and diagnosis is to obtain prior knowledge of the system that is the system representation. In addition, the system might be subjected to different types of faults. For the development of a suitable diagnosis scheme, it is important to obtain detailed knowledge about the nature and dynamics of such faults [94].

System knowledge can be presented in explicit or implicit form. For example, the dynamics of a system might be explicitly accessible in the form of an empirical model or a mathematical function [95]. In other cases, graphical approaches might be incorporated

to describe the system behavior [96]. Also, a knowledge-based, artificial neural network and expert systems consisting of production rules and heuristics are examples of implicit knowledge representation [97].

After system representation, the subsequent significant factor in the selection of the appropriate class of fault diagnosis is the type of faults. According to one of the classifications, faults are categorized as hardware, software, and communication faults. Hardware faults can further be classified according to the type of component failure: sensor faults, actuator faults, and controller faults [98]. Another classification can be based on the nature and dynamics of faults such as transient, permanent, intermittent, and incipient faults [99]. Transient faults are caused by sudden change; these faults disappear after a relatively short time [100]. Permanent faults cause system damage which cannot be removed unless the faulty component is replaced [101]. Intermittent faults have cyclic nature between active and inactive states [102]. Incipient faults exhibit slow and gradual changes in the state of faulty component variables [103].

### 2.6.2 Data collection

The purpose of the PMS for EV powertrain is to monitor its components and their health status. Abnormal conditions (fault or failure) or degradation can be identified and diagnosed. A prognosis can also be done to predict the remaining useful life of the components. The choice of the health monitoring technique mainly depends on the maintenance targets, components under observation, motor drive, and cost as well. Health monitoring requires measuring or estimating several pieces of information. For electrical machines, the most used data are: phase currents, vibration, temperature, airgap torque, power, magnetic flux, and acoustic emission [104]. Based on the investigations made in [105] and [106] a summary is done in Table 2.2.

**Table 2.2:** Fault indicators for different motor faults [105, 106]

Motor faults	Fault Indicators						
	Current	Vibration	Temperature	Airgap torque	Power	Magnetic flux	Acoustic emission
Winding	✓	✓	✓	✓	✓	✓	
Demagnetization	✓	✓			✓	✓	
Bearing	✓	✓	✓			✓	✓
eccentricity	✓	✓					
Rotor Shaft		✓					
Rotor core	✓	✓					
Stator core	✓	✓					

The results in Table 2.2 show that phase currents and vibration signals are relevant measurements to diagnose most of the faults in electrical machines. Stator current signature monitoring can provide information on the machine's health status without requiring additional sensors (which may be more expensive and less robust). Moreover, the stator current is often already monitored for safety, as well as the control of power converters [105, 107]. The vibration, temperature, acoustic emission, and magnetic flux analysis techniques are invasive and involve high costs for monitoring system development.

Different features can be extracted from the currents flowing in the stator windings. The symmetrical components of the stator current for stator winding fault detection in a PMSM [108]. The patterns of the stator current vector trajectory in the Concordia reference frame are also used for the identification of stator turn faults and even fault severity evaluation [109, 110]. The negative-sequence component has been also widely used as a fault signature for stator winding failure. However, the negative sequence current can also be caused by an unbalanced power supply or asymmetries. Therefore, it has been found ineffective for fault diagnosis. The zero-sequence voltage [111], and negative-sequence impedance [112] have been proposed as alternative solutions. For automotive applications, more sophisticated signal processing techniques may be needed to deal with the wide varying operating conditions. In the following various motor signal preprocessing and feature extraction are reviewed.

### 2.6.3 Data preprocessing and feature extraction

The sensor data contain a number of features from the system, some of them hold the fault signatures while some may not. Hence fault detection by analyzing the sensor raw data can be very tedious because of the high number of features to analyze. Hence data preprocessing is required to produce a set of features with the most important and compact facts from the sensor data. The goal of the data preprocessing is to search for the distinguishing features of the original sensor data that are invariant to irrelevant transformations of the input [113]. This can be performed by selecting the appropriate information domain analysis (time domain, frequency domain, or time-frequency domain), data dimension reduction, etc.

#### 2.6.3.1 Information domain analysis

##### 1. Time domain analysis

Time-domain techniques are more effective when the component is analyzed under stationary conditions, but are also helpful for some non-stationary conditions. Statistical features are usually calculated from this domain, and they provide basic information about the signal acquired such as signal shape, tendencies, frequency ranges, etc [114]. For a variable  $\mathbf{X} = (x_1, \dots, x_N)$  of  $N$  samples, the most used statistical features are shown in Table 2.3.

##### 2. Frequency domain Analysis

A Frequency-domain analysis is based, first, on the transformation of the acquired temporal array to the frequency-domain. The classical spectral analysis (by Fourier transform) allows the analysis of a temporal signal in terms of individual frequency components by analysing the parameters of each component. These techniques can

**Table 2.3:** Statistical features [115]

Mean ( $\mu$ )	$\mu = \frac{1}{N} \sum_{j=1}^N x_j$	(2.1)
Root Mean Square (RMS)	$RMS = \sqrt{\frac{1}{N} \sum_{j=1}^N (x_j)^2}$	(2.2)
Shape Factor (SF)	$SF = \frac{RMS}{\frac{1}{N} \sum_{j=1}^N  x_j }$	(2.3)
Crest Factor (F)	$F = \frac{\max(\mathbf{X})}{RMS}$	(2.4)
Variance ( $\sigma^2$ )	$\sigma^2 = \frac{1}{N-1} \sum_{j=1}^N (x_j - \mu)^2$	(2.5)
Skewness (Skw)	$Skw = \frac{1}{N} \sum_{j=1}^{N-1} \left( \frac{x_j - \mu}{\sigma} \right)^3$	(2.6)
Kurtosis (Kur)	$Kur = \frac{1}{N} \sum_{j=1}^{N-1} \left( \frac{x_j - \mu}{\sigma} \right)^4$	(2.7)

extract spectral information but are not able to deal with non-stationary conditions. The main techniques are non-parametric methods such as Discrete Fourier Transform, parametric models, and high-resolution methods. Usually, the features extracted from this domain consist of specific frequency bands that highlight a specific fault. One of the most popular fault diagnosis techniques based on motor current analysis is Motor Current Signature Analysis (MCSA) based on Fast Fourier Transform (FFT) [116]. However, the frequency domain analysis may fail to detect the fault from nonstationary signals, that is the case in EV [117].

### 3. Time-Frequency domain Analysis

Time-Frequency domain analysis performs, simultaneously, time and frequency analysis, mainly useful in case of transients of speed in the machine, where FFT causes averaging mistakes as it has been shown before. The time and frequency resolutions are the main reasons to select a specific time-frequency technique. The major drawback is that these methods require a huge computational cost making them unavailable for dealing with big datasets. Statistical features can also be calculated in this domain with proper segmentation of the time-frequency maps to obtain enough resolution. The main techniques are Short-Time Fourier Transform, Wavelet Transform, Discrete Wavelet Transform, Hilbert Huang Transform, Empirical Mode Decomposition, and others [118, 119, 120]. Usually, the features extracted from this domain depend on the used technique. Statistical features are also a popular choice in this domain.

#### 2.6.3.2 Data dimension reduction

Working with high dimensional datasets complicates the fault diagnosis, not only because of the possible presence of non-significant and redundant information in the data, but also because a proper convergence of the algorithms could be compromised. For these reasons,

there is a necessity to apply dimensionality reduction techniques in condition monitoring applications [121]. Principal Component Analysis (PCA) is one of the most used techniques for dimensionality reduction. It aims to find the linear projections that best capture the variability of the data [122]. By working on the projections that maximize the variance of the data, it is possible to highlight the anomalies that could appear during monitoring, therefore, PCA is used often in fault detection.

Linear discriminant analysis (LDA) is another well-known technique for linear dimensionality reduction in multi-class problems. LDA attempts to maximize the linear separation between data points belonging to different classes. In contrast to most other dimensionality reduction techniques, LDA, as a feature extraction technique, finds a linear mapping that maximizes the linear class separation in the low-dimensional representation of the data. The criteria that are used to formulate linear class separation in LDA are the within-class and the between-class scatter [123].

### 2.6.3.3 Other feature extraction techniques

The above signal-extracted statistical parameters and spectral properties are related to data-driven approach of fault detection. Moreover, they can also be extracted in terms of functional relationships among the process variables in quantitative model-based approaches, or qualitative rules in qualitative model-based approaches [124]. In the model-based approaches, the features are generated from the dynamic analytical models. The main model-based feature extraction techniques include parity space, observer, and parameter estimation [125].

## 2.6.4 Fault detection and identification methods

In the field of industrial machinery monitoring, many approaches regarding health monitoring schemes have been proposed during the last decade. The information on the monitored system's healthy, and faulty conditions are analyzed to train a classifier capable of assessing the condition of systems [126]. However, practical integration in the industry requires dealing with challenging scenarios that classical fault diagnosis methodologies cannot address. Unexpected events, like unpredicted fault scenarios, or deviations from the nominal operation can occur during the lifetime of the machinery under monitoring. These new operating conditions must be identified to avoid wrong diagnoses.

Detecting patterns different from those available during the training is called novelty detection [127]. Fault diagnosis methodologies must be able to identify novel operating conditions (novelty detection) while continuing the identification of the known fault scenarios. In this regard, the integration of novelty detection strategies into fault diagnosis methodologies is the first step to developing a reliable condition monitoring system. This can be done through probabilistic methods (Gaussian mixture models, Multivariate kernel density estimators), and distance-based methods (Nearest neighbors). Some well-known statistical and Artificial Intelligence approaches for fault detection and diagnosis are briefly presented in the following.

#### 2.6.4.1 Statistical methods

The first statistical analyses introduced in fault diagnosis have been the univariate statistical methods. They consist of examining statistical features of each system variable. This makes the interpretation and diagnosis of a fault condition very difficult and convoluted [128]. However, in a multivariate system like in electric vehicle applications, simultaneous monitoring of individual variables separately will fail to recognize possible cross-correlations that may exist and will increase the insensitivity of the control charts for detection of faults conditions [129]. This can be quite misleading as not all the variables are independent and only a few underlying events are driving the process at any one time. The extension of these statistical methods is defined by the simultaneous monitoring and analysis of all the variables. Some well known different multivariate statistical techniques are discriminant analysis, cluster analysis, principal component analysis (PCA), and factor analysis (FA) [130].

#### 2.6.4.2 Artificial intelligence technique

The Artificial Intelligence (AI) methods detect faults through the finding of the changes of patterns in the selected feature variables. They can be classified into supervised or unsupervised learning-based, and regression-based methods. These algorithms are constantly improved, and therefore, seem to be a promising research direction in the field of fault diagnosis [131]. Machine Learning (ML) has become a very popular technique and is an inherent part of the Artificial Intelligence (AI) field. Some usual ML algorithms are Decision Tree (DT), Support Vector Machine (SVM), and K-Nearest Neighbors (KNN). Other subcategories like Artificial Neural Networks (ANNs) and Deep Neural Networks (DNN) are algorithms whose operation is inspired by the human brain operating principle [132]. The usage of the above-mentioned methods can minimize human participation in fault diagnosis and help in automating this process. The usage of ML-based classifiers, and shallow and deep neural networks to detect various types of electric motor faults have been demonstrated in [133, 134].

## 2.7 Conclusion

This chapter has shown general consideration and overview of the importance of fault detection in electric vehicle's powertrains. It is referred to as the first macro-objective where the latest academic papers, reference books, and industrial publications were studied for a more detailed understanding of the state of the art of fault detection and diagnosis technologies in EV powertrains. The focus has been on:

- Description of the structure of a typical electric vehicle powertrain including the mechanical, electrical, and control components.
- Description of structure and operations of each system component with a focus on the electric motor and power converter.
- Classification of the different methodologies of fault detection and diagnosis, their advantages and drawbacks.

The ongoing of this thesis in the next chapter will be on a review of the different EV powertrain modelling for fault diagnosis.

## Chapter 3

# PMaSynRM modelling for fault diagnosis

### 3.1 Introduction

Modelling the conversion chain to include faults enables numerical simulation to be used to evaluate diagnostic methods while avoiding costly and potentially destructive testing. The models should be accurate under healthy and faulty conditions but also during transients and steady-state to develop sensitive fault detection and diagnostic algorithms [135]. The algorithms are expected to identify faults signatures even at their incipient stages despite the nuisances [136].

Models of electrical machines can be broadly classified into analytical and Finite Element Method (FEM) models. The analytical models are quite straightforward and fast but less accurate due to the assumptions on materials properties and geometry. FEM models help to address these assumptions but are computationally costly [137]. The combination of these two modelling techniques leads to hybrid models, which can benefit from the accuracy of numerical models and the computational speed of analytical models [138]. Figure 3.1 summarizes the different modelling techniques for Electrical Motors in terms of computation time and accuracy.

In the following, first, the three modelling techniques will be presented. Second, the most usual drive control techniques will be presented. Third, the model of the PMaSynRM motor drive for fault analysis will be presented with the simulation and experimental validation. Finally, the models of the different fault modes and their simulation results will be given.

### 3.2 PMaSynRM modelling

As stated in the previous chapter, the electrical machine of interest in the EV motor drive system under study is a three-phase wounded stator PMaSynRM motor. It belongs to the family of synchronous motors with an anisotropic rotor and permanent magnets as shown in Figure 3.2. Similarly to the other machines in the same family, the torque produced by the PMaSynRM is composed of the permanent magnet torque and the reluctance torque. The permanent magnet torque is the torque due to the interaction between stator currents and the permanent magnets, while the reluctance torque is due to the asymmetry of the magnetic circuit. The latter is generated to move the rotor to a position where the reluctance is minimal [140].

#### 3.2.1 Models Based on Coupled Circuits



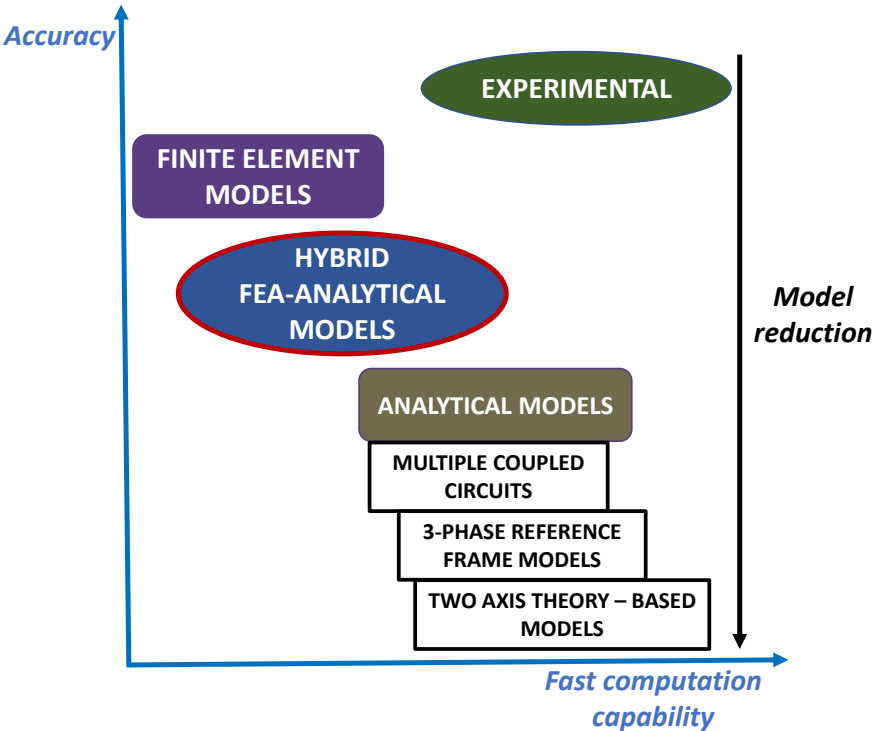


Figure 3.1: Electrical Motor modelling techniques [139]

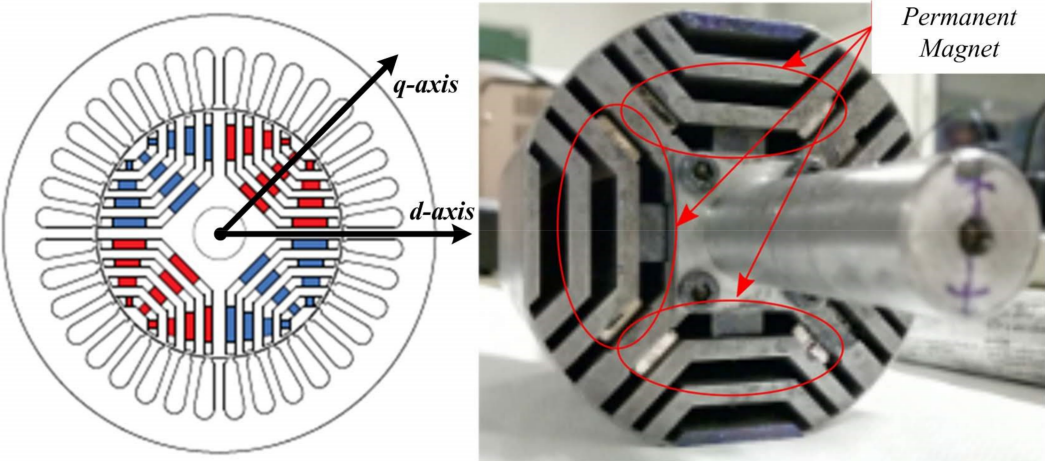


Figure 3.2: Rotor structure of a PMSynRM [141]

One of the most widely used models ( $d-q$  model) is based on coupling circuits and vector space decomposition. This model assumes symmetrical motors, linear iron permeability, air-gap uniformity, or the absence of a tangential induction in the air-gap. All these assumptions allow simplifying the resulting mathematical model that can be computed quickly and is accurate enough for control purposes. However, under faulty conditions, these assumptions may no longer be valid, and the model is no more relevant. In the following, a review of the multiple coupled circuits model of the PMSynRM and its  $d-q$  reference frame decomposition will be presented.

### 3.2.1.1 Modelling in the natural frame

The multiple coupled circuits models are developed considering that the stator is composed of multiple inductive circuits. Figure 3.3 shows the electrical equivalent circuit of a dynamic model of the PMSynRM. The Kirchhoff's second law and Newton's second law are applied to the electrical and mechanical parts of the motor to obtain the analytical model.

- **Electrical Part:** From this sketch, the time domain stator voltage equation for a healthy PMSynRM in the 3-phase reference frame is written in matrix form as follows:

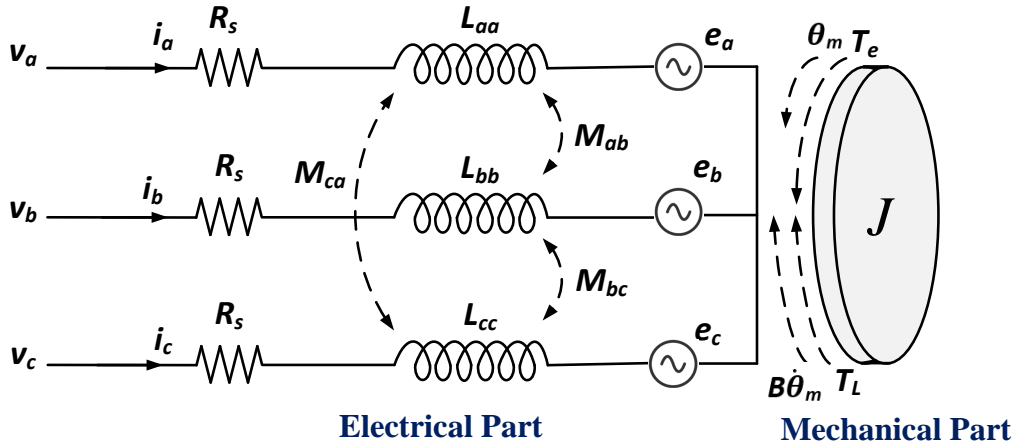


Figure 3.3: Equivalent circuit of a PMSynRM [142]

$$\mathbf{v}_{abc} = \mathbf{R}_s \cdot \mathbf{i}_{abc} + \frac{d}{dt} \psi_{abc} \quad (3.1)$$

Where  $\mathbf{v}_{abc}$ ,  $\mathbf{R}_s$ ,  $\mathbf{i}_{abc}$  and  $\psi_{abc}$  are the vector of phase voltages, resistances matrix, vector of phase currents and vector of flux-linkage, respectively [143].

$$\mathbf{v}_{abc} = [v_a \quad v_b \quad v_c]^T \quad (3.2)$$

$$\mathbf{i}_{abc} = [i_a \quad i_b \quad i_c]^T \quad (3.3)$$

$$\psi_{abc} = [\psi_a \quad \psi_b \quad \psi_c]^T \quad (3.4)$$

It is assumed that the iron has an infinite permeability, and there is no magnetic saturation. The flux-linkage composed of the flux linkages due to the stator current  $\mathbf{i}_{abc}$  and rotor magnets  $\phi_{abc}$  can be expressed as:

$$\psi_{abc} = \mathbf{L}_{abc} \cdot \mathbf{i}_{abc} + \phi_{abc} \quad (3.5)$$

Where  $\mathbf{L}_{abc}$  is the matrix of self inductances  $L_{ii} \forall i \in [a, b, c]$  and mutual inductances  $M_{ij} \forall i \neq j$  matrix.  $R_a$ ,  $R_b$  and  $R_c$  are stator phase  $a$ ,  $b$  and  $c$  resistances.

$$\mathbf{R}_s = \begin{bmatrix} R_a & 0 & 0 \\ 0 & R_b & 0 \\ 0 & 0 & R_c \end{bmatrix} \quad (3.6)$$

$$\mathbf{L}_{abc} = \begin{bmatrix} L_{aa} & M_{ab} & M_{ac} \\ M_{ba} & L_{bb} & M_{bc} \\ M_{ca} & M_{cb} & L_{cc} \end{bmatrix} \quad (3.7)$$

$$\phi_{abc} = \phi_{PM} \begin{bmatrix} \cos \theta_e \\ \cos(\theta_e - 2\pi/3) \\ \cos(\theta_e + 2\pi/3) \end{bmatrix} \quad (3.8)$$

$\theta_e$  is rotor angular position (electrical) and  $\phi_{PM}$  is the peak value of the permanent magnet flux linkage. In the flux linkage equations, inductances depend on  $\theta_e$ . Neglecting higher order harmonics, each self and mutual inductance is composed of a DC value and a second harmonic component as follows [144]:

$$\begin{aligned} L_{aa} &= L_{ls} + L_{0s} + L_{2s} \cos(2\theta_e) \\ L_{bb} &= L_{ls} + L_{0s} + L_{2s} \cos(2\theta_e - 4\pi/3) \\ L_{cc} &= L_{ls} + L_{0s} + L_{2s} \cos(2\theta_e + 4\pi/3) \\ M_{ab} &= -\frac{1}{2}L_{0s} - L_{2s} \cos(2\theta_e - 2\pi/3) \\ M_{bc} &= -\frac{1}{2}L_{0s} - L_{2s} \cos(2\theta_e) \\ M_{ca} &= -\frac{1}{2}L_{0s} - L_{2s} \cos(2\theta_e + 2\pi/3) \end{aligned}$$

where  $L_{ls}$  is the phase leakage inductance.  $L_{0s}$  and  $L_{2s}$  represent the average inductances due to space fundamental air-gap flux and the fluctuation due to the saliency, respectively. They can be expressed as follows:

$$L_{0s} = \mu r l N_s^2 \left( \frac{\pi}{8} \right) \left( \frac{1}{g_{min}} + \frac{1}{g_{max}} \right) \quad (3.9)$$

$$L_{2s} = \mu r l N_s^2 \left( \frac{\pi}{8} \right) \left( \frac{1}{g_{min}} - \frac{1}{g_{max}} \right) \quad (3.10)$$

Where  $g_{min}$  and  $g_{max}$  represent the  $d$ -axis and  $q$ -axis equivalent air-gaps, respectively.  $r$ ,  $l$  and  $N_s$  denote the radius, core length, and number of turns in series per phase. The motor flux-linkage equation becomes:

$$\begin{aligned}
 \psi_a &= (L_{ls} + \frac{3}{2}L_{0s} + \frac{1}{2}L_{2s}\cos(2\theta_e)) i_a + \frac{\sqrt{3}}{2}L_{2s}\sin(2\theta_e)(i_c - i_b) + \phi_{PM}\cos(\theta_e) \\
 \psi_b &= (L_{ls} + \frac{3}{2}L_{0s} + \frac{1}{2}L_{2s}\cos(2\theta_e - 4\pi/3)) i_b + \frac{\sqrt{3}}{2}L_{2s}\sin(2\theta_e - 4\pi/3)(i_a - i_c) + \\
 &\quad \phi_{PM}\cos(\theta_e - 2\pi/3) \\
 \psi_c &= (L_{ls} + \frac{3}{2}L_{0s} + \frac{1}{2}L_{2s}\cos(2\theta_e + 4\pi/3)) i_c + \frac{\sqrt{3}}{2}L_{2s}\sin(2\theta_e + 4\pi/3)(i_b - i_a) + \\
 &\quad \phi_{PM}\cos(\theta_e + 2\pi/3)
 \end{aligned} \tag{3.11}$$

- **Mechanical Part:** From Figure 3.3 the mechanical model of the motor with its load is expressed using Newton's second law as follows:

$$\frac{d^2\theta_m}{dt} = \frac{1}{J}(T_e - T_L - B\dot{\theta}_m) \tag{3.12}$$

Where  $\theta_m$  represents the mechanical angular displacement of the rotor  $\theta_m = \frac{\theta_e}{n_p}$ ,  $n_p$  is the motor pole-pair number.  $\dot{\theta}_m$  also represented by  $\omega_m$  is the mechanical angular velocity of the rotor.  $J$ ,  $B$ , and  $T_L$  are the moment of inertia, friction coefficient, and load torque, respectively.  $T_e$ , the electromagnetic torque can be calculated from the co-energy  $W_c$ , expressed by:

$$W_c = \frac{1}{2}\mathbf{L}_{abc} \cdot \mathbf{I}_{abc}^2 + \mathbf{I}_{abc} \cdot \phi_{abc} + W_{PM} \tag{3.13}$$

Where  $W_{PM}$  is the energy stored in the permanent magnets. Thus,

$$T_e = n_p \frac{\partial W_c}{\partial \theta_e} \tag{3.14}$$

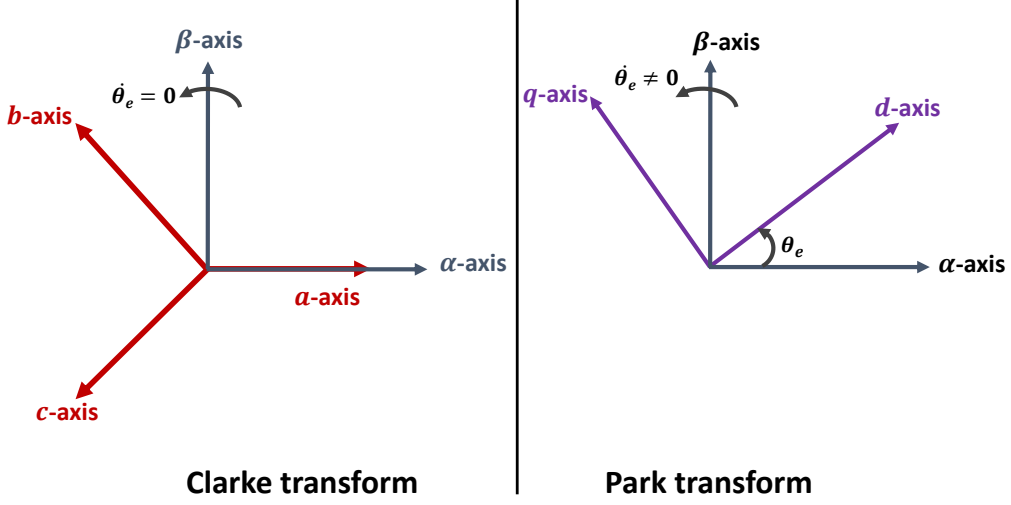
### 3.2.1.2 Modelling in the synchronous rotating frame

To minimize the complexity in solving the differential equation 3.1, the model is projected into the  $(d - q)$  reference frame attached to the rotating field. The three-phase stator voltages, currents, and flux linkages are first transformed into their equivalent two-phase coordinates in the stationary reference frame  $\alpha - \beta$ . This transformation is known as Clarke (or Concordia) transformation. To eliminate the time-varying parameters, a rotation is introduced. The combination of the two transformations, known as Park transform is illustrated in Figure 3.4.

As it is shown,  $\alpha$ -axis and  $\beta$ -axis are orthogonal. In order for the transformation to be invertible, a third variable, known as the zero-sequence component 0, is added. The equation of the Clarke transform of a three-phase variable  $\mathbf{f}_{abc}$  into a stationary variable  $\mathbf{f}_{\alpha\beta 0}$  using the transformation matrix  $\mathbf{T}_{\alpha\beta 0}$  is given by:

$$\mathbf{f}_{\alpha\beta 0} = \mathbf{T}_{\alpha\beta 0} \cdot \mathbf{f}_{abc} \tag{3.15}$$

$$\mathbf{T}_{\alpha\beta 0} = \begin{bmatrix} 1 & -\frac{1}{2} & -\frac{1}{2} \\ 0 & \frac{\sqrt{3}}{2} & -\frac{\sqrt{3}}{2} \\ \frac{1}{2} & \frac{1}{2} & \frac{1}{2} \end{bmatrix} \tag{3.16}$$


 Figure 3.4: Coordinate transformations  $abc$  to  $\alpha - \beta$  and  $\alpha - \beta$  to  $d - q$ 

The inverse transformation matrix  $\mathbf{T}_{\alpha\beta 0}^{-1}$  is given by:

$$\mathbf{f}_{\text{abc}} = \mathbf{T}_{\alpha\beta 0}^{-1} \cdot \mathbf{f}_{\alpha\beta 0} \quad (3.17)$$

$$\mathbf{T}_{\alpha\beta 0}^{-1} = \begin{bmatrix} 1 & 0 & 1 \\ -\frac{1}{2} & \frac{\sqrt{3}}{2} & 1 \\ -\frac{1}{2} & -\frac{\sqrt{3}}{2} & 1 \end{bmatrix} \quad (3.18)$$

Now that the three-phase variables are expressed in the  $\alpha - \beta$  stationary reference frame, they can be transformed into  $d - q$  rotating reference frame using Park transform matrix  $\mathbf{T}_{\text{dq}0}(\theta_e)$ . This leads to the voltages, currents, flux linkages and inductance equations having time-invariant coefficients. The transformation of a variable  $\mathbf{f}_{\alpha\beta 0}$  into  $\mathbf{f}_{\text{dq}0}$  is shown as follows:

$$\mathbf{f}_{\text{dq}0} = \mathbf{T}_{\text{dq}0}(\theta_e) \cdot \mathbf{f}_{\text{abc}} \quad (3.19)$$

$$\mathbf{T}_{\text{dq}0}(\theta_e) = \begin{bmatrix} \cos(\theta_e) & \cos(\theta_e - 2\pi/3) & \cos(\theta_e + 2\pi/3) \\ \sin(\theta_e) & \sin(\theta_e - 2\pi/3) & \sin(\theta_e + 2\pi/3) \\ \frac{1}{2} & \frac{1}{2} & \frac{1}{2} \end{bmatrix} \quad (3.20)$$

$\theta_e$  is the angular position of the Park's reference frame. The inverse transformation can be written as follows:

$$\mathbf{f}_{\alpha\beta 0} = \mathbf{T}_{\text{dq}0}^{-1}(\theta_e) \cdot \mathbf{f}_{\text{dq}0} \quad (3.21)$$

$$\mathbf{T}_{\text{dq}0}^{-1}(\theta) = \begin{bmatrix} \cos(\theta_e) & \sin(\theta_e) & 1 \\ \cos(\theta_e - 2\pi/3) & \sin(\theta_e - 2\pi/3) & 1 \\ \cos(\theta_e + 2\pi/3) & \sin(\theta_e + 2\pi/3) & 1 \end{bmatrix} \quad (3.22)$$

Equation 3.1, ( $\mathbf{v}_{abc} = \mathbf{R}_s \cdot \mathbf{i}_{abc} + \frac{d}{dt}\psi_{abc}$ ), can then be written as:

$$\mathbf{T}_{\alpha\beta 0}^{-1} \cdot \mathbf{T}_{dq0}^{-1}(\theta_e) \cdot \mathbf{v}_{dq} = \mathbf{R}_s \cdot \mathbf{T}_{\alpha\beta 0}^{-1} \cdot \mathbf{T}_{dq0}^{-1} \mathbf{i}_{abc} + \frac{d}{dt} (\mathbf{T}_{\alpha\beta 0}^{-1} \cdot \mathbf{T}_{dq0}^{-1} \cdot \psi_{dq}) \quad (3.23)$$

Let a transformation matrix  $\mathbf{K}^{-1}$  defined as  $\mathbf{K}^{-1} = \mathbf{T}_{\alpha\beta 0}^{-1} \cdot \mathbf{T}_{dq0}^{-1}(\theta_e)$ .

$$\mathbf{K}^{-1} \cdot \mathbf{v}_{dq} = \mathbf{R}_s \cdot \mathbf{K}^{-1} \cdot \mathbf{i}_{dq} + \frac{d\mathbf{K}^{-1}}{dt} \cdot \psi_{dq} + \mathbf{K}^{-1} \cdot \frac{d\psi_{dq}}{dt} \quad (3.24)$$

Multiplying each term of the equation by  $\mathbf{K}$ , we get:

$$\mathbf{v}_{dq} = \mathbf{R}_s \cdot \mathbf{i}_{dq} + \mathbf{K} \frac{d\mathbf{K}^{-1}}{dt} \cdot \psi_{dq} + \frac{d\psi_{dq}}{dt} \quad (3.25)$$

$\psi_{dq} = \mathbf{K}\psi_{abc}$ , from Equation 3.5, ( $\psi_{abc} = \mathbf{L}_{abc} \cdot \mathbf{i}_{abc} + \phi_{abc}$ ),  $\psi_{dq}$  can be written as:

$$\psi_{dq} = \mathbf{K} \cdot \mathbf{L}_{abc} \cdot \mathbf{i}_{abc} + \mathbf{K} \cdot \phi_{abc} \quad (3.26)$$

$$\begin{aligned} \psi_d &= \left( L_{ls} + \frac{3}{2}L_{0s} + \frac{1}{2}L_{2s} \right) i_d + \phi_{PM} \\ \psi_q &= \left( L_{ls} + \frac{3}{2}L_{0s} - \frac{1}{2}L_{2s} \right) i_q \end{aligned} \quad (3.27)$$

Let  $L_d = L_{ls} + \frac{3}{2}L_{0s} + \frac{1}{2}L_{2s}$  and  $L_q = L_{ls} + \frac{3}{2}L_{0s} - \frac{1}{2}L_{2s}$  be the stator inductances in the  $d-q$  reference frame. The stator voltage equations become as follows:

$$\begin{aligned} v_d &= R_s i_d + L_d \frac{di_d}{dt} - \omega_e L_q i_q \\ v_q &= R_s i_q + L_q \frac{di_q}{dt} + \omega_e (L_d i_d + \phi_{PM}) \end{aligned} \quad (3.28)$$

From these equations, the phasor of the PMSynRM in the  $d-q$  reference frame is shown in Figure 3.5.

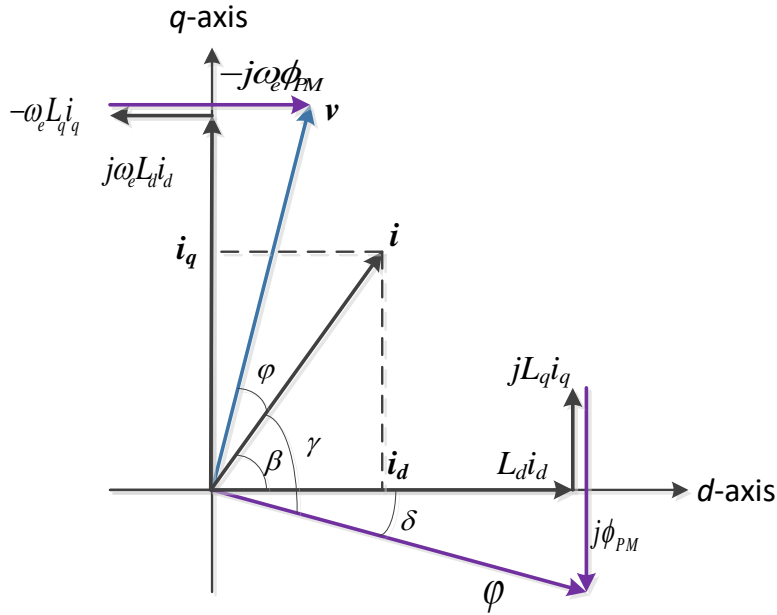


Figure 3.5: Phasor diagram of a PMSynRM [145]

In the following, the derivation of the electromagnetic torque  $T_e$  is detailed. The instantaneous input power  $\mathcal{P}$  can be calculated as [146]:

$$\mathcal{P} = v_a i_a + v_b i_b + v_c i_c \quad (3.29)$$

It can be expressed in the  $d - q$  reference frame, as:

$$\mathcal{P} = \frac{3}{2} (v_d i_d + v_q i_q) \quad (3.30)$$

After replacing  $v_d$  and  $v_q$  from 3.28, the mechanical power can be obtained :

$$\mathcal{P}_{mec} = \frac{3}{2} (\omega_e \psi_d i_q - \omega_e \psi_q i_d) \quad (3.31)$$

It can also be expressed as:

$$\mathcal{P}_{mec} = T_e \omega_m \quad (3.32)$$

Where  $\omega_m$  is the rotor mechanical speed ( $\omega_m = \frac{\omega_e}{n_p}$ ). Then, substituting 3.27, the electromagnetic torque is expressed as:

$$T_e = \frac{3}{2} n_p ((L_d - L_q) i_d i_q + \phi_{PM} i_q) \quad (3.33)$$

### 3.2.1.3 Modelling of motor faults based on Coupled Circuits

The method of Multiple Coupled Circuits has been used to model different types of stator and rotor faults as shown in Table 3.1.

**Table 3.1:** Coupled Circuits models of electric motor including faults

Multiple Coupled Circuit Models		Models in $d - q$ reference frame	
Fault	References	Fault	References
Stator short-circuit	[147, 148, 149]	Stator short-circuit	[150, 151, 152]
Stator open-circuit	[149]	Stator open-circuit	[153]
Static eccentricity	[154, 155, 156]	Static eccentricity	[157, 158]
Dynamic eccentricity	[154, 159, 156]	Dynamic eccentricity	[160, 157]
Mixed eccentricity	[154, 161]	Mixed eccentricity	[162]
-	-	Bearing fault (race defect)	[163]

The most critical issue when modelling faulty electrical machines is to provide the actual values of the parameters under faulty conditions. Regarding stator resistances, they are usually estimated through the examination of the dimensions of conducting paths. Another challenge is to accurately evaluate the coupling effects in a faulty machine. The Winding Function Approach (WFA) is one of the most popular methods to evaluate the stator self and mutual inductances under faulty conditions [147]. It consists of integrating the winding functions to obtain phase inductances. The integrals could be complex and time-consuming. To reduce the computation time, a method based on a single discrete circular convolution is proposed in [164]. With this solution, the mutual inductances of two phases are calculated for each relative angular position with a single equation that is solved with

Fast Fourier Transform. Although WFA includes the effect of space harmonics, it usually assumes the symmetry of the main magnetic circuit, which makes it unsuitable for the analysis of eccentricity faults, as shown in [165]. To overcome this drawback, the Modified Winding Function Approach (MWFA) method, which considers air-gap eccentricity for the inductance calculation is proposed. It can reproduce the effects of static, dynamic, or mixed eccentricity [154]. The models based on Multiple Coupled Circuits and their variants, such as WFA and MWFA, consider the geometry and winding layout of the machine without any restriction regarding the symmetry of the stator windings. Moreover, the effect of space harmonics is considered. Consequently, these models are suitable to analyze electrical motors with arbitrarily connected windings, and under unbalanced operating conditions[166].

### 3.2.2 Finite Element models

Finite Element Method (FEM) aims to model complex systems in which several physics interact, where different kinds of physical effects act simultaneously. Its basic concept is to model a problem domain by dividing it into small parts. The solutions for the entire problem domain are then obtained by combining the elements with continuity between elements ensured. The necessary boundary conditions are then imposed. For an electric machine, this analysis helps to predict physical behaviors. Regarding electrical machines, FEM can be used for:

- Electromagnetic finite element analysis,
- Thermal finite element analysis
- Mechanical Strength finite element analysis

In this PhD thesis, only the electromagnetic finite element analysis will be considered. From the FEM model the magnetic and geometric characteristics of the machine will be used to compute the magnetic field distribution that reflects the phenomenon in the stator, rotor, and mechanical parts [167]. Moreover, the FEM allows calculating parameters such as the magnetic flux density, inductances, and electromagnetic torque while including spatial harmonic effects and split winding pattern [168].

It has been shown that the analytical model of the PMSynRM is composed of partial differential equations. These equations are tedious to solve analytically because of the complexity of the domain under study, the nonlinearity of the material properties, and dynamic time behaviour. These limitations of the analytical model can be overcome with the FEM [169].

In the following, the theory of finite element analysis for electric motor modeling will be presented. The mathematical model will be first derived, and then the FEM technique will be applied to obtain the finite element model.

#### 3.2.2.1 Mathematical model

The fundamental basis of applying numerical methods is the modelling of electric machines. Electric machines receive power from external sources through electric circuits. This in turn requires the modelling of electromagnetic fields inside the machine to be coupled with electric circuit analysis. Moreover, electric machines are electro-mechanical conversion



devices. It is also important to take into account the interactions of electromagnetic fields, mechanical forces, and motions. Therefore comprehensive modelling of electromagnetic fields, circuits, and mechanical motion of an electrical machine system should be considered together. The mechanical motion equation has been derived in 3.12:  $\frac{d^2\theta_m}{dt} = \frac{1}{J}(T_e - T_L - B\dot{\theta}_m)$ .

### 1. Modelling of Electromagnetic Fields

Maxwell's equations are generally used to describe electromagnetic phenomena. The fundamental equations contain only fields and are described as follows:

$$\begin{aligned}\nabla \times \mathbf{E} &= -\frac{\partial \mathbf{B}}{\partial t} \\ \nabla \cdot \mathbf{B} &= 0\end{aligned}\quad (3.34)$$

Where  $\mathbf{E}$  is the electric field vector and  $\mathbf{B}$  magnetic flux density vector. The relationships between the fields and the sources are expressed as follows:

$$\begin{aligned}\nabla \times \mathbf{H} &= \frac{\partial \mathbf{D}}{\partial t} + \mathbf{J} \\ \nabla \cdot \mathbf{D} &= \rho\end{aligned}\quad (3.35)$$

Where  $\mathbf{H}$  is the magnetic field vector,  $\mathbf{D}$  electric flux density vector,  $\rho$  electric charge density and  $\mathbf{J}$  electric current density. For electrical machines, the quasi-static approximation is widely used. It states that displacement currents are negligible in comparison to the imposed currents. Moreover, electric charges are also negligible.

$$\left| \frac{\partial \mathbf{D}}{\partial t} \right| \ll \mathbf{J}, \quad |\rho| \ll 1$$

Maxwell's equation in the quasi-static assumption is summarized as follows:

$$\begin{aligned}\nabla \times \mathbf{H} &= \mathbf{J} \\ \nabla \times \mathbf{E} &= -\frac{\partial \mathbf{B}}{\partial t}\end{aligned}\quad (3.36)$$

To solve this system of equations, materials constitutive laws are required. They are expressed as follows [170]:

$$\begin{aligned}\mathbf{B} &= \mu_0 \mu_r \mathbf{H} \\ \mathbf{J} &= \sigma (\mathbf{E} + \mathbf{v} \times \mathbf{B})\end{aligned}\quad (3.37)$$

Where  $\mu_0$  is the magnetic permeability of free space,  $\mu_r$  relative permeability,  $\sigma$  material electric conductivity, and  $\mathbf{v}$  velocity of the material of interest in a given reference frame.  $\mu_r$  and  $\sigma$  depend on electromagnetic fields and other parameters such as time, temperature, and mechanical strain. If a system involves a moving region as an electric machine, the term with velocity in Equation 3.37 requires special attention. A coordinate system in which all the variables are fixed to the material is adopted. Hence the velocity is always zero in its own coordinate system [171].

#### Formulation Using the Magnetic Vector Potential

Since  $\mathbf{B}$  is divergence-free ( $\nabla \cdot \mathbf{B} = 0$ ), a magnetic vector potential  $\mathbf{A}$  can be found such that:

$$\mathbf{B} = \nabla \times \mathbf{A} \quad (3.38)$$

Thus, equations in 3.36 can be combined into one equation:

$$\nabla \times \mathbf{E} + \frac{\partial \mathbf{B}}{\partial t} = \nabla \times \left( \mathbf{E} + \frac{\partial \mathbf{A}}{\partial t} \right) = 0 \quad (3.39)$$

With equation 3.39, the current density with respect to a fixed-to-material frame can be written as:

$$\mathbf{J} = \sigma \mathbf{E} = \sigma \left( -\frac{\partial \mathbf{A}}{\partial t} - \nabla \Phi \right) \quad (3.40)$$

Replacing equation 3.40 in  $\nabla \times \mathbf{H} = \mathbf{J}$ , we get:

$$\nabla \times \left( \frac{1}{\mu_0 \mu_r} \nabla \times \mathbf{A} \right) = \sigma \left( -\frac{\partial \mathbf{A}}{\partial t} - \nabla \Phi \right) \quad (3.41)$$

Given the assumptions of 2D analysis, the magnetic induction is defined only in the  $Oxy$  plane. Therefore, the magnetic vector potential  $\mathbf{A} = A\mathbf{k}$  and current density  $\mathbf{J} = J\mathbf{k}$  have only one component, where  $\mathbf{k}$  is the unit vector in the  $z$  direction. Thus, equation 3.41 can be simplified as:

$$\frac{1}{\mu_0 \mu_r} \nabla^2 \mathbf{A} = \sigma \left( \frac{\partial \mathbf{A}}{\partial t} + \nabla \Phi \right) \quad (3.42)$$

In electric motor with PMs, the PMs are often characterized in the second quadrant of their magnetization curve. The usual parameters for describing a PM are the remanant flux density  $\mathbf{B}_0$  and the coercive magnetic field  $H_c$  (whose value is negative). The relative permeability of PM is usually taken as 1. In presence of PMs in an electric machine, equation 3.42 becomes:

$$\frac{1}{\mu_0 \mu_r} \nabla^2 \times \mathbf{A} = \sigma \left( -\frac{\partial \mathbf{A}}{\partial t} - \nabla \Phi \right) - \frac{\partial}{\partial x} \frac{1}{\mu} \mathbf{B}_{oy} + \frac{\partial}{\partial y} \frac{1}{\mu} \mathbf{B}_{ox} \quad (3.43)$$

The last two terms characterize the PMs, where  $\mathbf{B}_{ox}$  and  $\mathbf{B}_{oy}$  are  $\mathbf{B}_0$   $x$  and  $y$  components, respectively.

## 2. Circuit Equations

The approach to analyzing electrical machines commonly involves two-dimensional numerical methods with specified current sources for the conductors. The knowledge of input currents is essential for the successful field analysis of electrical devices. However, in practice, electric devices are mostly connected to voltage sources rather than current sources. Therefore, analysis of field problems with a voltage source is preferred. Circuit equations representing the relations between currents and voltages are needed. The coupling of circuit equations to the field analysis is necessary. The general governing equation for stator phase circuits in electrical machines is:

$$\begin{aligned}
V_s &= R_s i_s + L_e \frac{di_s}{dt} + \frac{1}{ms} \left( \int_{\Omega^+} \frac{\partial A}{\partial t} dx dy - \int_{\Omega^-} \frac{\partial A}{\partial t} dx dy \right) \\
&= R_s i_s + L_e \frac{di_s}{dt} + V_i
\end{aligned} \tag{3.44}$$

Where

$V_s =$	applied stator phase voltage
$i_s =$	stator phase current
$R_s =$	total equivalent resistance per phase
$L_e =$	total equivalent inductance of end winding
$l =$	the length of stator windings in Z-direction,
$m =$	number of stator winding branches in parallel connection
$s =$	equivalent cross section area of one turn of stator windings
$\Omega^+, \Omega^- =$	total cross section area of 'go' and 'return' windings per phase respectively
$V_i =$	induced voltage per phase

Equation 3.44 describes the relationship between external voltage source  $V_s$ , current  $i_s$  and vector potential  $A$ . Therefore we can calculate the field value  $A$  directly from the external voltage source  $V_s$ . It is quite effective in the computation of two dimensional electromagnetic fields with coupled external voltage sources[172].

### 3.2.2.2 Finite Element Analysis

Finite element method is a numerical tool used in solving partial differential equations in a given domain including the boundary conditions. Variational principle or the method of weighted residuals is used to derive the finite element equations [173]. The fundamental concept of the method is to divide the problem domain into a number of small subregions or elements. The unknown field values are approximated in those elements by simple shape functions, mostly linear or quadratic. After the finite element formulation of governing equation in each element and the assembly of all the elements, a large linear system of equations is generated. The solution to this system of equations gives the field values of the whole problem domain. Compared with other numerical methods, the main advantages of finite element methods are its flexibility for modelling complex geometries, the capability of handling nonlinearities and eddy currents, easy implementation and stable solutions.

In general, the following steps are involved in the finite element method:

- Define the problem of interest by partial differential equations;
- Subdivide the problem field region into many small subregions;
- Choose the interpolation function in terms of the nodal vales of the elements;
- Derive the finite element equations within each element in terms of energy related functions or weighted residual expressions;
- Assembly of the element equations and the global system of equations is generated;
- Impose boundary conditions;

- Solve the global system of equations with appropriate methods;
- Convert the field solutions to useful design quantities.

When the finite element field analysis is coupled with circuit analysis and mechanical motion, the following steps should also be included:

- the discretization of equations in time domain;
- the combination of field equations with the circuit equations;
- the simulation of the rotor motion [172].

### 3.2.2.3 Finite element modelling of Motor Faults

Finite element methods are used to model different stator and rotor faults fault types in electrical motors as shown in Table 3.2. As an example in [174] the effects of static eccentricity on electromagnetic parameters such as voltage, speed, torque, flux density, and flux distribution for a faulty motor are accurately represented through a Time Stepping Finite Element Method (TSFEM).

**Table 3.2:** Finite element models of electric motor faults

<b>Fault</b>	<b>References</b>
Stator short-circuit	[175, 176, 177]
Static eccentricity	[175, 174, 178]
Dynamic eccentricity	[179]
Mixed eccentricity	[180, 181]
Bearing fault (race defect)	[182, 183]

Although these models often produce better results in terms of accuracy, they require a significant computational capacity. Differences of 8h for a FEM analysis versus 1 min for the same analysis using WFA have been reported in [184]. On the other hand, the assumption of machine symmetry, which would reduce meshing and computing time, can no longer be maintained under faulty conditions [175]. These drawbacks limit the application of the Finite Element approach for the development of online fault diagnosis systems or Artificial Intelligence-based fault diagnosis systems. Indeed, it will require a wide range of scenarios including several fault severities and fault combinations. The evaluation of each scenario requires the simulation of the FEM model. Running these models in hardware simulators, which would allow for reducing simulation times, is still challenging [185].

### 3.2.3 Hybrid models

As mentioned above, the modelling based on FEM is very accurate but requires much computing power and long running times, when compared with analytical models. However, analytical models assume some simplifications, which affect their accuracy and often make them unsuitable for fault diagnosis. The combination of FEM and analytical models leads to a hybrid model that can be run in real-time simulators with a high accuracy [185]. These models use FEM to preset accurately the analytical model parameters, allowing

them to be run in real-time simulators, which is a need for fault diagnosis [186, 187]. For example, in [175] a hybrid model in  $d - q$  frame, through Equations 3.28- 3.33, and finite element analysis is developed for modelling short circuit faults in induction motor drives. It proposes the integration of the model with real-time simulators. In [188], an analytical model with the accuracy of FEM is proposed. This analytical model is implemented in a real-time simulator for testing different static eccentricities. Thereby, simulation times and memory resources are significantly reduced. Similarly, in [189], a complete geometry of an induction motor is solved through FEM to compute the coupling parameters exported to the analytical model. In this case, FEM analysis runs in parallel on multiple processors to speed up the simulations. Despite the improvements, these approaches still require a large number of simulations and memory resources to obtain the coupling parameters. In an attempt to overcome these issues, in [138], sparse identification is proposed to obtain a faulty motor model, reducing the required number of FEM simulations while keeping a good accuracy.

### 3.3 Controller design for the PMSynRM drive

The efficient operation of PMSynRM as part of adjustable electric drives demands a careful choice of control system. There are many ways of designing a PMSynRM control system. The concept of vector control, which allows controlling voltage and flux space vectors (magnitude, angular frequency, and instantaneous position), is common in modern high-performance AC motor drives.

The principle of vector control of an induction motor was proposed for the first time in [190] in 1972. In 1989, P. Pillay and R. Krishnan demonstrated the possibility of using a field-oriented control circuit for a PMSM [191]. Over the past decades, many variations have been proposed. The most usual vector control techniques can be classified into Field Oriented Control (FOC) and Direct Torque Control (DTC). The vector control techniques can differ depending on the type of current or speed controller that may induce different implementation structures and requirements: PI, Fuzzy Logic (FLC), and Model Predictive Controller (MPC) are among the most popular speed controllers [192]. In the following, the two main vector control techniques will be presented.

#### 3.3.1 Field Oriented Control techniques

The FOC's simplified block diagram for a PMSynRM drive with a rotor position sensor is shown in Figure 3.6.

In this circuit, the stator phase currents are measured and transformed to a two-phase  $\alpha - \beta$  system via Clarke Transformation. The value of the rotor angle, measured with a position sensor or estimated, is used for the Park Transformation. In accordance with the reference speed signals and the  $d$ -component of the stator current, taking into account the feedback signals, a decoupled control of the torque and the excitation flux is carried out. The FOC can be designed with (direct) or without a position sensor (indirect or sensorless). In the first case, the control is faster and more accurate. However, in several applications, a sensor is not suitable for reliability and cost issues [192]. A comparative analysis of the characteristics of a Field Oriented Controlled electric drive with a rotor position sensor using various speed regulators is provided in [192]. The following requirements are usually

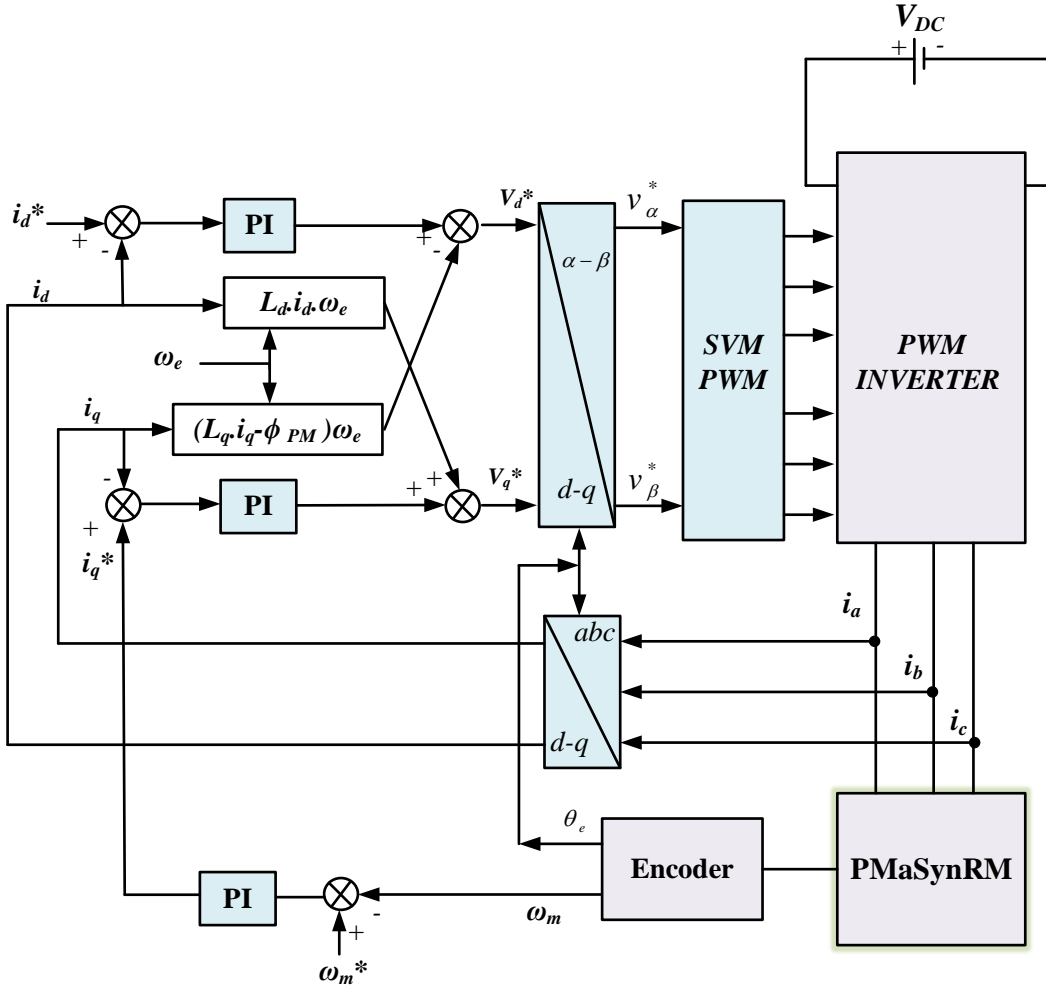


Figure 3.6: FOC for PMSynRM

retained:

- Start-up stator current overshoots,
- Transient process period at no-load start-up and at loading in a steady state,
- Maximum torque and speed overshoot.

According to the Simulink simulation results presented in [192], it can be concluded that the application of PI controller leads to significant current peaks at start-up, relatively long settling time, and speed overshoot, as well as torque ripples. MPC provides minimal current peaks and almost no speed or torque overshoots. FLC leads to lower overshoot, but the transient is longer. The peak in currents amplitude at start-up is slightly higher than for MPC.

### 3.3.2 Direct Torque Control techniques

DTC has a more simple structure than FOC as shown in Figure 3.7. It does not require a PWM inverter with PWM, a speed sensor, and reference frame transformations.

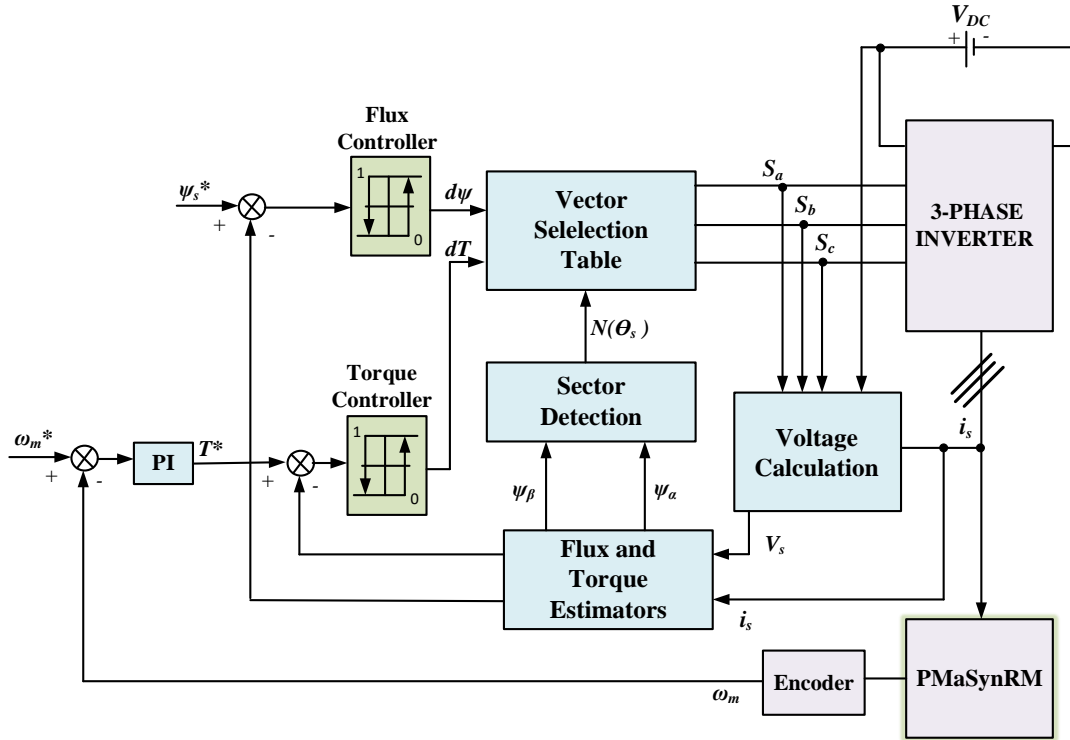


Figure 3.7: DTC for PMSynRM

All the calculations are performed in the stator reference frame and the exact rotor position of the rotor is not required (except in the start-up case of the synchronous motor). The requirements for the computational capabilities of the controllers are relatively low. DTC has high dynamic characteristics with quick response to load changes and is less sensitive to motor parameters variations, and disturbances. However, the steady-state operation is characterized with high ripples in the stator current, flux linkage, and torque, especially at low speeds, which greatly limit its application to high-precision drives [193].

The most common DTC is combined with Space Vector Modulation (SVM) that uses pulse width modulation to generate the voltage. There are several variations that significantly improve the efficiency of the control, compared to the original DTC. They provide reduction in the ripples, the control is carried out more smoothly, and start-up and running of the motor at low speeds is more stable. Meanwhile, with its high dynamics, this technique is still capable of ensuring FOC control accuracy [194].

### 3.4 Hybrid model of the PMSynRM motor drive

For our study, we develop a hybrid model based on the combination of an analytical model in the three-phase reference frame and a finite element model. The analytical model is based on the concept of inductances. Thus, to develop the model for fault analysis, we will calculate the inductances in healthy and faulty modes by Finite Element Analysis, and store them in N-dimensional lookup tables (LUT) that will be used in the analytical model. The flowchart of the modelling approach is displayed in Figure 3.8.

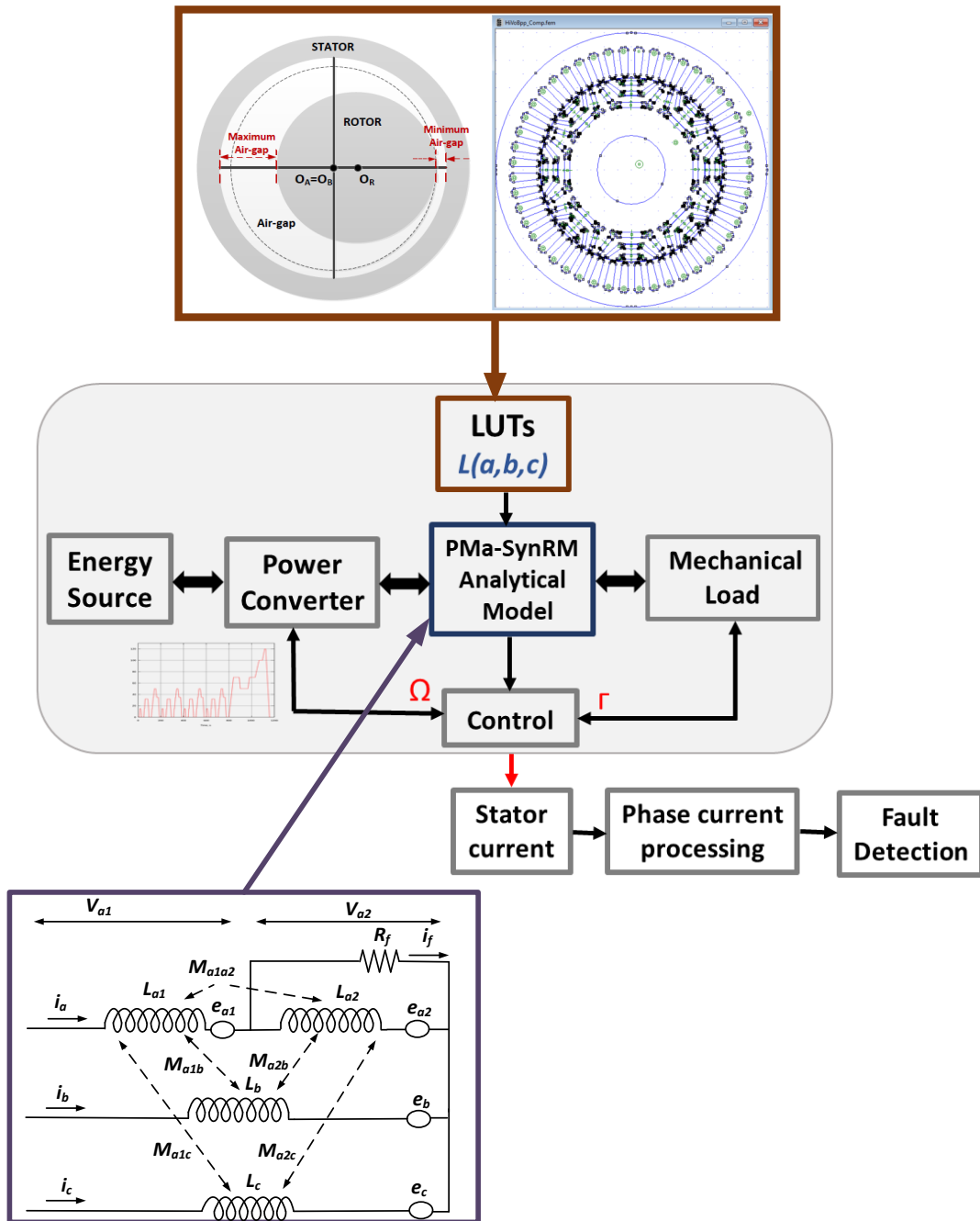


Figure 3.8: Schematic representation of the drive modelling



### 3.4.1 Analytical-finite element model of the PMSynRM

#### 3.4.1.1 Self and mutual inductances computation

The finite element model of the PMSynRM is designed with FEMM software [195]. The electromagnetic torque, flux, and flux density can be calculated for each excitation current  $I$  and rotor position  $\theta_m$ . When the coil is energized with a current source  $I$ , the flux can be computed from the magnetic vector potential  $\mathbf{A}$  in the coil region as follows:

$$\psi = \frac{1}{I} \int_{\Omega_W} \mathbf{A} \cdot \mathbf{J} d\Omega \quad (3.45)$$

Where  $\mathbf{J}$  is the given current density in the winding region and  $\Omega_W$  is the volume of the winding [196]. To determine a mutual inductance of a winding, it is interesting to compute the flux linkage of coils with zero current, in this case, the above equation is not applicable since  $I = 0$ . On the other hand, considering that the coil whose flux linkage is to be computed surrounds another coil with non-zero current, a simply connected domain  $\Omega'_W$  that incorporates the winding region  $\Omega_w$  is defined. This does not include any portion of any other coil (Figure 3.9). The flux linkage can be expressed with the help of the turn density function  $\mathbf{t} = \mathbf{J}/I$ . The equation 3.45 can now be written as:

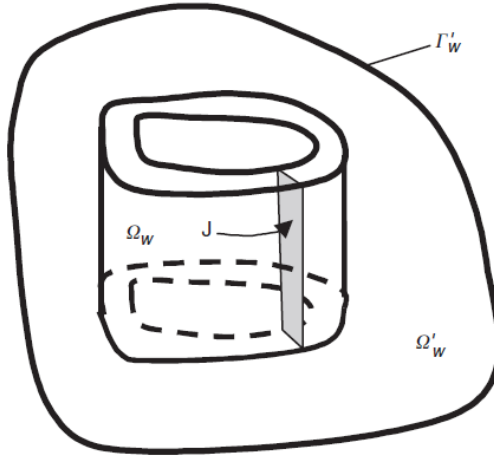


Figure 3.9: Selection of the connected domain  $\Omega'_W$  [196]

$$\psi = \int_{\Omega_W} \mathbf{A} \cdot \mathbf{t} d\Omega \quad (3.46)$$

The turn density can be expressed as:

$$\mathbf{t} = \text{curl } \mathbf{T}_u \quad (3.47)$$

Where  $\mathbf{T}_u$  is the current vector potential due to unit current. It has been proved in [196] that the knowledge of the magnetic flux density from the finite element solution is sufficient to compute the flux linkage of any coil, provided the vector potential corresponding to its turn density function is available. Because of no excitation current in  $\Omega'_W$  the turn density is zero everywhere outside  $\Omega_W$ . By extension, the flux in  $\Omega'_W$  can be estimated as:

$$\psi = \int_{\Omega'_W} \mathbf{T}_u \cdot \mathbf{B} d\Omega + \oint_{\Gamma'_W} \psi_u \mathbf{B} \cdot \mathbf{n} d\Gamma \quad (3.48)$$

Let  $\psi_u$  be a normalised total magnetic scalar potential on  $\Gamma'_W$ , so that  $\mathbf{T}_u$  is its negative gradient as follows:

$$\mathbf{T}_u = -\text{grad}\psi_u \text{ on } \Gamma'_W \quad (3.49)$$

In the PMSynRM, the relationship between currents and fluxes is non-linear, and the rotor angular position must be considered to include the effects of cross-magnetization. Therefore, flux linkages  $\psi$  are multivariate functions, as shown in the following equation where  $i_a, i_b, i_c$  and  $\theta_e$  are the 3-phase currents and the rotor angular position (electrical) [197], respectively.

$$\psi = f(i_a, i_b, i_c, \theta_e) \quad (3.50)$$

The computation of the self and mutual inductances  $L_{ii}$  and  $M_{ij}$  is as follows [198]:

$$L_{ii} = \frac{\psi_{ii}}{i_i}, \forall i \in [a, b, c], M_{ij} = \frac{\psi_{ij}}{i_j} \forall i \neq j \quad (3.51)$$

Where  $\psi_{ii}$  is the induced magnetic flux linkage in phase  $i$  windings produced by the current flowing in phase  $i$ . It is computed using equation 3.45.  $\psi_{ij}$  is the induced magnetic flux linkage in phase  $i$  windings produced by the current flowing in phase  $j$ . It is computed using equation 3.48. These calculated flux linkages give access to the self and mutual inductances. However, in the PMSynRM, there is a coupling between the fields from the armature current and permanent magnets. Because the inductances are linked to the contribution of the flux from the armature current, the frozen permeabilities technique is used to accurately separate the contributions [199], which is most critical when the motor runs under saturated conditions. To turn off the magnets, their magnetic coercivity  $H_c$  of the magnets is set to zero.

### 3.4.1.2 End-winding inductance computation

The self inductances of the motor windings are composed of several components due to (co)energy stored in the back iron, the air gap, the slots, and the end turns. The 2-D model of the motor considers only the effects in the back iron, the airgap, and the slots, but fails to including the windings end turns effect. The 3-D motor model that can handle this issue is out of the scope of this PhD thesis. The end winding inductances are generally neglected even if they can be a significant component of the inductances for motors with a low length/diameter ratio. To improve the accuracy of the inductances computed with the 2-D finite element model, the analytical expression of the end winding leakage inductances is included. Its expression is as follows [200]:

$$L_w = \frac{4m}{Q} q N_s^2 \mu_0 l_w \lambda_w \quad (3.52)$$

Where the average length of the end winding  $l_w$  and the product  $l_w \lambda_w$  are defined as:

$$\begin{aligned} l_w &= 2l_{ew} + W_{ew} \\ l_w \lambda_w &= 2l_{ew} \lambda_{ew} + W_{ew} \lambda_W \end{aligned} \quad (3.53)$$

And  $m$  is the number of motor winding phases,  $N_s$  the number of turns of the winding coils,  $Q$  the number of slots and  $q$  the number of slots per pole per phase and  $\mu_0$  the vacuum permeability. Finally,  $l_{ew}$  is the average conductor length of winding overhang,  $W_{ew}$  the coil span and  $\lambda_{l_{ew}}$  and  $\lambda_W$  the corresponding permeance factors. The permeance factor table is provided in the appendix (Figure A.1). The end-winding inductance term is added to the self inductances computed from the FEM. To the discrete data  $L_{abc}(i_a, i_b, i_c, \theta_e)$  is stored in 4-D lookup tables and will be used in the analytical model shown in Figure 3.8.

### 3.4.2 FOC for the hybrid model of the PMSynRM

For EV applications, an efficient control algorithm is needed. It can be realized by employing a mixed feedforward and feedback algorithm to operate the electric motor at its maximum capacity and efficiency. For the control of our hybrid analytical-FEM of the PMSynRM, we adopt the typical FOC with three PI controllers: two designed for currents  $i_d$  and  $i_q$  control loops, and one for the speed control loop. In accordance with the parametric formulations delineated by equation 3.28 for the PMSynRM model, it is deduced that the system representation of the PMSynRM is inherently characterized as a Multiple-Input Multiple-Output configuration. This classification stems from the presence of cross-couplings between the  $d$  – axis and  $q$  – axis, manifesting as interactions denoted by variables  $-\omega_e L_q i_q$  and  $\omega_e (L_d i_d + \phi_{PM})$ . Consequently, a feed-forward control is required to mitigate these coupled effects and facilitate independent control of the  $d$  and  $q$  current components. This feed-forward requires the assessment of the motor inductances in the  $d$  –  $q$  reference frame. The term  $\omega_e \phi_{PM}$  can be compensated by a feed-forward control as well [201]. The inductances  $L_d$  and  $L_q$  can be computed from the self and mutual inductance obtained in 3.51 as follows:

$$\mathbf{L}_{dq} = \mathbf{C}^T \mathbf{L}_{abc} \mathbf{C} \quad (3.54)$$

where

$$\mathbf{C} = \sqrt{\frac{2}{3}} \begin{bmatrix} \cos(\theta_e) & \sin(\theta_e) \\ \cos(\theta_e - 2\pi/3) & \sin(\theta_e - 2\pi/3) \\ \cos(\theta_e + 2\pi/3) & \sin(\theta_e + 2\pi/3) \end{bmatrix} \quad (3.55)$$

The diagram of the proposed FOC of the PMSynRM is shown in Figure 3.10. Similar to the motor modeling phase, the inductances  $L_d$  and  $L_q$  needed for the FOC are stored in the LUTs with respect to the level of stator winding currents ( $i_a, i_b, i_c$ ) and the rotor electrical position ( $\theta_e$ ).

#### 3.4.2.1 Design of the PI Controllers

- **PI design for current Controllers**

From the  $dq$  model of the PMSynRM with the cross-couplings with feed-forward control the  $d$ -axis and  $q$ -axis equations can be written as:

$$\begin{aligned} V_d &= V_d^* - \omega_e L_q i_q \\ V_q &= V_q^* + \omega_e L_d i_d + \omega_e \phi_{PM} \end{aligned} \quad (3.56)$$

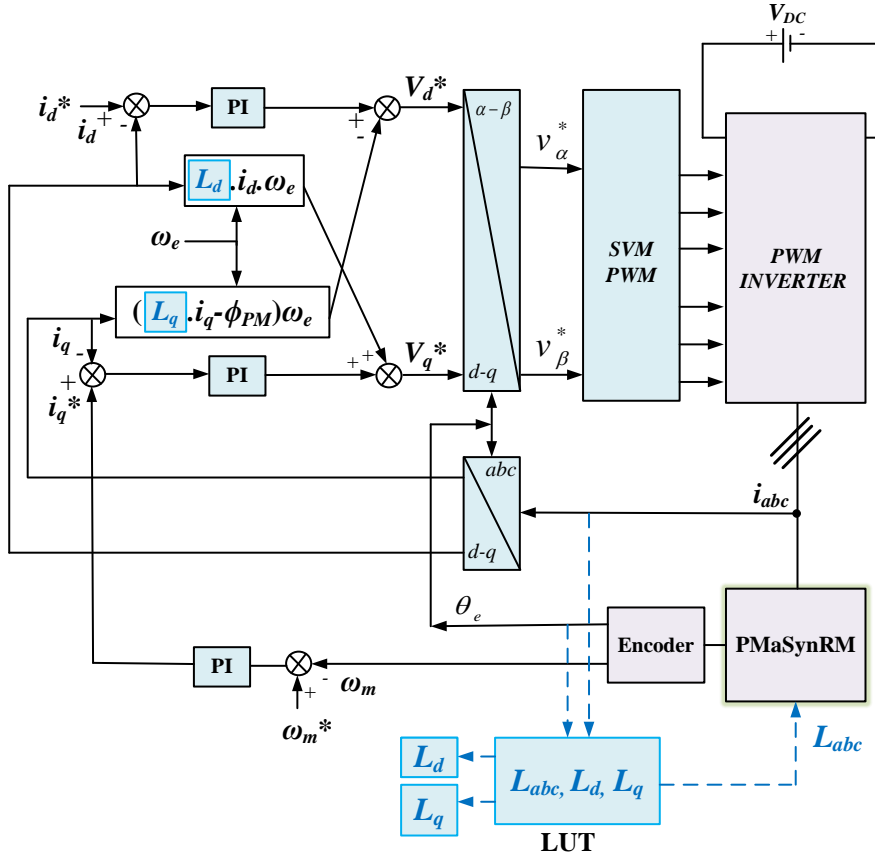


Figure 3.10: FOC for the hybrid model of the PMSynRM

Where  $V_d^*$  and  $V_q^*$  are the output PI controller of d-axis and q-axis respectively. By neglecting the resistance of the model  $R_s$ , the PMSynRM model equations can be written as follows:

$$\begin{aligned} L_d \frac{d}{dt} i_d &= V_d^* \\ L_q \frac{d}{dt} i_q &= V_q^* \end{aligned} \quad (3.57)$$

Hence, the "s-domain" transfer function of the d-axis and q-axis are as follows:

$$\begin{aligned} \frac{i_d}{V_d^*} &= \frac{1}{sL_d} \\ \frac{i_q}{V_q^*} &= \frac{1}{sL_q} \end{aligned} \quad (3.58)$$

The PI-current controllers can be written as:

$$\begin{aligned} G_{id}(s) &= kp_{id} \frac{1+ki_{id}s}{ki_{id}s} \\ G_{iq}(s) &= kp_{iq} \frac{1+ki_{iq}s}{ki_{iq}s} \end{aligned} \quad (3.59)$$

$(kp_{id}$  and  $ki_{id})$  and  $(kp_{iq}$  and  $ki_{iq})$  are the d-axis and q-axis currents PI controllers proportional and integral gains respectively. The frequency response method is chosen to tune the PI controllers with desired phase margin of  $\phi_m = 60^\circ$  and a crossover frequency

$\omega_{ic} = \frac{2\pi f_s}{10}$ , where  $f_s$  is the switching frequency of the inverter. For motor control loop, the DC bus voltage and inverter model need to be considered. For simplicity, the DC bus voltage assumed to be constant and the inverter modelled as a gain are include in the proportional gain  $Kp_i$  term. The open-loop transfer function is defined as the product of the simplified motor transfer function(  $RL$  equivalent circuit) and the PI controller transfer function as follows [202].

$$\begin{aligned} G_{oid}(s) &= \frac{kp_{id} (1+sk_{i_{id}})}{L_d k_{i_{id}} \frac{s^2}{s^2}} \\ G_{oiq}(s) &= \frac{kp_{iq} (1+sk_{i_{iq}})}{L_d k_{i_{iq}} \frac{s^2}{s^2}} \end{aligned} \quad (3.60)$$

The conditions of the frequency response method are for the d-axis and the q-axis are as follows:

$$\begin{cases} \arg(G_{oid}(j\omega_{ic})) = -180 + \phi_m \\ |G_{oid}(j\omega_{ic})| = 1 \end{cases} \quad (3.61)$$

$$\begin{cases} \arg(G_{oiq}(j\omega_{ic})) = -180 + \phi_m \\ |G_{oiq}(j\omega_{ic})| = 1 \end{cases} \quad (3.62)$$

From the the first conditions of the the d-axis and q-axis conditions,  $k_{i_{id}}$  and  $k_{i_{iq}}$  are found as:

$$k_{i_{id}} = k_{i_{iq}} = \frac{\tan 60^\circ}{\omega_{ic}} \quad (3.63)$$

$kp_{id}$  and  $kp_{iq}$  are found from the second conditions.

$$kp_{id} = \frac{L_d k_{i_{id}} \omega_{ic}^2}{\sqrt{1 + (k_{i_{id}} \omega_{ic})^2}} \quad (3.64)$$

$$kp_{iq} = \frac{L_q k_{i_{iq}} \omega_{ic}^2}{\sqrt{1 + (k_{i_{iq}} \omega_{ic})^2}} \quad (3.65)$$

Assuming that the gain of the feedback channel is 1, the closed-loop transfer function is expressed as of the currents loops are as follows:

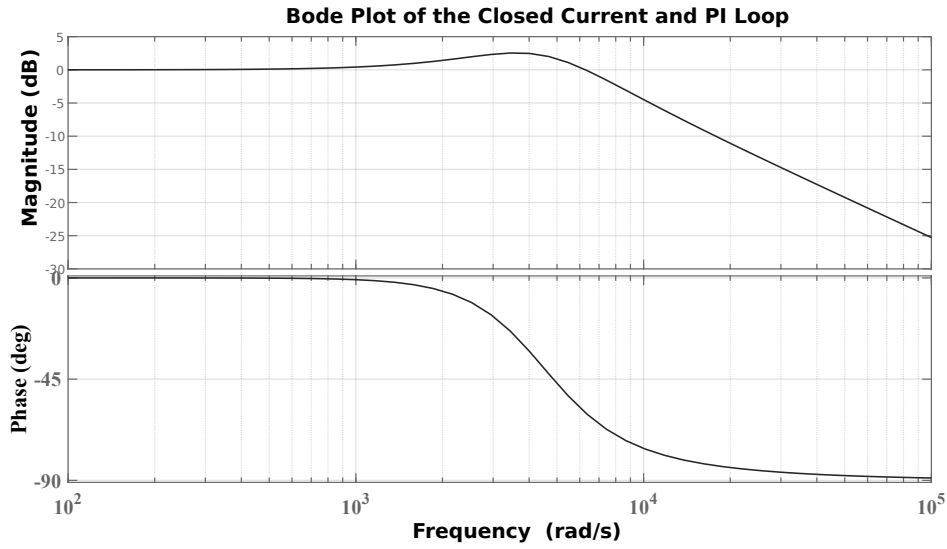
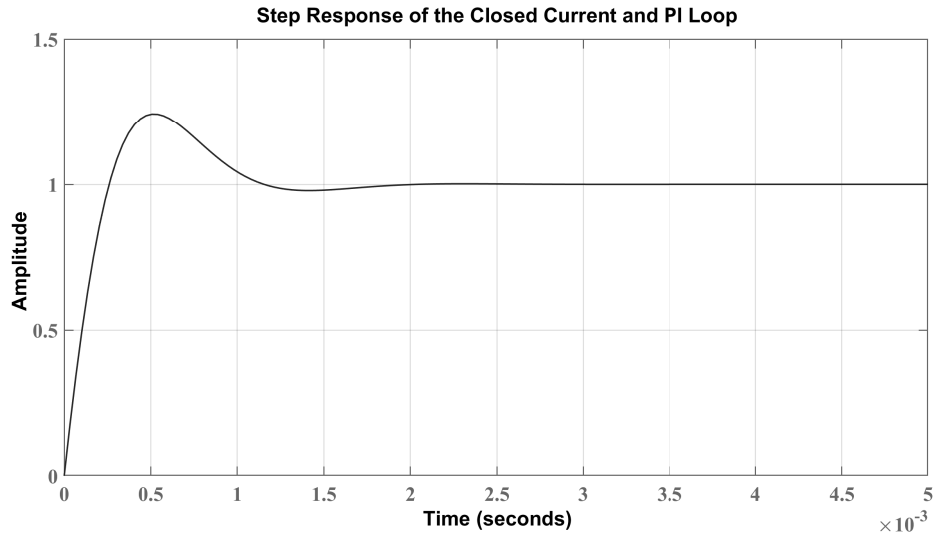
$$G_{cid}(s) = \frac{G_{oid}(s)}{1 + G_{oid}(s)} = \frac{1 + sk_{i_{id}}}{1 + sk_{i_{id}} + s^2 \frac{k_{i_{id}} L_d}{kp_{id}}} \quad (3.66)$$

$$G_{ciq}(s) = \frac{G_{oiq}(s)}{1 + G_{oiq}(s)} = \frac{1 + sk_{i_{iq}}}{1 + sk_{i_{iq}} + s^2 \frac{k_{i_{iq}} L_d}{kp_{iq}}} \quad (3.67)$$

Figures 3.11 and 3.12 show the Bode plot of the current  $i_q$  control closed-loop transfer function and its step response, respectively at  $I_{peak} = 50A$ .

- **PI design for speed controller**

The reference  $i_d^*$  current is set equal to zero to maximize the torque that is controlled through the torque current  $i_q$ . The speed loop includes an inner current loop as shown in the block diagram of the speed controller in Figure 3.13.


 Figure 3.11: Bode plot of the current  $i_q$  closed-loop for  $I_{peak} = 50A$ 

 Figure 3.12: Step response of  $i_q$  closed-loop at  $I_{peak} = 50A$ 

We define  $kp_\omega$  and  $ki_\omega$  as the speed PI controller proportional and integral gains respectively. We are considering an ideal situation where the inertia of the system is concentrated and unitary, assuming a rigid connection between the motor and the load and no viscous resistance. For simplicity purposes, the q-axis current loop transfer function can be assumed to be a first-order system. Its new transfer function can be written as follows:

$$G_{ciq} = \frac{1}{1 + \frac{s}{\omega_g}} \quad (3.68)$$

$\omega_g$  is the simplified system's crossover frequency, and a new gain margin is defined as  $\omega_1 = 10 \times (2\pi f_s)$ . The gain margin might be  $|G_{ciq}(j\omega_1)|$

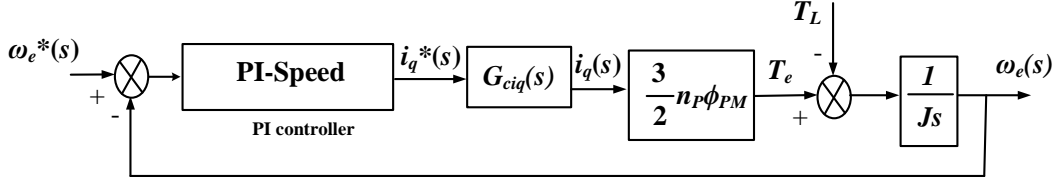


Figure 3.13: The speed control loop

$$|G_{ciq}(j\omega_1)| = \left| \frac{1 + j\omega_1 k i_{iq}}{1 + j\omega_1 k i_{iq} + (j\omega_1)^2 \frac{k i_{iq} L_q}{k p_{iq}}} \right| \quad (3.69)$$

The crossover frequency of the new closed-loop transfer function can be found as follows:

$$20 \log_{10}(G_{ciq}(\omega_1)) = |G_{ciq}(j\omega_1)| \quad (3.70)$$

The transfer function of the open speed loop can be expressed as:

$$G_{o\omega} = k p_{\omega} \frac{1 + k i_{\omega} s}{k i_{\omega} s} G_{ciq}(s) \frac{3 n_P}{2} \phi_{PM} \frac{1}{s J} \quad (3.71)$$

The Symmetric Optimum Method has employed for the computation of the speed PI parameters, aiming to achieve maximum phase margin  $\phi_m$  while maintaining balanced phase and magnitude characteristics. In this method, both the PI current loops, acting as a low-pass filter, and the PI speed controller reduce the magnitude by  $20dB$  after the crossover frequency. Consequently, the overall magnitude is decreased by  $40dB$  beyond the crossover frequency, denoted as  $\omega_g$ . As a result, the crossover frequency of the speed loop, denoted as  $\omega_{sc}$ , is positioned equidistantly between  $\omega_g$  and  $\omega_{si} = \frac{1}{T_{si}} = 1/T_{si}$ , which represents the crossover frequency of the PI-speed controller. Consequently, the variable  $\beta$  can be utilized to establish the relationship between these frequencies, as detailed below:

$$\omega_{sc} = \frac{1}{\beta} \omega_g \quad (3.72)$$

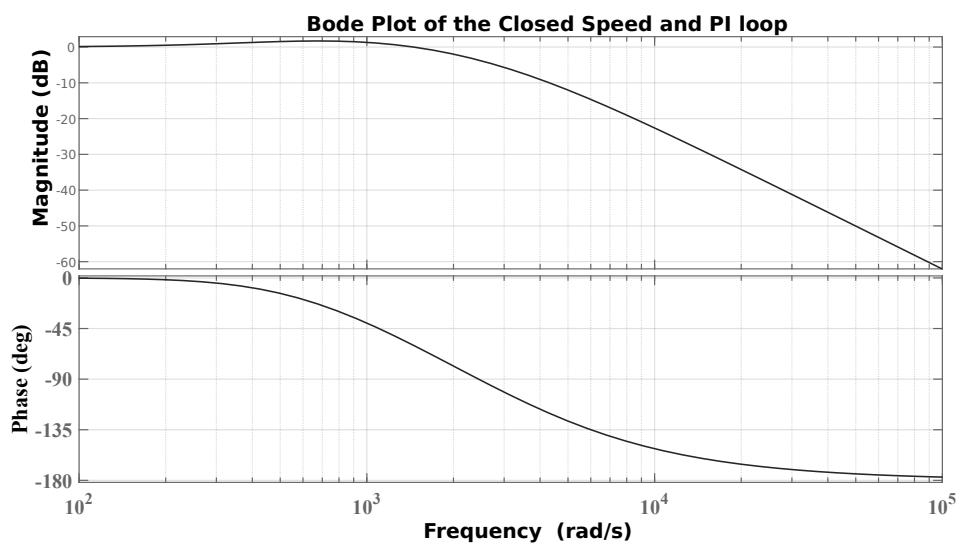
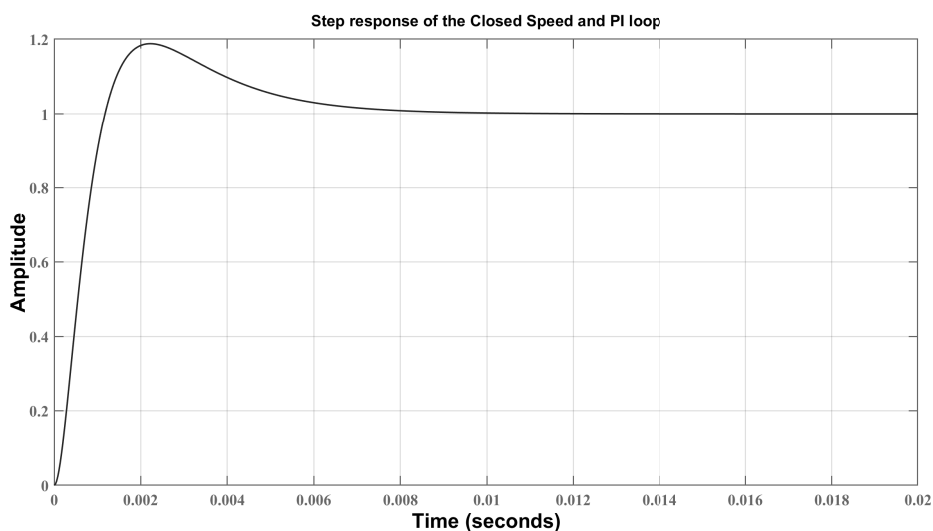
and

$$\omega_{si} = \frac{1}{\beta^2} \omega_g \quad (3.73)$$

The PI parameters can then be found by applying the following phase and magnitude conditions to the open-loop transfer function:

$$\begin{aligned} \arg(G_{o\omega}(j\omega_{sc})) &= \arg\left(G_{o\omega}\left(\frac{j\omega_g}{\beta}\right)\right) = -180 + \phi_m \\ |G_{o\omega}(j\omega_{sc})| &= \left|G_{o\omega}\left(\frac{j\omega_g}{\beta}\right)\right| = 1 \end{aligned} \quad (3.74)$$

The solutions of the A.2 to find the speed PI parameters are detailed in Appendix A.2. Figures 3.14 and 3.15 show the Bode plot of the speed control closed-loop transfer function and its step response, respectively at  $I_{peak} = 50A$ .

Figure 3.14: Bode plot of the speed closed-loop for  $I_{peak} = 50A$ Figure 3.15: Step response of the speed closed-loop at  $I_{peak} = 50A$ 

### 3.4.3 Simulation results of the Hybrid model of the PMSynRM

The FEM of the PMSynRM is first simulated using FEMM for inductances extraction. The data, stored in LUTs are used for the inductance-based analytical model of the electrical motor that is fed by an inverter. The torque and speed are controlled with a Field Oriented Control strategy. The drive is simulated with Matlab/Simulink.

#### 3.4.3.1 Simulation results of the finite element model of the motor

Figure 3.16 shows the cross-section of the PMSynRM under study. The electrical motor is designed with 48 slots/8 poles, and 3 layers rotor containing 5 NdFeB magnets per pole (Table 3.3).



**Table 3.3:** PMSynRM characteristics

Parameter	Value	Unit
Number of poles	8	
Number of PMs per pole	5	
Magnet type	N38UH	
Magnets thicknesses	3.6/3.2/3.2	mm
Magnets widths	16/10.5/10.5	mm
Magnetization	Radial	mm
Active length	175	mm
Stator outer diameter	200	mm
Stator inner diameter	135	mm
Rotor outer diameter	133	mm
Rotor inner diameter	50	mm
Air gap	0.6	mm
Rated power	208	kW
Rated torque	336	Nm
Rated speed	14000	rpm
Number of turns	8	
Winding connection	Star/ Wye	
Stator phase winding resistance value at 20°	6.1	mΩ

In our case study, a parametric computation is conducted by varying the mechanical position of the rotor and the current requirement (three excitation currents ( $I_{peak}$ ) of 50A, 300A, and 700A). Figure 3.17 shows the electromagnetic torque vs speed for the three different current requirements. It shows the current requirements at a specific speed to produce torque. Figure 3.18 shows the power versus the speed for the three different current requirements, respectively.

The combination of these graphs, at any given speed and torque, made it possible to extract the values of the current, which will be subsequently used as inputs for the field-oriented control. This helps to eliminate the difficulties associated with estimating the current input. Figures 3.19, 3.20 and 3.21 show the self and mutual inductances obtained from the FEM in the healthy mode for the three excitation currents, respectively. Both the self and mutual inductances change with the excitation current. Under low excitation current (50A), magnetic saturation is not severe. For higher excitation currents (300A, 700A) the magnetic saturation is more severe, and the accuracy of the inductance models deteriorates. However, the inductances models in this thesis do not focus on the effects of magnetic saturation.

### 3.4.3.2 The motor drive simulation in Simulink

The simulation of the PMSynRM drive with Matlab/Simulink is based on the diagram displayed in Figure 3.8. The motor is simulated in the 3-phase reference frame. A Space Vector Modulation Field Oriented Controller is used to control the motor speed and torque. The simulation parameters of the PMSynRM are tabulated in Table 3.4.

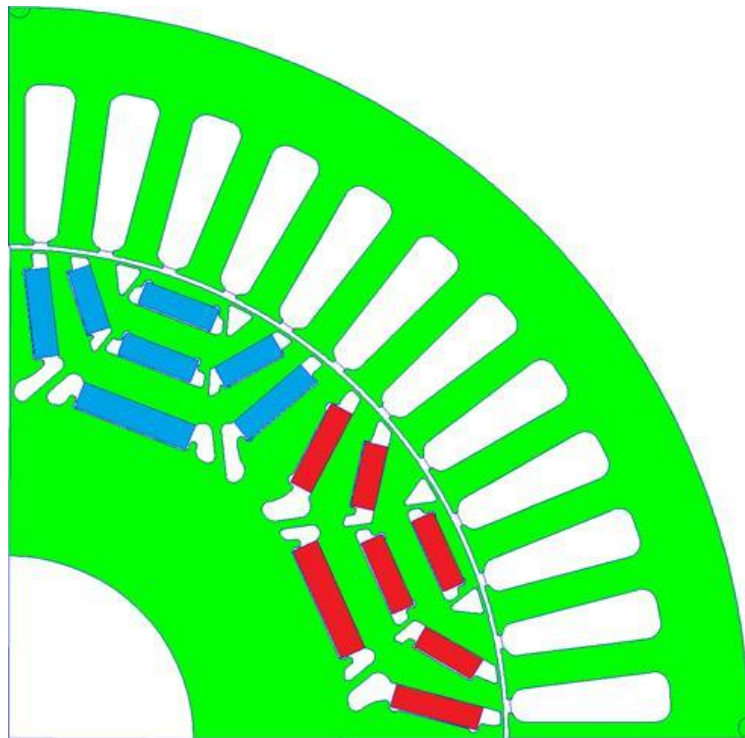


Figure 3.16: Design of the PMSynRM

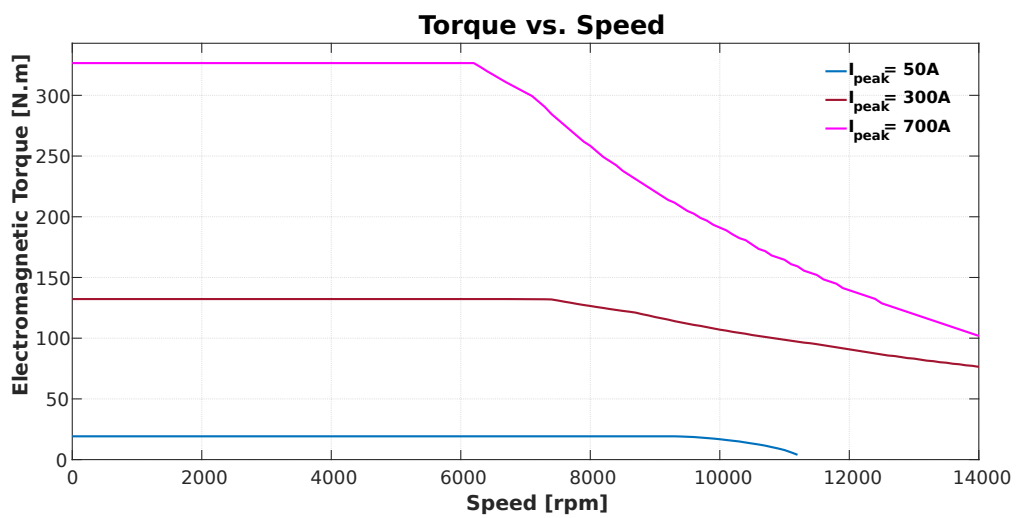


Figure 3.17: Torque-Speed curves of the PMSynRM drive

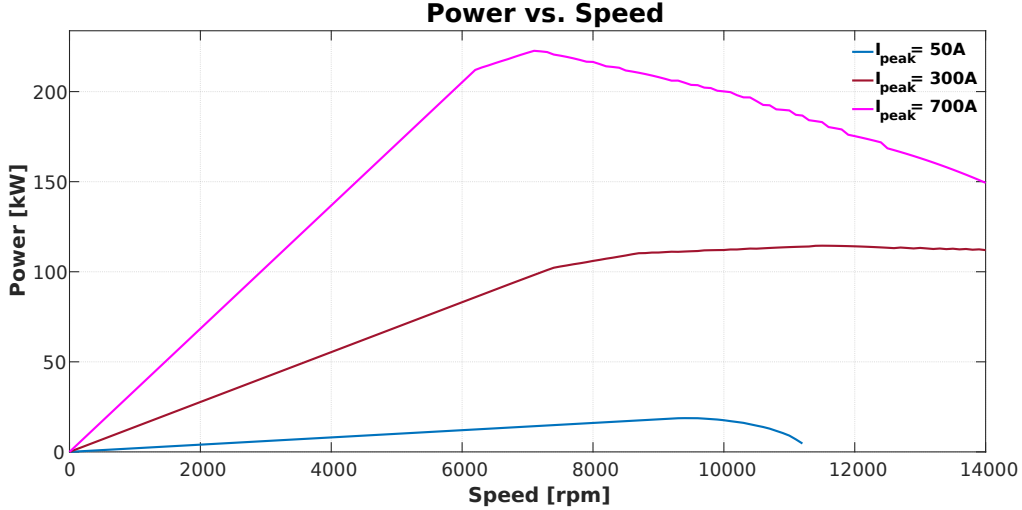


Figure 3.18: Power-Speed curves of the PMSynRM drive

**Table 3.4:** Simulation parameters

Parameter	Value	Unit
Permanent Magnet flux amplitude	$6.24 \times 10^{-2}$	<i>Wb</i>
Moment of inertia	0.0357	<i>kg.m<sup>2</sup></i>
Friction constant	0.1	<i>Nm/rad/s</i>
Input DC voltage amplitude	412	<i>V</i>
Load torque	[18, 134, 260]	<i>Nm</i>
Speed reference	1500	<i>rpm</i>

The simulation scenarios in this thesis cover the following situations:

- Generation of pulses for inverter,
- a step change in the commanded speed to 1500rpm,
- step changes in load torque to 18Nm at 0.1s; 134Nm at 3s and 260Nm at 6s,
- observation of transient and steady state behavior of the speed, torque and stator currents.

With the help of the field-orientation control method, high dynamics are achieved and the speed reaches its reference 0.3sec as shown in Figure 3.22. It also shows the actual torque. Sudden changes in the load torque as described previously cause changes in the speed, torque, and in the three-phase current. With the variation of the load, transient phenomena occur and after few seconds, the steady state condition is reached. It is observed that the sudden application of load torque causes a dip in the speed and an overshoot in the torque. The waveform of the stator phase *a* current is displayed in Figure 3.23. The simulation results showed that the controller effectively handled all the requests for torque delivery under each operating condition.

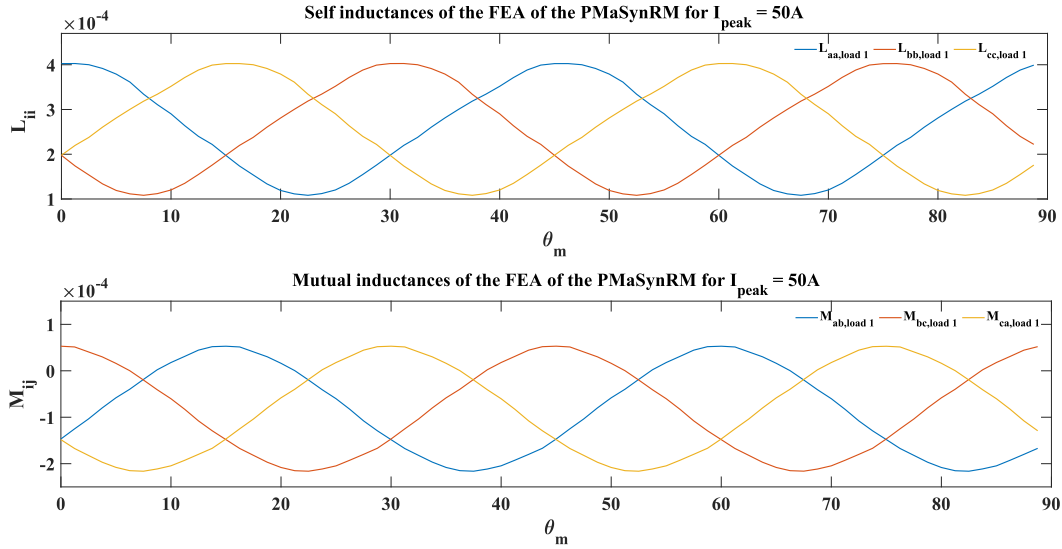


Figure 3.19: FEA Self and Mutual inductances of PMSynRM for  $I_{peak} = 50A$

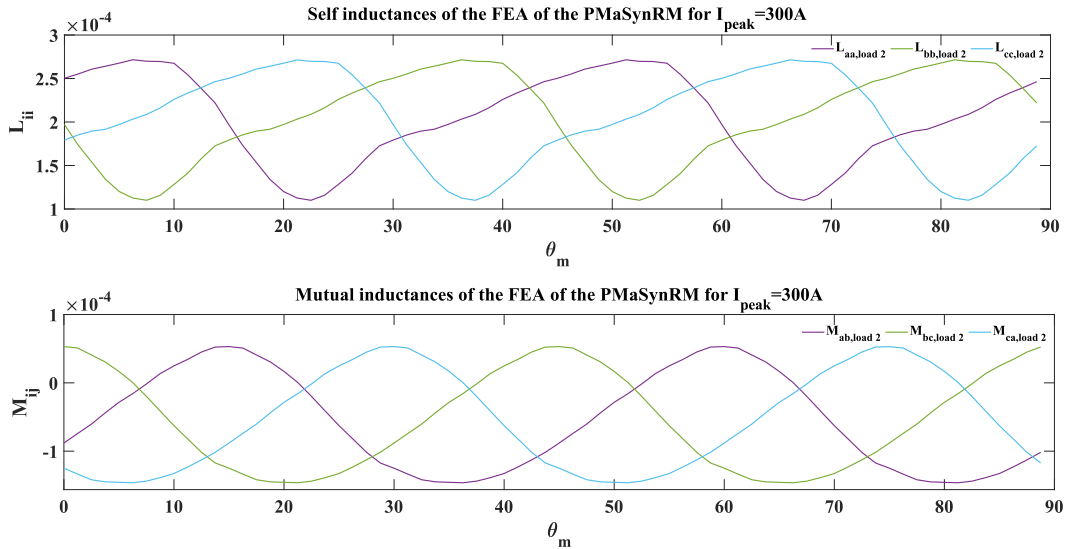


Figure 3.20: FEA Self and Mutual inductances of PMSynRM for  $I_{peak} = 300A$

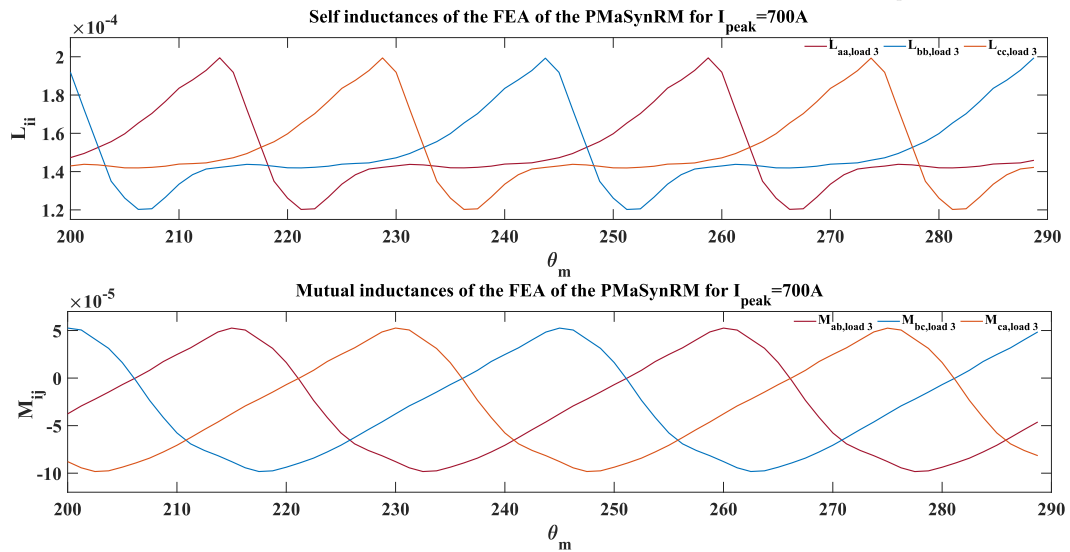


Figure 3.21: FEA Self and Mutual inductances of PMSynRM for  $I_{peak} = 700A$

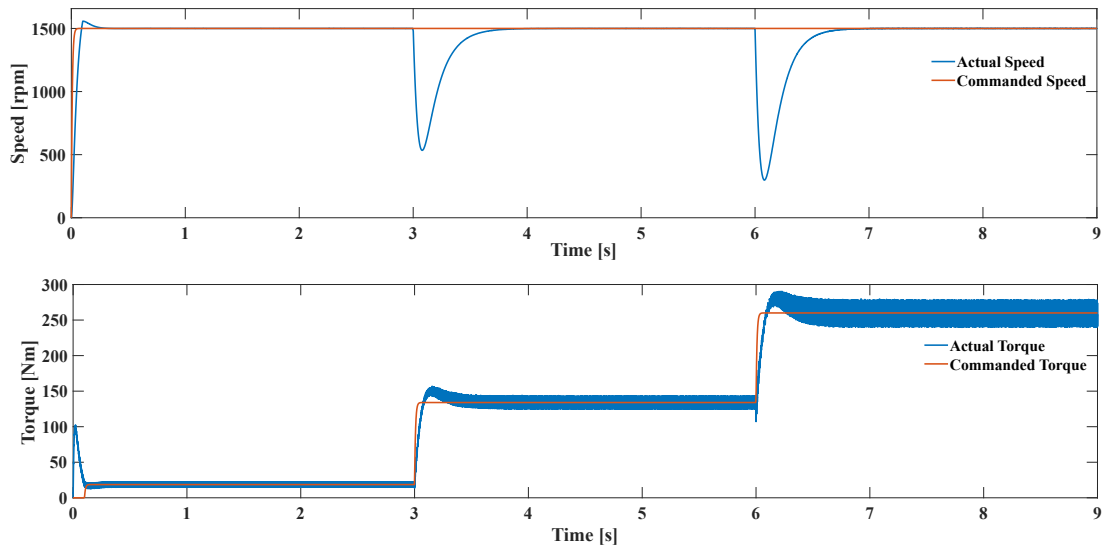


Figure 3.22: Speed and Torque response of the SVM using FOC

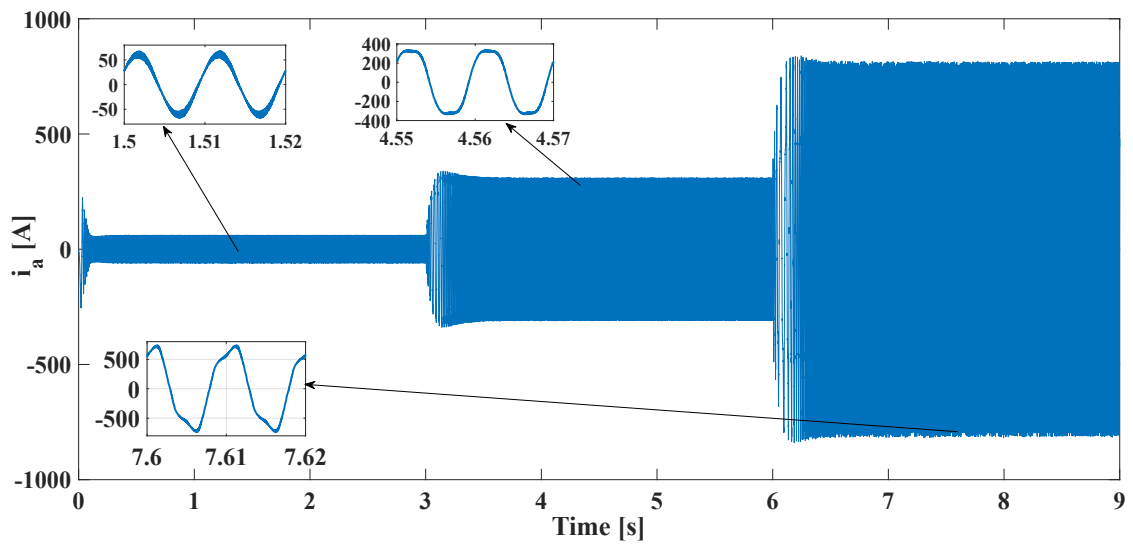


Figure 3.23: Stator phase  $a$  current for the three load cases

### 3.4.3.3 Experimental validation of the Hybrid model of the PMASynRM

The Motor Testbench features a PMSM coupled to PMASynRM. It provides a platform to validate models of electric motors, and innovative inverters' topologies with control techniques for high-performance variable speed drives. In our study, the PMASynRM is the device under test while the PMSM acts as a controllable load. Each of the electrical machines is run with its own inverter. The testbench features position, speed, and torque measurements as well as temperature monitoring of the machines. The testbench is displayed in Figure 3.24.

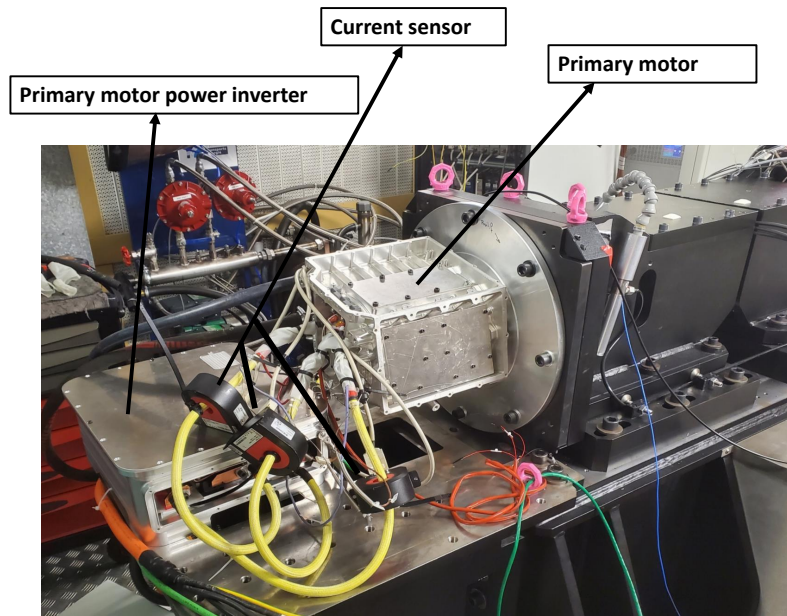


Figure 3.24: Snapshot of the experimental PMASynRM drive

Several experiments are conducted under the same conditions for the simulations. To illustrate the comparison between the model and the actual drive, the currents in phase  $a$  are plotted for the three different load cases in Figures 3.25, 3.26, 3.27, respectively. Likewise in the model of the self and mutual inductances, the accuracy of the stator winding current of the Hybrid model of the PMASynRM deteriorates with the rise of the excitation. The estimation of the accuracy of the hybrid model of the PMASynRM has been evaluated through the Root-Mean Square Error ( $RMSE$ ) and Correlation Coefficient ( $CC$ ). The results are:  $RMSE = 0.0065$ ,  $CC = 0.96$  for load 1,  $RMSE = 0.11$ ,  $CC = 0.73$  for load 2, and  $RMSE = 0.24$ ,  $CC = 0.70$  for load 3. These differences are mainly attributed to the accuracy of the inductances computation and the interpolation in the lookup tables used in the analytic model. The switching frequency is also higher in the experimental drive than in the simulations. Therefore, we have higher ripples in the simulated currents. However, the accuracy of the hybrid model is acceptable. Therefore, it can be used as a virtual testbench to emulate the faults and generate synthetic data that can be used to evaluate the fault detection methodology. The stator phase currents, already available for control purposes, will be used as input features for fault detection. This will contribute to simplify and reduce the monitoring cost.

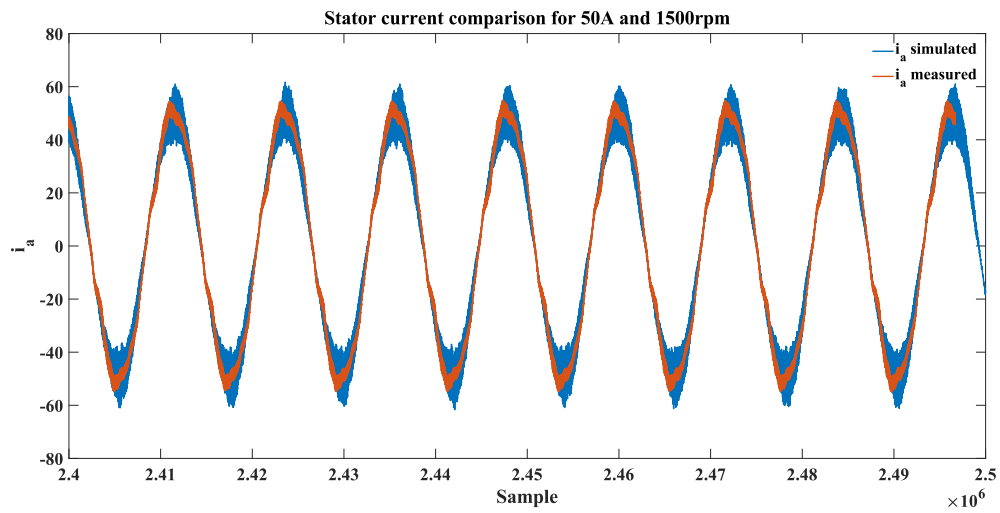


Figure 3.25: PMSynRM's simulation and experimental phase  $a$  currents comparison for load 1

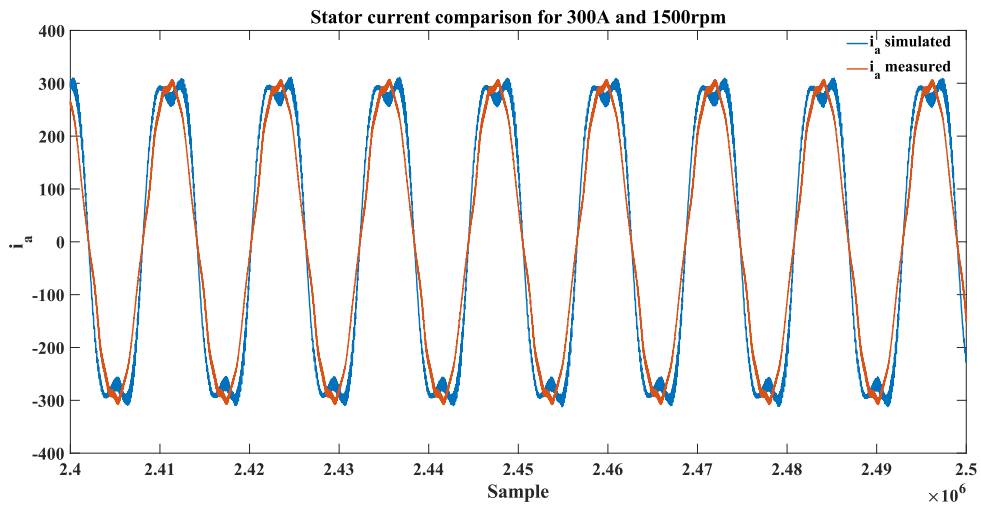


Figure 3.26: PMSynRM's simulation and experimental phase  $a$  currents comparison for load 2

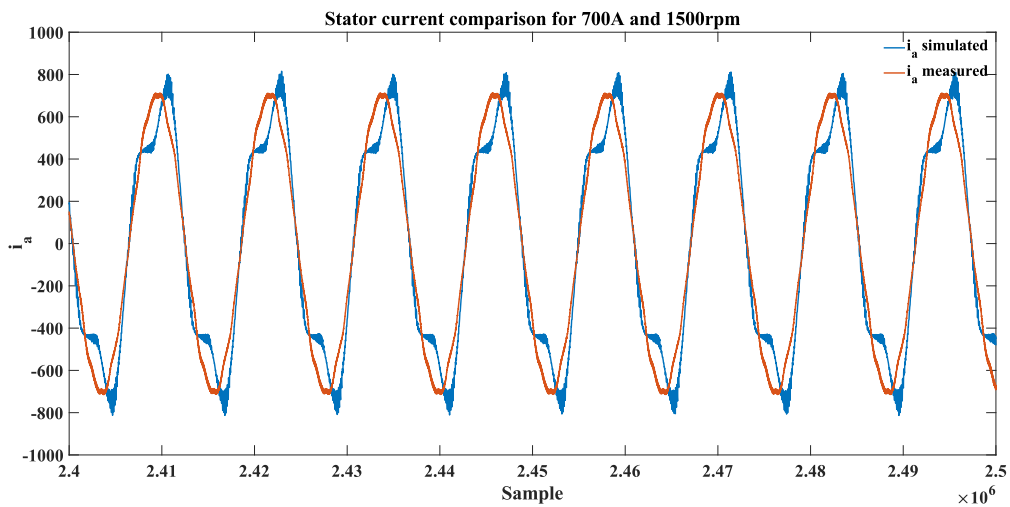


Figure 3.27: PMSynRM's simulation and experimental phase  $a$  currents comparison for load 3

## 3.5 Simulation of the Hybrid model of the PmaSynRM with Inter-turn Short-circuit fault

### 3.5.1 Stator winding inter-turn short-circuit fault modelling

We consider a motor with only one turn in a slot per phase and the fault is represented by a fault resistance  $R_f$  [203]. Considering that the winding in each phase is made of elementary coils per pole pair, the four pole pairs machine winding circuit is shown in Figure 3.28 where  $L_{bob}$  and  $M_{bob}$  denote the elementary coils self and mutual inductances of two consecutive elementary coils, respectively. The inductances can be represented by a  $12 \times 12$  matrix of  $L_{bob}$  and  $M_{bob}$  that can be determined from finite element analysis or experimental measures.

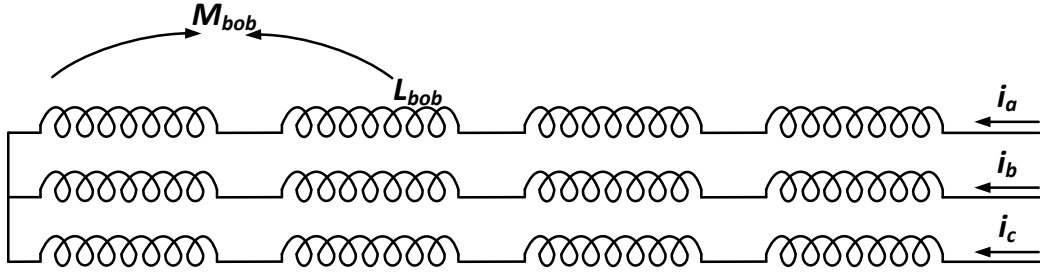


Figure 3.28: Elementary coils circuit in the 3-phase motor

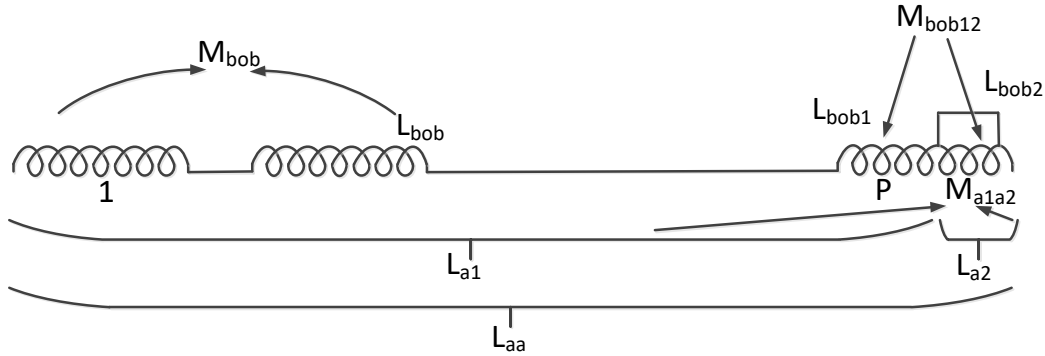


Figure 3.29: Interturn short-circuit fault in an elementary coil of one phase

The faulty phase under short-circuit is considered as two coils of inductances  $L_{bob1}$  and  $L_{bob2}$  perfectly coupled with a mutual inductance  $M_{bob12}$ . Under the assumption of  $N_{cc}$  short-circuited turns out of the total number of turns  $N_{tot}$  of the elementary coil, the faulty circuit is displayed in Figure 3.29, and the parameters can be calculated as follows:

$$L_{bob1} = (1 - P\mu)^2 L_{bob} \quad (3.75)$$

$$L_{bob2} = P^2 \mu^2 L_{bob} \quad (3.76)$$



$$M_{bob12} = P\mu(1 - P\mu)L_{bob} \quad (3.77)$$

$$\mu = \frac{N_{cc}}{N_s} \quad (3.78)$$

Where  $\mu$  is defined as the fault coefficient, and  $N_s$  the total number of turns in a phase winding. The electrical circuit of the motor winding under inter-turn short-circuit is displayed in Figure 3.30 where  $L_{a1}$  and  $L_{a2}$  represent the healthy and defective parts of the phase  $a$  winding, respectively.

In a healthy electrical machine, the stator resistances, self and mutual inductances are considered as balanced. If the machine is wye-connected the following condition is also satisfied:

$$i_a + i_b + i_c = 0 \quad (3.79)$$

When an inter-turn short-circuit occurs in phase  $a$  as it can be observed in Figure 3.30, the current  $i_a$  is split into two components  $i_s$  and  $i_f$ .

$$i_a = i_s + i_f \quad (3.80)$$

Where  $i_f$  is the fault current. The equation of the faulty motor in the 3-phase reference frame is shown in equation 3.81 where  $R_f$  is the fault resistance.

$$\begin{bmatrix} v_a \\ v_b \\ v_c \\ 0 \end{bmatrix} = \begin{bmatrix} R_a & 0 & 0 & -R_{a2} \\ 0 & R_b & 0 & 0 \\ 0 & 0 & R_c & 0 \\ -R_{a2} & 0 & R_c & -R_{a2} + R_f \end{bmatrix} \cdot \begin{bmatrix} i_a \\ i_b \\ i_c \\ i_f \end{bmatrix} + \begin{bmatrix} e_a \\ e_b \\ e_c \\ -e_{a2} \end{bmatrix} + \begin{bmatrix} L_{aa} & M_{ab} & M_{ac} & -L_{a2} - M_{a1a2} \\ M_{ba} & L_{bb} & M_{bc} & M_{ba2} \\ M_{ca} & M_{cb} & L_{cc} & M_{ca2} \\ -L_{a2} & M_{a2b} & M_{a2c} & L_{a2} \end{bmatrix} \cdot \frac{d}{dt} \begin{bmatrix} i_a \\ i_b \\ i_c \\ i_f \end{bmatrix} \quad (3.81)$$

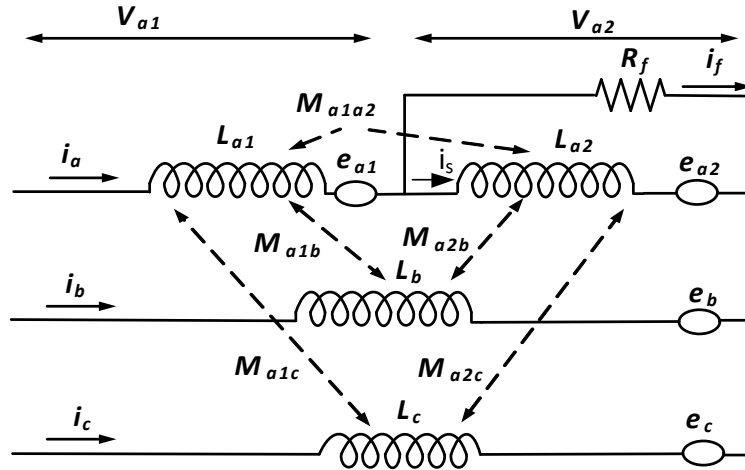
$$\begin{aligned} L_{aa} &= L_{bob2}, M_{a1a2} = P\mu(P - 1) + P\mu(P - 1)M_{bob} \\ M_{a2b} &= \mu M_{ab}, M_{a2c} = \mu M_{ac}, R_{a2} = \mu R_a, e_{a2} = \mu e_a \end{aligned}$$

Where  $R_{a2}$  and  $L_{a2}$  represent the resistance and inductance of the faulty sub-coil  $L_{a2}$ . The settings  $M_{a1a2}$ ,  $M_{a2b}$  and  $M_{a2c}$  denote the mutual inductances between the sub-coil  $L_{a2}$  and the coils  $L_b$ , and  $L_c$ , respectively. This analytical model of the faulty motor is valid for ideal values of the parameters  $L_{bob}$  and  $M_{bob}$  that satisfy the equation  $L_{aa} = L_{a1} + L_{a2} + M_{a1a2}$  or for the four pole pairs motor,  $L_{aa} = 4L_{bob} + 12M_{bob}$  [203].

Under healthy conditions,  $R_f$  is infinite [204]. If the insulation of the motor winding starts deteriorating, several turns start to be short-circuited leading to a decrease in the fault resistance  $R_f$ . The lower its value is, the higher the fault severity and the magnitude of the short-circuit current  $i_s$  are. This depends on  $R_f$  and the short-circuit coefficient  $\mu$ .

### 3.5.2 Simulation results of the drive with inter-turn short-circuit fault

The inter-turn fault model is simulated for seven different fault scenarios corresponding to seven severity levels, the fault resistance  $R_f = 10R_s$ , and for the three different load cases


 Figure 3.30: Motor windings with an inter-turn short-circuit fault in phase  $a$ 

as stated previously. The fault severity levels rank from 2 to 8 and are related to the number of short-circuited turns in phase  $a$  winding. For each fault scenario, the 1s time duration fault is introduced in steady state at three different instants 1s, 4s, and 7s for 9s total simulation time. Figure 3.31 shows the torque and speed response of the PMSynRM under the inter-turn short-circuit fault (Level 2), corresponding to 6.25% of the fault severity. When the fault is introduced, transient phenomena with low amplitudes occur in the speed response, and after a few seconds, the steady state condition is reached. This shows the robustness of the controller under inter-turn short-circuit conditions. On the other hand, the torque response of the motor suffers from oscillations during fault periods. Comparing the oscillation differences in the three load conditions, more variations are observed during low load conditions. This makes the torque signal a candidate among fault indicators that could be helpful in developing a diagnostic tool for such a fault.

Figure 3.32 shows the stator phase  $a$  current under healthy and fault (at severity Level 2) conditions in stator phase  $a$  winding for the three load levels. We can observe that even at the occurrence of the fault with the lowest severity, despite the action of the speed and current controllers, the amplitude of the current is significantly affected. Therefore, the variance of the phase currents can be considered a potential candidate for fault features extraction.

### 3.6 Simulation of the Hybrid model of the PMSynRM with Dynamic eccentricity fault

As mentioned in the previous chapter, dynamic eccentricity occurs when the center of the rotor is not at the center of rotation and the minimum air-gap revolves with the rotor. With respect to Figure 3.33 the axis of rotation  $O_B$  coincides with the stator axis  $O_A$  but not with the motor axis  $O_R$ . The non-uniformity of air-gap is a time-variant when dynamic eccentricity occurs. The percentage of dynamic eccentricity is defined as follows:

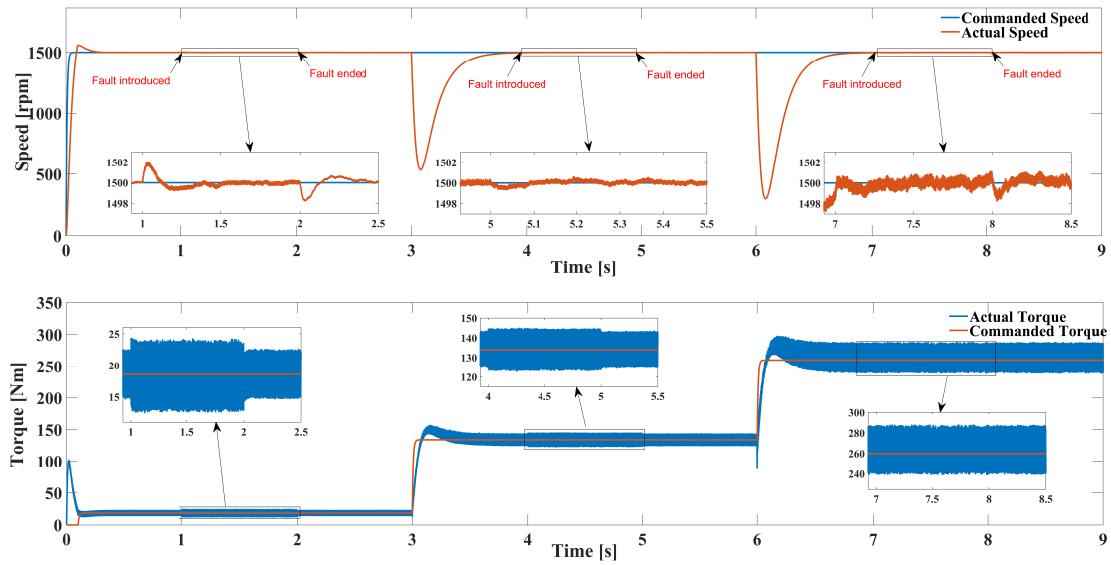


Figure 3.31: Speed and Torque response of the PMSynRM under inter-turn short-circuit Fault (level 2) for the three loads

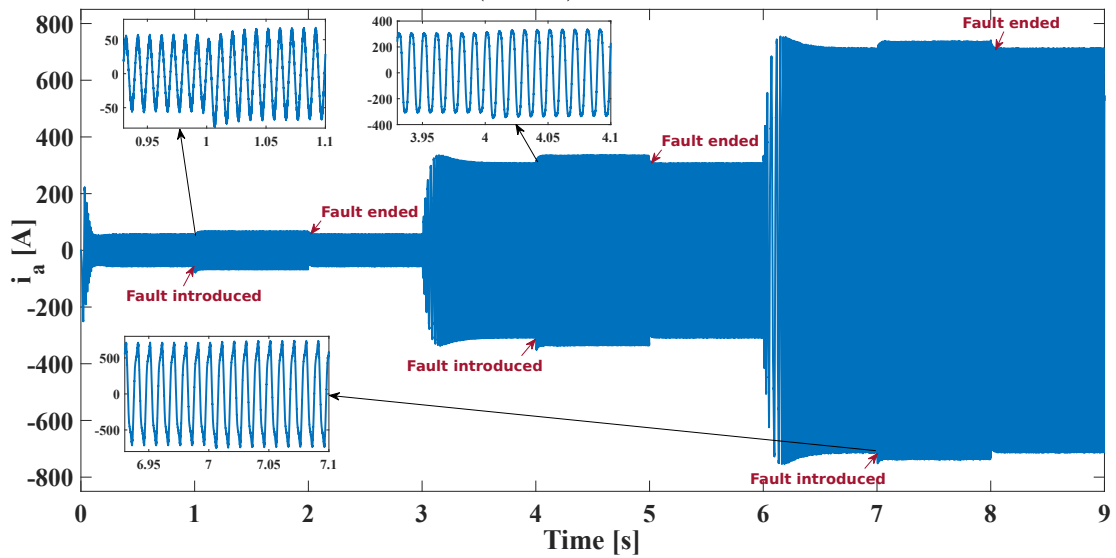


Figure 3.32: Time series of stator current in phase  $a$  of the PMSynRM under inter-turn short-circuit Fault (level 2) for the three loads

$$\epsilon_D = \left( \frac{O_B O_R}{g} \right) \times 100(\%) \quad (3.82)$$

Where  $\epsilon_D$  = represents the percentage of dynamic eccentricity between the stator and rotor axes,  $g$  is the radial air-gap length. The vector  $O_B O_R$  is called the dynamic transfer vector.

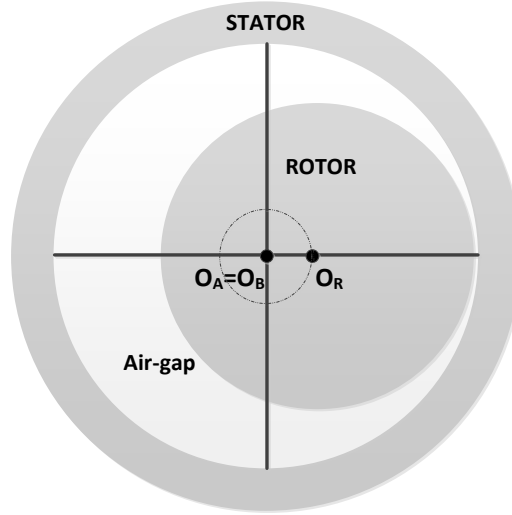


Figure 3.33: Schematic representation of dynamic eccentricity

To simulate the FEM of the PMSynRM, its geometrical structure is designed with the required percentage of dynamic eccentricity between the stator and rotor axes as described previously. When there is eccentricity present in the rotor, the magnetic field will become distorted and asymmetrical. This results in a variation of the magnetic flux density as the rotor rotates, which will be reflected in the inductances models. From the eccentricity model of the PMSynRM, the self, and mutual inductances have been modelled for the three excitation currents.

Figure 3.34 shows the self and mutual inductances of the healthy PMSynRm and the PMSynRM with 33% of dynamic eccentricity for the three excitation currents. Different variances in the inductances are observed. These variations evaluated in terms Root-Mean Square Error ( $RMSE$ ) and Correlation Coefficient ( $CC$ ) give the following results.

- ( $RMSE = 2.33 \times 10e^{-6}$ ,  $CC = 0.9999$ ) and ( $RMSE = 1.34 \times 10e^{-7}$ ,  $CC = 1$ ) for the self and mutual inductance for 50A excitation current, respectively,
- ( $RMSE = 2.13 \times 10e^{-6}$ ,  $CC = 0.9997$ ) and ( $RMSE = 1.46 \times 10e^{-7}$ ,  $CC = 1$ ) for the self and mutual inductance for 300A excitation current, respectively,
- ( $RMSE = 2.10 \times 10e^{-6}$ ,  $CC = 0.9994$ ) and ( $RMSE = 3.92 \times 10e^{-8}$ ,  $CC = 1$ ) for the self and mutual inductance for 700A excitation current, respectively.

As it can be observed, the dynamic eccentric fault causes more variation in the self inductance than in mutual inductances for all excitation currents.

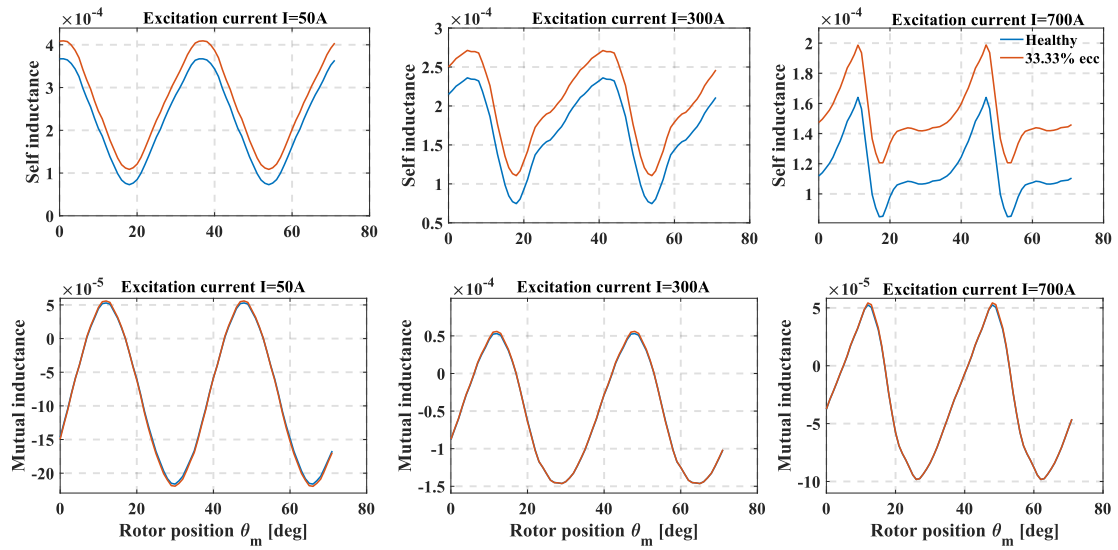


Figure 3.34: FEM inductances under healthy and faulty conditions

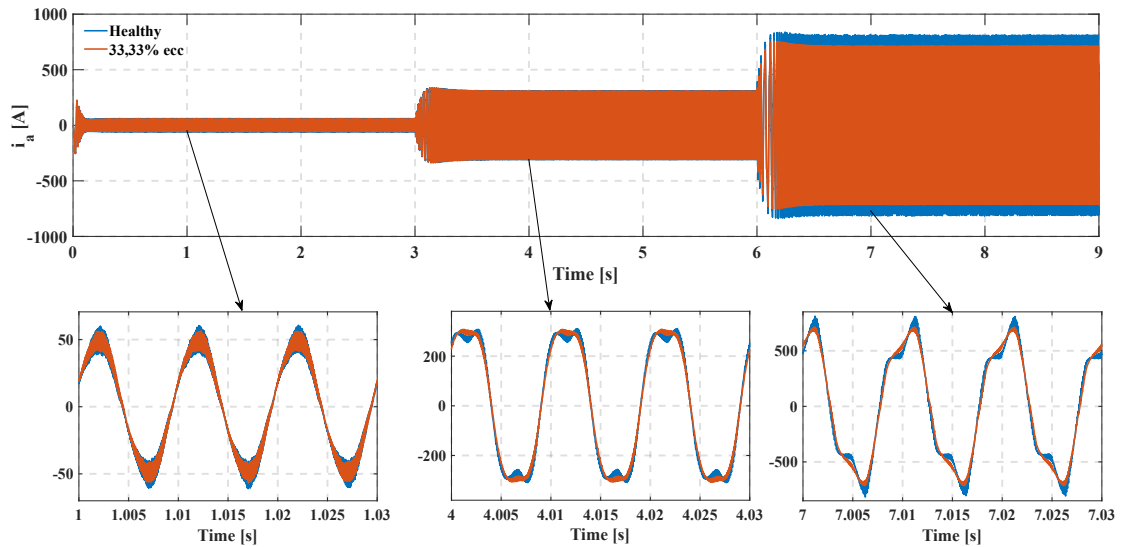


Figure 3.35: Stator phase  $a$  current of the healthy PMSynRM and the PMSynRM with dynamic eccentricity

To simulate the dynamic eccentricity fault of the PMSynRM with the proposed motor drive system in 3.8, the inductances obtained with dynamic eccentricity with FEM are included in the analytical model. The stator phase  $a$  current waveforms of the healthy and faulty PMSynRM are shown in Figure 3.35. The results are as follows:

- A variation of 0.01% in the self inductance for 50A excitation current causes variation of 0.07% in the phase currents magnitude,
- A variation of 0.03% in the self inductance for 300A excitation current causes a variation of 0.26% in the phase currents magnitude,
- A variation of 0.06% in the self inductance for 700A excitation current causes variation of 0.44% in the phase currents magnitude.

These results show that the variations in the stator phase currents have the same tendency as the variations in the PMSynRM inductances due to the dynamic eccentricity. This analysis shows that the PMSynRM inductances and stator currents are potential candidates as dynamic eccentricity fault features.

### 3.7 Conclusion

Accurate representation of faulty electric motors is crucial for research and development in the area of condition monitoring to avoid or reduce the use of expensive testbeds, and potentially destructive tests. There are three strategies for electric motor fault modelling in the literature: models based on coupled circuits, models based on numerical methods, and hybrid models. Nonlinearities and non-idealities of the electrical machine cannot be properly modelled using circuit-based models. On the other hand, although models based on numerical methods are more comprehensive, they require significant computational capacity and long simulation times. The accuracy of the model is crucial for the performance of the fault diagnosis method. But, because the fault detection time should be as short as possible, the model is expected to be computed in a short time. Therefore, it is recommended to develop a model that offers a good balance between accuracy and computation time. The hybrid model, based on the combination of circuit-based models and numerical ones is a relevant candidate as it can benefit from both approaches.

We developed for our study a hybrid model of a PMSynRM that combines a finite element model and an analytical model. The machine is at first designed and simulated with FEMM software to calculate the inductances in healthy and faulty modes. The calculated inductances are then stored in multidimensional lookup tables used in the three-phase inductance-based analytical model. The hybrid model is validated with experimental data under healthy conditions with over 70% accuracy. We also developed a model of the machine under inter-turn short-circuit and dynamic eccentricity. The analysis of the PMSynRM parameters under faulty conditions showed that the stator currents are potential good candidates as fault features for both faults.

## Chapter 4

# EV powertrain fault detection methodology based on statistical approaches

### 4.1 Introduction

In recent inverter-fed motor applications, conventional motor monitoring tools have faced challenges due to high noise levels, the dynamic changes affecting excitation frequencies, and closed-loop action that could affect the fault signatures [205]. This has created the need to develop universal fault diagnostic devices, valid for all applications, and suitable for various operational contexts. Statistical analysis techniques are emerging as an alternative to the conventional Motor Current Signal Analysis (MCSA) valid for utility-fed motors [206]. One of the essential characteristics of statistical methods is their ability to model data, capture the behaviour, and organize information into a concise set of rules or metrics. They consist of monitoring data variables statistics as well as control limits.

The first statistical analyses introduced in fault diagnosis were the univariate statistical methods. They consist of examining each system variable singularly and independently. This makes interpreting and diagnosing a fault condition very difficult and convoluted [128]. These methods only consider the magnitude of deviation inherent in a single system variable independently of all other system variables. However, in a multivariable system like in electric vehicle applications, simultaneous monitoring of individual variables separately will fail to recognize possible cross-correlations that may exist and will increase the insensitivity of the control charts for detection of fault conditions [129]. This can be misleading as not all the variables are independent, and only a few underlying events are driving the process at any one time. The improvement of these statistical methods is defined by the simultaneous monitoring of several variables.

In the following of this chapter, the main univariate and multivariate statistical methods will be presented first with their advantages and limitations. Some existing methodologies to overcome these limitations will also be presented with the evaluation of their performance for inter-turn short-circuit fault detection. At the end, our proposed methodology for inter-turn short-circuit fault detection robust against the uncertain and nonlinear dynamics of the drive system will be presented.

### 4.2 Univariate statistical methods for fault detection

The typical univariate statistical methods for fault detection are Shewhart charts, Cumulative Sum (CUSUM) plots, and Exponentially Weighted Moving Average (EWMA)

[207]. These control charts address the analysis of individual variables and consider the magnitude deviations. Consequently, any directional information resulting from variable interactions is ignored.

### 4.2.1 Shewhart chart

The Shewhart control chart uses an upper control limit ( $UCL$ ) and a lower control limit ( $LCL$ ). These limits are based on the variable mean ( $\mu_0$ ) and standard deviation ( $\sigma_0$ ) under healthy conditions. The control limits under the assumption that the data is normally distributed (99.73% of the statistics values lie within the control limits) are expressed as follows:

$$\begin{aligned} LCL &= \mu_0 - 3\sigma_0 \\ UCL &= \mu_0 + 3\sigma_0 \end{aligned} \quad (4.1)$$

As an illustration, Figure 4.1 shows the  $UCL$  and  $LCL$  in relation to the normal distribution. The center line (dashed line) represents the in-control average value. The two lines (golden lines) represent the Upper Control Limit and Lower Control Limit.

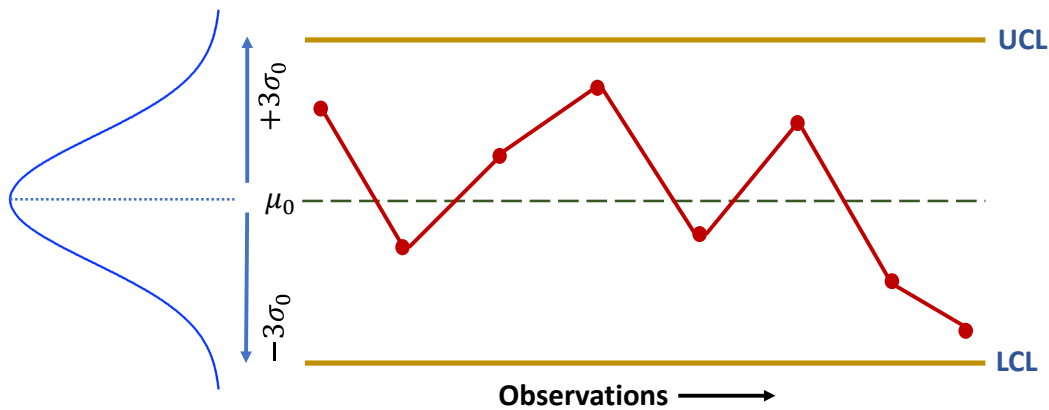


Figure 4.1: Shewhart control chart

The existence of outliers in the variable observations would cause wider control limits, thereby reducing the detection capability of the charts. Hence, a previous step of detecting potential outliers is required before estimating the control limits. An abnormal condition is detected when the statistic sample mean of a new observation lays out of the bounds defined by the control limits.

The attractiveness of the shewhart control chart is rooted in its simplicity and ability to detect large process average shifts quickly. However, it is also known to be relatively insensitive to small-sustained variable mean or variance shifts. Alternative control chart methodologies such as the CUSUM and the EWMA have been suggested to solve this problem [208].

### 4.2.2 EWMA chart



In the EWMA control scheme, the moving average is calculated by multiplying the historical observations with a weight coefficient that exponentially decays with time. The EWMA control chart consists of plotting the test statistic  $z_t$  versus time as follows:

$$z_t = \eta \times x_t + (1 - \eta)z_{t-1} \quad (4.2)$$

where  $\eta$  is a weight parameter, with  $0 < \eta \leq 1$ , and  $x_t$  is the mean value of the monitored variable from time  $t$ . The starting value  $x_0$  is set equal to an estimate of the mean  $\mu_0$  of the process in-control. Generally, smaller values of  $\eta$  increase the chart's sensitivity to smaller shifts in the process mean, while larger values of  $\eta$  increase its sensitivity to larger shifts [209].

Assuming the observations of  $x_t$  are independent random variables, let  $\mu_x$  be the mean and  $\sigma_x^2/n_t$  the variance of the variable in the time interval  $t$ .  $n_t$  is the sample size used at each time interval to calculate  $x_t$ . The mean value and variance of  $z_t$  are derived as follows:

$$\begin{aligned} \mu_{z_t} &= \mu_x \\ \sigma_{z_t}^2 &= \frac{\sigma_x^2}{n_t} \left( \frac{\eta}{2-\eta} \right) [1 - (1 - \eta)^{2t}] \end{aligned} \quad (4.3)$$

The EWMA Control limits are typically derived based on  $-L$  or  $+L$  sigma limits, where  $L$ , the control width is usually equal to 3, as in the design of Shewhart control chart limits. The time-varying upper and lower EWMA control limits,  $UCL(t)$  and  $LCL(t)$  are given by:

$$\begin{aligned} LCL(t) &= \mu_x - L\sigma_x \sqrt{\frac{\eta[1-(1-\eta)^{2t}]}{(2-\eta)n}} \\ UCL(t) &= \mu_x + L\sigma_x \sqrt{\frac{\eta[1-(1-\eta)^{2t}]}{(2-\eta)n}} \end{aligned} \quad (4.4)$$

As  $t$  increases,  $LCL(t)$  and  $UCL(t)$  converge to the asymptotic control limits,  $LCL$  and  $UCL$ , which are given by:

$$\begin{aligned} LCL &= \mu_x - L\sigma_x \sqrt{\frac{\eta}{2-\eta}} \\ UCL &= \mu_x + L\sigma_x \sqrt{\frac{\eta}{2-\eta}} \end{aligned} \quad (4.5)$$

The rate of convergence to the asymptotic values depends critically on  $\eta$ , with the convergence being much slower for small  $\eta$  [210]. The EWMA control scheme declares an anomaly when the value of  $z_t$  falls outside of the interval between the upper and lower bounds of the control limits.

### 4.2.3 CUSUM chart

The basic idea of the CUSUM chart is to test the existence of a change point sequentially by the recursive writing of the detection statistic as a function of the log-likelihood ratio (LLR) [211]. Let  $\mathbf{X}$  be the monitored variable with a series of observations  $[x_1, \dots, x_N]$ . Suppose that in the healthy state, the observations  $x_i$  are identically distributed according to the density distribution  $f_0(\cdot)$ . When a change-point occurs, this distribution changes and satisfies a post-change distribution  $f_1(\cdot) \neq f_0(\cdot)$ . We suppose that there exists only one change-point at time  $\nu$ , such that  $[x_1, \dots, x_{\nu-1}]$  are identically distributed according to the pre-change distribution  $f_0(\cdot)$ , and  $[x_\nu, \dots, x_N]$  according to the post-change distribution  $f_1(\cdot)$ . For  $n \geq 1$ , the issue of change-point detection is to sequentially test the null

hypothesis  $H_{0,N}$ , when no change-point occurred before time  $N$  against the alternative hypothesis  $H_{1,N}$  when a change-point occurred at the instant  $\nu \leq N$  (Equation 4.6) [212].

$$\begin{cases} H_{0,N} : \nu > N & x_t \sim f_0(\cdot) & \forall t = 1, \dots, N. \\ H_{1,N} : \exists \nu \leq N & x_t \sim f_0(\cdot) & \forall t = 1, \dots, (\nu - 1); \\ & x_t \sim f_1(\cdot) & \forall t = \nu, \dots, N. \end{cases} \quad (4.6)$$

When the two distributions  $f_0$  and  $f_1$  are known, the Log-Likelihood Ratio  $\mathbf{L}_t$  can be used to build the CUSUM statistic  $\mathbf{W}_t$  as follows:

$$\mathbf{L}_t = \log \left( \frac{f_1(x_t)}{f_0(x_t)} \right) \quad t \geq 1 \quad (4.7)$$

$$\mathbf{W}_t = \max \{0, \mathbf{W}_{t-1} + \mathbf{L}_t\}, \quad t \geq 1 \quad \mathbf{W}_0 = 0 \quad (4.8)$$

However, in practice,  $f_0$  and  $f_1$  are not always known. Hence it has been proposed in [213] to replace the LLR by a score function defined as:

$$\mathbf{S}_t(\delta, q) = \delta \cdot q^2 \mathbf{y}_t + \frac{1 - q^2}{2} \mathbf{y}_t^2 - \frac{\delta^2 \cdot q^2}{2} + \log(q) \quad (4.9)$$

where  $\mathbf{y}_t = (x_t - \mu_0)/\sigma_0$  is the centered and standardized data at time  $t$  under pre-change regime,  $\delta = (\mu_1 - \mu_0)/\sigma_0$  and  $q = \sigma_0/\sigma_1$ .

The parameters  $\delta$  and  $q$  are set according to the detection objective which concerns the mean and/or the variance. In practice, the expected type and level of change-point need to be known to set these parameters. The based-score CUSUM statistic is then defined recursively at time  $t$  as follows:

$$\mathbf{W}_t(\delta, q) = \max \{0, \mathbf{W}_{t-1}(\delta, q) + \mathbf{S}_t(\delta, q)\}, \quad t \geq 1 \quad \mathbf{W}_0(\delta, q) = 0 \quad (4.10)$$

- **For the change-point detection concerning the variance**,  $\mu_1 = \mu_0 = \mu$ , then  $\delta = 0$ . The score function is defined at time  $t$  as follows:

$$\mathbf{S}_t = \log \frac{\sigma_0}{\sigma_1} + \left( \frac{1}{\sigma_0^2} - \frac{1}{\sigma_1^2} \right) \frac{(x_t - \mu)^2}{2} \quad (4.11)$$

- **For the change-point detection concerning the mean**,  $\sigma_1 = \sigma_0 = \sigma$ , then  $q = 1$ . The score function is defined at the time  $t$  as follows:

$$\mathbf{S}_t = \frac{\mu_1 - \mu_0}{\sigma^2} \left( x_t - \frac{\mu_0 + \mu_1}{2} \right) \quad (4.12)$$

Under the post-change regime, knowing that the  $\mathbf{W}$ -statistic tends to grow gradually, it is essential to reject  $H_{0,t}$ , when the statistic  $\mathbf{W}_t$  exceeds a threshold. This threshold has to be chosen according to an objective of false alarm rate denoted  $\alpha$ . The stopping rule is to trigger an alarm to signal that a change-point has occurred before time  $t$  when  $\mathbf{W}_t(\delta, q)$  exceeds the detection threshold  $h(\alpha)$  set in advance [214]. An alarm occurs at a time  $T$  defined as follows:

$$T_{h(\alpha)} = \min \{t \geq 1 : \mathbf{W}_t(\delta, q) \geq h(\alpha)\} \quad (4.13)$$

We note that the choice of a statistic and a stopping rule defines a detection procedure that can be evaluated under the pre- and post-change regimes. Note that  $T$  is a stopping

time according to the filtration generated by the  $(\mathbf{W}_t)_{t \geq 0}$  and it is an estimator of the real change point  $\nu$  [212]. These different cases may arise:

- $T \geq \nu$ , the change-point  $\nu$  is detected with a delay  $(T - \nu)$ ;
- $T < \nu$ , the change-point  $\nu$  has not yet occurred at time  $T$ . It is said that the procedure triggered a false alarm;
- $\nu < +\infty, T = +\infty$ , the change-point  $\nu$  is not detected; this is a missed detection.

Three different thresholds have been identified from the literature: the constant threshold based on the Wald inequality [215], an empirical constant threshold identical to Tsiamyrtzis [216], and an empirical instantaneous threshold proposed by Margavio [217].

Figure 4.2 shows an example of a CUSUM chart where all black solid dots are values for  $\mathbf{W}_t$  when the process is in-control. During this time, data were sampled from a standard normal distribution. The points become empty after a shift in the mean occurs at  $\nu = 22$ . The points for  $\mathbf{W}_t$  are drawn in red after the change point is detected at  $T = 24$ .

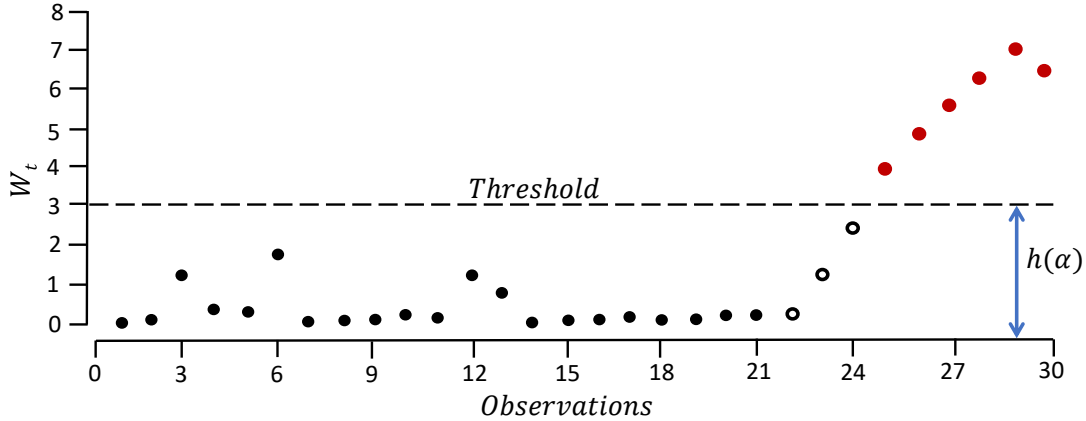


Figure 4.2: Example of CUSUM chart

### 4.3 Multivariate statistical methods for fault detection

Existing Multivariate Statistical Process Control methods, including Principal Component Analysis (PCA) and Independent Component Analysis (ICA), have been widely used in fault detection applications [218]. Although PCA and ICA can reduce dimensions and extract information from high-dimensional datasets, their original purpose was not to detect anomalies. Moreover, PCA-based models assume multivariate normality of the monitoring statistics, namely Hotelling's  $T^2$  and Squared Prediction Error ( $SPE$ ), while ICA-based models assume latent variables are non-Gaussian distributed [219]. Both methods make strong assumptions about specific data distributions, thereby limiting their performance in real-world applications [220]. The CUSUM and EWMA algorithm can also be extended to Multivariate Statistical Process Controls. The extended forms are called: Multivariate-CUSUM (MCUSUM) and Multivariate-EWMA (MEWMA), respectively. In the following, the focus will be on the modelling of PCA for fault detection.

### 4.3.1 Principal Component Analysis

#### 4.3.1.1 Principles of Principal Component Analysis

PCA is one of the most used multivariate techniques that has found widespread application in a variety of areas. It is concerned with explaining the variance-covariance structure of a dataset through a reduced set of linear combinations of the original variables. The objective of PCA is to represent a variable in terms of several underlying factors. PCA can perform the following operations.

- **Data Reduction:** Although the original data set may contain  $n$  variables, it is often the case that much of the variability can be accounted for by a smaller number ( $l < n$ ) of principal components.
- **Data Interpretation:** Relationships that were previously unsuspected can commonly be identified through PCA.

Considering that the original data have  $N$  observations for  $n$  measured variables, that are arranged in a data matrix  $\mathbf{X} \in \mathbb{R}^{N \times n}$ . In this matrix, each vector is written as  $\mathbf{x}_i^T = [x_{1,i}, \dots, x_{N,i}]$  where  $x_{j,i}$  is the  $j$ th observation of the  $i$ th variable. The most simple theoretical model for describing a variable in terms of several other variables is a linear one. Thus, PCA linearly transforms an original set of  $N$  variables  $\mathbf{x}_i^T = [x_{1,i}, \dots, x_{N,i}]$  into a substantially smaller set of uncorrelated  $l$  variables  $\hat{\mathbf{x}}_i^T = [\hat{x}_{1,i}, \dots, \hat{x}_{l,i}]$ . The new variable  $\hat{\mathbf{x}}_i^T$  represents most of the information contained in the original set of variables. PCA is based on Singular Value Decomposition (SVD) matrix processing routines to encompass data reduction, latent variable extraction, score and loading vectors, principal components modelling, and regression. The mathematics of PCA are expanded in subsection 4.3.1.2.

#### 4.3.1.2 Singular Value Decomposition

Singular Value Decomposition (SVD) is a matrix processing procedure rather than a direct statistical technique. SVD is an extension of the Eigenvalue Decomposition (ED) technique for non-square matrices. It shows that any real matrix can be diagonalized using two orthogonal matrices. If a matrix is square and symmetric, the two orthogonal matrices of SVD become equal, thus SVD and ED become equivalent. Any real ( $n \times n$ ) symmetric matrix  $\mathbf{A}$  can be decomposed into:

$$\mathbf{A} = \mathbf{U} \Lambda^2 \mathbf{U}^T \quad (4.14)$$

where  $\mathbf{U}$  is orthonormal ( $\mathbf{U}^T \mathbf{U} = \mathbf{I}$ ) and  $\Lambda^2$  is diagonal. This gives the normal eigenvalue equation:

$$\mathbf{A} u_i = u_i \lambda_i^2 \quad (4.15)$$

where  $u_i$  is the  $i^{\text{th}}$  column in  $\mathbf{U}$  and  $\lambda_i^2 = \Lambda_{i,i}^2$  or principal diagonal value. The decomposition of a rectangular ( $N \times n$ ) matrix is given by:

$$\mathbf{X} = \mathbf{U} \mathbf{S} \mathbf{V}^T \quad (4.16)$$

where  $\mathbf{X}$  is a ( $N \times n$ ) matrix,  $\mathbf{U}$  is a ( $N \times n$ ) column-orthonormal matrix (orthogonal and normalized) containing the eigenvectors of the symmetric matrix  $\mathbf{X} \mathbf{X}^T$  (left singular

vectors),  $\mathbf{S}$  is a  $(N \times n)$  diagonal symmetric matrix containing the singular values of matrix  $\mathbf{X}$ , and  $\mathbf{S}\mathbf{V}^T$  is a  $(n \times n)$  row-orthonormal matrix containing the eigenvectors of the symmetric matrix  $\mathbf{X}^T\mathbf{X}$  (right singular vectors).

PCA can identify combinations of variables that describe major trends in the data, and as mentioned previously, PCA relies upon SVD of a data matrix. This methodology is based on explaining the variance-covariance structure of the original data matrix in terms of a minority of linear combinations of the original variables. The principal component decomposition of an  $n$ -dimensional data set  $\mathbf{X} = [\mathbf{x}_1, \dots, \mathbf{x}_n]$  can be defined as:

$$\mathbf{X} = \mathbf{T}\mathbf{V}^T = \sum_{i=1}^n \mathbf{t}_i \mathbf{p}_i^T \quad (4.17)$$

$\mathbf{T} = [\mathbf{t}_1, \mathbf{t}_2, \dots, \mathbf{t}_n]$  is the matrix containing the principal component scores,  $\mathbf{P} = [\mathbf{p}_1, \mathbf{p}_2, \dots, \mathbf{p}_n]$  is the matrix containing the principal component loadings. The score vectors,  $\mathbf{t}_i$ , contain information on how the samples relate to each other, and the loading vectors,  $\mathbf{p}_i$ , contain information on how the variables relate to each other. The successful implementation of PCA depends upon the data structure (raw data, variance-covariance matrix, correlation matrix) and the used scaling parameters. The variance-covariance matrix and the correlation matrix are equal when the original data has been standardized but are not equal with the raw data matrix. The majority of analyses is performed on variance-covariance and correlation matrices of the original process variables rather than raw data matrices. Given a data matrix  $\mathbf{X}$  with  $N$  rows and  $n$  columns, the covariance matrix of  $\mathbf{X}$  is defined as:

$$\mathbf{S} = cov(\mathbf{X}) = \frac{\mathbf{X}^T\mathbf{X}}{N-1} \quad (4.18)$$

Where  $N - 1$  in the denominator of Equation 4.18 is the degree of freedom and it is used to give an unbiased estimate of the covariance matrix from a sample population. The true covariance matrix is unknown, and therefore an estimate  $\mathbf{S}$  is calculated.

As PCA is scale-dependent, the raw data must be scaled in a meaningful way. This can be achieved by mean centering, variance scaling, logarithmic scaling or combinations of these. A frequently used method is ‘autoscaling’ whereby the columns of the original data matrix  $\mathbf{X}$  are adjusted to zero mean and unit variance. This is commonly known as the Z-score normalization routine, which creates a new data matrix (of the same dimension as  $\mathbf{X}$ ) with zero mean and unit variance. The normalization of vector  $\mathbf{x}_i$  is done as follows:

$$\begin{aligned} \mu_{\mathbf{x}_i} &= \frac{1}{N} \sum_{j=1}^N x_{ji} \\ \sigma_{\mathbf{x}_i} &= \sqrt{\frac{1}{N-1} \sum_{j=1}^N (x_{ji} - \mu_{\mathbf{x}_i})^2} \\ \bar{x}_{ji} &= \frac{x_{ji} - \mu_{\mathbf{x}_i}}{\sigma_{\mathbf{x}_i}} \end{aligned} \quad (4.19)$$

where  $\mu_{\mathbf{x}_i}$  and  $\sigma_{\mathbf{x}_i}$  are the mean and standard deviation of  $\mathbf{x}_i$  respectively, and  $\bar{x}_{ji}$  is the re-scaled observation. In the rest of the report, the scaled data are considered without bar notation for simplicity. The reasoning behind scaling is to alleviate different magnitudes between variables and remove the effect of numerically large values. This difference has a significant impact on the analysis. The PCA decomposition in Equation 4.17 can be rewritten in terms of the score vectors  $\mathbf{t}_i$ :

$$\mathbf{T} = \mathbf{X}\mathbf{P} \quad (4.20)$$

where  $\mathbf{X}$  is the normalized data matrix,  $\mathbf{P}$  the matrix of loading coefficients which provide

information on which variables influence the direction of individual principal components, and  $\mathbf{T}$  the matrix of principal component scores that act ad interim for the process data.

#### 4.3.1.3 Method of Dimensionality Reduction

The loadings ( $\mathbf{P}$ ) are the eigenvectors of the variance-covariance matrix  $\mathbf{S}$  and from the normal eigenvalue relation, are related to the eigenvalues of the variance-covariance matrix (Equation 4.21):

$$\mathbf{S}\mathbf{p}_i = \lambda_i\mathbf{p}_i \quad (4.21)$$

where  $\lambda_i$  is the eigenvalue associated with the eigenvector  $\mathbf{p}_i$ . The eigenvalues of the variance-covariance matrix are a measure of the variance explained by each individual principal component and in this context, variance can be thought of as information. Maximising Equation 4.21 and rewriting it in standard matrix notation yields [221]:

$$[\mathbf{S} - \lambda\mathbf{I}]\mathbf{p}_i = 0 \quad (4.22)$$

where the inclusion of an identity matrix  $\mathbf{I}$  is to allow matrix subtraction. The score and loading pairs ( $\mathbf{t}_i, \mathbf{p}_i$ ) are arranged in descending order according to the associated eigenvalue ( $\lambda_i$ ), therefore the  $\lambda_i$  are a measure of the amount of variance described by the ( $\mathbf{t}_i, \mathbf{p}_i$ ) pair. The greatest amount of variance is captured by the first ( $\mathbf{t}_i, \mathbf{p}_i$ ) pair, the second greatest amount of variation that is orthogonal is captured by the second ( $\mathbf{t}_i, \mathbf{p}_i$ ) pair and so on.

After the transformation, there are as many principal components as the original variables. As they are computed in descending order, the lower order components embed fewer information and hence can be regarded as process noise (a stochastic component). The sum of the eigenvalues is defined by the trace of  $\mathbf{S}$ ,  $\text{Tr}(\mathbf{S})$  [222]:

$$\text{Tr}(\mathbf{S}) = \sum_{j=1}^n S_{jj} \quad (4.23)$$

The fraction of the "total sample variance" accounted for the eigenvector  $\mathbf{p}_i$  is expressed by:

$$\frac{\lambda_i}{\text{Tr}(\mathbf{S})} \quad (4.24)$$

In practice, only the principal components with the largest eigenvalues are kept, and the rest are discarded, thereby reducing the dimension of the problem. The number of components to keep is left to the data analyst's discretion, but it is generally chosen greater than 70% of the cumulative explained variance [223].

#### 4.3.2 PCA for fault detection

Fault detection in multivariate subspaces can be achieved in many different ways, but perhaps the two most commonly used and well-known methods are the Hotelling's  $T^2$  statistic and the squared prediction error ( $SPE$ ) or  $Q$  statistic. The  $T^2$  statistic is a measure of variation within a PCA model and it is calculated as the sum of the normalized squared scores. The  $Q$  statistic on the other hand indicates how well each sample conforms

to the PCA model and is calculated by the projection of a sample vector on the residual space [224].

The diagnosis of abnormal system behaviour can be greatly enhanced if similar system conditions and performance can be located in historical databases, thus essentially reducing this to a pattern recognition problem. Although not all of the faults will have occurred in historical records, the most common ones may reside in a similar process subspace, which in turn may assist in fault identification. Fault identification can be inferred from a PCA model, with both the  $T^2$  and  $SPE$  producing an ‘out-of-control’ signal when a fault occurs. In a process, it is possible to distinguish between two classes of change. The first class is a change in process operation, which may result in greater variation in some process variables. The relationship between the variables remains the same. However, the result is a shift in the mean value of one or more process variables. The metric used to detect this change is Hotelling’s  $T^2$ . The second class is associated with a change in the correlation structure of the process variables and the metric used to detect this change is the  $SPE$  [225]. Neither of these, however, provide any information about the cause of the fault, they are non-causal [226].

#### a) Hotelling’s $T^2$ Statistic

A traditional multivariate statistical approach to process monitoring is achieved through the use of the  $T^2$  statistic. In practice, it is usually necessary to estimate the mean and variance-covariance from a the data  $\mathbf{X}$  of  $N$  samples and  $n$  variables. This sample is assumed to be extracted from the system operating under steady-state conditions and follows a multivariate normal distribution. From the normalized data  $\mathbf{X}$ , the mean  $\bar{\mathbf{x}}$  and variance  $\check{\check{\Sigma}}$  of are calculated as follows:

$$\bar{\mathbf{x}}_j = \frac{1}{N} \sum_{j=1}^N \mathbf{x}_{ij} \quad (4.25)$$

$$\check{\check{\Sigma}} = \frac{1}{N-1} \sum_{j=1}^N (\mathbf{x}_j - \bar{\mathbf{x}})(\mathbf{x}_j - \bar{\mathbf{x}})^T \quad (4.26)$$

$\check{\check{\Sigma}}$  is often expressed in variance-covariance matrix form. Once the number of components  $l$  to retain is determined, the eigenvectors matrix  $\mathbf{P}$  and the principal component matrix  $\mathbf{T}$  are partitioned into the form:

$$\begin{aligned} \mathbf{P} &= \begin{pmatrix} \hat{\mathbf{P}}_l & \tilde{\mathbf{P}}_{n-l} \end{pmatrix} \\ \mathbf{T} &= \begin{pmatrix} \hat{\mathbf{T}}_l & \tilde{\mathbf{T}}_{n-l} \end{pmatrix} \end{aligned} \quad (4.27)$$

$\hat{\mathbf{X}}$  is the principal part of the data explained by the  $l$  first eigenvectors and the residual part  $\tilde{\mathbf{X}}$  is explained by the residual components [227]:

$$\begin{aligned} \hat{\mathbf{X}} &= \hat{\mathbf{P}}_l \hat{\mathbf{P}}_l^T \mathbf{X} \\ \tilde{\mathbf{X}} &= \tilde{\mathbf{P}}_{n-l} \tilde{\mathbf{P}}_{n-l}^T \mathbf{X} \end{aligned} \quad (4.28)$$

They respectively lead to the principal and residual subspaces used for fault diagnosis. The Hotelling’s test statistic is expressed as follows:

$$T^2 = \hat{\mathbf{X}}^T \hat{\Sigma}^{-1} \hat{\mathbf{X}} \quad (4.29)$$

$T^2$  is directly related to the  $F$  distribution, and depends upon the degrees of freedom in  $\hat{\Sigma}$  [228]. An upper limit,  $T_\alpha^2$  can be calculated from:

$$T_\alpha^2 = \frac{N^2 - 1}{N(N - l)} F_{\alpha, l, N-l} \quad (4.30)$$

where  $N$  is the number of samples used to develop the PCA model and  $l$  is the number of principal components (pc's) retained,  $F_{\alpha, l, N-l}$  is the upper  $100(1 - \alpha)\%$  critical point of the  $F$  distribution with  $(l, N - l)$  degrees of freedom. As this statistic is squared, the lower limit is equal to zero.

### b) Squared prediction error $SPE$

The  $SPE$  is a scalar measurement of the 'goodness-of-fit' of a sample  $\mathbf{X}$  to a PCA model. Once a model has been developed from nominal data (a healthy operating condition model) using a reduced set of principal components, the squared prediction error ( $SPE$ ) can be calculated. The  $SPE$  provides the facility to identify the onset of a new event not previously captured within the data. This is significant for identifying incipient drift, small dynamic differences, and ill-fitting models. A special event will generate new principal component and this has the effect of moving the new observation off the plane described by the  $l$  principal components. Such special events can be detected by computing the  $SPE$  of the residuals as follows [229].

$$SPE = \|\tilde{\mathbf{X}}\|^2 \quad (4.31)$$

A confidence limit for  $SPE$  can be established from the standard normal deviate, which corresponds to the  $100(1 - \alpha)$  percentile [230].

$$c = \theta_1 \frac{\left[ \left( \frac{SPE}{\theta_1} \right)^h - \frac{\theta_2 h - 0(h_0 - 1)}{\theta_1^2} - 1 \right]}{\sqrt{2\theta_2 h_0^2}} \quad (4.32)$$

Consequently, the critical value  $SPE_\alpha$  is:

$$SPE_\alpha = \theta_1 \left[ \frac{c_\alpha \sqrt{2\theta_2 h_0^2}}{\theta_1} + \frac{\theta_2 h_0 (h_0 - 1)}{\theta_1^2} + 1 \right]^{\frac{1}{h_0}} \quad (4.33)$$

Where

$$\theta_k = \sum_{j=l+1}^N \lambda_j^k \quad \text{for } k = (1, 2, 3) \quad (4.34)$$

and

$$h_0 = 1 - \frac{2\theta_1 \theta_3}{3\theta_2^2} \quad (4.35)$$

Where  $l$  is the number of principal components retained in the model and  $n$  is the total number of principal components.



### c) PCA fault detection improvement with Univariate Control Charts

The process monitoring using the  $T^2$  and the  $SPE$  is not always effective as they only use current observation information at the point for decision-making. Hence, these detection indices are relatively insensitive to minor changes in the process variables and thus may result in missed detections. To overcome these limitations, an alternative approach has been developed, in which the PCA is used as a modelling framework for fault detection using an EWMA or CUSUM control schemes [231]. This methodology framework can be described in two steps:

- First, a PCA model is developed and the fault detection indices are developed based on conventional monitoring indices such as  $T^2$  and  $SPE$ .
- In the second step, the CUSUM or EWMA control charts are applied to the monitoring indices  $T^2$  and  $SPE$  for fault detection. The summary of the methodology framework is shown in Table 4.1. Both CUSUM and EWMA charts are used to detect incipient irregularities in the process mean.

**Table 4.1:** Summary of PCA-based CUSUM and EWMA fault detection framework [232]

Step N°	Description
1.	<b>Given</b> <ul style="list-style-type: none"> <li>• A healthy dataset representing normal operating conditions and a faulty dataset representing different faulty conditions</li> </ul>
2.	<b>Data normalization</b> <ul style="list-style-type: none"> <li>• Normalize the data variables using Z-score normalization (Equation 4.19)</li> </ul>
3.	<b>PCA model development</b> <ul style="list-style-type: none"> <li>• Develop the PCA model as in section 4.3.1.2</li> <li>• Compute the control limits for <math>EWMA_{(T^2)}</math>, <math>EWMA_{(SPE)}</math>, <math>CUSUM_{(T^2)}</math> and <math>CUSUM_{(SPE)}</math> monitoring charts as in sections 4.2.2 and 4.2.3.</li> </ul>
4.	<b>Testing the faulty data</b> <ul style="list-style-type: none"> <li>• For faulty data, each variable is normalized using Z-score normalization</li> <li>• Compute the <math>EWMA_{(T^2)}</math>, <math>EWMA_{(SPE)}</math>, <math>CUSUM_{(T^2)}</math> and <math>CUSUM_{(SPE)}</math> monitoring statistics as in sections 4.2.2 and 4.2.3.</li> </ul>
5.	<b>Faulty detection</b> <ul style="list-style-type: none"> <li>• For faulty data, each variable is normalized using Z-score normalization</li> <li>• Finally, declare the fault if any of the monitoring statistics exceeds the control limit.</li> </ul>

## 4.4 Performance analysis of the statistical control charts

### 4.4.1 Concepts and definitions

In sequential change-point detection problems, one seeks a detection scheme to raise an alarm as soon as abnormal events happen at an unknown time  $\nu$  so that appropriate action

can be taken. The construction of the detection scheme is based on sequential observations that are observed sequentially, and it is assumed that the distributions of the variables will change if abnormal events occur. The decision whether to raise an alarm at time  $t$  will only depend on the first  $t$  observations. The current decision only depends on our current and past observations but not on future observations.

Let us consider fault detection as a binary classification case, in which the outcomes are labeled either as positive or negative. Thus, there are four possible outcomes from the binary classifier. If the outcome from a prediction is positive and the actual value is also positive, then it is called a true positive case, and the count of this kind of case is called true positive ( $TP$ ); however if the actual value is negative then it is said to be a false positive case, while the count is called false positive ( $FP$ ). Conversely, a true negative ( $TN$ ) is the count of cases that occurred when both the prediction outcome and the actual value are negative, and a false negative ( $FN$ ) is the count of cases when the prediction outcome is negative, while the actual value is positive. We can further define the true positive rate ( $TPR$ ) and the false positive rate ( $FPR$ ). The  $FPR$  quantifies the probability of the occurrence of an alarm when there is no fault. The  $TPR$  quantifies the probability of occurrence of alarm in the case of actual failure. From a set threshold for fault detection, the  $TPR$  and  $FPR$  are expressed as follows:

$$\begin{aligned} TPR &= \frac{TP}{TP+FN} \\ FPR &= \frac{FP}{FP+TN} \end{aligned} \quad (4.36)$$

The *sensitivity* and *specificity* are statistical measures of the accuracy of a diagnostic test. Sensitivity measures the proportion of actual positives that are correctly identified. Specificity measures the proportion of negatives that are correctly identified. Based on the previous definitions, we can obtain relationships such that *sensitivity* is  $TPR$  and *specificity* is  $(1 - FPR)$ .

In the literature, the performance of a fault detection scheme is typically evaluated by a measure of the  $FPR$  also known as the Probability of False Alarm ( $PFA$ ) and the  $1 - TPR$  also known as Probability of Missed Detection ( $PMD$ ). For the false alarm criterion, it is historically standard to use the ‘‘average run length’’ ( $ARL$ ) for a false alarm, which is the expected number of samples to be taken before a false alarm is signaled. Another performance measurement is the plot of the Receiver Operating Characteristic ( $ROC$ ) curve. The plot contains the  $TPR$  (*sensitivity*) on the  $y$ -axis and  $FPR$  ( $1 - specificity$ ) on the  $x$ -axis. The ideal scenario is a curve plot of an inverted L shape, which indicates that the fault detection is performed with 100%  $TPR$  and 0%  $FPR$ .

#### 4.4.2 Average run length (*ARL*)

The average run length (*ARL*) is the average number of observations plotted on a control chart before an out-of-control condition is indicated. There are two types of *ARL*: the in-control *ARL* that is measured when the process is actually in control and consequently the detected fault corresponds to a false alarm and the out-control *ARL* that is measured when the process is actually out of control and consequently the detected fault corresponds to a real alarm. The *ARL* is useful to compare the performance of statistical process control charts in terms of fault detection. The *ARL* computation is specific for every control chart algorithm. The main methods for computing *ARL* in the literature are the Markov chain approach, integral equation approach, and Monte Carlo simulation. The computation of the *ARL*s for the CUSUM and EWMA charts are presented in [233].

#### 4.4.3 Receiver operating characteristic (*ROC*) curve

The *ROC* curve offers a graphical illustration of the trade-off between *sensitivity* and *specificity* for any diagnostic test that uses a continuous variable. An illustration example of the *ROC* is shown in Figure 4.3.

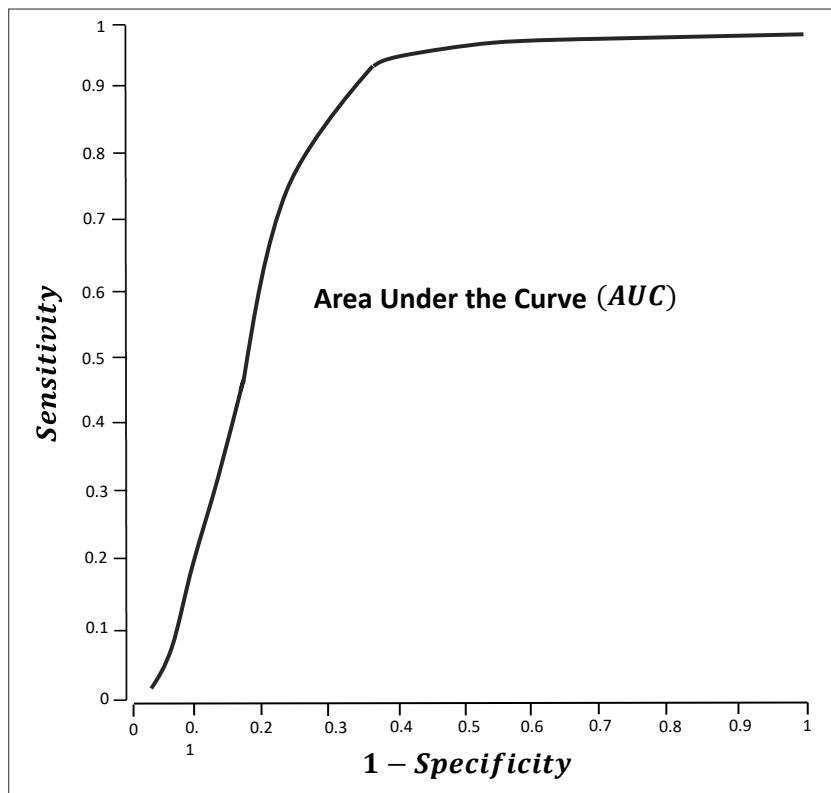


Figure 4.3: Receiver Operation Characteristic curve illustration

Ideally, the best limit value provides both the highest sensitivity and the highest specificity, easily located on the *ROC* curve by finding the highest point on the vertical axis and the

furthest to the left on the horizontal axis (upper left corner). However, it is rare that this ideal can be achieved. For example, one may opt to choose a higher sensitivity at the cost of lower specificity. The area under the ROC curve (*AUC*) is widely recognized as the measure of a diagnostic test's discriminatory power. The maximum value for the *AUC* is 1.0, thereby indicating a perfect test (100% sensitive and 100% specific) [234].

## 4.5 Stator inter-turn short-circuit detection

### 4.5.1 Modelling and data collection

In chapter 2), the developed hybrid model of the motor drive system has been retained as a virtual testbench to emulate the faults and generate synthetic data for fault diagnosis. From the system modeling in healthy and under the different fault conditions, the stator phase currents have been designated as interturn faults indicators. The data are generated from the simulation scenario described in Chapter 2. The hybrid model of the motor drive system has been simulated in a series of healthy and faulty modes. Seven faulty modes corresponding to seven severity levels ranking from 2 to 8 (corresponding to the number of short-circuited turns on phase *a* windings) have been considered. Each scenario has been simulated for 9s. The load change modes and faulty modes periods are described as follows:

- step changes in load torque to  $18Nm$  at  $0.1s$ ;  $134Nm$  at  $3s$  and  $260Nm$  at  $6s$ ,
- 1s time duration faulty mode is introduced in steady state at three different instants  $1s$ ,  $4s$ , and  $7s$  for 9s total simulation time.

Figure 4.4 illustrates the composition of the dataset pattern. The different modes and load variations are illustrated. The transients due to load changes and fault introductions are not included in the dataset. For each scenario, the three variables collected ( $\mathbf{I}_a$ ,  $\mathbf{I}_b$  and  $\mathbf{I}_c$ ) are collected for  $K$  observations.

### 4.5.2 Data preprocessing

In the preprocessing step, the statistical features, such Median Absolute Deviation (MAD), Variance ( $\sigma^2$ ), Skewness (*Skw*) and Kurtosis (*Kur*) are computed to get the first quantitative insights. Their evaluation helps in the selection of the features with the best discriminating capability. For feature extraction with less burden of large data, the computation of the statistical features on consecutive non-overlapping windows of fixed size is chosen. The statistical feature on sliding windows of size  $\omega$  of a variable  $\mathbf{I}^{(s)} = [I_1^{(s)}, \dots, I_K^{(s)}]$  of size  $K$  gives a new variable of size  $N = \frac{K}{\omega}$ . The first four statistical features on sliding windows of size  $\omega$  are described as follows [235]:

#### 1. Median Absolute Deviation (MAD)

The Median Absolute Deviation indicates the average distance between observations and their mean value. The **MAD** of  $\mathbf{I}^{(s)}$  is expressed as:

$$MAD_j = \text{median} \left( \left| \mathbf{I}_{\Omega_j}^{(s)} - \tilde{\mathbf{I}}_{\Omega_j}^{(s)} \right| \right); \quad j \in \{1, \dots, N\} \quad (4.37)$$

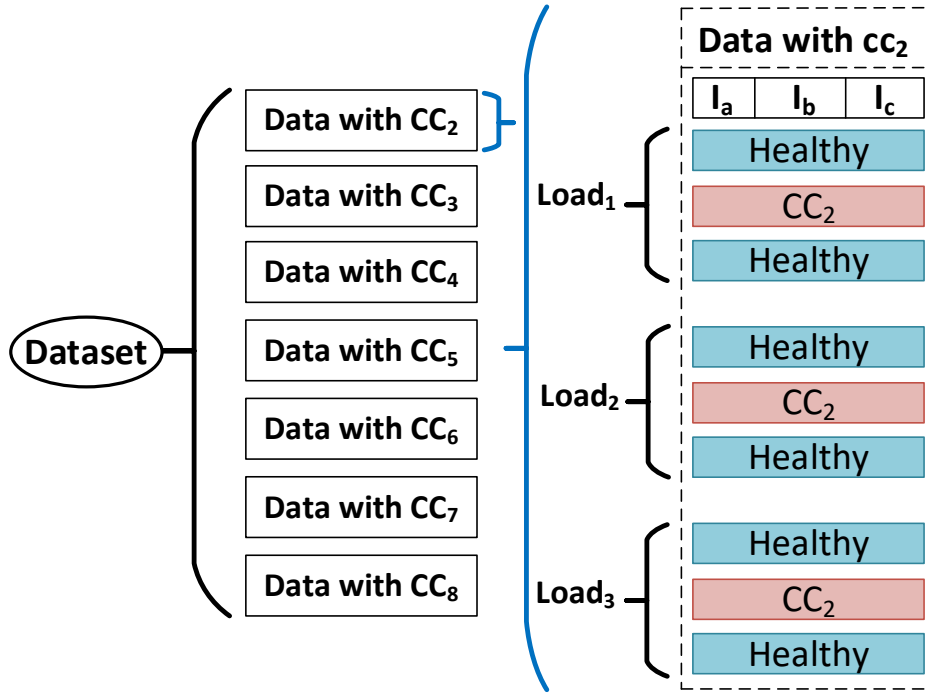


Figure 4.4: Layout of the dataset

where  $\tilde{\mathbf{I}}_{\Omega_j}^{(s)}$  is the median of the samples of the window  $\mathbf{I}_{\Omega_j}^{(s)} = \{I_{(j-1)\omega+1}^{(s)}, \dots, I_{j \times \omega}^{(s)}\}$ . The median is the measure of central tendency of a variable. For a given variable of  $n$  observations, the median when  $n$  is an odd number is expressed as follows:

$$\text{median} = \left[ \frac{n+1}{2} \right]^{th} \text{ observation} \quad (4.38)$$

When  $n$  is an even number, the median is expressed as follows:

$$\text{median} = \frac{\left[ \frac{n}{2} \right]^{th} \text{ observation} + \left[ \frac{n}{2} + 1 \right]^{th} \text{ observation}}{2} \quad (4.39)$$

## 2. Variance ( $\sigma^2$ )

The variance explains how a set of values is spread around their mean. The variance of  $\mathbf{I}^{(s)}$  is expressed as:

$$\sigma^2_j = \frac{1}{\omega - 1} \sum_{j=1}^{j=N} \left( \mathbf{I}_{\Omega_j}^{(s)} - \hat{\mu}_j \right)^2 \quad (4.40)$$

where  $\hat{\mu}_j$  is the mean of the samples of the window  $\mathbf{I}_{\Omega_j}^{(s)} = \{I_{(j-1)\omega+1}^{(s)}, \dots, I_{j \times \omega}^{(s)}\}$ .

## 3. Skewness (Skw)

The skewness measures the asymmetry of the data distribution. The Skewness of the variable  $\mathbf{I}^{(s)}$  is expressed as;

$$\mathbf{Skw}_j = \frac{1}{\omega - 1} \sum_{j=1}^{j=N} \left( \mathbf{I}_{\Omega_j}^{(s)} - \hat{\mu}_j \right)^3 \quad (4.41)$$

We can distinguish three types of distribution with respect to its skewness:

- symmetrical distribution: when both tails are symmetrical and the skewness is equal to zero,
- positive skew: when the right tail (with larger values) is longer. This informs about outliers that have values higher than the mean value and
- negative skew: the left tail (with small values) is longer. This informs about outliers that have values lower than the mean value.

#### 4. Kurtosis (**Kur**)

The kurtosis focuses on the tails of the distribution and explains whether the distribution is flat or rather with a high peak. The kurtosis of the variable  $\mathbf{I}^{(s)}$  is expressed as:

$$\mathbf{Kur}_j = \frac{1}{\omega - 1} \sum_{j=1}^{j=N} \left( \mathbf{I}_{\Omega_j}^{(s)} - \hat{\mu}_j \right)^4 \quad (4.42)$$

To guarantee the data features properties, and not violate the non-stationarity property of the data, the window size should be chosen carefully. In this case study, the window size equals to the number of observations in a period of the phase current. The four statistical features are computed for the 3-phase currents in healthy  $\mathbf{I}^{(h)_i}$  mode and in the seven faulty modes  $\mathbf{I}^{(cc_j)_i}$  for the three load conditions ( $j = 2, \dots, 8; i = 1, 2, 3$ ). To illustrate the effect of the fault severity on the features' values, the fitting normal distributions to the four features are presented in Figures 4.5 (for MAD), 4.6 (for variance), 4.7 (for skewness), and 4.8 for (kurtosis).

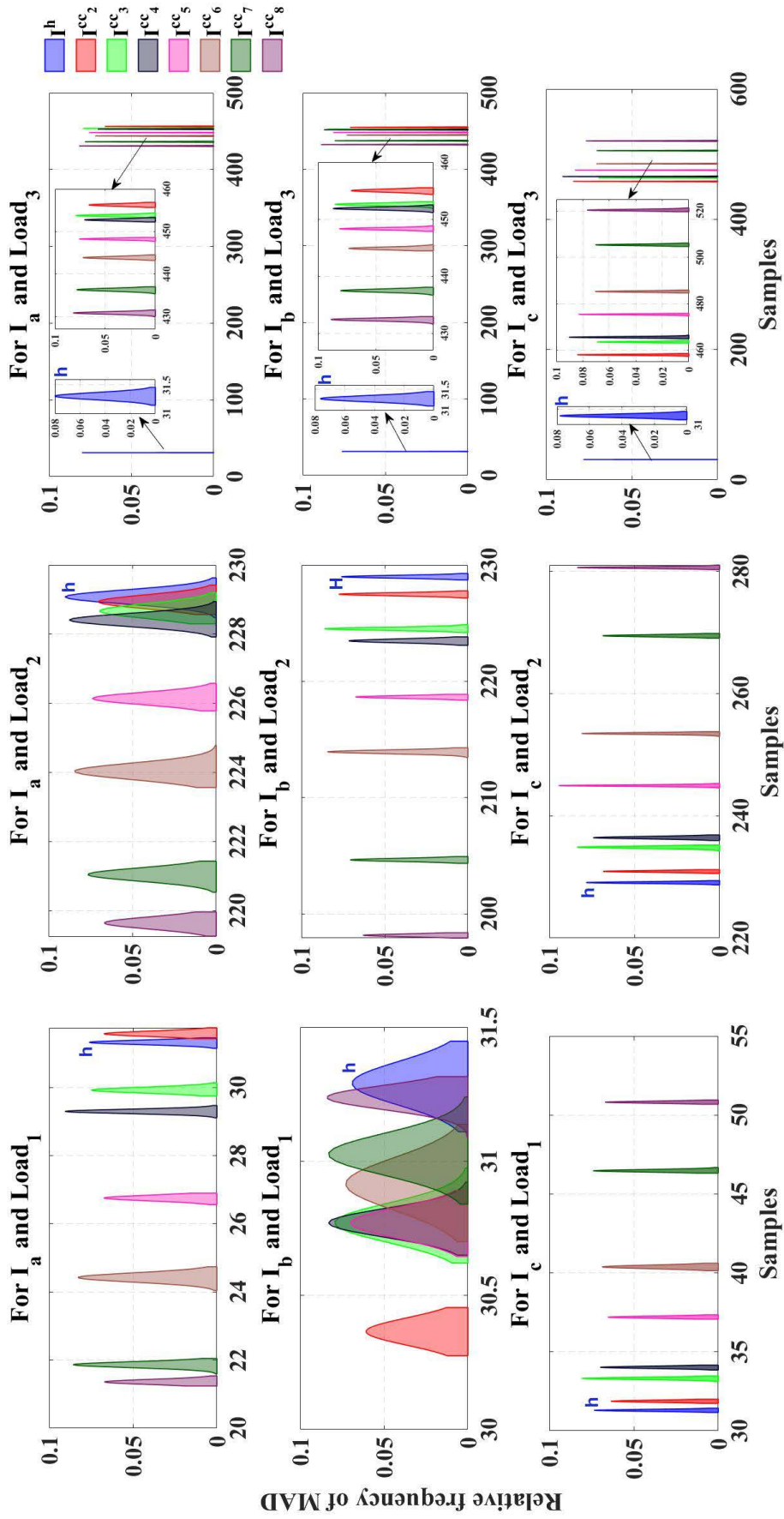


Figure 4.5: Fitting normal distribution to Median Absolute deviation

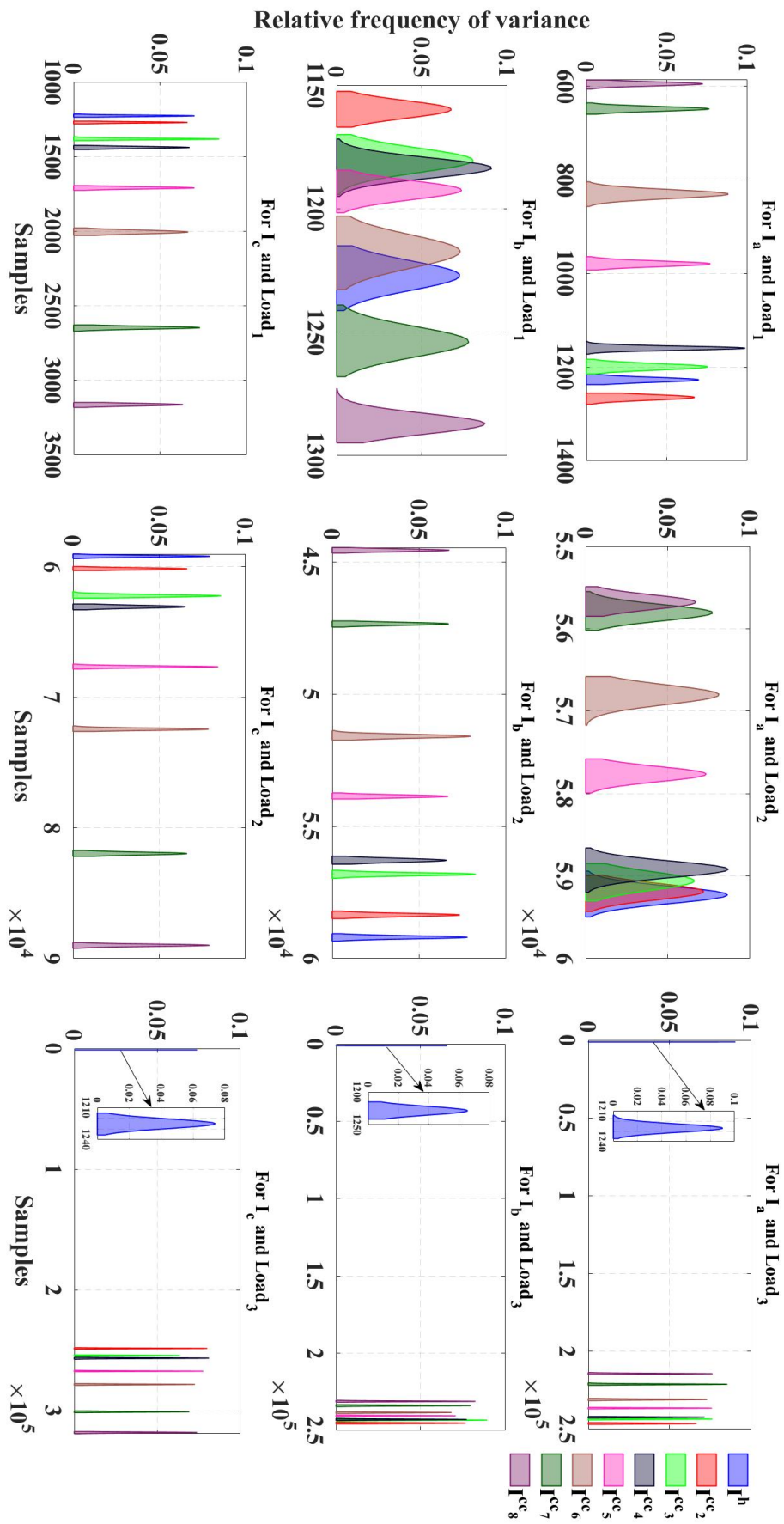


Figure 4.6: Fitting normal distribution to Variance



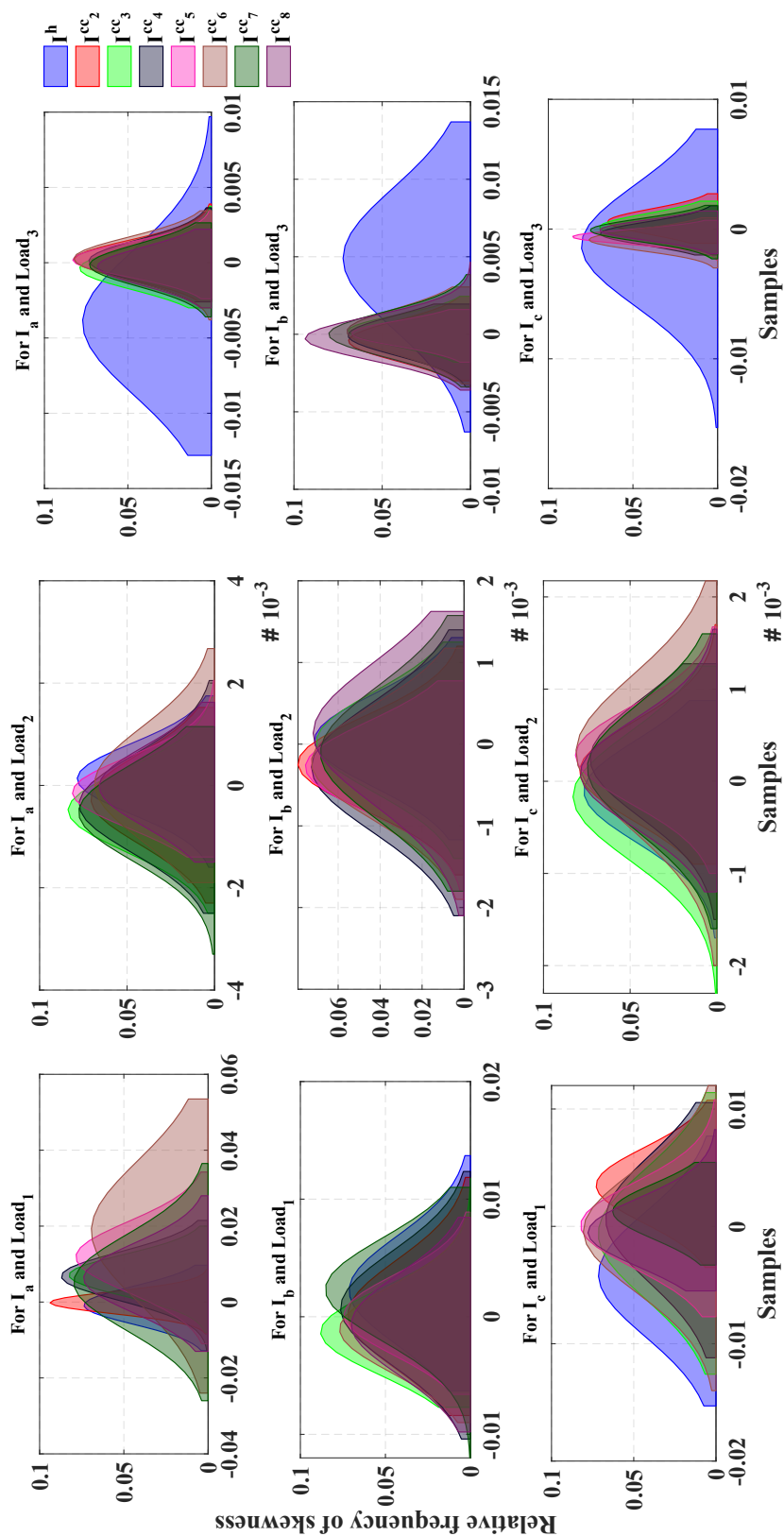


Figure 4.7: Fitting normal distribution to Skewness

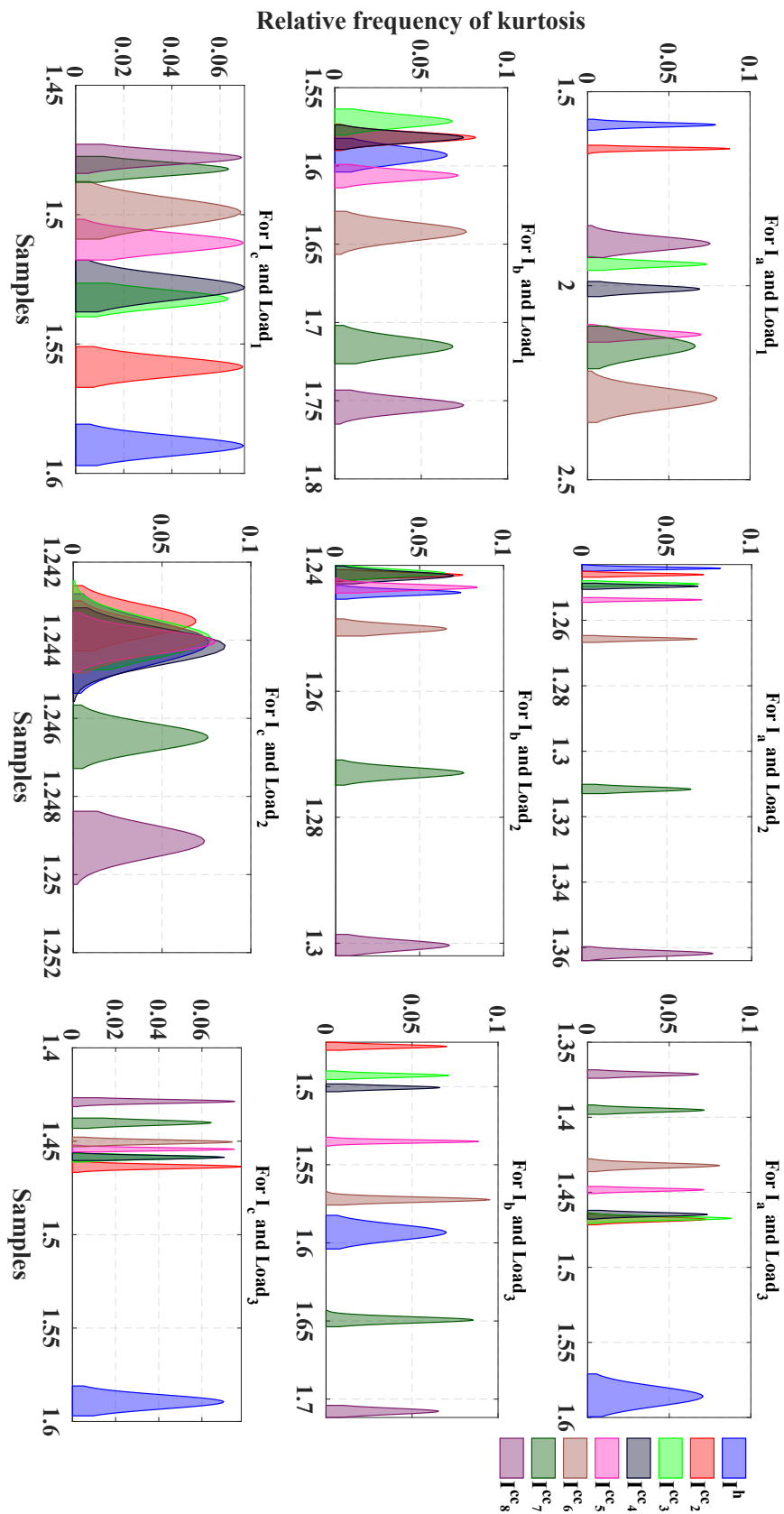


Figure 4.8: Fitting normal distribution to Kurtosis

The key findings by visual inspection of the fitting normal distributions are as follows:

1. For each fault severity and each load condition, the three-phase currents are affected differently. The fault patterns are more easily detected, from the healthy operation, on some phase currents than other for the MAD, variance and kurtosis.
2. For the skewness, for the three-phase currents, the difference between healthy and faulty conditions is weak.

These results indicate that the MAD, variance, and kurtosis can be selected as features with discriminant capability to detect interturn short-circuit faults, and also differentiate the severities of the fault. In the following, the data variable will be composed of the MAD, the variance, and the kurtosis of the three-phase currents. For each fault scenario, the data has  $N$  observations for 9 feature variables, arranged in a data matrix  $\mathbf{X} \in \mathbb{R}^{N \times 9}$ . In this matrix, each vector is written as  $\mathbf{x}_i^T = [x_{1,i}, \dots, x_{N,i}]$  where  $x_{j,i}$  is the  $j$ th observation of the  $i$ th variable. The observations of the variables of these three features in the three loads' operations are shown in Figure 4.9 for the healthy data and in Figure 4.10 for the data with *CC2* fault.

Each feature has three variables noted for a variable  $\mathbf{x}$ :  $\mathbf{x}_{j,a}$ ,  $\mathbf{x}_{j,b}$  and  $\mathbf{x}_{j,c}$  related to the phase  $a$ ,  $b$  and  $c$  respectively. The differences in the magnitude of the features and their variation with the load change can be well observed. For the MAD and variance, the magnitudes of the variables follow the evolution of load. This tendency is also observed in both healthy and faulty conditions. The kurtosis on the other hand shows dispersed evolution of its magnitudes with the evolution of the load in both healthy and faulty conditions. In the following, the Principal Component Analysis (PCA) will be adopted for the fault detection and diagnosis.

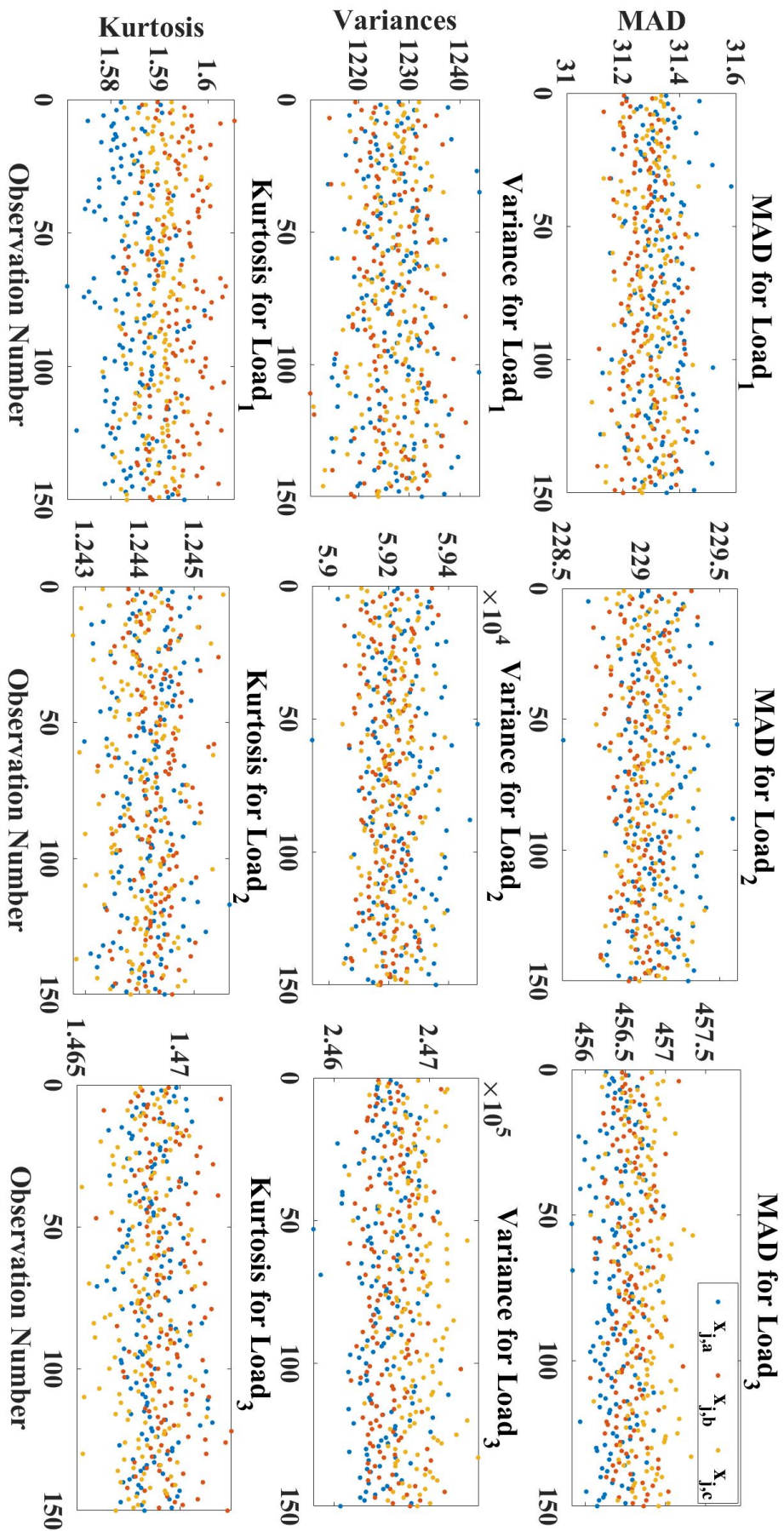


Figure 4.9: Features' variables in healthy condition

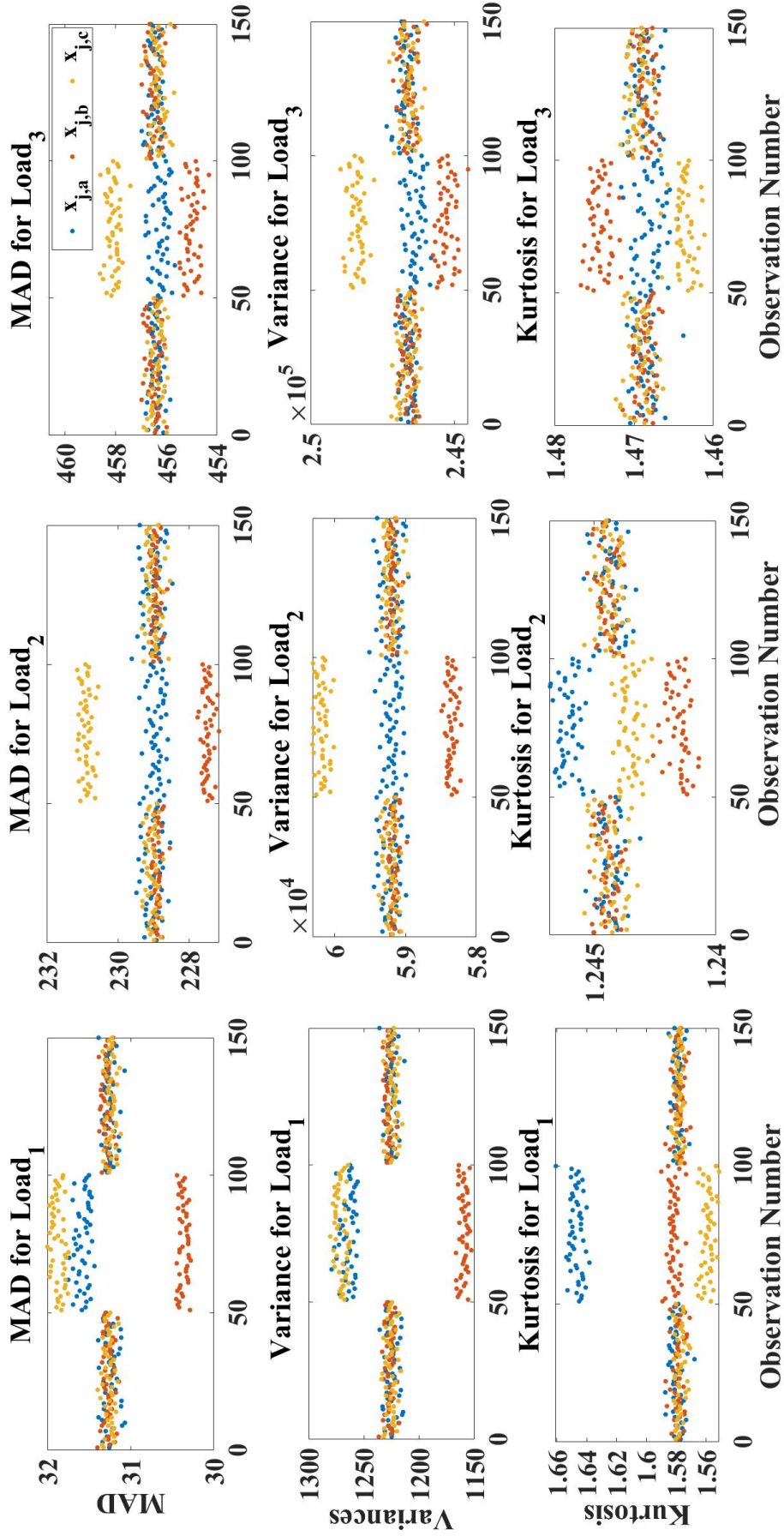


Figure 4.10: Features' variables for data with *CC2* fault

## 4.6 PCA for inter-turn fault detection

The EV traction motor has different operating criteria than those used in industries. While in industries, most loads are constant and classified, on the road, the EV may need to change speed, increase torque on slopes, and abruptly apply brakes. Figure 4.11 shows a typical load profile for an EV traction motor. Three load sections can be distinguished throughout the speed cycle (constant torque, constant power, and reduced power regions).

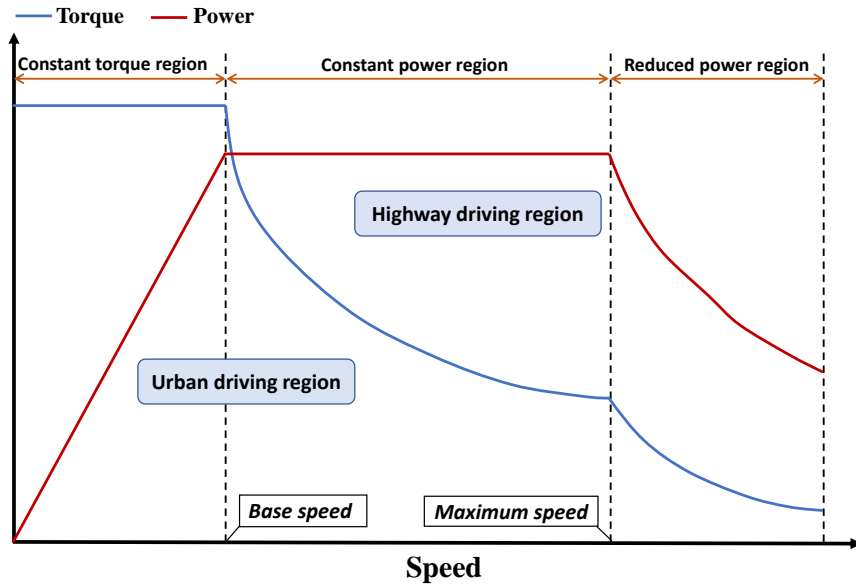


Figure 4.11: Typical EV motor speed–torque characteristics [236]

In process control of multivariate systems, Principal Component Analysis (PCA) is widely used because it requires no prior knowledge and is efficient to highlight the correlation among variables [237]. However, its application lies on the assumption that the variables are stationary (constant mean and variance over all the data time-series observations) and follow Gaussian distribution. Nevertheless, in a dynamic environment such as electric vehicles, the variables have non-stationary properties mostly related to the varying operation conditions. To address this limitation, extensions based on the analysis of time-series segmentation with fixed or moving windows have been proposed. For example, the Dynamic Principal Component Analysis (DPCA) has been proposed in [238] to deal with autocorrelations. PCA is applied to a new expanded data matrix with time-shifted duplicate vectors for all variables. However, it has been shown in [239] that the resultant score variables of the DPCA can still be correlated. Consequently, the Probability of a False Alarm ( $PFA$ ) is higher when using Hotelling's  $T^2$  statistic as the fault index. Multi-scale methods known as Multi-Scale PCA (MSPCA) have also been proposed for feature extraction for dynamic systems: each variable is extended to different forms of the variable at different scales. For example, in [240] wavelets are used to decompose the variables into various scale representations. Then PCA is used to obtain the coefficients for wavelet reconstitution. The PCA algorithm is applied to the reconstructed data for fault detection.

In the following two analyses will be presented. In the first analysis, fault detection in the different load conditions (stationary conditions) will be presented separately. In the second

analysis, fault detection in non-stationary conditions (the three load change conditions) will be presented.

#### 4.6.1 Fault detection under stationary conditions

The flowchart displayed in Figure 4.12 summarizes the PCA methodology for fault detection described in section 4.3.2.

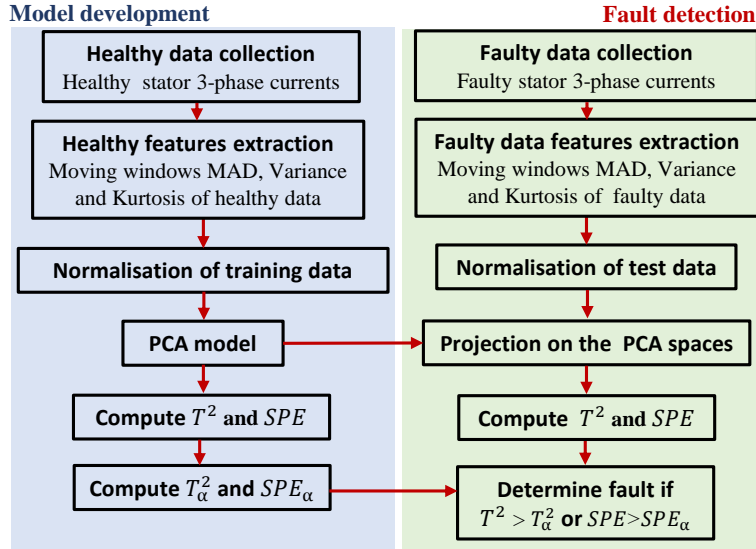


Figure 4.12: Flowchart of PCA for fault detection

As shown in the figure, the procedure is decomposed into two parts: one using the healthy data for modelling the process and the other considering the faulty data for fault detection. For the three load conditions, with the three different healthy data, the process is trained to construct the three PCA models. In this study, the threshold of cumulative variance is set to 90% to select the optimal number of features to form the principal subspace. Figure 4.13 describes the percentage explained variance with respect to a number of Principal components for the three conditions. This results in retaining the first five components for the principal subspace and the last four ones for the residual subspace. The percentage explained variance captured by the principal and the residual subspaces are (96.82% and 3.18%) for  $Load_1$ , (94.20% and 5.80%) for  $Load_2$  and (91.78% and 8.22%) for  $Load_3$ . The Hotelling  $T^2$  and the squared prediction error  $SPE$  will be used as fault indicators. The thresholds  $T_\alpha^2$  and  $SPE_\alpha$  are set at  $1 - 0.99$  confidence level, and are computed for  $\chi^2$  and  $z$  distributions, respectively. The results for the fault level 2 are shown in Figures 4.14, 4.15 and 4.16 for  $Load_1$ ,  $Load_2$  and  $Load_3$ , respectively. The horizontal dashed lines represent the thresholds. The vertical dashed lines represent the separation between the healthy and faulty periods. The blue solid dots are the observations of the monitoring metric  $T^2$  and  $SPE$  that are below the threshold, which symbolize healthy condition. The red solid dots are the observations of the monitoring metrics above the threshold, which symbolize faulty condition.

The detection results for monitoring  $T^2$  and  $SPE$  are compared with each other to verify the performance after injecting faulty data.

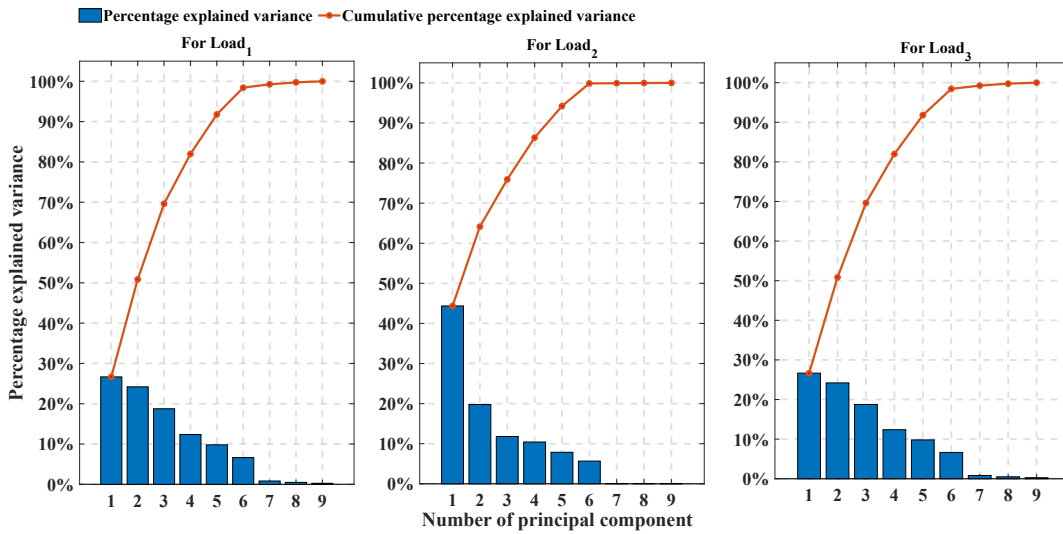


Figure 4.13: Variance captured by each principal component

1. Based on the detection results in  $Load_1$  condition shown in Figure 4.14, the  $T^2$  statistics showed no observations above the threshold before the fault injection and after the fault ended. All the red solid dots above the threshold are observed after the fault is introduced. From this observation, it can be noted that that the monitoring of  $T^2$  gives a fault detection with no False alarms and no missed detections. For  $SPE$ , few false alarms and no missed detection can be observed (see Figure 4.14).
2. The fault detection in  $Load_2$  condition shown in Figure 4.15 shows similar results to those in  $Load_1$  condition (see Figure 4.15).
3. The fault detection in  $Load_3$  condition shown in Figure 4.16 shows no false alarms for  $T^2$  and  $SPE$ . The  $T^2$  monitoring gives no missed detection but the  $SPE$  statistics fluctuates many times below the threshold after the fault injection. This shows high rate of missed detections (See Figure 4.16).

In the following, the reliability of the fault detection with PCA will be evaluated through the Probability of False Alarm ( $PFA$ ) and the Probability of Missed Detection ( $PMD$ ) achieved with the defined thresholds in each scenario. A summary of the performance of the fault detection with PCA in terms of  $PFA$  and  $PMD$  is given in Table 4.2. Usually, for fault detection, the acceptable  $PMD$  and  $PFA$  are typically set to 0.02 and 0.05 respectively[241]. In Table 4.2 the cases for which these thresholds are violated are highlighted in red. From the Table 4.2, it can be seen that the fault detection performance in terms of  $PMD$  is 100% when  $T^2$  is monitored. The monitoring of the  $SPE$  also gives excellent performance in terms of  $PMD$  in all scenarios except for  $CC_2$  and  $Load_3$  conditions. This shows that the incipient inter-turn fault is difficult to detect in the residual subspace for high load operation. In terms of  $PFA$ , the  $T^2$  shows acceptable performance with no violation of the threshold. The  $SPE$  monitoring on the other hand often violates the threshold. This shows that the fault detection with  $SPE$  is less accurate than the monitoring of  $T^2$ .



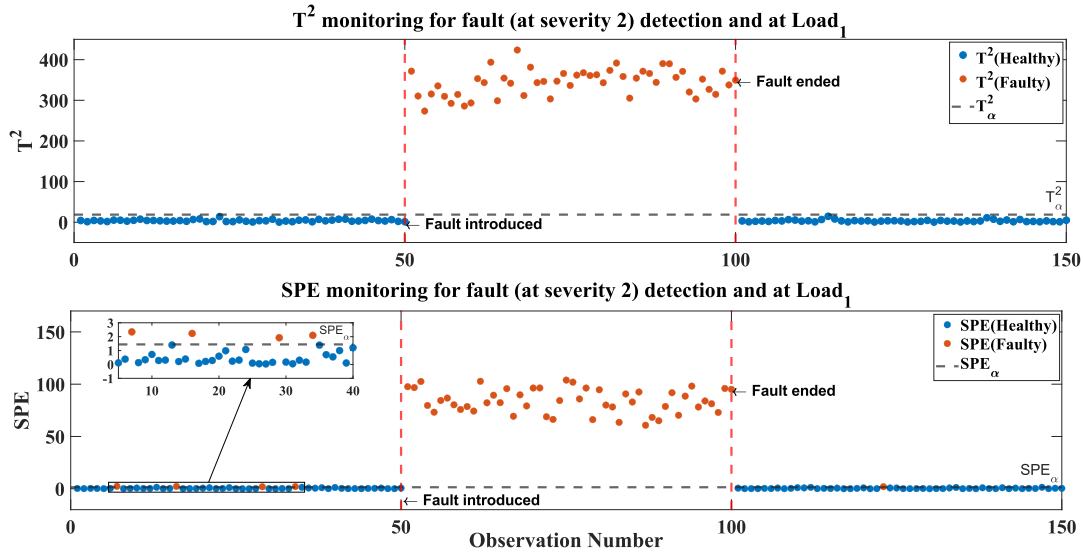


Figure 4.14: Fault level 2 detection with PCA at  $Load_1$  condition

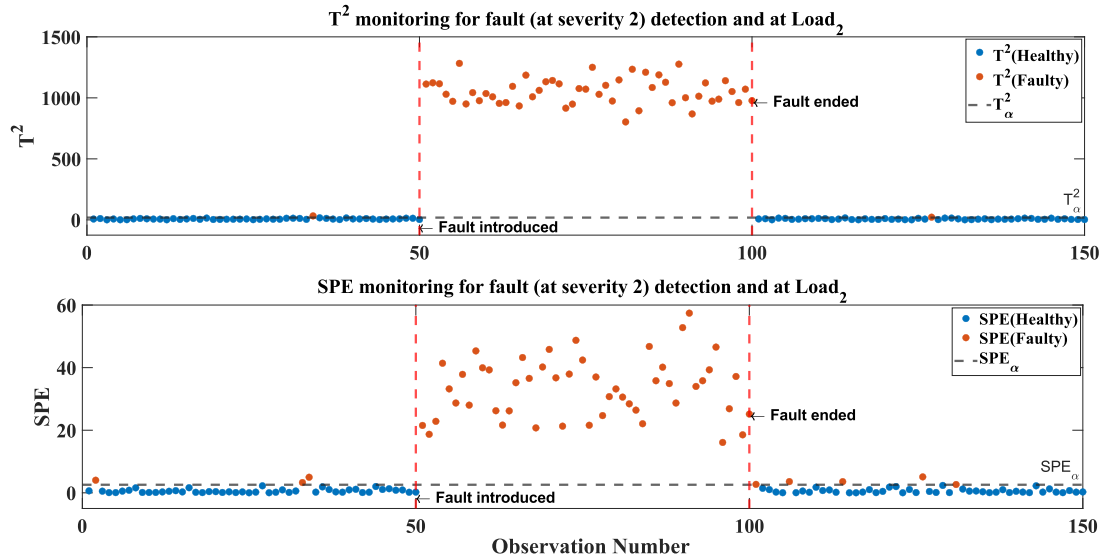


Figure 4.15: Fault level 2 detection with PCA at  $Load_2$  condition

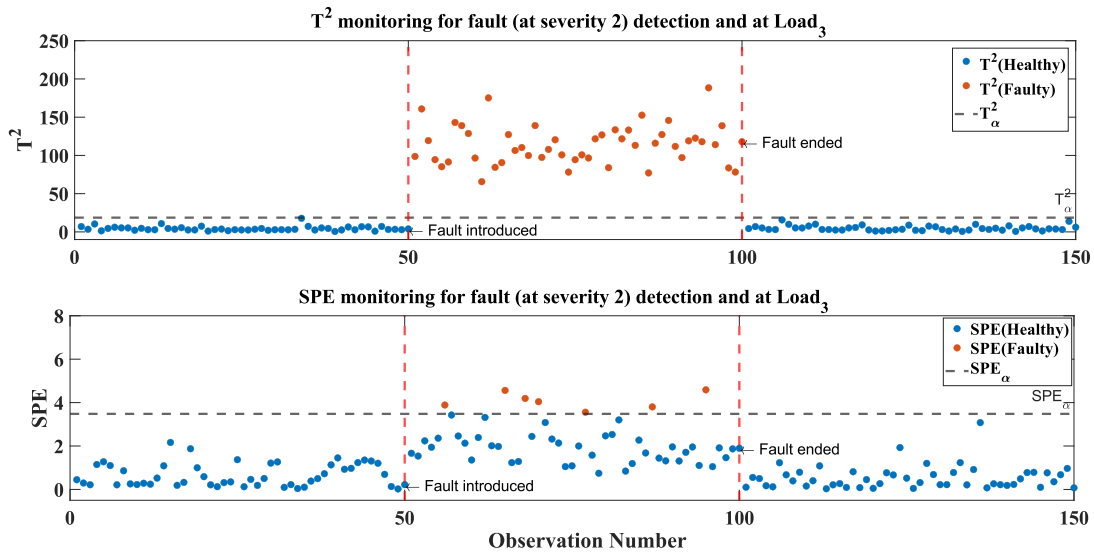


Figure 4.16: Fault level 2 detection with PCA at  $Load_3$  condition

**Table 4.2:** Performance evaluation of the fault detection with PCA  
(values greater than the thresholds are in red)

Scenario		PFA		PMD	
		$T^2$	SPE	$T^2$	SPE
Data with $CC_2$	$Load_1$	0	0.05	0	0
	$Load_2$	0.02	0.08	0	0
	$Load_3$	0	0	0	0.86
Data with $CC_3$	$Load_1$	0	0.1	0	0
	$Load_2$	0.05	0.06	0	0
	$Load_3$	0	0.01	0	0
Data with $CC_4$	$Load_1$	0	0.08	0	0
	$Load_2$	0	0.04	0	0
	$Load_3$	0	0	0	0
Data with $CC_5$	$Load_1$	0	0.04	0	0
	$Load_2$	0	0.1	0	0
	$Load_3$	0	0	0	0
Data with $CC_6$	$Load_1$	0	0.1	0	0
	$Load_2$	0	0.06	0	0
	$Load_3$	0	0.08	0	0
Data with $CC_7$	$Load_1$	0	0.1	0	0
	$Load_2$	0	0.06	0	0
	$Load_3$	0.04	0.04	0	0
Data with $CC_8$	$Load_1$	0	0.06	0	0
	$Load_2$	0.05	0.05	0	0
	$Load_3$	0	0	0	0

### 4.6.2 Fault detection under non-stationary condition

As stated in the subsection 4.6, the conventional PCA cannot be used under non-stationary conditions. Extensions of the PCA like Dynamic PCA, the Multi-Scale PCA have been proposed in the literature to cope with this limitation. However these extensions of the PCA come with some weaknesses like long response time, computational complexity, and their effectiveness is not always guaranteed.

In this work, we propose a simple method for detecting short-circuit faults between the turns of a PMSynRM windings under non-stationary conditions with different mechanical load operations. The Nuisance Attribute Projection (NAP) is applied to the raw data in the preprocessing step to get fault features that are only sensitive to the fault occurrence. After the elimination of the load effects, the features are normalized before being transformed with PCA to detect the fault. The flowchart displayed in Figure 4.17 summarizes the proposal.

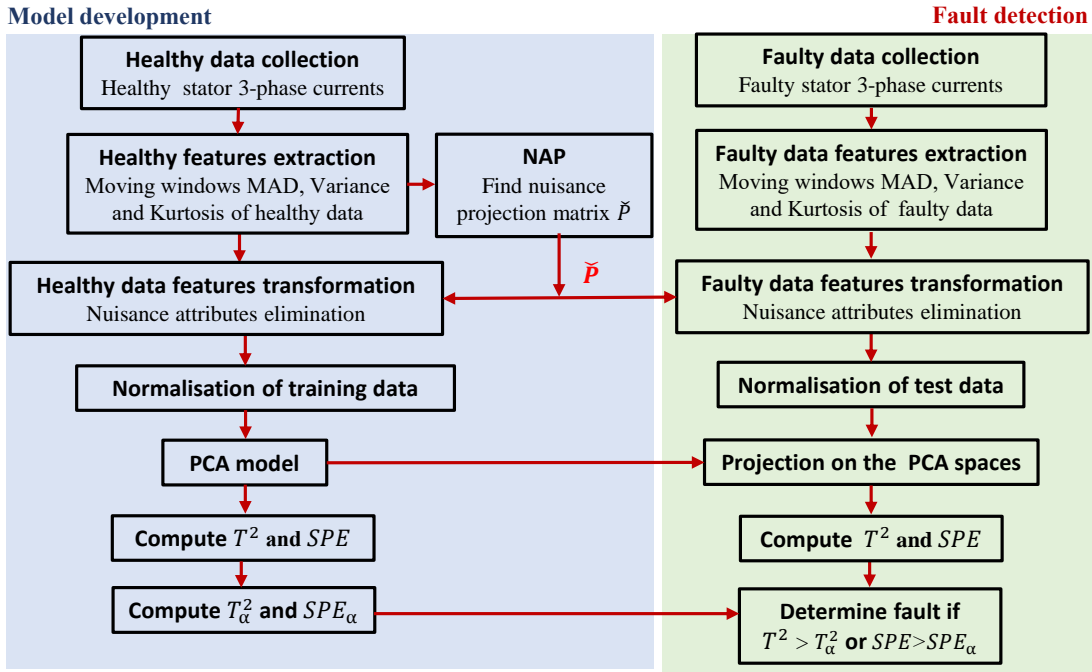


Figure 4.17: Flowchart of the NAP-based PCA for fault detection

#### a) Nuisance Attribute Projection

Originally applied to diminish the signal interference from different channels in speaker recognition, it has been recently applied in the condition-based maintenance field for better fault diagnostic results. Its principle is explained graphically in Figure 4.18.  $\mathbf{X}$  represents the feature vectors composed of the fault features and the other features related to the system dynamic named nuisance attributes. The dimensions of these vectors corresponding to the nuisance attributes are represented by the projection of  $\mathbf{X}$  onto the subspace representing nuisance attributes. These dimensions are projected out from  $\mathbf{X}$  to get  $\mathbf{X}'$  representing only the attributes related to fault patterns for all severity levels. Considering that the  $N$  observations for the  $n$  measured data matrix  $\mathbf{X}$  contain some dynamic attributes related

to the dynamics in the system operation, its transpose  $\mathbf{X}^T = [\mathbf{x}_1, \mathbf{x}_2, \dots, \mathbf{x}_N]$  is a matrix of vectors  $\mathbf{x}$  which are the vectors of variables of the  $i$ th observation. The NAP strategy tries to remove attributes related to the dynamic in the system in the feature space as follows:

$$\mathbf{X}' = \check{\mathbf{P}}\mathbf{X} \quad (4.43)$$

Where  $\check{\mathbf{P}} \in \mathbb{R}^{N \times n}$  is the projection matrix.

$$\check{\mathbf{P}} = \mathbf{I} - \sum_{i=1}^d \Delta_i \Delta_i^T \quad (4.44)$$

Where  $\mathbf{I}$  is an  $N \times N$  identity matrix,  $\Delta_i$  represents the  $i$ th NAP direction,  $d \leq N$  is the number of NAP directions to be removed from the feature space. The parameter  $d$  can be determined by making a compromise between the computational complexity and the projection effect since the larger  $d$  is, a better projection is obtained but the computation time is higher. The main principle of the NAP is to minimize the judgment of Projection Effect (**PE**) that is defined as the sum of the distance between each projection feature. The **PE** using the projection matrix  $\check{\mathbf{P}}$  is expressed as follows:

$$\mathbf{PE} = \sum_{i,j} W_{ij} \left\| \check{\mathbf{P}} \cdot \mathbf{x}_i - \check{\mathbf{P}} \cdot \mathbf{x}_j \right\|^2 \quad (4.45)$$

where  $W_{ij}$  is a weight coefficient that quantifies the relation between two feature vectors. If the nuisance variable is known (in our case the reference torque) and set in a label,  $W_{ij}$  is set positive when the observations  $\mathbf{x}_i$  and  $\mathbf{x}_j$  belong to the same operating conditions and negative otherwise. Its expression is as follows [242]:

$$W_{ij} = \begin{cases} 1 & \text{if operating condition}(\mathbf{x}_i) = \text{operating condition}(\mathbf{x}_j) \\ 0 & \text{otherwise} \end{cases} \quad (4.46)$$

The solution of the minimization of **PE** in Equation 4.45 can be transformed into finding the leading eigenvectors of the following eigenproblem (see Appendix A.3):

$$\mathbf{X}(\mathbf{W} - \text{diag}(\mathbf{W}\mathbf{U}))\mathbf{X}^T \Delta = \lambda \Delta \quad (4.47)$$

where  $\mathbf{U}$  is a column vector of all ones,  $\mathbf{W}$  the matrix of elements  $W_{ij}$ ,  $\lambda$  the eigenvalues, and  $\Delta$  the eigenvectors.

The NAP projection is at first computed using the healthy data to get the model  $\check{\mathbf{P}}$ , which is independent of the dynamic load variations. To compute the projection matrix  $\check{\mathbf{P}}$ , the weight matrix  $\mathbf{W}$  is generated to make the features independent. The minimization of the projection Effect (**PE**) is then achieved by setting the columns of  $\mathbf{v}$  to be the  $q$ th most principal eigenvectors of the eigenvalue analysis in Equation 4.47. In our case, we set  $q = \min(\dim_{\mathbf{X}}, d)$ ,  $\dim_{\mathbf{X}}$  as the dimension of the features, and  $d$  as the number of the NAP directions. The model projection matrix  $\check{\mathbf{P}}$  is used to remove from the healthy and actual features the effects of dynamic load variations. The transformed features are then used as inputs to the PCA for fault detection as described in Figure 4.17.

The non-stationary dataset is composed of the selected features MAD, the variance, and the kurtosis of the three-phase currents for the three load conditions. In our case study a series of data composed of  $N$  observations arranged in sections arranged in order:  $N/3$  observations for each load condition. The same seven fault scenarios are considered. In

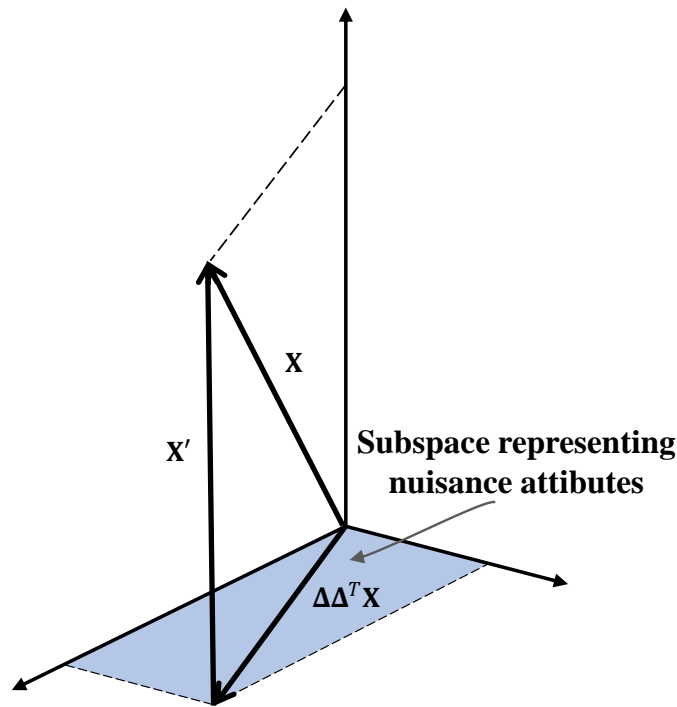


Figure 4.18: Schematic diagram of the NAP principle

the series of the three loads data, a section of faulty data at the same severity level is considered for diagnosis analysis. As shown in Figure 4.17, the procedure is composed of two sections. The first one (modelling) uses the healthy data to obtain the projection matrix  $\check{\mathbf{P}}$ , which is then used to transform training data and test data in the second section for fault detection. The number of NAP directions is set to  $d = 3$ . The observations of the three variables of the original features and the NAP score projected ones are shown in Figure 4.19, 4.20 and 4.21 for MAD, variance and Kurtosis, respectively.  $x_{j,a}$ ,  $x_{j,b}$  and  $x_{j,c}$  denote the features variables related to phase  $a$ ,  $b$  and  $c$  currents respectively. It can be clearly seen that after projection with the NAP, the new features are insensitive to load variations but sensitive to the faults. The three different faulty periods can be distinguished in the series of observations. The difference order in the features variable amplitudes due to NAP projection weights can also be observed.

The new healthy features scores are used to design the model for the PCA. The threshold of the cumulative percentage variance is set to 90%. Figure 4.22 shows that the first four principal components capture 98.56% of the information. Therefore, in the PCA model, the principal subspace is spanned with the first four components while the residual subspace is spanned with the five remaining ones.

Similarly to the analysis with stationary data, the Hotelling  $T^2$  and the squared prediction error  $SPE$  will be used as fault indicators. The thresholds  $T_\alpha^2$  and  $SPE_\alpha$  are set at  $1 - 0.99$  confidence level, and are computed for  $\chi^2$  and  $z$  distributions, respectively. The results for the fault level 2 are shown in Figure 4.23.

As shown in Figure 4.23, the  $T^2$  statistics showed no observations above the threshold before the fault injection and after the fault removal. All the red solid dots above the threshold are observed after the fault is introduced. From this observation, it can be noted

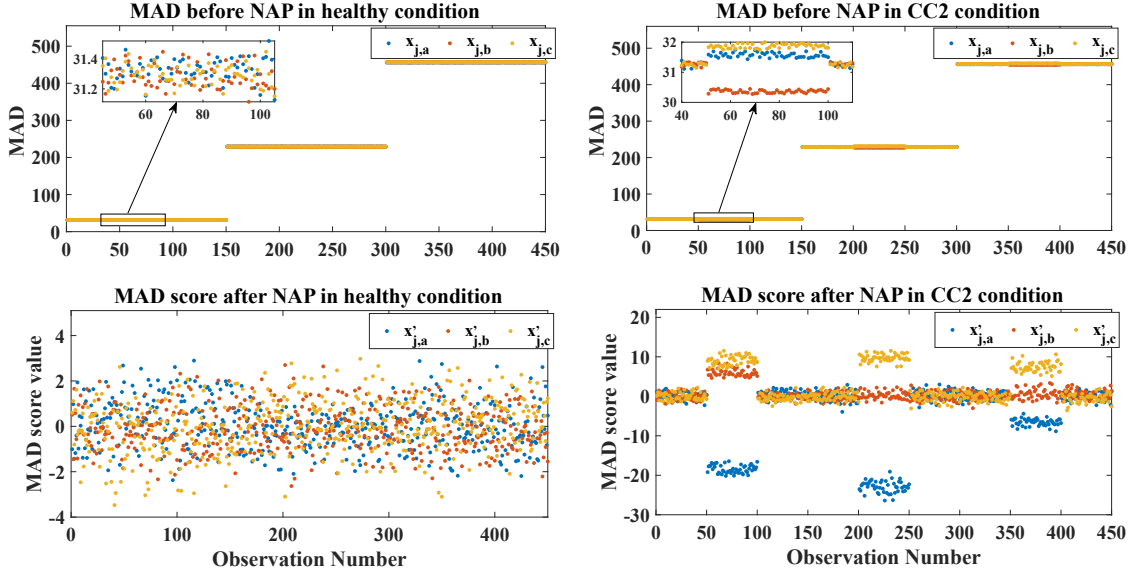


Figure 4.19: Comparison of MAD features before and after NAP

that the monitoring of  $T^2$  gives a fault detection with no False alarms and no missed detections. For the monitoring of the  $SPE$ , false alarms and no missed detections can be observed in each of the three load sections. Few false alarms can be observed under  $Load_1$  condition while more can be observed under  $Load_2$  and  $Load_3$  conditions.

A summary of the performance of the fault detection with the NAP-based PCA in terms of  $PFA$  and  $PMD$  is given in Table 4.3. The cases for which the thresholds are violated are highlighted in red. From the table, it can be seen that the fault detection performance in terms of  $PMD$  is 100% when  $T^2$  and  $SPE$  are monitored. In terms of  $PFA$ , the  $T^2$  exhibits acceptable performance with no violation of the threshold set at 0.05. The  $SPE$  monitoring on the other hand violates the threshold. It can be noticed that the  $PFA$  is much higher compared to the stationary cases. This shows that the NAP performs the requested task of removing dynamics related to the load variations but displaces the fault signatures in the PCA subspaces. This makes the fault detection monitoring the  $SPE$  with the NAP-based PCA less accurate than the monitoring of  $T^2$ .

In most of works reported in the literature, the PCA-based fault detection algorithm uses exclusively monitoring metrics related to the residual components of the PCA model. Indeed, this is valid in ideal systems where the presence of faults affects mostly the components in the residual subspace, but this is not always true. In some cases, the system modelling errors could be projected onto the residual subspace making it less sensitive to the fault and the principal subspace more sensitive. This is the case we came across in our case study in both stationary and non-stationary data. The least fault signature observed in the residual subspace when the NAP is applied can be due to the presence of NAP projection errors in the residual subspace. Based on the latter results and the result with the stationary data, in the following analysis, only the  $T^2$  will be considered as fault monitoring metric. For all the following analyses, only the non-stationary condition case study presented previously will be considered.

#### 4.6.3 Fault diagnosis for noisy data

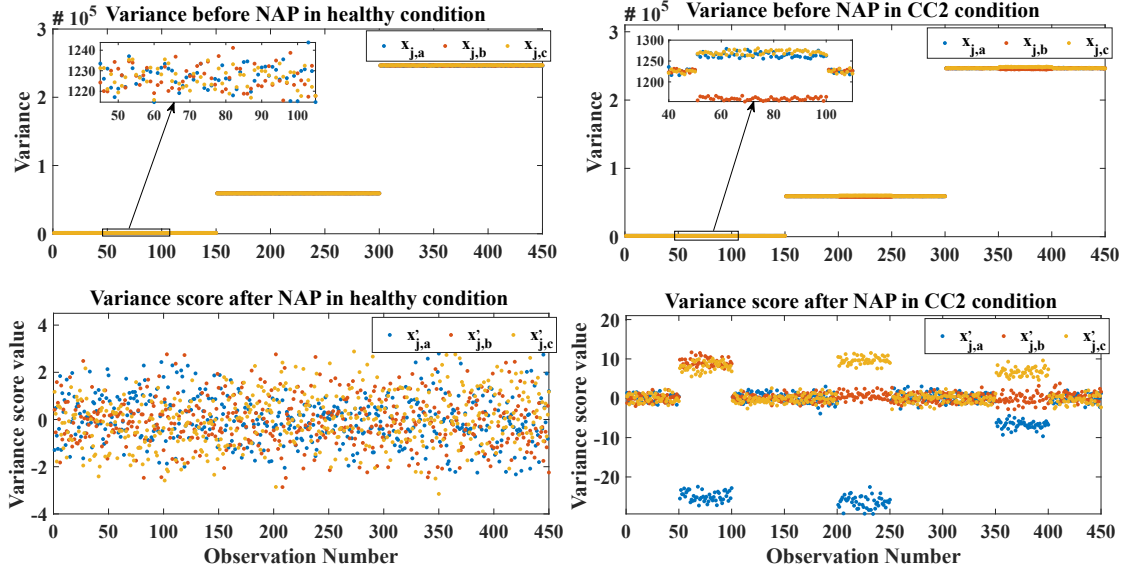


Figure 4.20: Comparison of variance features before and after NAP

Electrical machines drive systems working environments are susceptible to various kinds of noise that may come from sensor devices, power converter or environment. In the electric motor fault detection with electrical signals, the noise effect may corrupt monitoring metrics. Signal with low  $SNR$  (signal to noise ratio) may mask signal component, making it hard to extract key features for accurate fault detection and classification. Therefore, the effects of noise on the processed signals must be considered. For evaluating the performance of the proposed fault detection with noisy signal, additive white Gaussian noise with varying  $SNR$  is added to the collected signal. The choice of WGN is based on the fact that real noise is the composition of multiple weak noises and the frequency spectrum is wide. Besides, according to central-limit theorem, real noise is drawn from normal distribution. Thus, WGN may be the best approximation for any random noise [243]. To intuitively observe the influence of noise, WGN with different  $SNR$  are added to the original dataset. Adding noise to a signal is expressed as follows:

$$\hat{\mathbf{x}} = \mathbf{x} + \mathbf{wgn} \quad (4.48)$$

where  $\hat{\mathbf{x}}$  is the noisy signal and  $\mathbf{wgn}$  represents white Gaussian noise at specified  $SNR = 10 \times \log_{10} \frac{\sigma_x^2}{\sigma_v^2}$ .  $\sigma_x^2$  is the variance of the original signal, and  $\sigma_v^2$  is the variance of the Gaussian distributed noise  $v \sim \mathcal{N}(0, \sigma_v^2)$ . Figure 4.24 shows the noise-free signal and signals after adding WGN at  $SNR = 10dB$ ,  $15dB$  and  $20dB$ . The overwhelmed effect of the noisy signal on the noise-free signal as the  $SNR$  decreases can be observed. The increase of the features variable magnitude with noise level can be observed too.

To investigate the noise effect on the PCA subspaces selection, the variation of the PCA scores with the noise level is analysed. Figure 4.25 describes the percentage explained variance with respect to a number of Principal components for the noise-free data and the three noisy cases.

The threshold of cumulative variance is set to 90% to select the optimal number of features to form the principal subspace. This results in retaining the first four components for the principal subspace and the last five ones for the residual subspace. The percentage

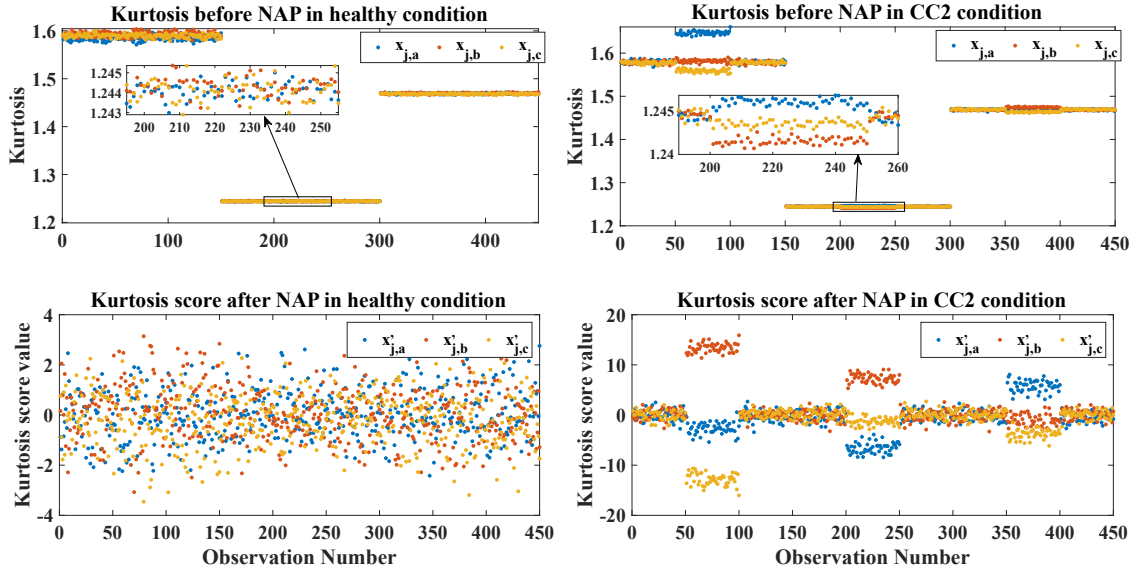


Figure 4.21: Comparison of kurtosis features before and after NAP

explained variance captured by the principal subspaces are 98.56%, 99.02%, 99.33% and 99.49% for the noise-free data, noisy data at  $SNR = 20$ ,  $SNR = 15$  and  $SNR = 10$ , respectively. The selected number of principal components to form the PCA subspaces is not affected by the noise level. We can assume that noise down to  $SNR = 10dB$  has no impact on the selected principal components in fault diagnosis with PCA.

As stated at the end the previous section, the Hotelling  $T^2$  will be used as monitoring metric. Likewise in the previous analysis, the thresholds  $T_\alpha^2$  is set at  $1 - 0.99$  confidence level. A summary of the performance of the fault detection with the NAP-based PCA in terms of  $PFA$  and  $PMD$  for the noise-free and noisy data is given in Table 4.4. The cases in which accepted thresholds are violated are still highlighted in red.

From Table 4.4, it can be seen that the fault detection performance in terms of  $PMD$  is 100% for the noise-free data while missed detections are observed for the noisy data. The  $PMD$  increases with the noise level for the incipient fault ( $CC2$ ). This shows that a lower  $SNR$  reduces the sensitivity of the detection test to small fault amplitude. In terms of  $PFA$ , acceptable performance with no violation of the threshold is observed for the noise-free data while few violations are observed for the noisy data. This shows that noise in the data can introduce features with characteristics similar to the fault signature, which may increase false alarms. This analysis shows the limited robustness of our proposed fault detection methodology to incipient faults ( $CC2$  and  $CC3$ ) in a noisy environment.



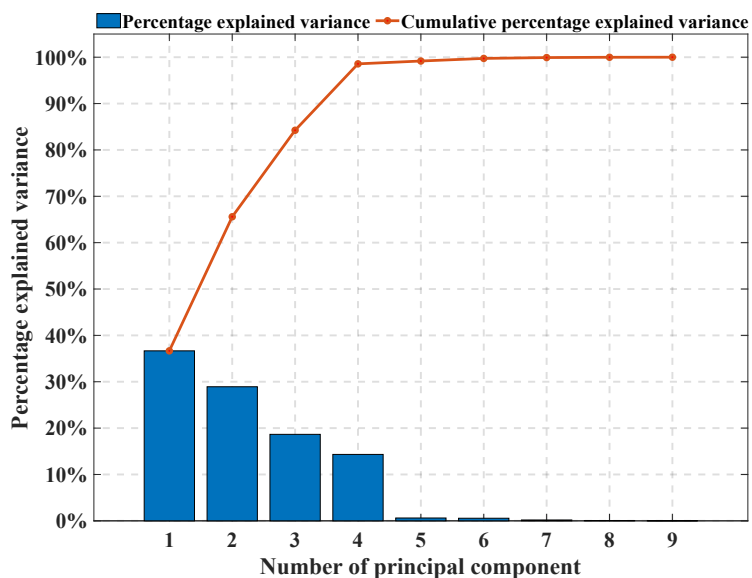


Figure 4.22: Variance captured by each principal component for the the NAP score data

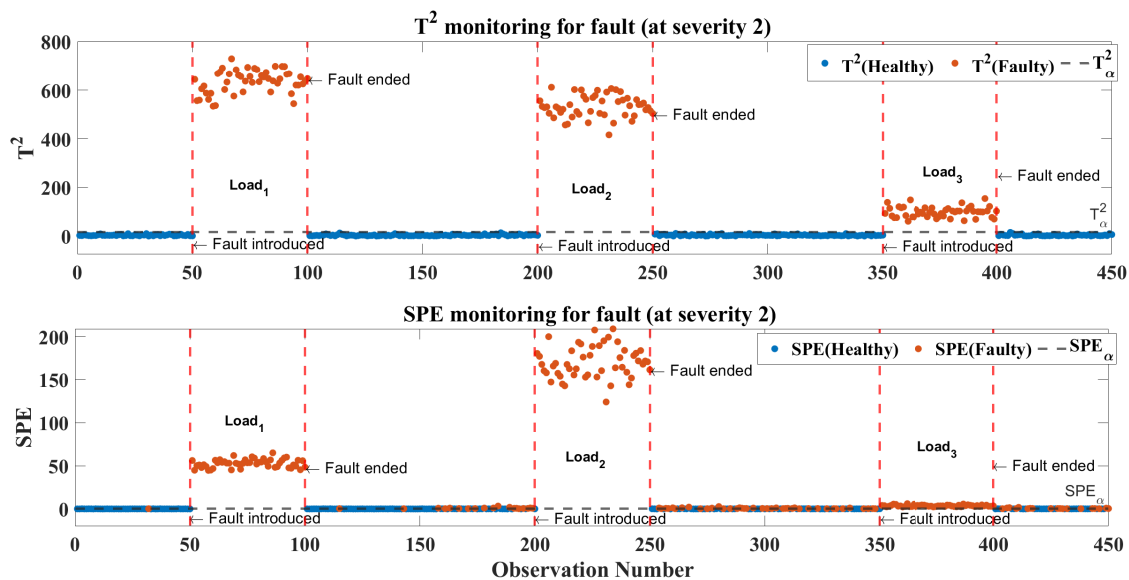


Figure 4.23: Fault level 2 detection with NAP-based PCA

**Table 4.3:** Performance evaluation of the fault detection with NAP-based PCA (values greater than the thresholds are in red)

Scenario	PFA		PMD	
	$T^2$	SPE	$T^2$	SPE
Data with $CC_2$	0.003	0.25	0	0
Data with $CC_3$	0.003	0.3	0	0
Data with $CC_4$	0	0.32	0	0
Data with $CC_5$	0	0.25	0	0
Data with $CC_6$	0	0.21	0	0
Data with $CC_7$	0.013	0.19	0	0
Data with $CC_8$	0.003	0.24	0	0

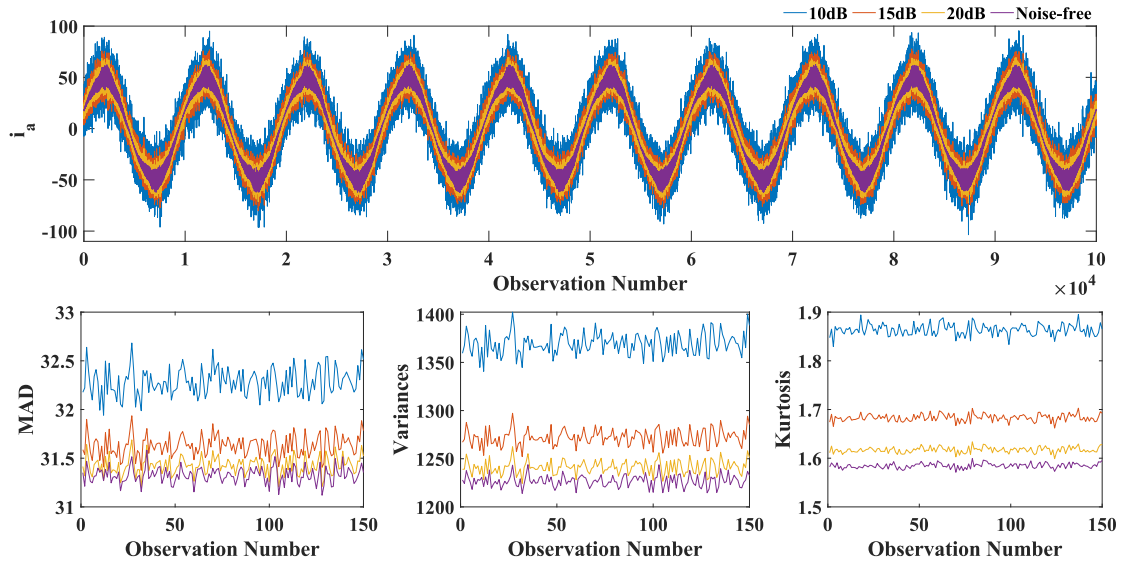


Figure 4.24: Comparison of the noise-free and noisy data and selected features

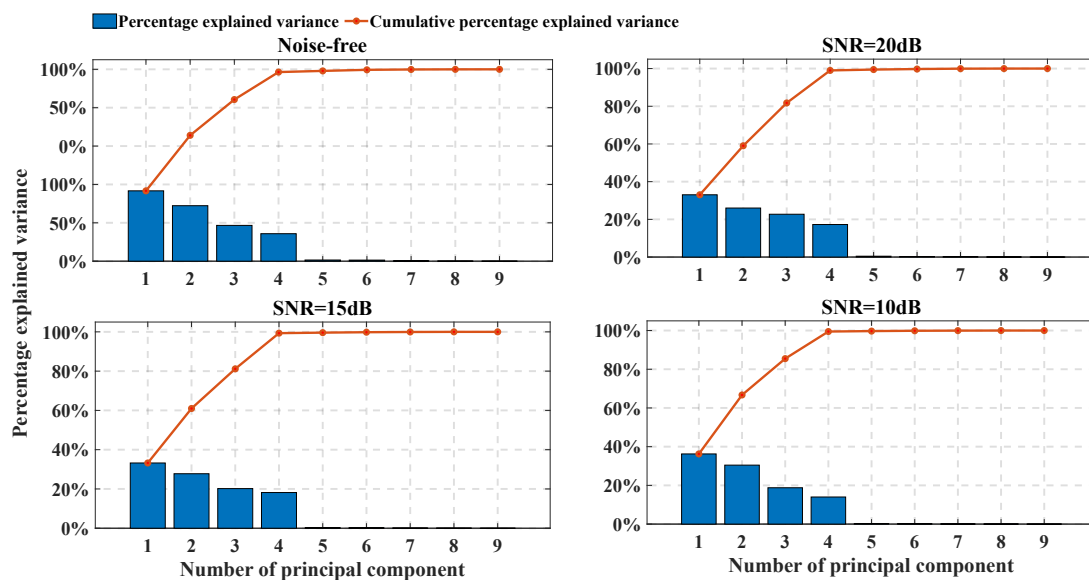


Figure 4.25: Variance captured by each principal component for the noise-free and noisy data

**Table 4.4:** Comparison of fault detection performance with noise-free and noisy data  
(values greater than the thresholds are in red)

Scenario	Noise-free		SNR=20dB		SNR=15dB		SNR=10dB	
	<i>PFA</i>	<i>PMD</i>	<i>PFA</i>	<i>PMD</i>	<i>PFA</i>	<i>PMD</i>	<i>PFA</i>	<i>PMD</i>
Data with $CC_2$	0.003	0	0.023	0.026	0.010	0.30	0.010	0.593
Data with $CC_3$	0.003	0	0.020	0	0.003	0	0.003	0.133
Data with $CC_4$	0	0	0.046	0	0.060	0	0.046	0
Data with $CC_5$	0	0	0.013	0	0.013	0	0.007	0
Data with $CC_6$	0	0	0.013	0	0.033	0	0.060	0
Data with $CC_7$	0.013	0	0.533	0	0.027	0	0	0
Data with $CC_8$	0.003	0	0.033	0	0.020	0	0.033	0

## 4.7 Inter-turn fault severity estimation

Determining the severity levels of identified faults is one of the crucial operations of the diagnosis. Indeed, it allows making the appropriate safety decision. The CUSUM decision function has proven to be an effective tool for estimating the severity of faults in electrical systems [244]. Once the defect is detected, the estimation of the severity level is obtained by the inversion of the analytical model of the evolution of the slope of the CUSUM decision function.

Let us consider  $\mu_{T_0^2}$  the mean value of the monitoring metric  $T^2$  under healthy conditions. As it can be noticed in Figure 4.23 it deviates when a fault is introduced. Let  $\mu_{T_1^2}$  be the new mean value. Assuming that the variance  $\sigma_{T^2}^2$  is constant, the instantaneous likelihood ratio  $s(i)$  of the  $i^{th}$  observation of the distribution of  $T^2$  is given as follows [213]:

$$s(i) = \frac{\mu_{T_1^2} - \mu_{T_0^2}}{\sigma_{T^2}^2} \left( T^2(i) - \frac{\mu_{T_1^2} + \mu_{T_0^2}}{2} \right) \quad (4.49)$$

The CUSUM function  $S_N$  for the  $N$  observations of  $T^2$  and the CUSUM decision law  $\mathbf{D}_{S_N}$  are given as follows [213]:

$$S_N = \sum_{i=1}^N s(i) \\ \mathbf{D}_{S_N} = \left( S_{N_i} - \min_{1 \leq t \leq i} (S_{N_t}) \right) \quad (4.50)$$

A fault is detected when  $\mathbf{D}_{S_N}$  is greater than the threshold  $T_\alpha^2$ . The top of the Figure 4.26 shows a clear change in the  $T^2$ , despite fluctuations, while the bottom of the figure shows the evolution of the CUSUM decision function for the fault level 2. The latter also represents a relevant fault indicator too. The time occurrence of the faults and the actual time the fault is detected are shown. The fault is detected without any delay. The CUSUM monitoring gives the same performance of fault detection as the one with the  $T^2$  monitoring shown in Table 4.4.

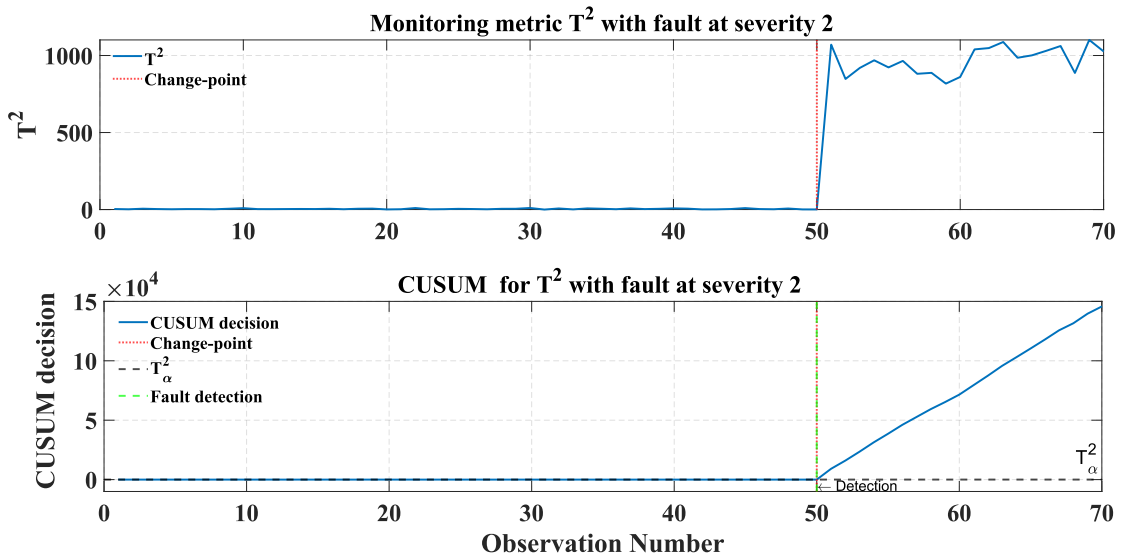


Figure 4.26: CUSUM for fault monitoring

The severity of the faults varies from 0.25 to 1, corresponding to the number of short-circuited turns from 2 to 8. Figure 4.27 shows the evolution of the slope of the CUSUM decision function as a function of fault severity for the three load conditions. It can be observed that the slope of the decision function increases monotonically with the severity of the defect regardless of the mechanical load. Therefore, it is a relevant characteristic that can be used to estimate the fault severity.

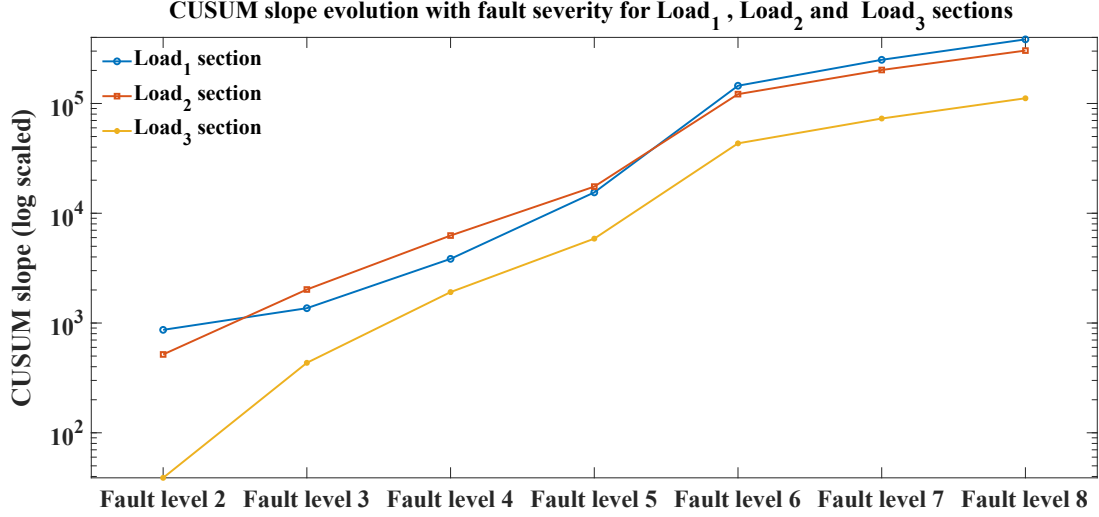


Figure 4.27: Slope of CUSUM decision function

The different evolutions of the CUSUM slope with the load level can also be observed in the figure. This is due to the difference in the fault signature with the load level. This makes the load level label an essential input information for the fault estimation with CUSUM slope. For the three load sections, the evolution of the slope of the CUSUM decision  $dS_N$  as a function of fault severity  $f$  can be approximated by an exponential function as follows:

$$dS_N = ae^{b \times f} \quad (4.51)$$

where  $a$  and  $b$  are coefficients determined from the three load sections. Figure 4.28 shows the evolution of the actual and analytical approximation of  $dS_N$  for the three load sections. An exponential fitting approach consisting of weighted sums of exponential functions with slowly varying weight functions has been applied to get the approximated coefficients  $a$  and  $b$  for the three loads. The approximated exponential functions  $y_{Load1}$ ,  $y_{Load2}$  and  $y_{Load3}$  are shown in Equation 4.52.

$$\begin{aligned} y_{Load1} &= 59.844e^{9.238 \times x} \\ y_{Load2} &= 70.583e^{8.942 \times x} \\ y_{Load3} &= 6.311e^{10.644 \times x} \end{aligned} \quad (4.52)$$

The accuracies of the approximated exponential functions are evaluated through the characterization of the difference between the actual and the estimated severities with the normalized root mean square error (NRMSE). For a quantity measurement  $\mathbf{y}$  and its estimated  $\tilde{\mathbf{y}}$  the *NRMSE* is expressed as:

$$NRMSE = \frac{\sqrt{\frac{\sum_{i=1}^N (y_i - \tilde{y}_i)^2}{N}}}{\bar{y}} \quad (4.53)$$

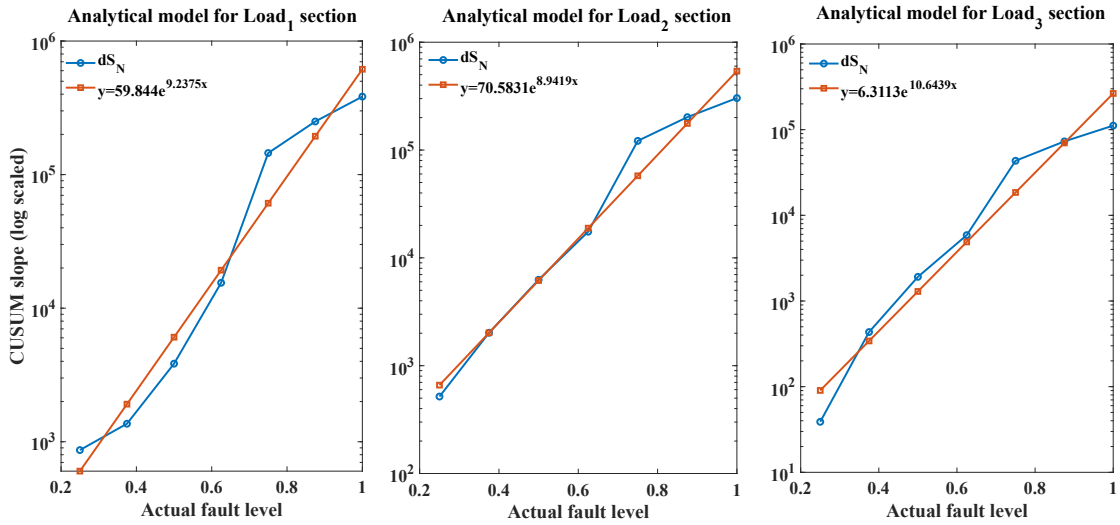


Figure 4.28: Analytical approximation of  $dS_N$

where  $y_i$  and  $\tilde{y}_i$  are the  $i$ th observations of the actual and estimated quantity, respectively.  $N$  is the number of observations and  $\bar{y}$  is the mean value of the actual quantity. The results are:  $NRMSE = 0.0059$ , for  $Load_1$ ,  $NRMSE = 0.0031$ , for  $Load_2$ , and  $NRMSE = 0.0036$ , for  $Load_3$ . This results correspond to a very good performance of the exponential approximation of  $dS_N$  curves. For each fault case with the load level label known, once the CUSUM slope is computed, the severity can be estimated by inverting the exponential function. To evaluate the effect of the interference of noise on the fault estimation, the fault severities have been first estimated for different fault levels for the noise-free and noisy data. Figure 4.29 shows the estimated fault levels and the actual fault level of the noise-free data and for noisy data with  $SNR = 40dB$ . Larger deviations of the estimations from the actual fault levels for the noisy data can be observed.

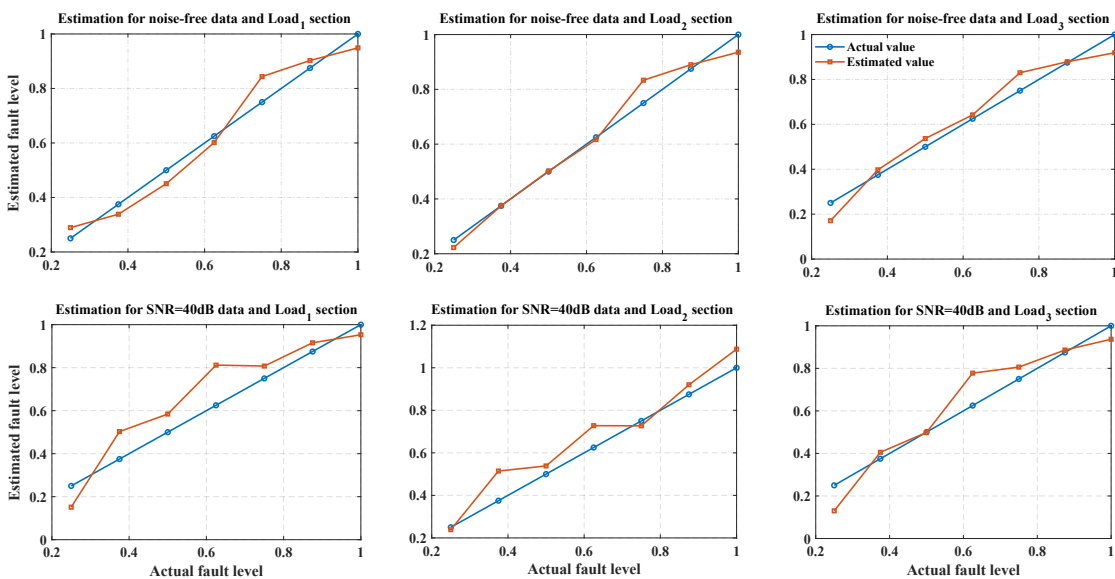


Figure 4.29: Fault severity estimation

Figure 4.30 shows the evolution of the fault estimation performance in terms of NRMSE with the noise level. The increase of the NRMSE with the noise level can be observed. These results show that the performance of the fault estimation degrades with increasing the noise level. The degradation of the performance becomes significant for  $SNR < 30dB$

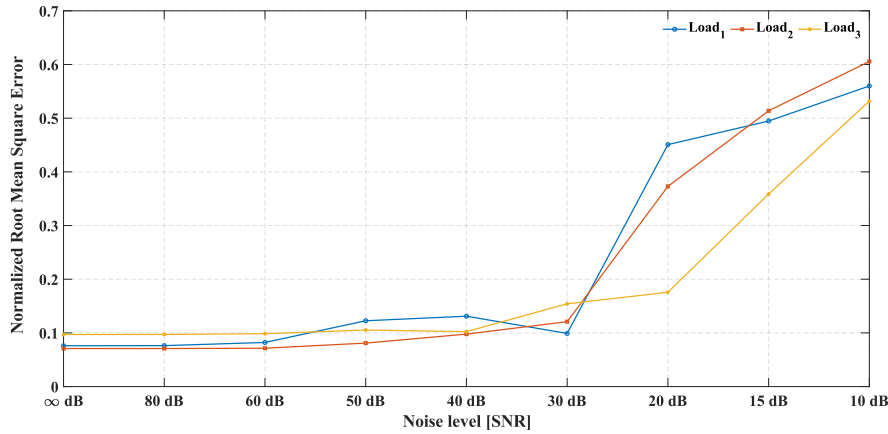


Figure 4.30: Fault estimation and noise interference

## 4.8 Conclusion

In this chapter, univariate and multivariate statistical methods for fault detection and diagnosis have been reviewed. The different performance evaluation of these methods have been presented too. A case study of inter-turn short-circuit detection is proposed. A dataset composed of healthy and faulty stator currents (from incipient to the severe fault cases) at three different load levels has been built. At the data preprocessing stage, sliding window Median Absolute Deviation (MAD), variance, skewness and kurtosis have been proposed for feature extraction. Through the analysis of the fitting normal distributions of the features, the MAD, variance and kurtosis have been selected for fault diagnosis as they show more discriminant capacity for the fault detection. A NAP-based PCA has been proposed to eliminate the effects of load variations in the non-stationary conditions due to the load change operations. This helped to develop a fault detection regardless of the load change in non-stationary conditions. The fault detection performance analyses helped to set the Hotelling  $T^2$  as the monitoring metric for the inter-turn fault detection with PCA. The robustness of our proposed fault detection methodology noise interferences showed some weakness for incipient faults. An analytical model of the slope of the CUSUM decision function is derived, from which the fault severity is estimated. The faults with noise-free data have been estimated with accuracy higher than 99%. The robustness of the fault estimation has been tested too and showed robustness to noise for  $SNR$  greater than  $30dB$ . A limitation of this fault estimation is its requirement of the load level label as the fault signature varies with the load level. This limitation can be overcome with an efficient classification tool that discriminates the load level and the fault severity. The robustness of the fault estimation can be improved by filtering the noise before the fault detection.



## Chapter 5

# General Conclusion

### 5.1 Conclusion

This thesis was devoted to examining approaches for the detection and diagnosis of faults affecting electric motors within an electric powertrain. The main objective of this study was to develop a fault detection methodology intended to be integrated into a predictive maintenance system for the electric drive system of electrified vehicles. The targeted exploration of existing opportunities in electric motor condition monitoring has made it possible to identify previously unexplored areas in applications related to electrified vehicles. These uninvestigated areas include:

- the ability to diagnose faults without additional sensors than those already present in the device,
- the ability to perform the diagnosis regardless of the varying operating conditions,
- and the ability to perform diagnosis in closed-loop operation.

However, for automotive applications, more advanced signal processing techniques may be required to cope with the large fluctuations in operating conditions. Therefore, the majority of reports present in the literature opt for a combination of results from several distinct sensors and different processing methods to meet this requirement. The distinctive feature of our proposed approach lies in its exclusive focus on motor stator phase currents to address this challenge.

Based on identified research gaps, we defined the scope of our project with the following objectives:

1. Build a model of the motor that is accurate enough to model fault characteristics, yet fast enough to be integrated with the other drive system components, including the inverter and controllers.
2. Select the optimal statistical analysis methodology for processing stator phase current data to extract fault signatures independent of the motor operational state.
3. Develop a fault detection methodology with the ability to detect a fault and estimate its severity, regardless of the operational state of the motor and the noise interference on the motor stator currents.

To achieve these objectives, a preliminary research phase was undertaken, consisting of an exhaustive review of the most recent academic publications, reference works, and relevant

industrial publications. This approach aimed to gain an in-depth understanding of the current state of fault detection and diagnostic technologies, as well as motor drive system modeling for fault detection. The general introductory section demonstrated in a methodical way how predictive maintenance systems bring important benefits to owners of electric vehicles. These systems have been rigorously established to accurately anticipate maintenance needs, allowing vehicle owners to proactively troubleshoot issues with their vehicles. Benefits of this approach include reduced downtime, lower maintenance costs, improved safety, increased vehicle performance, and a significant reduction in carbon footprint.

In Chapter 2, a review was carried out on the motor technologies used for electric powertrains, the electric motor faults statistics, and the different fault detection methodologies. Critical discussions of the review topics have been provided too. Because of the lack of appropriate data on motor drive system failure in electrified vehicles throughout the literature, the need to build synthetic data arises. An adaptive motor drive system modeling is one of the solutions to help collect data that will be used for the fault prediction session. The most serious issue in this part of the research has been the lack of reliability and maintenance information on electrified vehicle motor drive systems. The youth of the technology and the reluctance of manufacturers to divulge and share sensitive data, have been the main causes for the scarcity of this information. This issue could be resolved by researching information from similar technologies, more mature than electrified vehicles, but with comparable run conditions and operations.

To achieve the intended **objective (1)**, a comparative study was undertaken in chapter 3 to evaluate three main methods of modeling electric motors, namely models based on coupled circuits, models based on numerical methods, and hybrid models. Regarding the accuracy, it appeared that models based on coupled circuits show relatively lower performance compared to the best results obtained with numerical models. However, when it comes to computational capabilities, circuit-based models outperform numerical ones. To satisfy the accuracy and computational capability requirements of electric motors for fault diagnosis purposes, the hybrid model was found to be the optimal choice. As part of our study, we developed a hybrid model for a PMSynRM by combining a finite element model with an analytical model. The initial design of the PMSynRM was carried out and simulated using FEMM software, allowing the calculation of inductances under healthy and faulty conditions. The values of the calculated inductances were then stored in multidimensional lookup tables, which were integrated into the analytical model based on the three-phase inductance. The validation of this hybrid model was carried out by comparing its results with experimental data obtained under healthy operating conditions and reached an accuracy higher than 70%. Furthermore, as part of our study, we developed a model of the machine taking into account inter-turn short-circuit and dynamic eccentricity scenarios. An analysis of PMSynRM parameters under faulty conditions identified stator currents as relevant and effective indicators for fault diagnosis.

To meet **objectives (2) and (3)**, an investigative study was undertaken to examine current trends in the field of fault diagnosis. With respect to modern electric motor drives, it has been found that conventional fault monitoring techniques are not always effective. This is due to the high levels of noise, dynamics, and closed-loop operations, all of which can mask fault signatures. To address the need for more robust diagnostic methods, we chose statistical analysis techniques because of their ability to model data, capture behaviors, and organize the information into concise rules and metrics. We reviewed univariate

and multivariate statistical methods for fault diagnosis to assess their suitability for our purposes of inter-turn fault detection. Preliminary steps were to define a data set including healthy and faulty stator currents, covering a range of faults from incipient to more severe. Data preprocessing techniques like sliding windows median absolute deviation (MAD), variance, and kurtosis were selected to extract relevant features from our dataset.

For fault analysis, we opted for principal component analysis (PCA), a method widely adopted in fault diagnosis due to its data compression characteristics and its ability to highlight correlations between data variables, without requiring prior knowledge. To achieve our goals, we proposed an extension version of PCA based on Nuisance Attribute Projection (NAP), allowing us to filter out the non-stationarity in the data due to load variation. This made it possible to develop fault detection independent of load variations. After analyzing the fault detection performance, we selected Hotelling's  $T^2$  as a reliable monitoring metric for inter-turn fault detection with PCA. The robustness of our proposed fault detection methodology to noise interference was assessed and has revealed some limitations in detecting incipient faults.

We looked at analytical and artificial intelligence methods for our last goal, which is to estimate the fault severity. We chose an analytical method due to the limited data availability for our study. We developed an analytical model of the slope of the CUSUM decision function of the monitoring metric  $T^2$  to estimate the fault severity. From this analytical model, we made fault estimation on noise-free data with an accuracy exceeding 99%. We also tested the robustness of our defect estimation method against noise interference, which showed resistance to noise when the signal-to-noise ratio ( $SNR$ ) was less than 30  $dB$ . A limitation of this fault estimation method is the need for a load level label, as the fault signature is sensitive to the load variation.

## 5.2 Contribution

This research project has made a substantial contribution to the field of fault detection and diagnosis, particularly concerning the modeling of electric motor drive systems for fault diagnosis, as well as the use of statistical methods for fault diagnosis. It has generated new knowledge and in-depth understanding that stands out for its originality. The main contributions to the advancement of knowledge are listed below:

### 1. International Conference paper

**Title:** Stator winding Inter-turn short-circuit and air gap eccentricity fault detection of a Permanent Magnet-Assisted Synchronous Reluctance Motor in Electrified vehicle.

**Authors:** Pakedam Lare, Siyamak Sarabi, Claude Delpha, Andre Nasr and Demba Diallo.

**Conference:** 2021 International Conference on Electrical Machines and Systems, Gyeongju, Korea, from October 31 to November 3, 2021 [245].

### 2. National Conference paper

**Title:** Modelling of a PMA-SynRM for the detection of inter-turn short-circuit.

**Authors:** Pakedam Lare, Siyamak Sarabi, Claude Delpha and Demba Diallo.

**Conference:** Conférence des Jeunes Chercheurs en Génie Electrique,(JCGE 2022), Le Croisic, France, from June 14 to 17 June, 2022 [246].

### 3. International Conference paper

**Title:** A PMSynRM stator winding fault detection approach using an optimized PCA-based EWMA control scheme.

**Authors:** Pakedam Lare, Siyamak Sarabi, Claude Delpha and Demba Diallo.

**Conference:** 2023 IEEE 32nd International Symposium on Industrial Electronics (ISIE), Helsinki, Finland, from June 19 to June 21, 2023 [247].

### 4. International Conference paper (Accepted for publication)

**Title:** Diagnosis of stator windings short-circuits with PCA and Nuisance Attribute Projection.

**Authors:** Pakedam Lare, Siyamak Sarabi, Claude Delpha and Demba Diallo.

**Conference:** IECON 2023: the 49th Annual Conference of the IEEE Industrial Electronics Society (IES), Singapore, from October 16 to October 19, 2023.

## 5.3 Perspectives

Further research is underway to improve the performance of the fault estimation approach, independent of the load level label. Investigations are underway to explore other analytical methods and artificial intelligence approaches suitable for the limited size of our dataset. At the same time, efforts are being made to expand our dataset by developing reliable methods for generating synthetic data, thereby paving the way for the exploration of artificial intelligence-based techniques.

### 5.3.1 Improvement of the electric powertrain modelling for fault diagnosis

To refine the powertrain model used in fault diagnosis, improvements are needed in engine modeling. Currently, we have used a 2D finite element model for simplicity, but it is envisaged to complement this model by including the estimation of the end-windings inductances using a 3D finite element model. Additionally, magnetic saturation effects were neglected in the analysis for simplicity. An analysis taking these effects into account could improve the model accuracy, especially under high load conditions, which has not been explored in our study. For in-depth and effective monitoring of electric powertrain faults, the development of more advanced techniques to detect various types of faults in all powertrain components is essential. The fault diagnosis can also be challenging when multiple faults cause overlapping features. Our results showed that stator phase currents are potential indicators of motor mechanical and electrical faults. Further analysis of these fault indicators, aimed at detecting other types of powertrain faults ((inverter, DC bus capacitor, sensors, etc), would be highly beneficial.

In our previous study, we sought to contribute to the collection of data relating to the diagnosis of electric motor faults in the context of electrified vehicles. However, due to limitations in technical resources, we were restricted to generating experimental data for the healthy mode of operation of the PMSynRM. We have developed a specification of the resources required for carrying out experimental tests on the motor in the presence of inter-turn faults and dynamic eccentricity. To design a test bench aimed at analyzing short-circuit and eccentricity faults, we considered two distinct approaches. For the short

circuit fault, we examined the feasibility of using an electric motor whose configuration allows access to the windings, to which connectors would be attached to delimit the winding turns. These connectors would serve as connection points for a device aimed at setting short circuit faults, with a contact resistance varying depending on the number of turns shorted-circuited. To design the eccentricity fault, we considered the possibility of emulating the fault by replacing the motor original bearing with another bearing in with noncoaxial inner and outer rings. This eccentricity withing the bearing could be modulated to reproduce the eccentricity defect with the desired severity level. Further studies are required to define the test bench configuration to conduct other fault analyses on different motor technologies used in electric powertrains.

### **5.3.2 Methodology improvement toward fault prognosis**

The fault diagnosis and prognosis represent the essential foundations of a predictive maintenance strategy in applications, where critical importance is given to safety, reliability, and availability. Regarding the objective of this PhD work, to provide a methodology to accomplish both fault diagnosis and prognosis, it should be noted that the work has been limited to the accomplishment of the first task.

Our contribution includes first in the choice of a data-driven approach over the system model-based one, which requires an in-depth knowledge of the system. The adoption of the system model-based approach would have required the identification and experimental validation of fault variables. This task is often complex and difficult to generalize, given that it typically involves long-term experiments under controlled conditions that do not necessarily reflect real situations. Our data-driven approach only requires direct monitoring of motor stator current signals. Second, our contribution extends to feature selection and derivation of the  $T^2$  statistic as an early fault detection metric, thus enabling early identification of faulty components. These steps are of particular importance in the context of fault prognosis. The next phase of the prognosis methodology involves the building of a model aimed at predicting the occurrence of a fault and estimating the time before the failure occurrence. Our attempt to accomplish this has been with an analytical model of the slope of the CUSUM decision function of the monitoring metric  $T^2$  to estimate the fault severity. This attempt is attractive for its simplicity but needs further improvement to address its weaknesses regarding its requirement of load level information and limited robustness to noise interference.

Another approach at this stage is the use of machine learning models, which are available across different learning domains. These models can be supervised, in the case where sufficient quality historical data are available, or unsupervised, when little or no historical data are available. In our context, the unsupervised version is more appropriate due to the lack of data available in adequate quantities and the resulting economic considerations. Among the approaches commonly used in unsupervised learning, clustering is one of the most frequent. This method consists of grouping the response variables into clusters defined either by the user, or models based on distance, model, density, or class.

## Résumé en français

Le début du XXI<sup>e</sup> siècle a été marqué par une transformation significative de l'électricité dans toutes les applications embarquées. Des progrès notables ont été réalisés grâce à l'adoption croissante de véhicules électrifiés. Ces véhicules constituent une solution pour atténuer la pollution environnementale résultant du transport routier et pour répondre aux préoccupations concernant la hausse des coûts du pétrole brut. L'utilisation généralisée des véhicules électrifiés a donné lieu à des problèmes de coûts de matériels, nécessitant l'adoption d'une optimisation de la conception pour réduire les dépenses, la masse et le volume. Au-delà de la réduction du poids et de la compacité, d'autres défis majeurs auxquels est confrontée l'industrie automobile électrique comprennent l'amélioration de l'efficacité, la réduction des coûts de fabrication et la garantie de la disponibilité et de la fiabilité.

Dans le groupe motopropulseur électrique, les composants électromécaniques sont principalement constitués de machines électriques. La machine et ses éléments d'entraînement moteur sont fréquemment soumis à des cycles transitoires répétés, provoquant des contraintes mécaniques et thermiques. Un défaut au sein d'un composant peut se propager, entraînant une efficacité opérationnelle réduite et engendrant des coûts supplémentaires pour les procédures de diagnostic et les actions correctives. De plus, cela peut compromettre le fonctionnement du véhicule et la sécurité des passagers [3]. Par conséquent, il est primordial de remédier de manière préventive aux pannes du système pour garantir la sécurité et la fiabilité des véhicules électriques.

Les méthodologies de maintenance traditionnelles, en raison de leur inefficacité et de leurs coûts élevés, peuvent conduire à des incidents inattendus et des périodes prolongées d'immobilisation des véhicules. Heureusement, les systèmes de maintenance prédictive sont entrain de changer la donne. En tirant parti des techniques analytiques avancées et l'exploration de données en temps réel, ces systèmes s'avèrent capables d'identifier les besoins de maintenance avec une précision exceptionnelle. Dans les véhicules électrifiés, il s'agit d'une surveillance et d'une analyse continue des paramètres (électriques, vibratoires, de température, etc). L'analyse des signaux électriques est de plus en plus appliquée aux moteurs électriques, à cause de son caractère non intrusif et sa viabilité technique et économique.

L'objectif principal de ce travail de thèse est de développer une méthodologie structurée pour le déploiement de techniques de maintenance prédictive pour les machines électriques synchrones utilisées dans le groupe motopropulseur électrique [6]. L'accent a été mis sur les défauts de court-circuit inter-spores pour leur pertinence pour éviter la plupart des défauts des entraînements de moteurs électriques. Pour la modélisation du groupe motopropulseur, nous avons développé un modèle hybride de la moteur Synchro-réductant assisté par aimant permanent (MSRAP)) en combinant son modèle analytique et son modèle éléments finis. Une validation a été réalisée en comparant les caractéristiques du modèle

avec celles mesurées sur le banc expérimental. Une analyse approfondie des perspectives existantes dans le domaine de la surveillance de l'état des moteurs électriques a conduit à l'identification de lacunes dans le domaine de recherche lié aux applications des véhicules électrifiés. Ces lacunes comprennent :

- l'absence de diagnostic des défauts tenant en compte les différentes conditions de fonctionnement des moteurs électriques dans les véhicules électrifiés,
- l'absence de diagnostic des défauts du moteur dans les entraînements en boucle fermée.

Pour combler cette lacune, nous avons proposé une méthodologie permettant de détecter les courts-circuits inter-spores du stator d'un moteur électrique avec charge variable et en boucle fermée. L'exploitation des signaux des courants statoriques qui sont déjà disponibles dans l'unité de contrôle est choisie comme approche pertinente pour construire un outil de diagnostic embarqué pour la détection de défauts.

Le **chapitre 2** a montré une considération générale et un aperçu de l'importance de détection de défauts dans les groupes motopropulseurs des véhicules électriques. Il représente un point de vue global du sujet où les derniers articles académiques, ouvrages de référence et les publications industrielles ont été étudiées. Ceci pour une compréhension plus détaillée de la l'état de l'art des technologies de détection et de diagnostic des défauts dans les groupes motopropulseurs des véhicules électriques. L'accent a été mis sur :

- La description de la structure d'un groupe motopropulseur typique d'un véhicule électrique, y compris les composants mécaniques, électriques et de contrôle.
- La description de la structure et des opérations de chaque composant du système avec une focalisation sur le moteur électrique et le convertisseur de puissance.
- Une classification des différentes méthodologies de détection et de diagnostic des défauts, leurs avantages et inconvénients.

Les investigations menées dans [57] et dans [58] ont montré que la répartition des défauts dans les machines électriques est liée à leurs tailles (Figure 5.1). Elle a montré que, pour les machines haute tension, les défauts statoriques sont les défauts prédominants et représentent les deux tiers du taux total de défauts. Les véhicules électriques fonctionnant avec des moteurs à haute tension, pour ça, ce travail s'est focalisé sur les défauts de court-circuit inter-spores pour leur fréquence d'apparition et leur pertinence pour éviter la plupart des défauts des moteurs électriques. Une revue des méthodologies de pointe pour la détection et le diagnostic des défauts a permis d'identifier cinq étapes principales pour effectuer une détection de défauts. Un organigramme de de la procédure généralisée de détection et de diagnostic des défaut est présenté à la Figure 2.20. La première étape est la modélisation qui consiste à construire des connaissances. Le modèle peut être basé sur des relations analytiques, une description du langage ou données historiques. La deuxième étape consiste à prétraiter les données brutes dans le domaine d'information le plus approprié pour extraire les caractéristiques de sensibilité aux défauts ou des signatures à la troisième étape. La quatrième et la cinquième étapes sont dédiées à l'analyse des caractéristiques pour prendre la décision finale sur les états de santé.

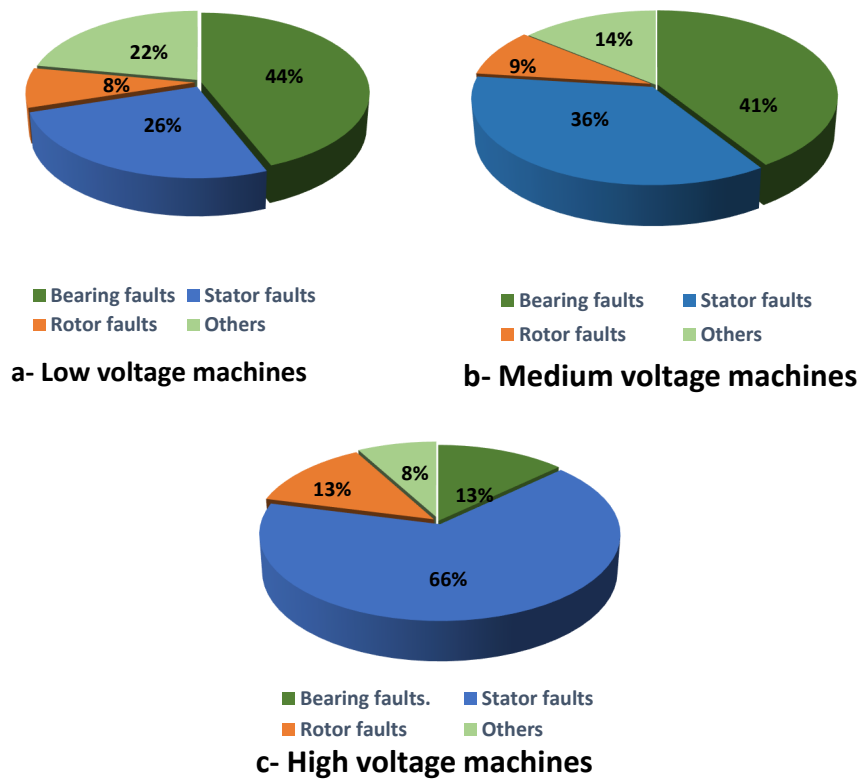


Figure 5.1: Statistiques des défauts des composants des machines électriques:  
 a- Machines basse tension, b- Machine moyenne tension et  
 c- Machine haute tension [60, 61, 59]

En raison du manque de données appropriées sur les défauts du système de motorisation des véhicules électrifiés dans la littérature, nous avons choisi de générer des données synthétiques à partir de la simulation d'un modèle suffisamment précis du système de motorisation. Dans le **chapitre 3**, une étude comparative a été entreprise pour évaluer trois méthodes principales de modélisation des moteurs électriques, à savoir les modèles basés sur des circuits couplés, les modèles basés sur des méthodes numériques et les modèles hybrides. Concernant la précision, il est apparu que les modèles basés sur des circuits couplés montrent des performances relativement inférieures par rapport aux meilleurs résultats obtenus avec les modèles numériques. Cependant, en termes de temps de calcul, les modèles basés sur des circuits sont moins coûteux que les modèles numériques. Pour satisfaire les exigences de précision et de capacité de calcul des moteurs électriques à des fins de diagnostic des défaut, le modèle hybride s'est avéré être le choix optimal. Dans le cadre de notre étude, nous avons développé un modèle hybride d'un MSRAP en combinant son modèle éléments finis avec son modèle analytique. La conception initiale du MSRAP a été réalisée et simulée à l'aide du logiciel FEMM, permettant le calcul des inductances en conditions saines et en défaut. Les valeurs des inductances calculées ont ensuite été stockées dans des tabulation Lookup Table (LUT), qui ont été intégrées au modèle analytique basé



sur les fonctions des inductances dans le référentiel triphasé. La validation de ce modèle hybride a été réalisée en comparant ses résultats avec des données expérimentales obtenues dans des conditions saines de fonctionnement et a atteint une précision supérieure à 70%. De plus, dans le cadre de notre étude, nous avons développé un modèle de la machine considérant des scénarios de court-circuit inter-tours et d'excentricité dynamique. Une analyse des paramètres du MSRAP dans des conditions de défauts ont permis d'identifier les courants statoriques comme des indicateurs pertinents et efficaces pour le diagnostic de ces défauts modélisés. L'organigramme de l'approche de modélisation proposé est présenté à la Figure 5.2.

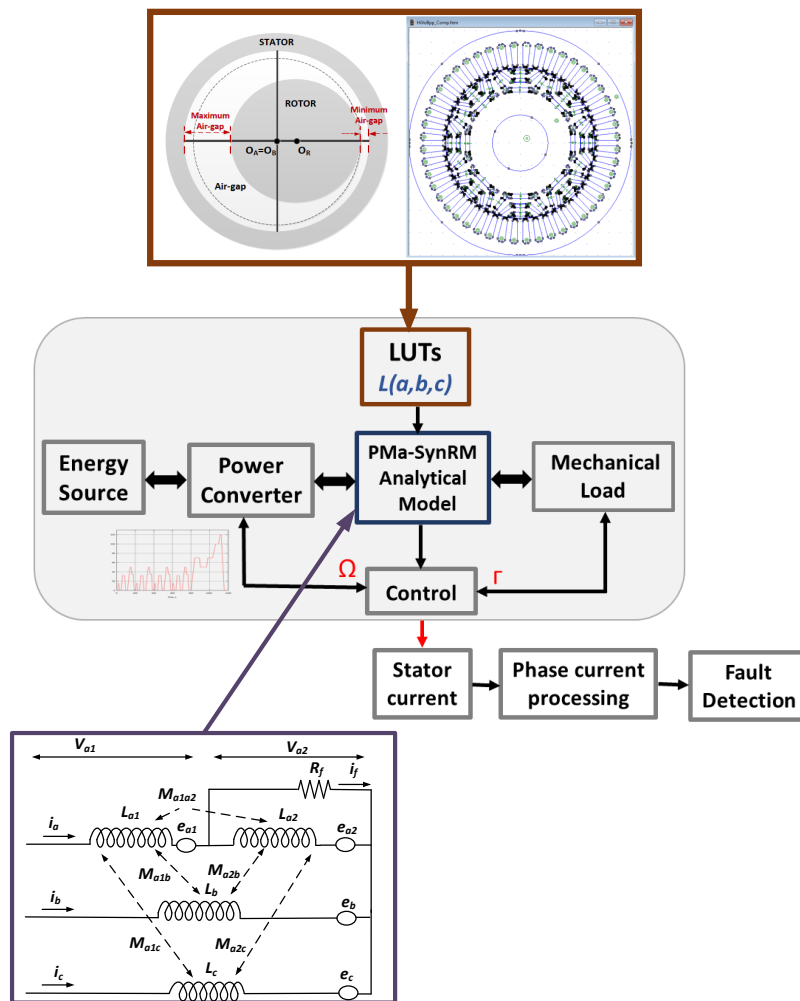


Figure 5.2: Représentation schématique de la modélisation du système de traction électrique

Dans le **chapitre 4**, une étude d'investigation a été entreprise pour examiner les tendances actuelles dans le domaine du diagnostic des défauts pour les applications récentes de moteurs alimentés par des onduleurs. En ce qui concerne les moteurs électriques modernes en industrie, il a été constaté que les techniques conventionnelles de surveillance d'état de santé ne sont pas toujours efficaces. Cela a créé la nécessité de développer des dispositifs de diagnostic de défaut universels, valables pour toutes les applications et adaptés à une var-

ité de contextes opérationnels. Les techniques d'analyse statistique émergent comme une alternative à l'analyse conventionnelle du signal de courant moteur connu sous l'acronyme (MCSA: Motor Current signal Analysis) valable pour les moteurs alimentés par le secteur [206]. L'une des caractéristiques les plus essentielles des méthodes d'analyse statistique est leur capacité à modéliser les données pour capturer le comportement et à organiser ces informations dans un ensemble concis de règles ou de mesures. Ils consistent à surveiller les statistiques des variables de données ainsi que les limites de contrôle. Nous avons examiné les méthodes statistiques suivantes pour le diagnostic des défauts afin d'évaluer leur adéquation à nos objectifs de détection des défauts de court-circuit inter-spores.

- **Méthodes statistiques univariées** qui incluent les graphiques de Shewhart, les tracés de somme cumulée connu sous l'acronyme (CUSUM) et la moyenne mobile à pondération exponentielle connu sous l'acronyme (EWMA). Ces méthodes de surveillance d'état de santé abordent l'analyse de variables individuelles. Par conséquent, toute information résultant d'interactions variables est ignorée.
- **Méthodes statistiques multivariées** qui incluent l'Analyse des composantes principales (ACP) et Analyse des composantes indépendantes (ACI), ont été largement utilisés dans les applications de détection de défauts. L'objectif de l'ACP est de représenter un variable en fonction de plusieurs facteurs sous-jacents. L'ACP peut effectuer la réduction de dimension des données: bien que l'ensemble de données d'origine puisse contenir  $n$  variables, il arrive souvent qu'une grande partie de la variabilité puisse être expliquée par un plus petit nombre  $l$  de composantes principales. Ce qui permet de définir deux sous espaces: le sous espace principal qui est composé des  $l$  premières composantes principales et le sous espace résiduel qui est composé du reste des composantes principales. L'ACP aide à l'interprétation des données : des relations auparavant insoupçonnées peuvent généralement être identifiés via l'ACP.

La détection des défauts par les méthodes multivariées peut être réalisée par l'analyse de deux mesures couramment utilisées et les plus connues qui sont la statistique  $T^2$  et l'erreur quadratique de prédiction  $SPE$ . La statistique  $T^2$  est une mesure de variation au sein d'un modèle l'ACP calculée par la somme des scores des variables de des données projetés dans le sous espace principal. La statistique  $SPE$  d'autre part, est calculée par la projection des variables de des données dans le sous espace résiduel. La modélisation de l'ACP est basée sur l'hypothèse d'une normalité des données pour calculer les mesures statistiques de surveillance, tandis que celle de l'ICA est basée l'hypothèse que les données ne sont pas normalement distribuées. Les deux méthodes sont basées sur des hypothèses fortes sur la distribution des données, ce qui limite leur performance dans leurs applications dans le monde réel [220]. Le CUSUM et l'EWMA peuvent également être étendu au processus de surveillance statistique multivariés. Les formes étendues sont appelées : CUSMU Multivarié (MCUSUM) et EWMA Multivarie (MEWMA) respectivement.

Le modèle hybride développé du système d'entraînement motorisé au chapitre 3 a servi comme banc de test virtuel pour émuler les défauts et générer des données synthétiques pour le diagnostic des défauts. De la modélisation du système en mode sain et dans les différentes conditions de défaut, les courants de phase du stator ont été désignés comme indicateurs de défauts inter-spores. Le modèle hybride du moteur Le système d'entraînement

a été simulé dans une série de modes sains et de modes de défaut. Sept modes de défaut correspondant à sept niveaux de sévérité classés de 2 à 8 (liés au nombre de spires court-circuitées) ont été prises en compte. La Figure 5.3 illustre la composition du modèle d'ensemble de données. Les différents modes et la variation de charge sont illustrés. Les sessions de signaux correspondant aux états transitoires de changement de charge et d'introduction de défauts ne sont pas incluses dans l'ensemble de données. Pour chaque scénario, nous disposons des données de trois variables ( $\mathbf{I}_a$ ,  $\mathbf{I}_b$  and  $\mathbf{I}_c$ ) de  $\hat{N}$  observations chacun.

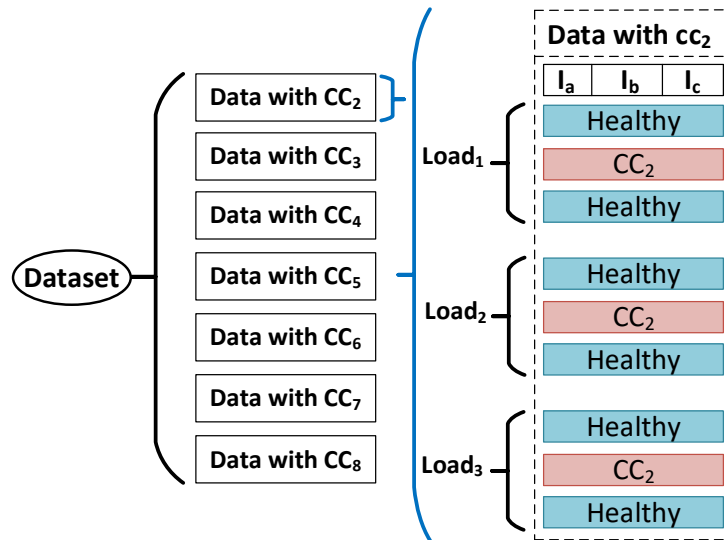


Figure 5.3: Modèle d'ensemble de données

Les analyses préliminaires ont consisté à définir un ensemble de données comprenant les courants statoriques sains et en mode de défauts, pour toute la gamme de défauts allant des défauts naissant aux défauts avec la sévérité la plus élevée. Des techniques de pré-traitement des données telles que l'écart absolu médian (MAD), le Skewness et le Kurtosis calculés sur des fenêtres glissantes ont été sélectionnées pour extraire les caractéristiques pertinentes de notre ensemble de données.

Pour l'analyse des défauts, nous avons opté pour l'ACP, et nous avons considéré deux conditions des données. Dans la première analyse, nous analysons les défauts dans les différentes conditions de charge (conditions stationnaires) des séries de données séparées. Dans la deuxième analyse, nous analysons les défauts dans des conditions non stationnaires où les données des trois conditions de changement de charge sont dans la même série de donnée. Un résumé des performances de la détection de défauts avec l'ACP dans la première analyse, en termes de probabilité de fausses alarmes (PFA) et de probabilité de détection manquée PMD sont indiqués dans le Tableau 5.1. Habituellement, pour la détection des défauts, les seuils de PMD et PFA sont généralement fixés respectivement à 0,02 et 0,05 [241].

Dans le Tableau 5.1, les cas dans lesquels ces seuils sont violés sont mis en évidence en rouge. D'après le tableau, on peut voir que les performances de détection des défauts en termes de PMD sont tous acceptables lorsque la mesure de surveillance  $T^2$  est exploitée.

**Table 5.1:** Évaluation des performances de la détection de défauts avec l'ACP (les valeurs supérieures aux seuils sont en rouge)

Scenario		PFA		PMD	
		$T^2$	$SPE$	$T^2$	$SPE$
Data with $CC_2$	$Load_1$	0	0.05	0	0
	$Load_2$	0.02	<b>0.08</b>	0	0
	$Load_3$	0	0	0	<b>0.86</b>
Data with $CC_3$	$Load_1$	0	<b>0.1</b>	0	0
	$Load_2$	0.05	<b>0.06</b>	0	0
	$Load_3$	0	0.01	0	0
Data with $CC_4$	$Load_1$	0	<b>0.08</b>	0	0
	$Load_2$	0	0.04	0	0
	$Load_3$	0	0	0	0
Data with $CC_5$	$Load_1$	0	0.04	0	0
	$Load_2$	0	<b>0.1</b>	0	0
	$Load_3$	0	0	0	0
Data with $CC_6$	$Load_1$	0	<b>0.1</b>	0	0
	$Load_2$	0	<b>0.06</b>	0	0
	$Load_3$	0	<b>0.08</b>	0	0
Data with $CC_7$	$Load_1$	0	<b>0.1</b>	0	0
	$Load_2$	0	<b>0.06</b>	0	0
	$Load_3$	0.04	0.04	0	0
Data with $CC_8$	$Load_1$	0	<b>0.06</b>	0	0
	$Load_2$	0.05	0.05	0	0
	$Load_3$	0	0	0	0

La mesure de surveillance  $SPE$  offre également d'excellentes performances en termes de PMD dans tous les scénarios, sauf dans le cas de données avec conditions de défaut de sévérité 2 ( $CC_2$ ) et sous la charge 3 ( $Load_3$ ). Cela montre que le défaut de court-circuit inter-spire au stade naissant a une faible signature dans le sous-espace résiduel, dans le fonctionnement du moteur à charges élevées. En termes de PFA, le  $T^2$  a donné des performances acceptables sans violation du seuil. La surveillance par  $SPE$  d'autre part a donné de nombreuses violations du seuil. Cela montre que la surveillance de détection par la mesure du  $SPE$  est moins précise que la surveillance de  $T^2$ . Dans notre deuxième analyse avec les données non-stationnaires, l'ACP conventionnelle ne convient plus. Des extensions de l'ACP comme l'ACP dynamique, l'ACP multi-échelle ont été proposées dans la littérature pour faire face à ce problème. Cependant, ces extensions de l'ACP présentent certains inconvénients comme de long temps de réponse, la complexité de calcul et leur efficacité est pas toujours garanti.

Dans nos travaux, nous avons proposé une méthode simple pour détecter les courts-circuits inter-spices du MSRAP dans un état non-stationnaire avec opérations sous une charge mé-

canique variable. Nous avons introduit la projection des attributs de nuisance connu sous l'acronyme NAP qui a été appliquée aux données brutes lors de l'étape de prétraitement. Ceci a permis d'obtenir de nouvelles données avec les caractéristiques des défauts qui ne sont sensibles qu'aux défauts. Après l'élimination du effets de de la variation de charge, les variables sont normalisées avant d'être traitées par l'ACP pour la détection de défaut. L'organigramme présenté à la Figure 5.4 résume notre proposition de méthodologie de défaut indépendamment du niveau de charge du MSRAP.

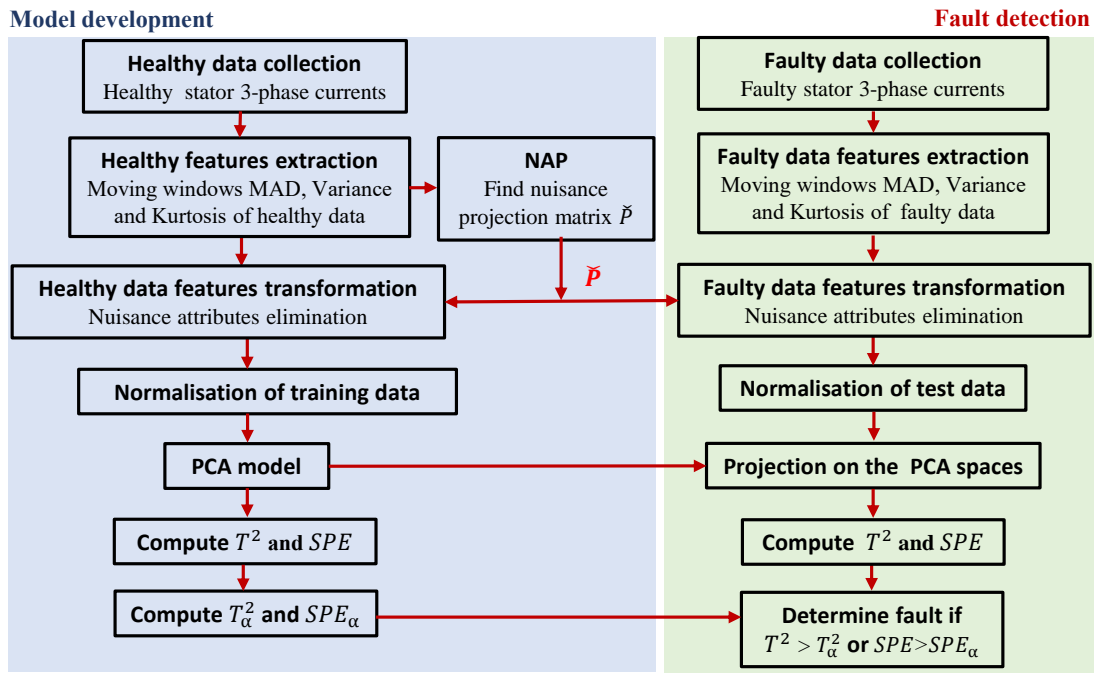


Figure 5.4: Organigramme de l'ACP basée sur le NAP pour la détection de défaut

Un résumé de la performance de la détection des défauts avec l'ACP basée sur le NAP, en termes de PFA et de PMD est donnée dans le Tableau 5.2.

Les cas dans lesquels les seuils de performance du diagnostic de défaut sont violés sont mis en évidence en rouge. D'après le tableau, on peut voir que les performances en termes de PMD sont de tous satisfaisant lorsque  $T^2$  et  $SPE$  sont surveillés. En termes de PFA, le  $T^2$  a donné des performances acceptables sans violation du seuil typique. La surveillance  $SPE$ , en revanche, dépasse le seuil en termes de de PFA. Dans l'analyse avec les données stationnaire présentée précédemment, moins de violations du seuil de PFA ont été observées. Cela montre que le NAP a effectué la suppression la dynamique dans les données liée à la variation de charge mais déplace les signatures de défauts dans le Sous-espaces principale de l'ACP. Cela fait que la détection du défauts en surveillant le  $SPE$  avec l'ACP basée sur le NAP est moins précise que la surveillance du  $T^2$ . De ces performance de détection de défauts nous avons sélectionné le  $T^2$  comme mesure de surveillance fiable pour la détection des défauts inter-spaires par l'ACP.

Nous avons examiné les méthodes analytiques et d'intelligence artificielle pour estimer la sévérité du défaut une fois détecté. Nous avons choisi la méthode analytique en raison de la quantité limitée des données pour notre étude. Nous avons développé un modèle analytique basée sur la pente de la fonction de décision CUSUM de  $T^2$  pour estimer la sévérité du

**Table 5.2:** Évaluation des performances de la détection de défauts avec l'ACP basée sur le NAP (les valeurs supérieures aux seuils sont en rouge)

Scenario	PFA		PMD	
	$T^2$	SPE	$T^2$	SPE
Data with $CC_2$	0.003	0.25	0	0
Data with $CC_3$	0.003	0.3	0	0
Data with $CC_4$	0	0.32	0	0
Data with $CC_5$	0	25	0	0
Data with $CC_6$	0	0.21	0	0
Data with $CC_7$	0.013	0.19	0	0
Data with $CC_8$	0.003	0.24	0	0

défaut. A partir de ce modèle analytique, nous avons réalisé une estimation des défauts sur des données sans bruit avec une précision supérieure à 99%. Nous avons également testé la robustesse de notre méthode d'estimation des défauts face aux interférences sonores, qui a montré une résistance au bruit lorsque le rapport signal sur bruit (SNR) était inférieur à  $30dB$ . Une autre limitation de cette méthode d'estimation des défauts est la nécessité d'une étiquette de niveau de charge, car la signature du défaut est sensible à la variation de charge.

Dans la **Conclusion**, un résumé des travaux développés avec les résultats obtenus a été présenté. Nous avons ensuite présenté une discussion sur les limites inhérentes à notre approche et formulé des suggestions de recherches futures pour les surmonter.

# Bibliography

- [1] J. Carey, “The other benefit of electric vehicles,” *Proceedings of the National Academy of Sciences*, vol. 120, no. 3, p. e2220923120, 2023.
- [2] P. Nag, U. Ghanekar, and J. Harmalkar, “A novel multi-core approach for functional safety compliance of automotive electronic control unit according to iso 26262,” in *2019 IEEE 5th International Conference for Convergence in Technology (I2CT)*, 2019, pp. 1–5.
- [3] A. Muetze and E. G. Strangas, “Guest editorial special issue on failure analysis and prevention in electrified transportation applications,” *IEEE Transactions on Transportation Electrification*, vol. 7, no. 1, pp. 3–5, 2021.
- [4] CARSCOOPS, “California Will Require All EVs To Have Standardized Diagnostics System In 2026,” <https://www.carscoops.com/2023/11/california-to-require-all-evs-to-have-standardized-diagnostics-system-in-2026/>, 2023, [Online; accessed November 14, 2023].
- [5] B. Zhang, W. Shi, and A. Ge, “Electric vehicle fault diagnosis system based on can-bus,” in *Proceedings of SAE-China Congress 2014: Selected Papers*. Springer, 2015, pp. 105–110.
- [6] F. Arena, M. Collotta, L. Luca, M. Ruggieri, and F. G. Termine, “Predictive maintenance in the automotive sector: A literature review,” *Mathematical and Computational Applications*, vol. 27, no. 1, p. 2, 2021.
- [7] Y. Ran, X. Zhou, P. Lin, Y. Wen, and R. Deng, “A survey of predictive maintenance: Systems, purposes and approaches,” *arXiv preprint arXiv:1912.07383*, 2019.
- [8] S. Zheng, X. Zhu, Z. Xiang, L. Xu, L. Zhang, and C. H. Lee, “Technology trends, challenges, and opportunities of reduced-rare-earth pm motor for modern electric vehicles,” *Green Energy and Intelligent Transportation*, vol. 1, no. 1, p. 100012, 2022.
- [9] D. T. Blagoeva, P. Aves Dias, A. Marmier, and C. Pavel, “Assessment of potential bottlenecks along the materials supply chain for the future deployment of low-carbon energy and transport technologies in the eu,” *Wind power, photovoltaic and electric vehicles technologies, time frame*, vol. 2030, pp. 4280–4290, 2015.
- [10] W. Neß and K. Raggl, “E-motor types for secondary electric drives in comparison,” *MTZ worldwide*, vol. 83, no. 2, pp. 40–45, 2022.

- [11] A. Credo, M. Villani, G. Fabri, and M. Popescu, "Adoption of the synchronous reluctance motor in electric vehicles: A focus on the flux weakening capability," *IEEE Transactions on Transportation Electrification*, vol. 9, no. 1, pp. 805–818, 2022.
- [12] J. Hong, S. Park, D. Hyun, T.-j. Kang, S. B. Lee, C. Kral, and A. Haumer, "Detection and classification of rotor demagnetization and eccentricity faults for pm synchronous motors," *IEEE Transactions on Industry Applications*, vol. 48, no. 3, pp. 923–932, 2012.
- [13] M. Cheng, J. Hang, and J. Zhang, "Overview of fault diagnosis theory and method for permanent magnet machine," *Chinese Journal of Electrical Engineering*, vol. 1, no. 1, pp. 21–36, 2015.
- [14] J. K. Park and J. Hur, "Detection of Inter-Turn and Dynamic Eccentricity Faults Using Stator Current Frequency Pattern in IPM-Type BLDC Motors," *IEEE Transactions on Industrial Electronics*, vol. 63, no. 3, pp. 1771–1780, 2016.
- [15] K. Mostafa, M. A. Mueller, and Q. Jiang, "Bearing wear detection and rotor eccentricity calculation in radial flux air-gap winding permanent magnet machines," *7th IET International Conference on Power Electronics, Machines and Drives, PEMD 2014*, no. 1, pp. 1–6, 2014.
- [16] O. V. Thorsen and M. Dalva, "A Survey of Faults on Induction Motors in Offshore Oil Industry, Petrochemical Industry, Gas Terminals, and Oil Refineries," *IEEE Transactions on Industry Applications*, vol. 31, no. 5, pp. 1186–1196, 1995.
- [17] J. De Santiago, H. Bernhoff, B. Ekergård, S. Eriksson, S. Ferhatovic, R. Waters, and M. Leijon, "Electrical motor drivelines in commercial all-electric vehicles: A review," *IEEE Transactions on vehicular technology*, vol. 61, no. 2, pp. 475–484, 2011.
- [18] S. Heydari, P. Fajri, M. Rasheduzzaman, and R. Sabzehgar, "Maximizing regenerative braking energy recovery of electric vehicles through dynamic low-speed cutoff point detection," *IEEE Transactions on Transportation Electrification*, vol. 5, no. 1, pp. 262–270, 2019.
- [19] S. Heydari, S. Member, and P. Fajri, "Maximizing Regenerative Braking Energy Recovery of Electric Vehicles Through Dynamic Low-Speed Cutoff Point Detection," *IEEE Transactions on Transportation Electrification*, vol. 5, no. 1, pp. 262–270, 2019.
- [20] K. T. Chau and W. Li, "Overview of electric machines for electric and hybrid vehicles," *International Journal of Vehicle Design*, vol. 64, no. 1, pp. 46–71, 2014.
- [21] C. Wu, R. Sehab, A. Akrad, and C. Morel, "Fault diagnosis methods and fault tolerant control strategies for the electric vehicle powertrains," *Energies*, vol. 15, no. 13, p. 4840, 2022.
- [22] A. Chernyshev, T. Lisovskaya, and R. Lisovskiy, "Comparative analysis of different electrical motor types as a traction drive part in electrical transmission," in *2017 International Conference on Industrial Engineering, Applications and Manufacturing (ICIEAM)*. St. Petersburg, Russia: IEEE, 2017, pp. 1–5.



- [23] G. Dancygier and J.-C. Dolhagaray, "Motor control law and comfort law in the peugeot and citroën electric vehicles driven by a dc commutator motor," pp. 370–374, 1998.
- [24] N. Hashemnia and B. Asaei, "Comparative study of using different electric motors in the electric vehicles," in *2008 18th International Conference on Electrical Machines*, Vilamoura, Portugal, 2008, pp. 1–5.
- [25] R. Thomas, L. Garbuio, L. Gerbaud, and H. Chazal, "Modeling and design analysis of the tesla model s induction motor," in *2020 International Conference on Electrical Machines (ICEM)*, vol. 1, Gothenburg, Sweden, 2020, pp. 495–501.
- [26] gomechanic, "gomechanic," <https://gomechanic.in/blog/electric-vehicles-types-explained/>, 2023, [Online; accessed May 10, 2023].
- [27] C. C. Chan and K. T. Chau, *Modern Electric Vehicle Technology*. Oxford University Press, 2001.
- [28] C. C. Chan and K. Chau, "An overview of power electronics in electric vehicles," *IEEE transactions on Industrial Electronics*, vol. 44, no. 1, pp. 3–13, 1997.
- [29] Y. Takano, M. Takeno, N. Hoshi, A. Chiba, M. Takemoto, S. Ogasawara, and M. A. Rahman, "Design and analysis of a switched reluctance motor for next generation hybrid vehicle without pm materials," in *The 2010 International Power Electronics Conference-ECCE ASIA-*. Sapporo, Japan: IEEE, 2010, pp. 1801–1806.
- [30] Z. Qianfan, C. Shumei, and T. Xinjia, "Hybrid switched reluctance motor applied in electric vehicles," in *2007 IEEE Vehicle Power and Propulsion Conference*. Arlington, TX, USA: IEEE, 2007, pp. 359–363.
- [31] G. Friedrich, "Comparative study of three control strategies for the synchronous salient poles and wound rotor machine in automotive applications with on board energy," 1994.
- [32] Tesla, "Tesla Model 3," <https://www.tesla.com/model3>, 2019, [Online; accessed 22-march-2023].
- [33] K. Smith Stegen, "Heavy rare earths, permanent magnets, and renewable energies: An imminent crisis," *Energy Policy*, vol. 79, pp. 1–8, 2015. [Online]. Available: <https://www.sciencedirect.com/science/article/pii/S0301421514006806>
- [34] J. D. Widmer, R. Martin, and M. Kimiabeigi, "Electric vehicle traction motors without rare earth magnets," *Sustainable Materials and Technologies*, vol. 3, pp. 7–13, 2015.
- [35] P. Size and M. Dynamics, "Research Collection," 2018.
- [36] N. Hashemnia and B. Asaei, "Comparative study of using different electric motors in the electric vehicles," pp. 1–5, 2008.
- [37] H. Lovatt, V. Ramsden, and B. Mecrow, "Design of an in-wheel motor for a solar-powered electric vehicle," *IEE Proceedings-Electric Power Applications*, vol. 145, no. 5, pp. 402–408, 1998.

- [38] C. Cambrier, “Brushless motors and controllers designed for gm sunrayce,” *IEEE Aerospace and Electronic Systems Magazine*, vol. 5, no. 8, pp. 13–15, 1990.
- [39] O. Lopez, J. Álvarez, J. Doval-Gandoy, and F. D. Freijedo, “Multilevel multiphase space vector pwm algorithm with switching state redundancy,” *IEEE Transactions on industrial electronics*, vol. 56, no. 3, pp. 792–804, 2008.
- [40] E. Levi, “Multiphase electric machines for variable-speed applications,” *IEEE Transactions on industrial electronics*, vol. 55, no. 5, pp. 1893–1909, 2008.
- [41] M. G. Simões and P. Vieira, “A high-torque low-speed multiphase brushless machine—a perspective application for electric vehicles,” *IEEE Transactions on Industrial Electronics*, vol. 49, no. 5, pp. 1154–1164, 2002.
- [42] Y. K. Kim, J. W. Lee, Y. K. Lee, Y. Y. Choe, and H. S. Mok, “Drive system of 25kw in wheel type ipmsm for electric vehicle,” in *2010 International Conference on Electrical Machines and Systems*. Incheon, Korea (South): IEEE, 2010, pp. 904–907.
- [43] L. Chang, “Comparison of ac drives for electric vehicles—a report on experts’ opinion survey,” *IEEE Aerospace and Electronic Systems Magazine*, vol. 9, no. 8, pp. 7–11, 1994.
- [44] H. Z. De La Parra, F. Magnussen, and S. Bosga, “Challenges for electric machines and power electronics in automotive applications,” in *International Conference on Ecological Vehicles and Renewable Energies, (EVER’09)*, 2009, pp. 1–9.
- [45] A. M. Mendes and A. J. Marques Cardoso, “Voltage source inverter fault diagnosis in variable speed AC drives, by the average current Park’s vector approach,” *IEEE International Electric Machines and Drives Conference, IEMDC 1999 - Proceedings*, pp. 704–706, 1999.
- [46] D. Kastha and B. K. Bose, “Investigation of fault modes of voltage-fed inverter system for induction motor drive,” *IEEE transactions on industry applications*, vol. 30, no. 4, pp. 1028–1038, 1994.
- [47] S. Manzetti and F. Mariasiu, “Electric vehicle battery technologies: From present state to future systems,” *Renewable and Sustainable Energy Reviews*, vol. 51, pp. 1004–1012, 2015.
- [48] F. J. G. Navarro, L. J. Yebra, F. J. G. Medina, and A. Giménez-Fernandez, “Dc-dc linearized converter model for faster simulation of lightweight urban electric vehicles,” *IEEE Access*, vol. 8, pp. 85 380–85 394, 2020.
- [49] M. S. H. Lipu, M. Faisal, S. Ansari, M. A. Hannan, T. F. Karim, A. Ayob, A. Hussain, M. S. Miah, and M. H. M. Saad, “Review of electric vehicle converter configurations, control schemes and optimizations: Challenges and suggestions,” *Electronics*, vol. 10, no. 4, p. 477, 2021.
- [50] M. Adler, K. Owyang, B. Baliga, and R. Kokosa, “The evolution of power device technology,” *IEEE Transactions on Electron Devices*, vol. 31, no. 11, pp. 1570–1591, 1984.

- [51] B. K. Bose, "Modern power electronics: evolution, technology, and applications," in *Modern power electronics: evolution, technology, and applications*, 1992, pp. 597–597.
- [52] T. Burress and S. Campbell, "Benchmarking ev and hev power electronics and electric machines," in *2013 IEEE Transportation Electrification Conference and Expo (ITEC)*. IEEE, 2013, pp. 1–6.
- [53] M. Ehsani, O. H. Stielau, J. D. van Wyk, and I. J. Pitel, "Integrated reactive components in power electronic circuits," *IEEE transactions on power electronics*, vol. 8, no. 2, pp. 208–215, 1993.
- [54] C. Chan, W. Leung, and C. Ng, "Adaptive decoupling control of induction motor drives," *IEEE Transactions on industrial electronics*, vol. 37, no. 1, pp. 41–47, 1990.
- [55] V. I. Utkin, "Sliding mode control design principles and applications to electric drives," *IEEE transactions on industrial electronics*, vol. 40, no. 1, pp. 23–36, 1993.
- [56] C. Chan and K. Chau, "A novel pwm algorithm for single-chip microcomputer-based three-phase inverter," in *Proc. Int. Conf. Power Electronics Motor Controllers*, 1990, pp. 445–449.
- [57] O. V. Thorsen and M. Dalva, "Failure identification and analysis for high-voltage induction motors in the petrochemical industry," *IEEE Transactions on Industry Applications*, vol. 35, no. 4, pp. 810–818, 1999.
- [58] P. Albrecht, J. Appiarius, R. McCoy, E. Owen, and D. Sharma, "Assessment of the reliability of motors in utility applications—updated," *IEEE Transactions on Energy conversion*, no. 1, pp. 39–46, 1986.
- [59] P. Zhang, Y. Du, T. G. Habetler, and B. Lu, "A survey of condition monitoring and protection methods for medium-voltage induction motors," *IEEE Transactions on Industry Applications*, vol. 47, no. 1, pp. 34–46, 2010.
- [60] S. Nandi, H. A. Toliyat, and X. Li, "Condition monitoring and fault diagnosis of electrical motors—a review," *IEEE Transactions on energy conversion*, vol. 20, no. 4, pp. 719–729, 2005.
- [61] P. J. Tavner, "Review of condition monitoring of rotating electrical machines," *IET electric power applications*, vol. 2, no. 4, pp. 215–247, 2008.
- [62] S. Heydari, P. Fajri, M. Rasheduzzaman, and R. Sabzehgar, "Maximizing regenerative braking energy recovery of electric vehicles through dynamic low-speed cutoff point detection," *IEEE Transactions on Transportation Electrification*, vol. 5, no. 1, pp. 262–270, 2019.
- [63] S. Yang, A. Bryant, P. Mawby, D. Xiang, L. Ran, and P. Tavner, "An industry-based survey of reliability in power electronic converters," *IEEE Transactions on Industry Applications*, vol. 47, no. 3, pp. 1441–1451, 2011.
- [64] J. K. Avor and C.-K. Chang, "Reliability analysis of application of variable frequency drive on condensate pump in nuclear power plant," *Journal of International Council on Electrical Engineering*, vol. 9, no. 1, pp. 8–14, 2019.

- [65] P. Tavner, L. Ran, J. Penman, and H. Sedding, *Condition monitoring of rotating electrical machines*. IET, 2008, vol. 56.
- [66] A. Vassilev, A. Ferber, C. Wehrmann, O. Pinaud, M. Schilling, and A. R. Ruddle, “Magnetic field exposure assessment in electric vehicles,” *IEEE Transactions on electromagnetic compatibility*, vol. 57, no. 1, pp. 35–43, 2014.
- [67] J. Hong, D. Hyun, S. B. Lee, J.-Y. Yoo, and K.-W. Lee, “Automated monitoring of magnet quality for permanent-magnet synchronous motors at standstill,” *IEEE Transactions on Industry Applications*, vol. 46, no. 4, pp. 1397–1405, 2010.
- [68] T. Miller, “Permanent magnet and reluctance motor drives,” *Oxf. Univ. Press, New York*, 1989.
- [69] J. D. McFarland and T. M. Jahns, “Investigation of the rotor demagnetization characteristics of interior pm synchronous machines during fault conditions,” *IEEE Transactions on Industry Applications*, vol. 50, no. 4, pp. 2768–2775, 2013.
- [70] W. Le Roux, R. G. Harley, and T. G. Habetler, “Detecting rotor faults in low power permanent magnet synchronous machines,” *IEEE Transactions on Power Electronics*, vol. 22, no. 1, pp. 322–328, 2007.
- [71] J. Faiz and M. Ojaghi, “Different indexes for eccentricity faults diagnosis in three-phase squirrel-cage induction motors: A review,” *Mechatronics*, vol. 19, no. 1, pp. 2–13, 2009.
- [72] R. Sabir, D. Rosato, S. Hartmann, and C. Gühmann, “Detection and localization of electrical faults in a three phase synchronous generator with rectifier,” in *2019 International Conference on Electrical Drives & Power Electronics (EDPE)*. The High Tatras, Slovakia: IEEE, 2019, pp. 18–23.
- [73] I.-H. Kao, W.-J. Wang, Y.-H. Lai, and J.-W. Perng, “Analysis of permanent magnet synchronous motor fault diagnosis based on learning,” *IEEE Transactions on Instrumentation and Measurement*, vol. 68, no. 2, pp. 310–324, 2018.
- [74] A. Bellini, F. Filippetti, C. Tassoni, and G.-A. Capolino, “Advances in diagnostic techniques for induction machines,” *IEEE Transactions on industrial electronics*, vol. 55, no. 12, pp. 4109–4126, 2008.
- [75] A. AlShalalfeh and L. Shalalfeh, “Bearing fault diagnosis approach under data quality issues,” *Applied Sciences*, vol. 11, no. 7, p. 3289, 2021.
- [76] Z. Gao, C. Cecati, and S. X. Ding, “A survey of fault diagnosis and fault-tolerant techniques—part i: Fault diagnosis with model-based and signal-based approaches,” *IEEE transactions on industrial electronics*, vol. 62, no. 6, pp. 3757–3767, 2015.
- [77] W. Zhang, D. Xu, P. N. Enjeti, H. Li, J. T. Hawke, and H. S. Krishnamoorthy, “Survey on fault-tolerant techniques for power electronic converters,” *IEEE Transactions on Power Electronics*, vol. 29, no. 12, pp. 6319–6331, 2014.

- [78] S. Yang, D. Xiang, A. Bryant, P. Mawby, L. Ran, and P. Tavner, "Condition monitoring for device reliability in power electronic converters: A review," *IEEE transactions on power electronics*, vol. 25, no. 11, pp. 2734–2752, 2010.
- [79] C. Gan, J. Wu, Y. Hu, S. Yang, W. Cao, and J. M. Guerrero, "New integrated multilevel converter for switched reluctance motor drives in plug-in hybrid electric vehicles with flexible energy conversion," *IEEE Transactions on Power Electronics*, vol. 32, no. 5, pp. 3754–3766, 2016.
- [80] G. Zhiwei, C. Cecati, and S. X. Ding, "A survey of fault diagnosis and fault-tolerant techniques—part ii: Fault diagnosis with knowledge-based and hybrid approaches," 2015.
- [81] B. Tabbache, A. Kheloui, M. Benbouzid, A. Mamoune, and D. Diallo, "Research on fault analysis and fault-tolerant control of ev/hev powertrain," in *2014 First International Conference on Green Energy ICGE 2014*. Sfax, Tunisia: IEEE, 2014, pp. 284–289.
- [82] S. M. Cruz, M. Ferreira, A. M. Mendes, and A. J. M. Cardoso, "Analysis and diagnosis of open-circuit faults in matrix converters," *IEEE Transactions on Industrial Electronics*, vol. 58, no. 5, pp. 1648–1661, 2010.
- [83] M. Glavanovics, T. Detzel, and K. Weber, "Impact of thermal overload operation on wirebond and metallization reliability in smart power devices," in *Proceedings of the 30th European Solid-State Circuits Conference (IEEE Cat. No. 04EX850)*. Leuven, Belgium: IEEE, 2004, pp. 273–276.
- [84] P. Agyakwa, W. Loh, M. Corfield, E. Liotti, S. Hogg, and C. Johnson, "Anomalous reliability behaviour of 99.99% and 99.999% pure aluminium wire bonds under thermal cycling," *Proc. 41st IMAPS*, pp. 658–665, 2008.
- [85] R. Mandeya, C. Chen, V. Pickert, R. Naayagi, and B. Ji, "Gate-emitter pre-threshold voltage as a health-sensitive parameter for igbt chip failure monitoring in high-voltage multichip igbt power modules," *IEEE Transactions on Power Electronics*, vol. 34, no. 9, pp. 9158–9169, 2018.
- [86] F. Richardeau, F. Boige, and S. Lefebvre, "Gate leakage-current, damaged gate and open-circuit failure-mode of recent sic power mosfet: Overview and analysis of unique properties for converter protection and possible future safety management," in *2018 IEEE International Conference on Electrical Systems for Aircraft, Railway, Ship Propulsion and Road Vehicles & International Transportation Electrification Conference (ESARS-ITEC)*. Nottingham, UK: IEEE, 2018, pp. 1–6.
- [87] Y. Xiong, X. Cheng, Z. J. Shen, C. Mi, H. Wu, and V. K. Garg, "Prognostic and warning system for power-electronic modules in electric, hybrid electric, and fuel-cell vehicles," *IEEE Transactions on Industrial Electronics*, vol. 55, no. 6, pp. 2268–2276, 2008.
- [88] S. Ravyts, G. Van den Broeck, L. Hallemans, M. Dalla Vecchia, and J. Driesen, "Fuse-based short-circuit protection of converter controlled low-voltage dc grids," *IEEE Transactions on Power Electronics*, vol. 35, no. 11, pp. 11 694–11 706, 2020.

- [89] Y. Zhang, B. Duan, and Y. Yang, "Simulation study on dynamic and static characteristics of novel sic gate-controlled bipolar-field-effect composite transistor," *IEEE Journal of the Electron Devices Society*, vol. 8, pp. 1082–1088, 2020.
- [90] K. Heumann and M. Quenum, "Second breakdown and latch-up behavior of igbts," in *1993 Fifth European Conference on Power Electronics and Applications*. Brighton, UK: IET, 1993, pp. 301–305.
- [91] C. Kulkarni, G. Biswas, and X. Koutsoukos, "A prognosis case study for electrolytic capacitor degradation in dc-dc converters," in *PHM Conference*, 2009.
- [92] L. Wu, Y. Guan, Y. Du, S. Zhou, and W. Pan, "Deterioration analysis of aluminum electrolytic capacitor for dc-dc converter," *Int. J. Phys. Sci*, vol. 6, no. 7, pp. 1653–1664, 2011.
- [93] D. Diallo and C. Delpha, "Incipient offset current sensor fault detection and diagnosis using statistical analysis and the kullback leibler divergence for ac drive," in *IECON 2017-43rd Annual Conference of the IEEE Industrial Electronics Society*. IEEE, 2017, pp. 8070–8075.
- [94] A. Abid, M. T. Khan, and J. Iqbal, "A review on fault detection and diagnosis techniques: basics and beyond," *Artificial Intelligence Review*, vol. 54, pp. 3639–3664, 2021.
- [95] M. S. Ballal, Z. J. Khan, H. M. Suryawanshi, and R. L. Sonolikar, "Adaptive neural fuzzy inference system for the detection of inter-turn insulation and bearing wear faults in induction motor," *IEEE Transactions on Industrial Electronics*, vol. 54, no. 1, pp. 250–258, 2007.
- [96] A. T. James, O. Gandhi, and S. Deshmukh, "Fault diagnosis of automobile systems using fault tree based on digraph modeling," *International Journal of System Assurance Engineering and Management*, vol. 9, pp. 494–508, 2018.
- [97] Z. Feng, Z. Zhou, C. Hu, X. Yin, G. Hu, and F. Zhao, "Fault diagnosis based on belief rule base with considering attribute correlation," *IEEE access*, vol. 6, pp. 2055–2067, 2017.
- [98] G. Jiang, P. Xie, H. He, and J. Yan, "Wind turbine fault detection using a denoising autoencoder with temporal information," *IEEE/Asme transactions on mechatronics*, vol. 23, no. 1, pp. 89–100, 2017.
- [99] J. Wang, J. Zhang, B. Qu, H. Wu, and J. Zhou, "Unified architecture of active fault detection and partial active fault-tolerant control for incipient faults," *IEEE Transactions on Systems, Man, and Cybernetics: Systems*, vol. 47, no. 7, pp. 1688–1700, 2017.
- [100] I. Sadeghkhani, M. E. H. Golshan, A. Mehrizi-Sani, J. M. Guerrero, and A. Ketabi, "Transient monitoring function-based fault detection for inverter-interfaced microgrids," *IEEE Transactions on Smart Grid*, vol. 9, no. 3, pp. 2097–2107, 2016.
- [101] S. Hekmat and R. Ravanmehr, "Real time fault detection and isolation: a comparative study," *Int J Comput Appl*, vol. 134, no. 6, pp. 8–15, 2016.

- [102] K. Goebel and W. Yan, "Correcting sensor drift and intermittency faults with data fusion and automated learning," *IEEE systems journal*, vol. 2, no. 2, pp. 189–197, 2008.
- [103] A. Abid, M. T. Khan, and C. De Silva, "Fault detection in mobile robots using sensor fusion," in *2015 10th International Conference on Computer Science & Education (ICCSE)*. Cambridge, UK: IEEE, 2015, pp. 8–13.
- [104] Y. Han and Y. Song, "Condition monitoring techniques for electrical equipment—a literature survey," *IEEE Transactions on Power delivery*, vol. 18, no. 1, pp. 4–13, 2003.
- [105] D. Basak, A. Tiwari, and S. Das, "Fault diagnosis and condition monitoring of electrical machines—a review," in *2006 IEEE International Conference on Industrial Technology*. IEEE, 2006, pp. 3061–3066.
- [106] A. Ruddle, A. Galarza, B. Sedano, I. Unanue, I. Ibarra, and L. Low, "Safety and failure analysis of electrical powertrain for fully electric vehicles and the development of a prognostic health monitoring system," in *IET Hybrid and Electric Vehicles Conference 2013 (HEVC 2013)*. London, UK: IET, 2013, pp. 1–6.
- [107] C. Kral, H. Kapeller, and F. Pirker, "A stator and rotor fault detection technique for induction machines in traction applications for electric or hybrid electric vehicles," *World Electric Vehicle Journal*, vol. 1, no. 1, pp. 184–189, 2007.
- [108] J. Rosero, L. Romeral, E. Rosero, and J. Urresty, "Fault detection in dynamic conditions by means of discrete wavelet decomposition for pmsm running under bearing damage," in *2009 Twenty-Fourth Annual IEEE Applied Power Electronics Conference and Exposition*. Washington, DC, USA: IEEE, 2009, pp. 951–956.
- [109] T. G. Amaral, V. F. Pires, J. Martins, A. Pires, and M. M. Crisostomo, "Statistic moment based method for the detection and diagnosis of induction motor stator fault."
- [110] M. Hadeif, A. Djerdir, N. Ikhlef, M. Mekideche, and A. N'diaye, "A fault severity index for stator winding faults detection in vector controlled pm synchronous motor," *Journal of Electrical Engineering and Technology*, vol. 10, no. 6, pp. 2326–2333, 2015.
- [111] M. A. Cash, T. G. Habetler, and G. B. Kliman, "Insulation failure prediction in ac machines using line-neutral voltages," *IEEE Transactions on Industry Applications*, vol. 34, no. 6, pp. 1234–1239, 1998.
- [112] J. L. Kohler, J. Sottile, and F. C. Trutt, "Alternatives for assessing the electrical integrity of induction motors," *IEEE Transactions on Industry Applications*, vol. 28, no. 5, pp. 1109–1117, 1992.
- [113] Y. Chen, S. Liang, W. Li, H. Liang, and C. Wang, "Faults and diagnosis methods of permanent magnet synchronous motors: A review," *Applied Sciences (Switzerland)*, vol. 9, no. 10, 2019.

- [114] J. B. Ali, N. Fnaiech, L. Saidi, B. Chebel-Morello, and F. Fnaiech, "Application of empirical mode decomposition and artificial neural network for automatic bearing fault diagnosis based on vibration signals," *Applied Acoustics*, vol. 89, pp. 16–27, 2015.
- [115] M. Baghli, C. Delpha, D. Diallo, A. Hallouche, D. Mba, and T. Wang, "Three-level npc inverter incipient fault detection and classification using output current statistical analysis," *Energies*, vol. 12, no. 7, p. 1372, 2019.
- [116] C.-S. Wang, I.-H. Kao, and J.-W. Perng, "Fault diagnosis and fault frequency determination of permanent magnet synchronous motor based on deep learning," *Sensors*, vol. 21, no. 11, p. 3608, 2021.
- [117] L. Cohen, *Time-frequency analysis*. Prentice hall New Jersey, 1995, vol. 778.
- [118] P. Pietrzak and M. Wolkiewicz, "Comparison of selected methods for the stator winding condition monitoring of a pmsm using the stator phase currents," *Energies*, vol. 14, no. 6, p. 1630, 2021.
- [119] J. Hang, J. Zhang, M. Xia, S. Ding, and W. Hua, "Interturn fault diagnosis for model-predictive-controlled-pmsm based on cost function and wavelet transform," *IEEE Transactions on Power Electronics*, vol. 35, no. 6, pp. 6405–6418, 2019.
- [120] A. Maqsood, D. Oslebo, K. Corzine, L. Parsa, and Y. Ma, "Stft cluster analysis for dc pulsed load monitoring and fault detection on naval shipboard power systems," *IEEE Transactions on Transportation Electrification*, vol. 6, no. 2, pp. 821–831, 2020.
- [121] S. D. Villalba and P. Cunningham, "An evaluation of dimension reduction techniques for one-class classification," University College Dublin. School of Computer Science and Informatics, Tech. Rep., 2007.
- [122] H. Abdi and L. J. Williams, "Principal component analysis," *Wiley interdisciplinary reviews: computational statistics*, vol. 2, no. 4, pp. 433–459, 2010.
- [123] T. Mu and A. K. Nandi, "Multiclass classification based on extended support vector data description," *IEEE Transactions on Systems, Man, and Cybernetics, Part B (Cybernetics)*, vol. 39, no. 5, pp. 1206–1216, 2009.
- [124] P. M. Frank, "Analytical and qualitative model-based fault diagnosis—a survey and some new results," *European Journal of control*, vol. 2, no. 1, pp. 6–28, 1996.
- [125] R. Isermann, "Model-based fault detection and diagnosis-status and applications," *IFAC Proceedings Volumes*, vol. 37, no. 6, pp. 49–60, 2004.
- [126] J. Huang, G. Chen, L. Shu, S. Wang, and Y. Zhang, "An experimental study of clogging fault diagnosis in heat exchangers based on vibration signals," *IEEE access*, vol. 4, pp. 1800–1809, 2016.
- [127] Q.-F. Zhou, H. Zhou, Y.-P. Ning, F. Yang, and T. Li, "Two approaches for novelty detection using random forest," *Expert Systems with Applications*, vol. 42, no. 10, pp. 4840–4850, 2015.



- [128] J. F. MacGregor and T. Kourti, "Statistical process control of multivariate processes," *Control engineering practice*, vol. 3, no. 3, pp. 403–414, 1995.
- [129] B. Samanta, "Multivariate control charts for grade control using principal-component analysis and time-series modelling," *Mining Technology*, vol. 111, no. 2, pp. 149–157, 2002.
- [130] I. Arshad and R. Umar, "Urban groundwater pollution: Causes, impacts and mitigation," in *Current Directions in Water Scarcity Research*. Elsevier, 2022, vol. 5, pp. 379–397.
- [131] M. Z. Ali, M. N. S. K. Shabbir, X. Liang, Y. Zhang, and T. Hu, "Machine learning-based fault diagnosis for single-and multi-faults in induction motors using measured stator currents and vibration signals," *IEEE Transactions on Industry Applications*, vol. 55, no. 3, pp. 2378–2391, 2019.
- [132] Y. LeCun, Y. Bengio, and G. Hinton, "Deep learning," *Nature*, vol. 521, no. 7553, pp. 436–444, 2015.
- [133] M. Skowron, T. Orłowska-Kowalska, and C. T. Kowalski, "Application of simplified convolutional neural networks for initial stator winding fault detection of the pmsm drive using different raw signal data," *IET Electric Power Applications*, vol. 15, no. 7, pp. 932–946, 2021.
- [134] P. Ewert, T. Orłowska-Kowalska, and K. Jankowska, "Effectiveness analysis of pmsm motor rolling bearing fault detectors based on vibration analysis and shallow neural networks," *Energies*, vol. 14, no. 3, p. 712, 2021.
- [135] B. Sen, J. Wang, and P. Lazari, "A high-fidelity computationally efficient transient model of interior permanent-magnet machine with stator turn fault," *IEEE Transactions on Industrial Electronics*, vol. 63, no. 2, pp. 773–783, 2015.
- [136] T. D. Michalski, J. L. R. Martinez, and G. Mino-Aguilar, "Healthy and open phase pmasynrm model based on virtual reluctance concept," *IEEE Transactions on Industrial Electronics*, vol. 69, no. 12, pp. 12 191–12 200, 2021.
- [137] G. Jang, J. Chang, D. Hong, and K. Kim, "Finite-element analysis of an electromechanical field of a bldc motor considering speed control and mechanical flexibility," *IEEE transactions on magnetics*, vol. 38, no. 2, pp. 945–948, 2002.
- [138] A. Sapena-Bañó, F. Chinesta, M. Pineda-Sanchez, J. Aguado, D. Borzacchiello, and R. Puche-Panadero, "Induction machine model with finite element accuracy for condition monitoring running in real time using hardware in the loop system," *International Journal of Electrical Power & Energy Systems*, vol. 111, pp. 315–324, 2019.
- [139] F. Le Berr, A. Abdelli, D.-M. Postariu, and R. Benlamine, "Design and optimization of future hybrid and electric propulsion systems: An advanced tool integrated in a complete workflow to study electric devices," *Oil & Gas Science and Technology—Revue d'IFP Energies nouvelles*, vol. 67, no. 4, pp. 547–562, 2012.

- [140] L. Song, D. Jiang, S. Cui, and S. Sheng, "Reluctance torque analysis and reactance calculation of ipm for hevs based on fem," in *2010 IEEE Vehicle Power and Propulsion Conference*. IEEE, 2010, pp. 1–4.
- [141] S. Sriprang, N. Poonnoy, D. Guilbert, B. Nahid-Mobarakeh, N. Takorabet, N. Bizon, and P. Thounthong, "Design, modeling, and differential flatness based control of permanent magnet-assisted synchronous reluctance motor for e-vehicle applications," *Sustainability*, vol. 13, no. 17, p. 9502, 2021.
- [142] C.-M. Liaw, M.-Z. Lu, P.-H. Jhou, and K.-Y. Chou, "Driving control technologies of new high-efficient motors," in *Applied Electromechanical Devices and Machines for Electric Mobility Solutions*. IntechOpen, 2019.
- [143] M. Mohr, O. Biro, A. Stermecki, and F. Diwoy, "An improved physical phase variable model for permanent magnet machines," in *2012 XXth International Conference on Electrical Machines*. IEEE, 2012, pp. 53–58.
- [144] T. Matsuo and T. A. Lipo, "Rotor position detection scheme for synchronous reluctance motor based on current measurements," in *Proceedings of 1994 IEEE Industry Applications Society Annual Meeting*, vol. 1. IEEE, 1994, pp. 627–634.
- [145] T. A. Huynh, M.-F. Hsieh, K.-J. Shih, and H.-F. Kuo, "An investigation into the effect of pm arrangements on pma-synrm performance," *IEEE Transactions on Industry Applications*, vol. 54, no. 6, pp. 5856–5868, 2018.
- [146] H. Kim and H. Akagi, "The instantaneous power theory on the rotating pqr reference frames," in *Proceedings of the IEEE 1999 International Conference on Power Electronics and Drive Systems. PEDS'99 (Cat. No. 99TH8475)*, vol. 1. Hong Kong, China: IEEE, 1999, pp. 422–427.
- [147] J. Tang, J. Chen, K. Dong, Y. Yang, H. Lv, and Z. Liu, "Modeling and evaluation of stator and rotor faults for induction motors," *Energies*, vol. 13, no. 1, p. 133, 2019.
- [148] M. S. R. Krishna and K. S. Ravi, "Fault diagnosis of induction motor using motor current signature analysis," in *2013 international conference on circuits, power and computing technologies (ICCPCT)*. Nagercoil, India: IEEE, 2013, pp. 180–186.
- [149] G. Houdouin, G. Barakat, B. Dakyo, and E. Destobbeleer, "A winding function theory based global method for the simulation of faulty induction machines," in *IEEE International Electric Machines and Drives Conference, 2003. IEMDC'03.*, vol. 1. IEEE, 2003, pp. 297–303.
- [150] N. Yassa and M. Rachek, "Modeling and detecting the stator winding inter turn fault of permanent magnet synchronous motors using stator current signature analysis," *Mathematics and Computers in Simulation*, vol. 167, pp. 325–339, 2020.
- [151] A. Choudhary, D. C. Meena, and A. K. Patra, "Asynchronous motor modeling in simulink for stator and rotor fault analysis," in *2019 International Conference on Green and Human Information Technology (ICGHIT)*. Kuala Lumpur, Malaysia: IEEE, 2019, pp. 82–85.

- [152] A. Guezmil, H. Berriri, R. Pusca, A. Sakly, R. Romary, and M. F. Mimouni, "Detecting inter-turn short-circuit fault in induction machine using high-order sliding mode observer: simulation and experimental verification," *Journal of Control, Automation and Electrical Systems*, vol. 28, pp. 532–540, 2017.
- [153] M. Jannati, N. Idris, and Z. Salam, "A new method for modeling and vector control of unbalanced induction motors," in *2012 IEEE Energy Conversion Congress and Exposition (ECCE)*. IEEE, 2012, pp. 3625–3632.
- [154] N. Yassa, M. Rachek, and H. Houassine, "Motor current signature analysis for the air gap eccentricity detection in the squirrel cage induction machines," *Energy Procedia*, vol. 162, pp. 251–262, 2019.
- [155] T. Ilamparithi and S. Nandi, "Comparison of results for eccentric cage induction motor using finite element method and modified winding function approach," in *2010 Joint International Conference on Power Electronics, Drives and Energy Systems & 2010 Power India*. IEEE, 2010, pp. 1–7.
- [156] J. Faiz and M. Ojaghi, "Unified winding function approach for dynamic simulation of different kinds of eccentricity faults in cage induction machines," *IET electric power applications*, vol. 3, no. 5, pp. 461–470, 2009.
- [157] L. M. R. Baccarini, B. R. de Menezes, and W. M. Caminhas, "Fault induction dynamic model, suitable for computer simulation: Simulation results and experimental validation," *Mechanical Systems and Signal Processing*, vol. 24, no. 1, pp. 300–311, 2010.
- [158] S. Bindu and V. V. Thomas, "Detection of static air-gap eccentricity in three-phase squirrel cage induction motor through stator current and vibration analysis," *Advances in Power Systems and Energy Management: ETAEERE-2016*, pp. 511–518, 2018.
- [159] G. M. Joksimovic, M. D. Durovic, J. Penman, and N. Arthur, "Dynamic simulation of dynamic eccentricity in induction machines-winding function approach," *IEEE Transactions on Energy Conversion*, vol. 15, no. 2, pp. 143–148, 2000.
- [160] J. F. Bangura, R. J. Povinelli, N. A. Demerdash, and R. H. Brown, "Diagnostics of eccentricities and bar/end-ring connector breakages in polyphase induction motors through a combination of time-series data mining and time-stepping coupled fe-state-space techniques," *IEEE Transactions on Industry Applications*, vol. 39, no. 4, pp. 1005–1013, 2003.
- [161] R. S. C. Pal and A. R. Mohanty, "A simplified dynamical model of mixed eccentricity fault in a three-phase induction motor," *IEEE Transactions on Industrial Electronics*, vol. 68, no. 5, pp. 4341–4350, 2020.
- [162] S. Bindu and V. V. Thomas, "A modified direct-quadrature axis model for characterization of air-gap mixed eccentricity faults in three-phase induction motor," *International Review on Modelling and Simulations*, vol. 11, no. 6, pp. 359–365, 2018.

- 
- [163] S. Zhang, B. Wang, M. Kanemaru, C. Lin, D. Liu, M. Miyoshi, K. H. Teo, and T. G. Habetler, "Model-based analysis and quantification of bearing faults in induction machines," *IEEE Transactions on Industry Applications*, vol. 56, no. 3, pp. 2158–2170, 2020.
- [164] A. Sapena-Bano, J. Martinez-Roman, R. Puche-Panadero, M. Pineda-Sanchez, J. Perez-Cruz, and M. Riera-Guasp, "Induction machine model with space harmonics for fault diagnosis based on the convolution theorem," *International Journal of Electrical Power & Energy Systems*, vol. 100, pp. 463–481, 2018.
- [165] G. Joksimovic, "Double-fed induction machine dynamic modeling using winding function approach," in *2007 IEEE International Electric Machines & Drives Conference*, vol. 1. IEEE, 2007, pp. 694–697.
- [166] M. Y. Kaikaa, M. Hadjami, and A. Khezzer, "Effects of the simultaneous presence of static eccentricity and broken rotor bars on the stator current of induction machine," *IEEE Transactions on Industrial Electronics*, vol. 61, no. 5, pp. 2452–2463, 2013.
- [167] J. Faiz, B. M. Ebrahimi, and H. A. Toliyat, "Effect of magnetic saturation on static and mixed eccentricity fault diagnosis in induction motor," *IEEE Transactions on magnetics*, vol. 45, no. 8, pp. 3137–3144, 2009.
- [168] R. Qin and M. Rahman, "Magnetic equivalent circuit of pm hysteresis synchronous motor," *IEEE Transactions on Magnetism*, vol. 39, no. 5, pp. 2998–3000, 2003.
- [169] R. E. Bechari, "Optimization and reliability analysis for electrical machines modeled by finite element method," Ph.D. dissertation, Centrale Lille, 2020.
- [170] A. Kumar and A. Arockiarajan, "Evolution of nonlinear magneto-elastic constitutive laws in ferromagnetic materials: A comprehensive review," *Journal of Magnetism and Magnetic Materials*, vol. 546, p. 168821, 2022.
- [171] Y. Li, "Finite element analysis of motor eccentric forces and effects on vibration," Ph.D. dissertation, Texas AM University, 2019.
- [172] D. JING, "Computational analysis of a permanent magnet synchronous machine using numerical techniques," Ph.D. dissertation, DEPARTMENT OF ELECTRICAL COMPUTER ENGINEERING, NATIONAL UNIVERSITY OF SINGAPORE, 2004.
- [173] S. J. Salon, *Finite element analysis of electrical machines*. Kluwer academic publishers Boston, 1995, vol. 101.
- [174] S. Viswanath, N. Praveen Kumar, and T. Isha, "Static eccentricity fault in induction motor drive using finite element method," in *Advances in Electrical and Computer Technologies: Select Proceedings of ICAECT 2019*. Springer, 2020, pp. 1291–1302.
- [175] A.-I. CONSTANTIN, "Detection based on stator current signature of the single and combined short-circuit, broken bar and eccentricity faults in induction motors," in *2019 11th International Symposium on Advanced Topics in Electrical Engineering (ATEE)*. IEEE, 2019, pp. 1–6.

- [176] H. H. Eldeeb, A. Berzoy, and O. Mohammed, "Stator fault detection on dtc-driven im via magnetic signatures aided by 2-d fea co-simulation," *IEEE Transactions on Magnetism*, vol. 55, no. 6, pp. 1–5, 2019.
- [177] K. Prasob, N. P. Kumar, and T. Isha, "Inter-turn short circuit fault analysis of pwm inverter fed three-phase induction motor using finite element method," in *2017 international conference on circuit, power and computing technologies (ICCPCT)*. IEEE, 2017, pp. 1–6.
- [178] M. M. Mafruddin, S. Suwarno, and A. Abu-Siada, "Finite element simulation of a 126 mw salient pole synchronous generator with rotor eccentricity," in *2019 2nd International Conference on High Voltage Engineering and Power Systems (ICHVEPS)*. IEEE, 2019, pp. 1–96.
- [179] A. Bouzida, R. Abdelli, O. Touhami, and A. Aibeche, "Dynamic eccentricity fault diagnosis in induction motors using finite element method and experimental tests," *International Journal of Industrial Electronics and Drives*, vol. 3, no. 4, pp. 199–209, 2017.
- [180] H. Torkaman, E. Afjei, and P. Yadegari, "Static, dynamic, and mixed eccentricity faults diagnosis in switched reluctance motors using transient finite element method and experiments," *IEEE Transactions on Magnetism*, vol. 48, no. 8, pp. 2254–2264, 2012.
- [181] J. Faiz and S. M. M. Moosavi, "Detection of mixed eccentricity fault in doubly-fed induction generator based on reactive power spectrum," *IET Electric Power Applications*, vol. 11, no. 6, pp. 1076–1084, 2017.
- [182] Y. Gao, X. Liu, and J. Xiang, "Fem simulation-based generative adversarial networks to detect bearing faults," *IEEE Transactions on Industrial Informatics*, vol. 16, no. 7, pp. 4961–4971, 2020.
- [183] C. Vinothraj, N. P. Kumar, and T. Isha, "Bearing fault analysis in induction motor drives using finite element method," *Int. J. Eng. Technol*, vol. 7, no. 3, p. 6, 2018.
- [184] T. Lubin, T. Hamiti, H. Razik, and A. Rezzoug, "Comparison between finite-element analysis and winding function theory for inductances and torque calculation of a synchronous reluctance machine," *IEEE Transactions on Magnetism*, vol. 43, no. 8, pp. 3406–3410, 2007.
- [185] C. Terron-Santiago, J. Martinez-Roman, R. Puche-Panadero, and A. Sapena-Bano, "A review of techniques used for induction machine fault modelling," *Sensors*, vol. 21, no. 14, p. 4855, 2021.
- [186] S. Bachir, S. Tnani, J.-C. Trigeassou, and G. Champenois, "Diagnosis by parameter estimation of stator and rotor faults occurring in induction machines," *IEEE Transactions on industrial electronics*, vol. 53, no. 3, pp. 963–973, 2006.
- [187] J. Martinez, A. Belahcen, and J. Detoni, "A 2d magnetic and 3d mechanical coupled finite element model for the study of the dynamic vibrations in the stator of induction motors," *Mechanical Systems and Signal Processing*, vol. 66, pp. 640–656, 2016.

- 
- [188] A. Sapena-Bano, M. Riera-Guasp, J. Martinez-Roman, M. Pineda-Sanchez, R. Puche-Panadero, and J. Perez-Cruz, "Fem-analytical hybrid model for real time simulation of ims under static eccentricity fault," in *2019 IEEE 12th International Symposium on Diagnostics for Electrical Machines, Power Electronics and Drives (SDEMPED)*. IEEE, 2019, pp. 108–114.
- [189] B. Asad, T. Vaimann, A. Belahcen, A. Kallaste, A. Rassölkin, and M. N. Iqbal, "The cluster computation-based hybrid fem–analytical model of induction motor for fault diagnostics," *Applied Sciences*, vol. 10, no. 21, p. 7572, 2020.
- [190] F. Blaschke, "The principle of field orientation as applied to the new transvector closed loop control system in a pwm inverter induction motor drive," *Siemens Rev*, vol. 39, no. 5, pp. 217–220, 1972.
- [191] P. Pillay and R. Krishnan, "Modeling, simulation, and analysis of permanent-magnet motor drives. i. the permanent-magnet synchronous motor drive," *IEEE Transactions on industry applications*, vol. 25, no. 2, pp. 265–273, 1989.
- [192] S. Hussain and M. A. Bazaz, "Comparative analysis of speed control strategies for vector controlled pmsm drive," in *2016 International Conference on Computing, Communication and Automation (ICCCA)*. IEEE, 2016, pp. 1314–1319.
- [193] G. S. Buja and M. P. Kazmierkowski, "Direct torque control of pwm inverter-fed ac motors-a survey," *IEEE Transactions on industrial electronics*, vol. 51, no. 4, pp. 744–757, 2004.
- [194] M. S. Basar, M. M. Bech, T. O. Andersen, P. Scavenius, and T. Thomas-Basar, "Comparison of sensorless fof and svm-dtfc of pmsm for low-speed applications," in *4th International Conference on Power Engineering, Energy and Electrical Drives*. IEEE, 2013, pp. 864–869.
- [195] D. Meeker, N. Bianchi, J. Gyselinck, R. Sabariego, L. Alberti, G. Pellegrino, and F. Cupertino, "Electrical machine analysis using free software," in *2017 IEEE Energy Conversion Congress and Exposition (ECCE)*. IEEE, 2017.
- [196] S. Huang, F. Tu, Q. Guo, B. Wu, Z. Huang, and H. Chen, "Double closed-loop pi controller tuning for motor control," in *Journal of Physics: Conference Series*, vol. 2005, no. 1. IOP Publishing, 2021, p. 012132.
- [197] J. Pando-Acedo, A. Rassölkin, A. Lehtikoinen, T. Vaimann, A. Kallaste, E. Romero-Cadaval, and A. Belahcen, "Hybrid fea-simulink modelling of permanent magnet assisted synchronous reluctance motor with unbalanced magnet flux," in *2019 IEEE 12th International Symposium on Diagnostics for Electrical Machines, Power Electronics and Drives (SDEMPED)*. IEEE, 2019, pp. 174–180.
- [198] E. Albáñez, J. Rengifo, A. Bueno, and J. M. Aller, "Modeling of the synchronous reluctance machine based on finite element method for drive applications considering saturation," *Ciménics Xiii*, p. 12, 2016.
- [199] J. A. Walker, D. G. Dorrell, and C. Cossar, "Flux-linkage calculation in permanent-magnet motors using the frozen permeabilities method," *IEEE Transactions on Magnetics*, vol. 41, no. 10, pp. 3946–3948, 2005.

- [200] J. Pyrhönen, T. Jokinen, and V. Hrabovcová, *Design of Rotating Electrical Machines*. John Wiley & Sons, Ltd, 2008.
- [201] R. Leuzzi, P. Lino, G. Maione, S. Stasi, F. Padula, and A. Visioli, “Combined fractional feedback-feedforward controller design for electrical drives,” in *ICFDA’14 International Conference on Fractional Differentiation and Its Applications 2014*, 2014, pp. 1–6.
- [202] M. Facta, A. Priyadi, M. H. Purnomo *et al.*, “Investigation of symmetrical optimum pi controller based on plant and feedback linearization in grid-tie inverter systems,” *International Journal of Renewable Energy Research (IJRER)*, vol. 7, no. 3, pp. 1228–1234, 2017.
- [203] M. BOUAKOURA, “Contribution au diagnostic et à la gestion d’une commande tolérante pour une machine asynchrone,” Ph.D. dissertation, Université de Batna 2, 2019.
- [204] Y. Zhang, G. Liu, W. Zhao, H. Zhou, Q. Chen, and M. Wei, “Online diagnosis of slight interturn short-circuit fault for a low-speed permanent magnet synchronous motor,” *IEEE Transactions on Transportation Electrification*, vol. 7, no. 1, pp. 104–113, 2020.
- [205] F. Briz, M. W. Degner, P. Garcia, and A. B. Diez, “High-frequency carrier-signal voltage selection for stator winding fault diagnosis in inverter-fed ac machines,” *IEEE Transactions on Industrial Electronics*, vol. 55, no. 12, pp. 4181–4190, 2008.
- [206] B. Ayhan, M. Chow, H. Trussell, M. Song, E. Kang, and H. Woe, “Statistical analysis on a case study of load effect on psd technique for induction motor broken rotor bar fault detection,” in *4th IEEE International Symposium on Diagnostics for Electric Machines, Power Electronics and Drives, 2003. SDEMPED 2003.*, 2003, pp. 119–123.
- [207] D. Rosa Lakus, M. Pizzolato, F. de Medeiros Albano, and P. Langer Menin, “Shewhart, cusum and ewma control charts: A comparative study on intermediate check of balances,” *MAPAN*, vol. 37, no. 2, pp. 453–464, 2022.
- [208] M. Klein, “Two alternatives to the shewhart x control chart,” *Journal of Quality Technology*, vol. 32, no. 4, pp. 427–431, 2000.
- [209] S. H. Steiner, “Ewma control charts with time-varying control limits and fast initial response,” *Journal of Quality Technology*, vol. 31, no. 1, pp. 75–86, 1999.
- [210] D. C. Montgomery, *Introduction to statistical quality control*. John Wiley & Sons, 2020.
- [211] G. Liu, X. Pu, L. Wang, and D. Xiang, “Cusum chart for detecting range shifts when monotonicity of likelihood ratio is invalid,” *Journal of Applied Statistics*, vol. 42, no. 8, pp. 1635–1644, 2015.
- [212] Y. Cao, A. Thompson, M. Wang, and Y. Xie, “Sketching for sequential change-point detection,” *EURASIP Journal on Advances in Signal Processing*, vol. 2019, no. 1, pp. 1–22, 2019.

- [213] M. Basseville and I. V. Nikiforov, *Detection of abrupt changes: theory and application*. prentice Hall Englewood Cliffs, 1993, vol. 104.
- [214] E. S. Page, “Continuous inspection schemes,” *Biometrika*, vol. 41, no. 1/2, pp. 100–115, 1954.
- [215] A. Wald, “Sequential tests of statistical hypotheses,” in *Breakthroughs in statistics: Foundations and basic theory*. Springer, 1992, pp. 256–298.
- [216] P. Tsiamyrtzis and D. M. Hawkins, “Bayesian statistical process control for phase i count type data,” *Applied Stochastic Models in Business and Industry*, vol. 35, no. 3, pp. 766–787, 2019.
- [217] T. M. Margavio, M. D. Conerly, W. H. Woodall, and L. G. Drake, “Alarm rates for quality control charts,” *Statistics & Probability Letters*, vol. 24, no. 3, pp. 219–224, 1995.
- [218] A. Ajami and M. Daneshvar, “Data driven approach for fault detection and diagnosis of turbine in thermal power plant using independent component analysis (ica),” *International Journal of Electrical Power & Energy Systems*, vol. 43, no. 1, pp. 728–735, 2012.
- [219] Z. Ge and Z. Song, “Process monitoring based on independent component analysis-principal component analysis (ica- pca) and similarity factors,” *Industrial & Engineering Chemistry Research*, vol. 46, no. 7, pp. 2054–2063, 2007.
- [220] J.-M. Lee, S. J. Qin, and I.-B. Lee, “Fault detection and diagnosis based on modified independent component analysis,” *AIChE journal*, vol. 52, no. 10, pp. 3501–3514, 2006.
- [221] J. E. Jackson, *A user’s guide to principal components*. John Wiley & Sons, 2005.
- [222] C. Flamant, M. Mattheakis, and P. Protopapas, “Methods of dimensionality reduction: Principal component analysis.”
- [223] I. T. Jolliffe and J. Cadima, “Principal component analysis: a review and recent developments,” *Philosophical transactions of the royal society A: Mathematical, Physical and Engineering Sciences*, vol. 374, no. 2065, p. 20150202, 2016.
- [224] Q. Chen, U. Kruger, M. Meronk, and A. Leung, “Synthesis of t2 and q statistics for process monitoring,” *Control Engineering Practice*, vol. 12, no. 6, pp. 745–755, 2004.
- [225] S. Kumar, E. B. Martin, and J. Morris, “Detection of process model change in pls based performance monitoring,” *IFAC Proceedings Volumes*, vol. 35, no. 1, pp. 125–130, 2002.
- [226] C. Undey and A. Cinar, “Statistical monitoring of multistage, multiphase batch processes,” *IEEE Control systems magazine*, vol. 22, no. 5, pp. 40–52, 2002.
- [227] Y. Tharrault, G. Mourot, and J. Ragot, “Fault detection and isolation with robust principal component analysis,” in *2008 16th Mediterranean Conference on Control and Automation*, 2008, pp. 59–64.



- [228] I. T. Jolliffe, *Principal component analysis for special types of data*. Springer, 2002.
- [229] J. F. MacGregor, H. Yu, S. G. Muñoz, and J. Flores-Cerrillo, “Data-based latent variable methods for process analysis, monitoring and control,” *Computers & chemical engineering*, vol. 29, no. 6, pp. 1217–1223, 2005.
- [230] J. E. Jackson and G. S. Mudholkar, “Control procedures for residuals associated with principal component analysis,” *Technometrics*, vol. 21, no. 3, pp. 341–349, 1979.
- [231] M. Nawaz, A. S. Maulud, H. Zabiri, S. A. A. Taqvi, and A. Idris, “Improved process monitoring using the cusum and ewma-based multiscale pca fault detection framework,” *Chinese Journal of Chemical Engineering*, vol. 29, pp. 253–265, 2021.
- [232] F. Harrou, M. Nounou, and H. Nounou, “A statistical fault detection strategy using pca based ewma control schemes,” in *2013 9th Asian Control Conference (ASCC)*. IEEE, 2013, pp. 1–4.
- [233] Z. Li, C. Zou, Z. Gong, and Z. Wang, “The computation of average run length and average time to signal: an overview,” *Journal of Statistical Computation and Simulation*, vol. 84, no. 8, pp. 1779–1802, 2014.
- [234] J. Fan, S. Upadhye, and A. Worster, “Understanding receiver operating characteristic (roc) curves,” *Canadian Journal of Emergency Medicine*, vol. 8, no. 1, pp. 19–20, 2006.
- [235] E. Villarreal-López, “A new scheme for multiple fault detection and isolation for rotational mechatronic systems, by means of analytical redundancy and adaptive filtering,” *Dyna*, vol. 86, no. 209, pp. 40–48, 2019.
- [236] H. El Hadraoui, M. Zegrari, A. Chebak, O. Laayati, and N. Guennouni, “A multi-criteria analysis and trends of electric motors for electric vehicles,” *World Electric Vehicle Journal*, vol. 13, no. 4, p. 65, 2022.
- [237] T. He, W. Xie, Q. Wu, and T. Shi, “Process fault detection and diagnosis based on principal component analysis,” in *2006 International Conference on Machine Learning and Cybernetics*, 2006, pp. 3551–3556.
- [238] W. Ku, R. H. Storer, and C. Georgakis, “Disturbance detection and isolation by dynamic principal component analysis,” *Chemometrics and intelligent laboratory systems*, vol. 30, no. 1, pp. 179–196, 1995.
- [239] U. Kruger, Y. Zhou, and G. W. Irwin, “Improved principal component monitoring of large-scale processes,” *Journal of Process Control*, vol. 14, no. 8, pp. 879–888, 2004.
- [240] B. R. Bakshi, “Multiscale pca with application to multivariate statistical process monitoring,” *AIChE journal*, vol. 44, no. 7, pp. 1596–1610, 1998.
- [241] P. Weber, D. Theilliol, C. Aubrun, and A. Evsukoff, “Increasing effectiveness of model-based fault diagnosis: A dynamic bayesian network design for decision making,” *IFAC Proceedings Volumes*, vol. 39, no. 13, pp. 90–95, 2006.

- [242] W. M. Campbell, D. E. Sturim, D. A. Reynolds, and A. Solomonoff, "Svm based speaker verification using a gmm supervector kernel and nap variability compensation," in *2006 IEEE International conference on acoustics speech and signal processing proceedings*, vol. 1. IEEE, 2006, pp. I–I.
- [243] G. Reeves, "Conditional central limit theorems for gaussian projections," in *2017 IEEE International Symposium on Information Theory (ISIT)*, 2017, pp. 3045–3049.
- [244] C. Delpha, D. Diallo, H. Al Samrout, and N. Moubayed, "Multiple incipient fault diagnosis in three-phase electrical systems using multivariate statistical signal processing," *Engineering Applications of Artificial Intelligence*, vol. 73, pp. 68–79, 2018.
- [245] P. Lare, S. Sarabi, C. Delpha, A. Nasr, and D. Diallo, "Stator winding inter-turn short-circuit and air gap eccentricity fault detection of a permanent magnet-assisted synchronous reluctance motor in electrified vehicle," in *2021 24th International Conference on Electrical Machines and Systems (ICEMS)*. IEEE, 2021, pp. 932–937.
- [246] P. Lare, S. Sarabi, C. Delpha, and D. Diallo, "Modelling of a pma-synrm for the detection of inter-turn short-circuit," in *Conférence des Jeunes Chercheurs en Génie Electrique,(JCGE 2022)*, 2022.
- [247] —, "A pmasynrm stator winding fault detection approach using an optimized pca-based ewma control scheme," in *2023 IEEE 32nd International Symposium on Industrial Electronics (ISIE)*. IEEE, 2023, pp. 1–6.
- [248] Q. Al Azze, "Field-oriented control of permanent magnet synchronous motors based on dsp controller," Ph.D. dissertation, Master's thesis, Southern Illinois University Edwardsville, 2014.
- [249] E. Kokiopoulou, J. Chen, and Y. Saad, "Trace optimization and eigenproblems in dimension reduction methods," *Numerical Linear Algebra with Applications*, vol. 18, no. 3, pp. 565–602, 2011.

# Appendix

## A.1 Permeance factors of the end windings







Cross-section of end winding	Nonsalient-pole machine		Salient-pole machine	
	$\lambda_{lew}$	$\lambda_w$	$\lambda_{lew}$	$\lambda_w$
	0.342	0.413	0.297	0.232
	0.380	0.130	0.324	0.215
	0.371	0.166	0.324	0.243
	0.493	0.074	0.440	0.170
	0.571	0.073	0.477	0.187
	0.605	0.028	0.518	0.138

Figure A.1: Permeance factors of the end windings in a synchronous machine

## A.2 Solutions of the speed PI parameters

The speed PI parameters can be found from the following conditions described in section 3.4.2.1.

$$\begin{aligned} \arg(G_{o\omega}(j\omega_{sc})) &= \arg\left(G_{o\omega}\left(\frac{j\omega_g}{\beta}\right)\right) = -180 + \phi_m \\ |G_{o\omega}(j\omega_{sc})| &= \left|G_{o\omega}\left(\frac{j\omega_g}{\beta}\right)\right| = 1 \end{aligned} \quad (\text{A.1})$$

Finding  $\beta$  from the phase margin is expressed as follows:

$$\begin{aligned} \tan^{-1}\left(\frac{\omega_g}{\beta} T_{si}\right) - \tan^{-1}\left(\frac{\omega_g}{\beta} T_g\right) - \pi &= -\pi + \frac{\pi}{3} \\ \tan^{-1}\left(\frac{\omega_g}{\beta} \frac{1}{\omega_{sc}}\right) - \tan^{-1}\left(\frac{\omega_g}{\beta} \frac{1}{\omega_g}\right) &= \frac{\pi}{3} \end{aligned} \quad (\text{A.2})$$

$$\tan^{-1}(\beta) - \tan^{-1}\left(\frac{1}{\beta}\right) = \frac{\pi}{3} \quad (\text{A.3})$$

This equation becomes [248]:

$$\beta^2 - 2\tan\left(\frac{\pi}{3}\right)\beta - 1 = 0 \quad (\text{A.4})$$

After finding  $\beta$ , the magnitude condition  $\left|G_{\omega}\left(\frac{j\omega_g}{\beta}\right)\right| = 1$  can be applied to find  $kp_{\omega}$ .

$$Kp_{\omega} = \frac{1}{\frac{3n_p}{4J\omega_g}\phi_{PM}\sqrt{\frac{1+\beta^2}{1+\left(\frac{1}{\beta}\right)^2}}} \quad (\text{A.5})$$

$$Ki_{\omega} = \frac{\beta^2}{\omega_g} \quad (\text{A.6})$$

### A.3 NAP Projection Effect minimization problem

The main principle of the NAP is to minimize the judgment of Projection Effect (**PE**) that is defined as the sum of the distance between each projection feature. The **PE** using the projection matrix  $\check{\mathbf{P}}$  is expressed as follows:

$$\mathbf{PE} = \sum_{i,j} W_{ij} \left\| \check{\mathbf{P}} \cdot \mathbf{x}_i - \check{\mathbf{P}} \cdot \mathbf{x}_j \right\|^2 \quad (\text{A.7})$$

where  $W_{ij}$  is a weight coefficient that quantifies the relation between two feature vectors.  $W_{ij}$  is set positive when the observations  $\mathbf{x}_i$  and  $\mathbf{x}_j$  belong to the same operating conditions and negative otherwise.

$$W_{ij} = \begin{cases} 1 & \text{if operating condition}(\mathbf{x}_i) = \text{operating condition}(\mathbf{x}_j) \\ 0 & \text{otherwise} \end{cases} \quad (\text{A.8})$$

$\check{\mathbf{P}} \in \mathbb{R}^{N \times n}$  is the projection matrix.

$$\check{\mathbf{P}} = \mathbf{I} - \sum_{i=1}^d \mathbf{\Delta}_i \mathbf{\Delta}_i^T \quad (\text{A.9})$$

where  $\mathbf{I}$  is an  $N \times N$  identity matrix,  $\mathbf{\Delta}_i$  represents the  $i^{\text{th}}$  NAP direction,  $d \leq N$  is the number of NAP directions to be removed from the feature space.

To find **PE**, let's define the difference  $\mathbf{d}_{ij} = (\mathbf{x}_i - \mathbf{x}_j)$ . **PE** can then be expressed as:

$$\begin{aligned} \mathbf{PE} &= \sum_{i,j} W_{ij} \left( \check{\mathbf{P}} \mathbf{d}_{ij} \right)^T \left( \check{\mathbf{P}} \mathbf{d}_{ij} \right) \\ &= \sum_{i,j} W_{ij} \mathbf{d}_{ij}^T \left( \mathbf{I} - \mathbf{\Delta}_i \mathbf{\Delta}_i^T \right)^T \left( \mathbf{I} - \mathbf{\Delta} \mathbf{\Delta}^T \right) \mathbf{d}_{ij} \\ &= \sum_{i,j} W_{ij} \mathbf{d}_{ij}^T \mathbf{d}_{ij} - \sum_{i,j} W_{ij} \mathbf{d}_{ij}^T \mathbf{\Delta} \mathbf{\Delta}^T \mathbf{d}_{ij} \end{aligned} \quad (\text{A.10})$$

with the constraint  $\mathbf{\Delta} \mathbf{\Delta}^T = \mathbf{I}$ . Ignoring terms independent  $\mathbf{\Delta}$ , we have,

$$\begin{aligned} \mathbf{PE} &= - \sum_{i,j} W_{ij} (\mathbf{x}_i - \mathbf{x}_j)^T \mathbf{\Delta} \mathbf{\Delta}^T (\mathbf{x}_i - \mathbf{x}_j) \\ &= - \sum_{i,j} W_{ij} \mathbf{x}_i^T \mathbf{\Delta} \mathbf{\Delta}^T \mathbf{x}_i - \sum_{i,j} W_{ij} \mathbf{x}_j^T \mathbf{\Delta} \mathbf{\Delta}^T \mathbf{x}_j \\ &\quad + 2 \sum_{i,j} W_{ij} \mathbf{x}_i^T \mathbf{\Delta} \mathbf{\Delta}^T \mathbf{x}_j \\ &= -2 \sum_{i,j} W_{ij} \mathbf{x}_i^T \mathbf{\Delta} \mathbf{\Delta}^T \mathbf{x}_i + 2 \sum_{i,j} W_{ij} \mathbf{x}_i^T \mathbf{\Delta} \mathbf{\Delta}^T \mathbf{x}_j \end{aligned} \quad (\text{A.11})$$

Using the identity  $\mathbf{A}^T \mathbf{B} \mathbf{B}^T \mathbf{A} = \text{Tr} \{ \mathbf{B}^T \mathbf{A} \mathbf{A}^T \mathbf{B} \}$ , where  $\text{Tr}$  stands for matrix trace, Equation A.10 can be written as:

$$\begin{aligned}
\mathbf{PE} &= -2\text{Tr} \left\{ \sum_{i,j} W_{ij} \mathbf{\Delta}^T \mathbf{x}_i \mathbf{x}_i^T \mathbf{\Delta} \right\} + 2\text{Tr} \left\{ \sum_{i,j} W_{ij} \mathbf{\Delta}^T \mathbf{x}_i \mathbf{x}_j^T \mathbf{\Delta} \right\} \\
&= -2\text{Tr} \left\{ \mathbf{\Delta}^T \mathbf{X} \text{diag}(\mathbf{W}\mathbf{U}) \mathbf{X}^T \mathbf{\Delta} \right\} + 2\text{Tr} \left\{ \mathbf{\Delta}^T \mathbf{X} \mathbf{W} \mathbf{X}^T \mathbf{\Delta} \right\} \\
&= 2\text{Tr} \left\{ \mathbf{\Delta}^T \mathbf{X} [\mathbf{W} - \text{diag}(\mathbf{W}\mathbf{U})] \mathbf{X}^T \mathbf{\Delta} \right\}
\end{aligned} \tag{A.12}$$

where  $\text{diag}(\mathbf{a})$  means converting  $\mathbf{a}$  into a diagonal matrix,  $\mathbf{U}$  is a column vector of all ones,  $\mathbf{W}$  the matrix of elements  $W_{ij}$ . It can be shown that minimizing  $\mathbf{PE}$  in Equation A.12 with the constraint  $\mathbf{\Delta}^T \mathbf{\Delta} = \mathbf{I}$  is equivalent to finding the eigenvectors with the smallest eigenvalues of [249]:

$$\mathbf{X} [\mathbf{W} - \text{diag}(\mathbf{W}\mathbf{U})] \mathbf{X}^T \mathbf{\Delta} = \lambda \mathbf{\Delta} \tag{A.13}$$

where  $\lambda$  the eigenvalues, and  $\mathbf{\Delta}$  the eigenvectors.